PRECISION ENGINEERING CENTER

2007 ANNUAL REPORT
VOLUME XXV
March 2008

Sponsors:	3M Corporation Lexmark International, Inc. Panasonic Boston Laboratory Vistakon, Johnson & Johnson Vision Care Inc. National Science Foundation Optical Research Associates Aerotech Precision MicroDynamics B & W Y-12
Faculty:	Thomas Dow, Editor Jeffrey Eischen Ronald Scattergood
Graduate Students:	David Brehl Qunyi Chen Stephen Furst Timothy Kennedy Lucas Lamonds Yanbo Yin
Staff:	Kenneth Garrard Alexander Sohn Paula Kelley
Consultants:	Karl Falter David Youden

TABLE OF CONTENTS

SUMMARY

The goals of the Precision Engineering Center are: 1) to develop new technology in the areas of precision metrology, actuation, manufacturing and assembly; and 2) to train a new generation of engineers and scientists with the background and experience to transfer this technology to industry. Because the problems related to precision engineering originate from a variety of sources, significant progress can only be achieved by applying a multidisciplinary approach; one in which the faculty, students, staff and sponsors work together to identify important research issues and find the optimum solutions. Such an environment has been created and nurtured at the PEC for over 25 years and the 100+ graduates attest to the quality of the results.

The 2007 Annual Report summarizes the progress over the past year by the faculty, students and staff in the Precision Engineering Center. During the past year, this group included 3 faculty, 6 graduate students, 2 full-time technical staff members and 1 administrative staff member. This diverse group of scientists and engineers provides a wealth of experience to address precision engineering problems. The format of this Annual Report separates the research effort into individual projects but there is significant interaction that occurs among the faculty, staff and students. Weekly seminars by the students and faculty provide information exchange and feedback as well as practice in technical presentations. Teamwork and group interactions are a hallmark of research at the PEC and this contributes to both the quality of the results as well as the education of the graduates.

The summaries of individual projects that follow are arranged in the same order as the body of the report, 1) design, 2) fabrication and 3) metrology.

1) DESIGN

Projects with an emphasis on design range from design of optical systems to dynamic, mechanical systems to control systems. The current projects involve Fresnel lenses and fast tool servos.

Fresnel Lens Design Software

Fresnel lenses are attractive for scanning systems because they provide optical power from a thin lens which are less expensive to manufacture and have less chromatic dispersion. However the discontinuous structure of the Fresnel zone transitions can generate undesirable diffraction effects. Matlab™ code has been developed both for designing several types of focusing Fresnel lenses and for analyzing the diffracted optical field at the image plane.

Fast Long Range Actuator - FLORA

The goal of this project is to develop a Fast Long Range Actuator (FLORA) to produce optical quality freeform surfaces with a range of ±2 mm at 20 Hz. The prototype uses a linear motor, air bearing supported lightweight triangular piston and a high-resolution, glass-scale linear encoder. Changes to the encoder, amplifier and controller have resulted in improvements in following error and disturbance rejection.

2) FABRICATION

Fabrication of precision components is an emphasis area for the PEC. Current projects include machining of Fresnel lenses, freeform optics, MEMS devices and single crystal silicon.

Fresnel Lens Testing and Fabrication

The PEC is fabricating and measuring Fresnel lenses for application to laser scanning systems. The performance of a commercial, conical groove Fresnel lens and a custom aspheric lens made at the PEC were measured using a CMOS array digital camera. The camera was calibrated to provide input light intensity as a function of image light levels from the pixel array to measure spot sizes. The conical Fresnel lens revealed too much diffraction but the aspheric lens showed promise. Fabrication techniques to create the fine groove spacing required are described.

Rake Angle Variation in Diamond Turning

A recent application of a fast tool servo to fabricate non-rotationally symmetric optical surfaces identified the change in force with rake angle as a significant error source of figure error. The part had a small amplitude sine wave on the periphery but the amplitude to wavelength ratio resulted in a large variation in rake angle(-45° to +45°). Based on measured cutting forces, a compensation technique is discussed.

High Pressure Phase Transformation of Silicon

Single point diamond turning was performed on (100) Si along the <011> direction using both -30° and -45° diamond tools with different feedrates for t-lathe and parallel fly cutting. Dislocation loops and slip planes were observed in TEM images at depths up to 250 nm below the surface of the t-lathe machined samples. In the fly cut samples no dislocations were found. TEM analysis is planned to analyze subsurface damage and to determine the deformation mode; that is, either high pressure phase transformation (HPPT) or dislocation movement.

Elliptical Vibration-Assisted Machining

The Ultramill EVAM tool has been used to machine millimeter-scale freeform optical surfaces. Simple spherical reflectors were made to evaluate and eliminate sources of surface errors to less than 60 nm RMS. A freeform fiber-optic beam splitter was designed and fabricated featuring a

high-sag off-axis ellipsoidal reflecting surface machined using the Ultramill. This beam splitter eliminates additional refracting elements, such as ball lenses, needed for collimation in existing designs. A test reflector was made and initial performance test and metrology results are presented.

3) METROLOGY

Metrology is at the heart of precision engineering – from measuring fabricated parts to calibration artifacts to dynamic system characterization.

Automatic machining process for thin-walled hemispheric shells

The fabrication of precision hemispheric shells requires substantial human effort to machine the inside and outside surfaces including transferring the shell and centering it on the spindle. To automate this process, a technique for part measurement and transfer is demonstrated. Measurement errors are tracked to ensure that the necessary tolerances are maintained. Future work will include automatic measurement and realignment of the shell on the chuck.

1 FRESNEL LENS DESIGN SOFTWARE

Kenneth Garrard
Precision Engineering Center Staff

Fresnel lenses are attractive for scanning systems because they provide optical power from a thin lens. Thin lenses are less expensive to manufacture via injection molding and have less chromatic dispersion. However the discontinuous structure of the Fresnel zone transitions may generate undesirable diffraction effects. Matlab™ code has been developed both for designing several types of focusing Fresnel lenses and for analyzing the diffracted optical field at the image plane. The concept of phase-matching was explored as a technique of ensuring that light waves from the zone structures constructively interfere at the image plane.

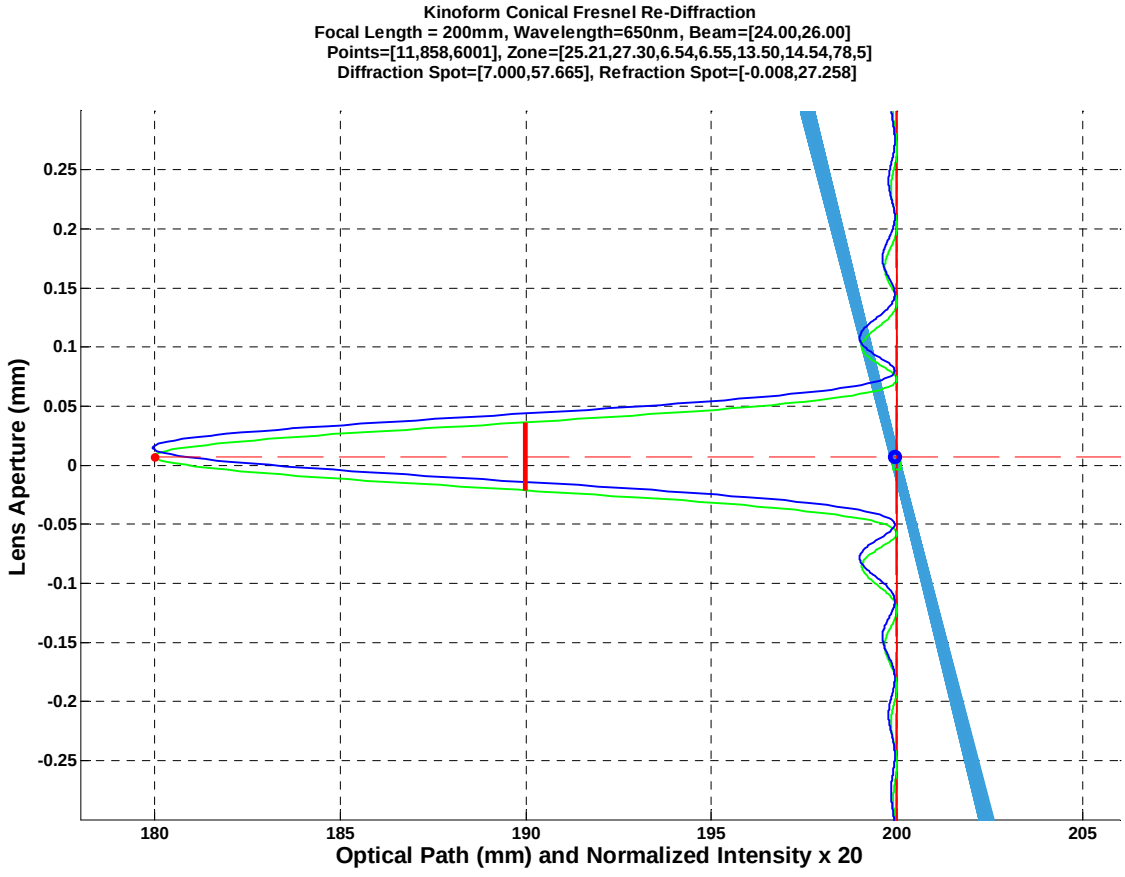

1.1 INTRODUCTION

Fresnel lenses are not typically used for imaging applications, because of the undesirable effects of groove structure on image quality. For this reason, optical design software for imaging applications generally only addresses Fresnel lenses in a very simplified manner. For example Zemax, Code V and Oslo treat Fresnel surfaces as ideal thin lenses with a surface curvature function to give the lens power[1]. This thin lens may be flat or superimposed on a curved substrate, which also provides power. In particular, the design codes do not consider the groove structure or manufacturing artifacts of Fresnel lenses. While this approach is adequate for many applications, it appears to lack attention to the item of most concern in the design of Fresnel lenses for laser scanning systems: The influence of the groove structures. For this reason a more direct design and modeling approach has been taken and tailor-made optical design software has been developed. Recent progress in the development of this software is described below.

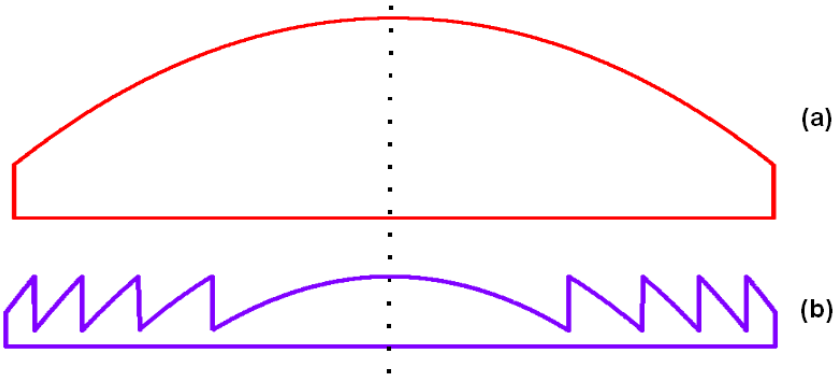

Figure 1. A conventional lens (a) is collapsed to form a Fresnel lens (b).

Fresnel lenses can provide optical power without the bulk of a conventional lens. Figure 1 shows how a plano-convex lens is collapsed into a Fresnel lens to provide a thinner lens with similar optical properties. Optical power is due to the curvature of a lens, not its thickness. Thinner lenses are easier and less expensive to replicate via molding than thick lenses or lenses with a large thickness variation. A thinner lens can also be expected to absorb less light. Previous work describing an iterative procedure for creating such a lens with conical grooves can be found in [1]. The resulting lens has uniform zone depth and zone width decreases with increasing radial offset. Such a lens focuses well when analyzed using Snell's law and ray tracing, even with a constant slope within each zone. However diffraction from the structure at each zone boundary influences the focusing characteristics of the lens and its transmission efficiency when the wave nature of light is considered. Variation in the zone shape, width, depth

[1] Non-sequential ray trace software such as TracePro and Zemax EE can analyze arbitrary surfaces but do not support their design or optimization.

and position along the optical path can all be used to control the interference of light from adjacent zones and hence diffraction at the image plane. In particular, matching the optical path length from the lens to the focus at adjacent zones ensures that all rays of light reaching the focal point have the same phase. Code for designing a phase matched kinoform Fresnel lens is described and an analysis of diffraction at the image plane is presented.

1.2 ASPHERIC FRESNEL LENS DESIGN CODE

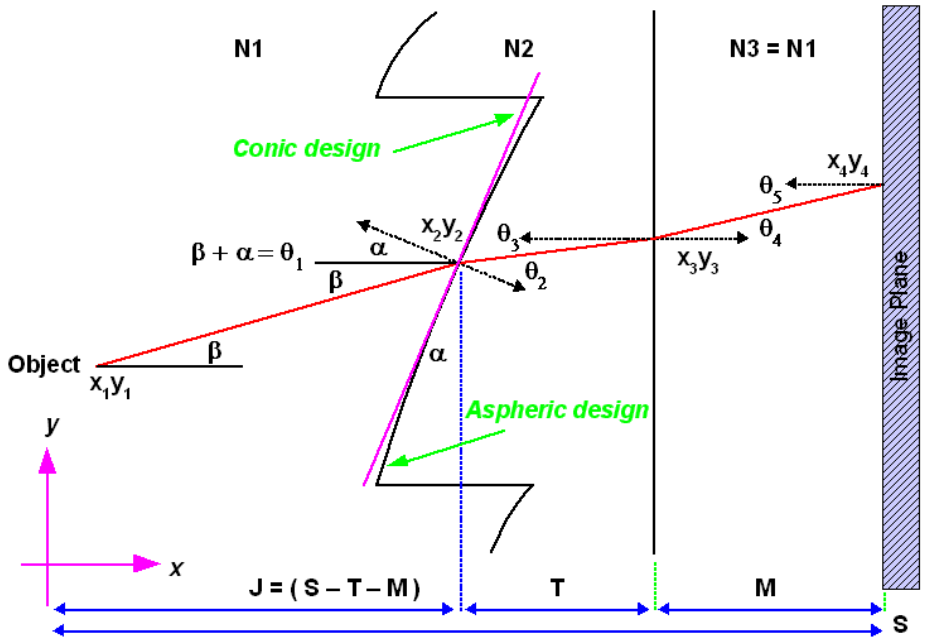

Figure 2. Ray propagation through a single Fresnel lens zone. For a conic design the surface slope for the central ray shown in red is used for an entire zone, whereas for an aspheric design, the slope changes continuously through the zone to focus each ray onto the image plane.

Ray propagation through a single lens is shown in Figure 2 for both a conic (i.e., flat) and an aspheric Fresnel lens zone. The equations describing the relationship between the ray heights and refraction angles are given in [1,2]. The conical Fresnel lens design code produces a lens with constant zone width and varying depth. Only one ray at the center of each zone is used to find the slope for that zone (as shown in magenta in Figure 2). That ray exactly intersects the focal plane at the desired ray height; however other rays in that zone intersect the focal plane above or below the focal point. By reducing the ray height spacing more conical zones (i.e., prisms) are produced and more rays arrive at the correct location on the focal plane. But there are disadvantages to increasing the number of zones. A larger percentage of the lens surface is either shadowed or does not direct incoming light toward the focal plane (e.g., rays incident on groove radii). For a scanned beam, as the beam angle increases the amount of light that enters the lens on the vertical zone boundaries increase. Also with increasing radius the slope of each

prism is steeper and since zone width is constant the depth must increase. Thus the zone step height increases. Machining a conical Fresnel surface with many zones requires a small radius or dead-sharp tool which is fragile. The time to achieve an acceptable surface finish may be very long and tool wear and process stability will limit performance.

An alternative to conical Fresnel zones with constant slope is to vary the slope with radius so that all incident rays converge at the desired focal point. For example, in Figure 1 the curvature of the plano-convex lens (a) is replicated in each zone of the collapsed Fresnel lens (b). Since the surface of each zone is translated along the optical path and the lens is thinner, the curvature of each zone must change to maintain focus. The required slope at each intersection point on the lens with a ray from the source is identical to that derived for the conical design and is calculated by solving the same equations [1,2]. However, instead of one ray at the center of each zone defining the slope for the entire zone, multiple rays are used to develop a curve as illustrated in Figure 2. An analytic formulation of how the curvature changes as a result of the collapsing process with respect to the optical characteristics of the lens (i.e., incoming and outgoing wavefront) is being studied. For the long focal length lenses designed in this manner, individual zone curvature is nearly parabolic.

1.2.1 ITERATIVE LENS DESIGN

A numeric algorithm for iteratively designing an aspheric Fresnel lens has been developed [1]. Coded in Matlab, this algorithm finds the required surface slope for each ray in a one element optical system. It does not optimize the slope for multiple rays with different object and image requirements, i.e., the beam scanning problem. Instead each ray is considered independently and by iterating from the inside (optical axis) to the outside (maximum radius) a lens shape is found that focuses each ray to an image point. The intersection of each incoming ray with the extension of the surface from the previous iteration is found. Then a new slope is calculated for this point that satisfies the focal criteria and the process continues. By considering a large number of closely spaced parallel rays, an approximation to the continuous surface that perfectly focuses the light is built point-by-point.

Without constraining the x or y location of points on the lens surface a general plano-convex aspheric lens is produced. For a Fresnel lens, displacement parallel to the optical axis (x direction) is limited to a fixed amount and a step in the negative direction (back toward the object) is taken when this limit is exceeded as shown in Figure 3. The result is a Fresnel lens with constant zone depth, arbitrary zone widths and curved zone profiles. Figure 4 shows the profile of a 200 mm focal length Fresnel lens (object at infinity) with 100 mm aperture that was designed by this code. The lens is 2.33 mm thick (top of zone steps to lens back). As expected, the constant depth zone profiles become narrower and steeper with increasing radius.

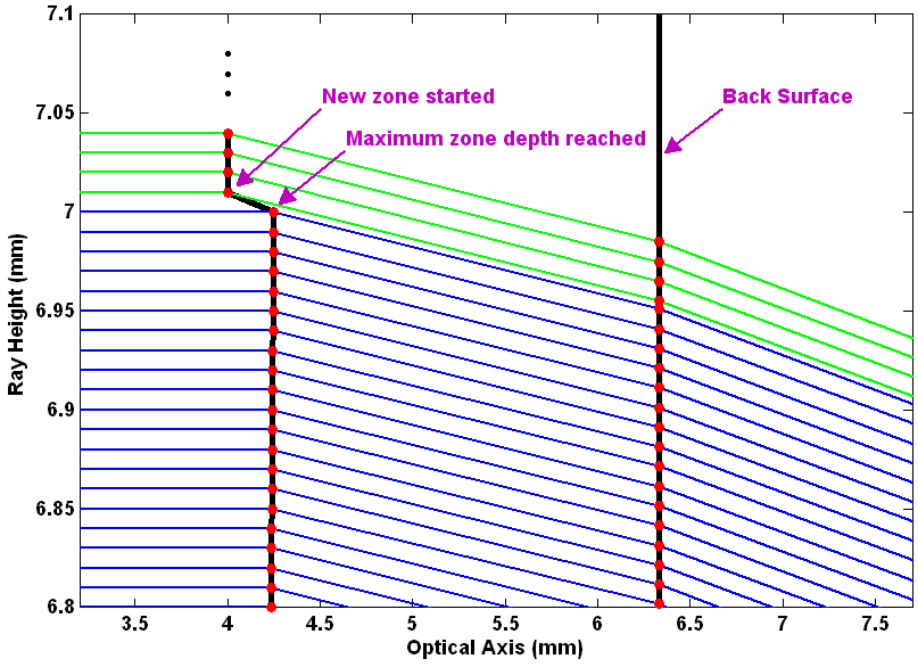

Figure 3. Aspheric lens design process. When the maximum zone depth is reached (blue), a new zone is started (green).

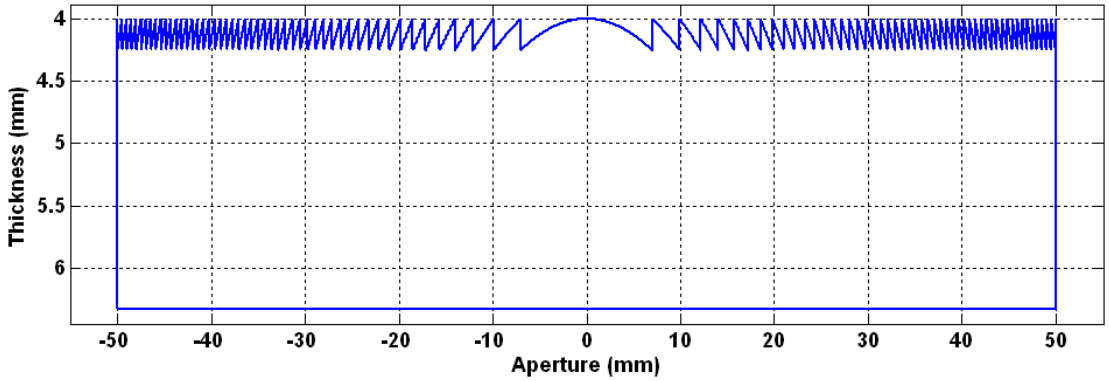

Figure 4. F200 Aspheric Fresnel lens with 51 zones. (The aspect ratio of the plot is not 1:1).

Each iteration of the design code depends on the prior ray trace results only in that those rays were used to arrive at the local slope of the current ray-surface intersection point. Thus the constraints: incoming rays parallel and normal to the lens, focus at a single point on the image plane, constant zone depth, unrestricted zone width and plano back surface are not limitations of the algorithm. As long as the only unknown parameter for each ray is the surface slope on one side of the lens, a unique solution can be found with a nonlinear root finding procedure [2]. The principle difficulty with varying the zone depth and width or having a curved lens back surface is determining the criteria for changing those parameters.

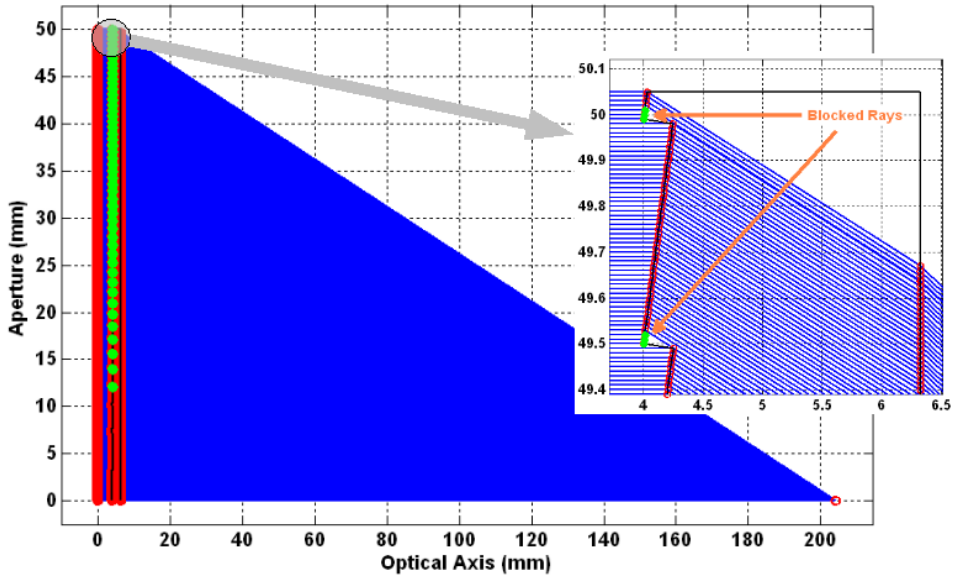

Figure 5. Complete aspheric lens design with blocked rays indicated by green dots.

Figure 5 shows a completed aspheric design ray trace with intersection points marked by red circles and blocked rays indicated by green dots. A ray is blocked when it is refracted at the front surface of the lens so that it does not intersect the back of the lens. As seen in Figure 5 this happens at the start of a new zone when the surface slope is steep enough to cause the refracted ray to strike the inside of the prior zone step. More rays are blocked if the zones are deeper or the aspheric surface curvature increases. For this lens, about 2.8% of a normal incidence, parallel wavefront is blocked.

1.2.2 TOOLING ARTIFACTS

It is apparent from Figure 4 that the shape of the front surface of this Fresnel lens cannot be machined with a convex tool. The bottom of each zone is the concave intersection of a straight line (zone step) and a convex curve and thus has no curvature. A close approximation to the surface can be machined with a small radius tool at the expense of long cutting time to achieve acceptable surface finish. For a circular tool profile in a radial plane, the path of the tool center that results in the tool edge tracing out the desired surface shape must be calculated. For a continuous surface this is a straightforward process, but for a Fresnel lens the zone intersections must be handled as a special case. At each zone boundary the tool must be tangent to both the aspheric profile and the nearly vertical, flat wall of the zone step. However as shown in Figure 6a the tool cannot cut one surface completely without over-cutting into the other surface at the concave intersections. The intersection of normal vectors from each surface with lengths equal to the tool radius identifies this transition point. The convex intersection can be achieved with a radius tool. The transition point is the intersection of the two tool paths after extending each along the same slope as its endpoint. Matlab code that finds these intersections (see Appendix

C) and generates a motion program for the PEC's custom controller for the ASG 2500 Diamond Turning Machine has been written [1].

The intersection of each zone asphere with the zone step will resemble the shape of the tool as the transition is made in the cutting path from negative slope to positive slope at the bottom of each zone. Figure 6b shows a plot of the surface that would be machined by the cutting path generated by Fresnel tool radius compensation code discussed above. This process is equivalent to the morphological dilation of the tool path (an image) with the projection of the tool into the cutting plane (a structuring element).

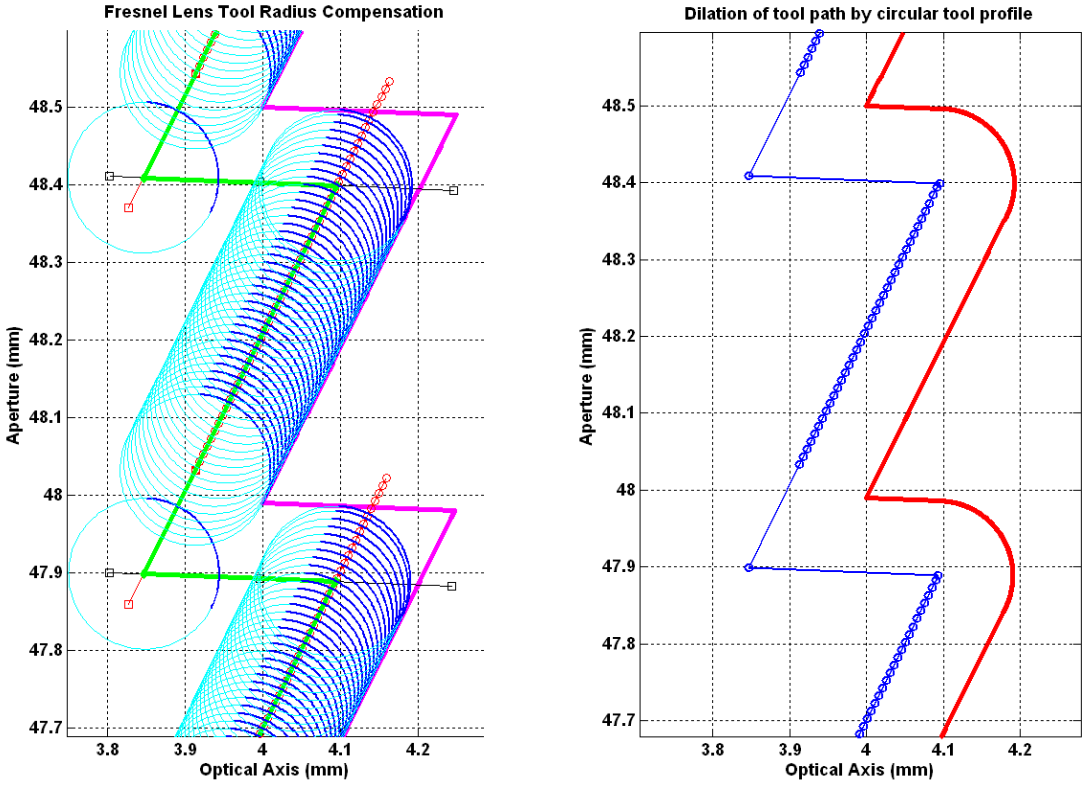

(a) (b)

Figure 6. Tool radius compensation for a Fresnel lens. In (a) the magenta line is the aspheric Fresnel lens, the green line is the tool path and the blue arcs are successive tool edge positions. In (b) the blue line with dots is the path followed by the center of the tool and the solid red line is the resulting machined surface with a radius at the bottom of each zone transition.

A procedure to trace rays through the as-fabricated lens shape was written to 1) validate the process of creating the tool path from the design (i.e., Do parallel rays converge at the focal point?) and 2) investigate the effects of the diverging rays incident on the concave arcs left by the tool at the zone boundaries. This code is given in [1] and can also be used to simulate the

effect of thickness variation on focus, tilt in the incoming wavefront and numerous other geometric variations. Figure 7 shows the ray trace results for an 80 mm focal length Fresnel lens. Note that the ray fans diverge from the concave tooling arc corners and cover the image plane. None of these rays converge to the focal point, but they do represent a loss of efficiency. However some light incident near the top of the convex zone transitions that would be blocked by perfect intersections at the bottom of each zone makes it through the lens because the intersection is truncated into a rounded corner.

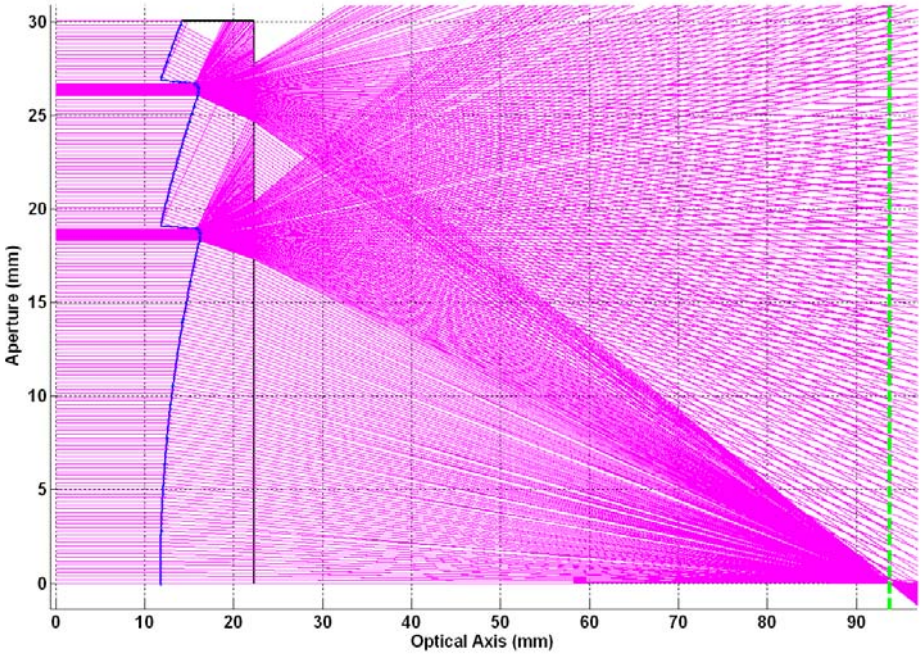

Figure 7. Raytrace through a Fresnel lens. The diverging rays from the tooling arcs flood the image plane from about 1 mm above the focal point to infinity. Some of these rays internally reflect at the back surface. The rays through the aspheric zones converge at the focal point.

1.3 DIFFRACTION

1.3.1 THEORY

In the 17th century Christiaan Huygens explained the propagation of light by assuming that every point on a wavefront acts as the source of a spherical secondary wave of the same frequency that spreads out in all directions. The envelope of all the secondary waves forms a new wavefront. Fresnel extended the Huygens principle to account for diffraction by considering the mutual interference of the secondary wavelets and how their superposition can be used to find the amplitude and phase of the optical field at any point in space.

In the late 19th century Kirchhoff formulated the Fresnel-Huygens principle mathematically as illustrated in Figure 8. Equation 1 relates the electromagnetic disturbance seen by an observer at point *P* to a light source at P_0 through an aperture, *A*.

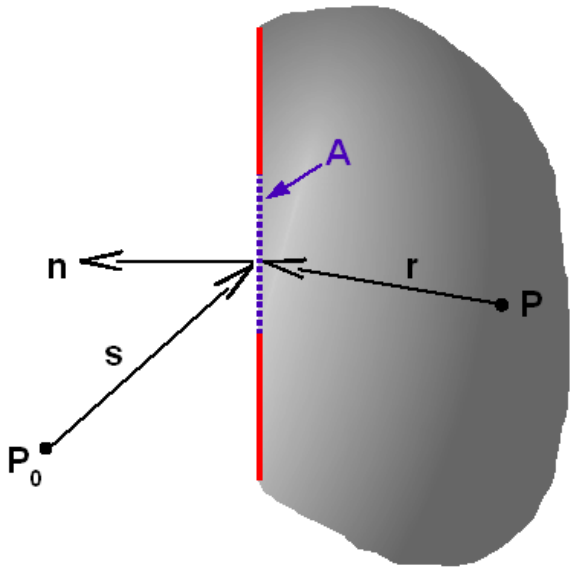

Figure 8. Geometry of the Fresnel-Kirchhoff diffraction formula.

$$U_P = \frac{-iU_0}{2\lambda}\iint_A \frac{e^{i\frac{2\pi}{\lambda}(r+s)}}{r\cdot s}\left[\cos(n,r)-\cos(n,s)\right]ds \tag{1}$$

U_P is the optical field at *P*, U_0 is the light amplitude and phase at P_0, λ is the wavelength and the vectors *r*, *s* and *n* have a common endpoint on the aperture. The integration is taken over all vectors from P_0 to *P* through the aperture. The quantity *cos(a,b)* is the cosine of the angle between arbitrary vectors *a* and *b*. This dependence of the optical field at an image point on the angular difference between incident and propagated light at the aperture interface is known as the inclination factor. Using the dot product operator to calculate the angles between the aperture normal, *n*, and vectors to *P* and P_0 (*r* and *s* respectively), gives Equation 2.

$$U_P = \frac{-iU_0}{2\lambda}\iint_A \frac{e^{i\frac{2\pi}{\lambda}(r+s)}}{r\cdot s}\left[\frac{n\cdot r}{|n||r|}-\frac{n\cdot s}{|n||s|}\right]ds \tag{2}$$

The primary difficulty in solving Equation 2 for arbitrary apertures (e.g., an aspheric Fresnel lens) is the $r \cdot s$ term in the denominator of the integrand, specifically finding an algebraic representation for the lengths of *r* and *s*. The Fresnel approximation expands the product as a

Taylor series, retaining only the scalar and quadratic terms and hence assumes that wavefront curvature is parabolic instead of spherical. This is reasonable as long as P_0 and P are relatively distant from the aperture with respect to λ. If the observation point is very distant with respect to aperture size then rays reaching P are nearly parallel. In this case, wavefront curvature can be ignored leaving only linear terms that contribute to the value of the integral. This latter case is the Fraunhofer approximation and can be used when Equation 3 is satisfied.

$$A^2\left(\frac{1}{r}+\frac{1}{s}\right) << 2\lambda \tag{3}$$

Fraunhofer diffraction from single and multiple slit apertures and a circular aperture can be solved analytically. A tilted aperture changes the direction of the maximum intensity of the propagating wave and can also be calculated with Equation 2. Furthermore in the Fraunhofer regime it can be shown that the aperture shape function and the diffraction pattern form a Fourier transform pair. However for a scanning lens system utilizing a discontinuous surface such as a Fresnel lens with arbitrary zone spacing, depth and curvature, an analytic formulation of the diffraction pattern is not feasible. And unless the system has a very long focal length the Fraunhofer integrals cannot be used. For these reasons a numeric approach based on a straightforward interpretation of the Fresnel-Huygens principle was taken.

1.3.2 NUMERICAL SIMULATION OF DIFFRACTION

Light arriving at an image point from all possible paths through an aperture contributes to the magnitude and phase at that point. Equation 2 calculates the diffraction pattern for each observation point, P, as a weighted sum of secondary spherical sources of light from all aperture locations. Each vector from the aperture to P is weighted in proportion to the cosine of the angle between that vector and the normal vector of the aperture. Thus a vector perpendicular to the source wavefront has maximum intensity and a vector parallel to the wavefront has no intensity. The phase of the light for each vector is simply the remainder of the optical path length divided by the wavelength. That is, the fractional portion of the wave when it reaches the image plane. By integrating over the aperture and preserving both magnitude and phase, the secondary wavelets interfere constructively and destructively to produce a diffraction pattern across an image plane. The equivalence of this process with the Fourier transform should be apparent. The magnitude and phase of a signal at any point in time is the sum of many waves of varying frequencies, amplitudes and initial phases.

Matlab code has been written to implement this process. The function given in Appendix A iterates over a given number of image point locations (not necessarily on a plane) and calculates the magnitude and phase of light reaching each point from all aperture locations. The aperture

locations are *(x,y,z)* coordinates on a lens surface. Difficulties with the functional representation of complex aperture shapes and vector distances are avoided by directly calculating the optical path length between all lens and image points. By considering a large number (i.e., thousands) of closely spaced points on the lens and the image plane, diffraction from a Fresnel lens or other discontinuous aperture is easily modeled. Equation 4 calculates the magnitude and phase of light at point P for a set of vectors from the aperture, r, the lengths of those vectors, L, normal vectors from the aperture, n, the initial optical field, U_L, the source wavelength, λ, and the refractive index of the medium, M_x.

$$U_P = \sum_A \left[U_L \cos\left(\tan^{-1}\left(\frac{\|r \times n\|}{r \cdot n} \right) \right) \frac{e^{iM_x \frac{2\pi}{\lambda} L}}{L} \right] \tag{4}$$

Equation 4 is calculated for all points on the image plane. The diffraction intensity distribution at the image plane is the squared absolute value of the resulting complex vector. The distribution is then normalized by dividing the distribution by its maximum value. The initial optical field, U_L, is calculated from Equation 5 for a parallel incoming wavefront. The refractive index of the lens is R_x and d is a vector of distances the light travels through the lens before reaching the set of aperture locations.

$$U_L = e^{iR_x \frac{2\pi}{\lambda} d} \tag{5}$$

Utilizing the parallel vector computation capabilities of Matlab about 15 seconds is needed to compute the diffraction pattern of a lens aperture represented by 858 data points and an image plane of 6001 points, or just over 5 million vectors from aperture to image.

Algorithm Validation

Before using the diffraction code for analysis of a Fresnel lens, several test cases were run for well understood simple aperture geometries. Figures 9 and 10 show the diffraction patterns of light from a single slit aperture observed at a distance significantly larger than either the wavelength or the aperture width, that is, the Fraunhofer condition (Equation 3) is satisfied. In Figure 10 the aperture is tilted 2° with respect to the image plane. In both cases the diffraction pattern is a squared sinc function, which is the analytical result found in numerous optics texts [6-8]. The tilted aperture shifts the diffraction peak on the image plane according to Snell's Law. The plots show a single refracted ray through the center of the aperture and its intersection with the image plane as a large dot.

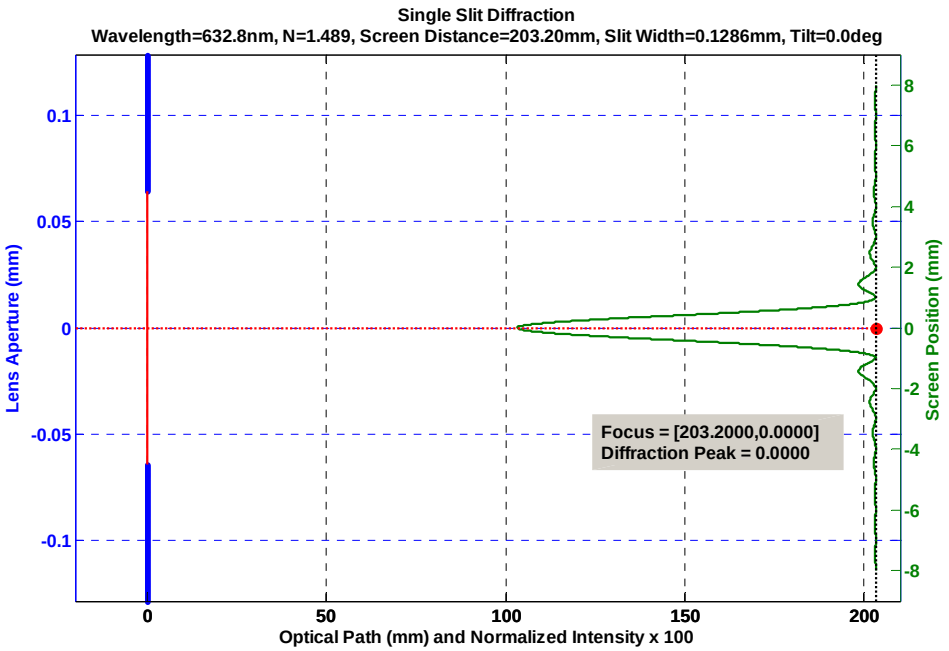

Figure 9. Diffraction from a single slit.

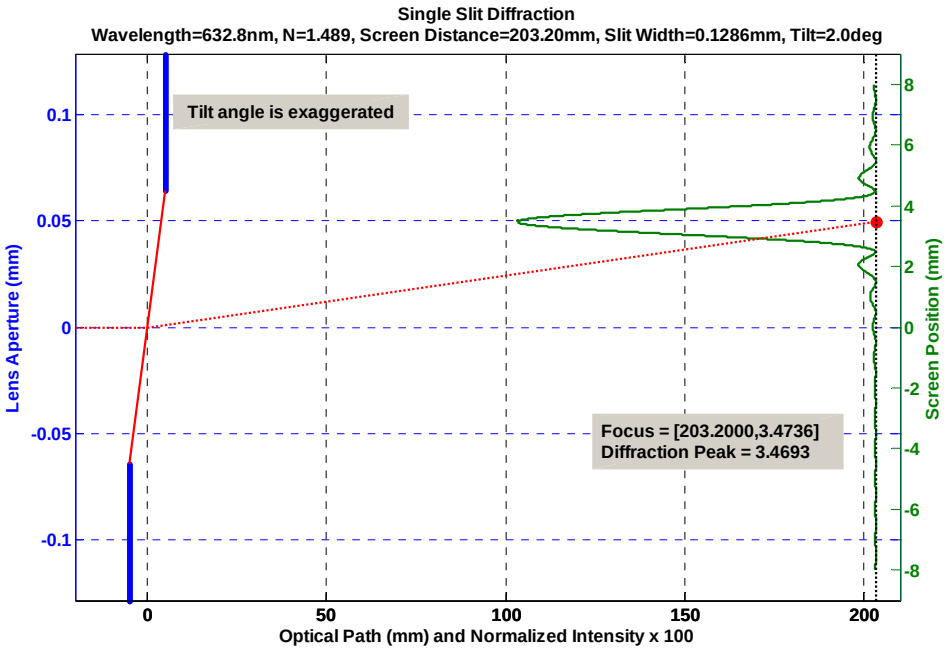

Figure 10. Diffraction from a single slit tilted 2°.

Figures 11 and 12 illustrate diffraction of light through an aperture which is masked to form 5 slits. In Figure 12 the aperture is tilted 2° with respect to the image plane and in both cases the observation screen is distant and the Fraunhofer requirement holds. For multiple slits there is interference between the secondary spherical wavefronts propagated through each slit. The

resulting multi-peaked pattern is the same as the textbook analytic solution which is the convolution of the squared sinc functions for each sub-aperture slit. As with the single slit, tilting the aperture shifts the pattern on the image plane in the same direction and by approximately the same amount as that of the central refracted ray.

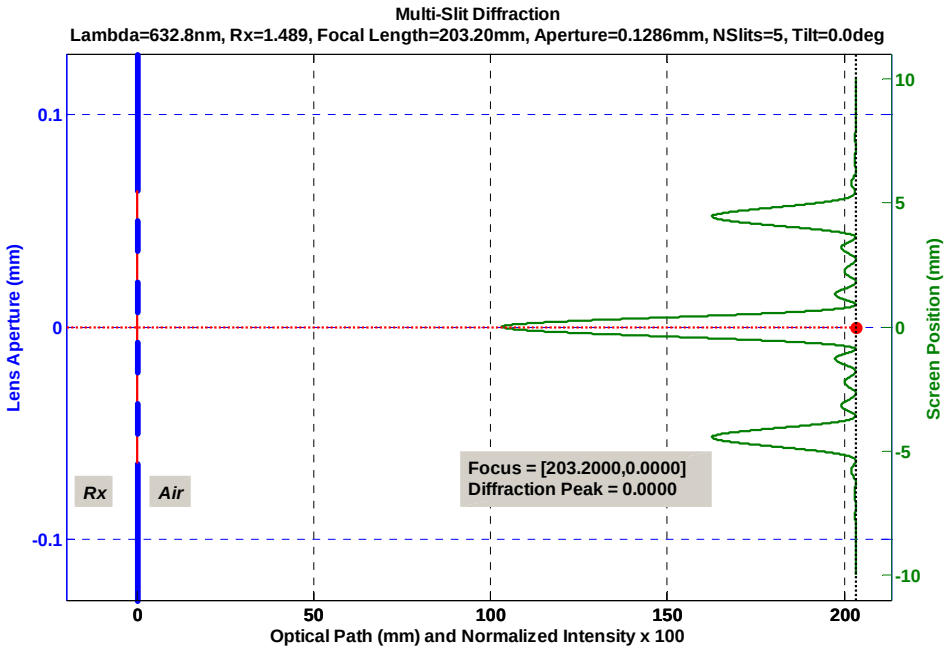

Figure 11. Diffraction from a multiple slit aperture.

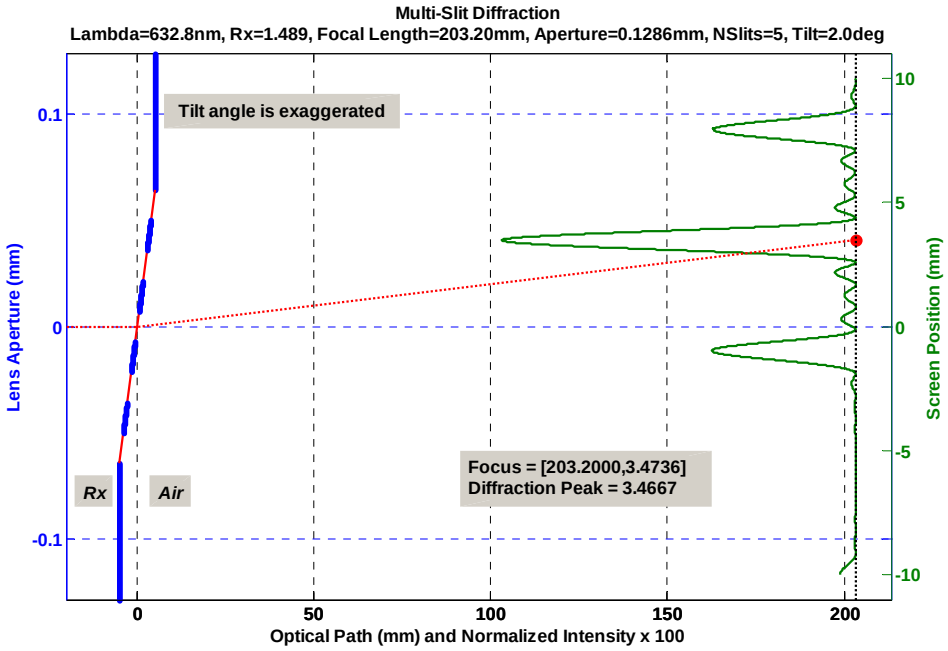

Figure 12. Diffraction from a multiple slit aperture tilted 2°.

Extension to Multi-element lenses

The numerical simulation code is currently being extended to implement both refraction and diffraction of light through multiple apertures and refractive index changes. Hybrid refraction/diffraction ray tracing code could be implemented by iteratively applying the Fresnel-Huygens principle (Equation 4) and Snell's Law at each surface between light source and image plane. At each interface a large number of complex rays would be propagated in all directions until they intersect with another surface. At each of those intersection points the process is repeated for another spherical wavefront modeled as a large set of rays extending in all directions. This brute force approach quickly becomes intractable as the total number of rays increases geometrically with the number of surfaces. Furthermore a large percentage of rays may refract away from the image plane, reflect or refract non-sequentially (i.e., the next surface cannot be predetermined from the system geometry), or reflect inside a lens an unknown number of times. In fact, for an arbitrary lens system determining if a ray from the source ever reaches the image plane is recursively undecidable.

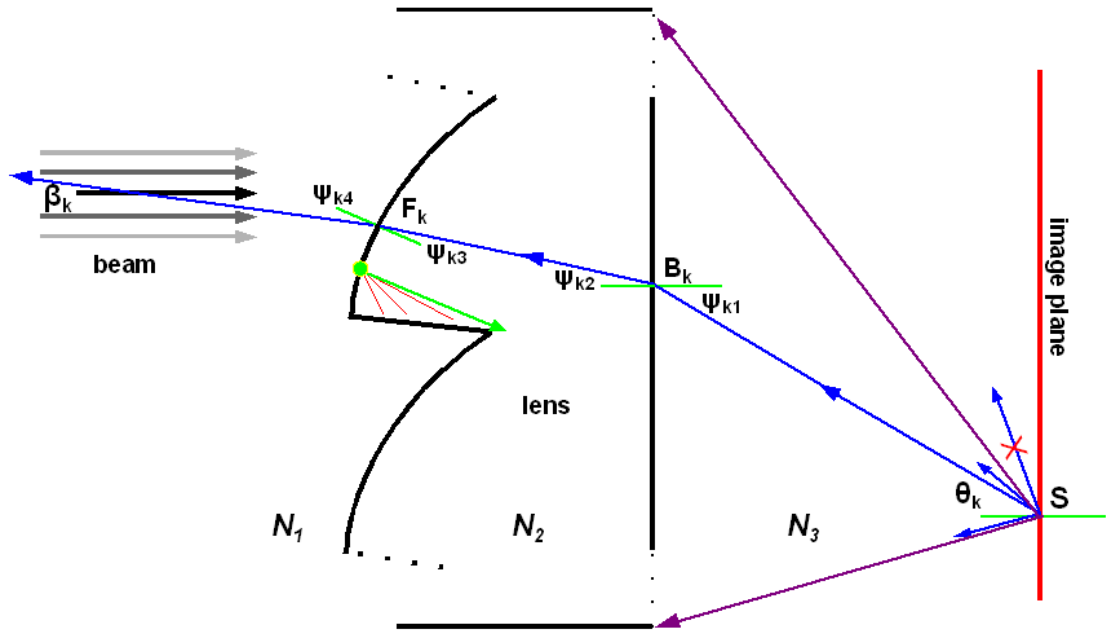

Figure 13. Refraction of diffracted light in a Fresnel lens.

A different approach is to start with a number of equally spaced points on the image plane and trace the wavefront backwards from each one toward the source. For example, consider a Fresnel lens with the grooved side facing toward a source beam of light as illustrated in Figure 13. The phase and amplitude of light reaching point S is the sum of the phases and amplitudes of rays taking all possible paths from the intersection of the incident beam on the front surface of the lens to S. The diffraction intensity distribution is the square of the absolute value of this

complex sum. Looking backward from each image point toward the source, only those rays that eventually intersect the incident beam can contribute to the diffraction pattern.

The following procedure is proposed for each point, S, on the image plane,

1. Find the angular range of beam rays that can refract through the lens to the image plane. A worst case estimate includes the entire back surface of the lens. However many rays are blocked by lens features or internally reflected. Reflections can be considered, but the number of ray – surface intersections must be limited to prevent infinite iteration.
2. For each candidate ray, θ_k, at S,
   a. Trace the ray from S to the lens front surface arriving at point F_k. Find Ψ_{k1}, Ψ_{k2}, Ψ_{k3}, Ψ_{k4}. using Snell's Law.
   b. Find the angle, β_k, between the refracted ray at F_k and the incoming beam.
   c. Calculate the phase at S as the sum of the initial phase at F_k, the optical path length from S to B_k and the optical path length from B_k to F_k.
   d. Calculate the amplitude contribution of this ray at S as the initial amplitude at F_k times an inclination factor. This initial amplitude is based on a Gaussian beam and the inclination factor is the cosine of β_k.
3. Sum amplitudes and phases over all rays at S to calculate the diffraction amplitude and phase at that point.

1.4 PHASE MATCHED LENS DESIGN

The purpose of the lens system for a scanner is to focus the source laser beam into a small spot on the image plane. The ideal spot location is a linear function of scan angle (i.e., the F-theta condition). The size and shape of the spot is determined by both refraction and diffraction. Even if the lens surfaces were designed so that all rays converge at the same location on the image plane, the spot size will not be zero due to diffraction. The best possible case for a single circular aperture is an intensity cross-section similar to Figures 9 and 10 with 95% of the light energy concentrated in a central area of angular diameter $1.22\ \lambda / D$, where D is the diameter of the aperture and λ is the wavelength. As shown by the multiple slit examples, each slit generates a similar pattern with a peak directed to a different location on the image plane. The final result is a complex summation (i.e., amplitude and phase) that produces the multiple peaks shown in Figures 11 and 12 and hence a larger and more complex central spot.

Each zone of a Fresnel lens both redirects incident light toward a focal point and produces a diffraction pattern due to the discontinuous boundaries with adjacent zones. However it is possible for the diffraction peaks to all be directed to the same point on the image plane. This is done by varying the width and depth of the zones to ensure that the optical path length from the center of each zone is an integer multiple of the incident light wavelength. This apodization

process (i.e., aperture tuning), matches the phase of the refracted light so that the location of constructive interference can be controlled.

1.4.1 KINOFORM LENS

The resulting lens is known as a kinoform lens and may be designed using Equation 6 to select the radial distance, R_j, from the center of the aperture to the boundary of each Fresnel zone [3].

$$R_j^2 = 2jM_j\lambda L \tag{6}$$

The wavelength is λ, L is the distance to the focal point as measured parallel to the optic axis, j is the zone number and M_j is the phase match order for the j^{th} zone. The phase match order specifies how many integer multiples of wavelength there are in the difference between the optical path lengths for zone j and zone j-1. Equation 6 is approximate and valid only in the paraxial case, that is, when $L >> R$. However, it is simpe to find an exact relation for the radial separation of adjacent Fresnel zone boundaries such that light from all zones arrive at the focal point in-phase.

Exact Phase Matching

Figure 14 illustrates the kinoform phase matching concept for two adjacent zones of a conical Fresnel lens. The light rays incident at heights R_1 and R_2 will be in-phase when they reach the focus if D_1 and D_2 differ by an integer multiple (the phase match order) of the wavelength.

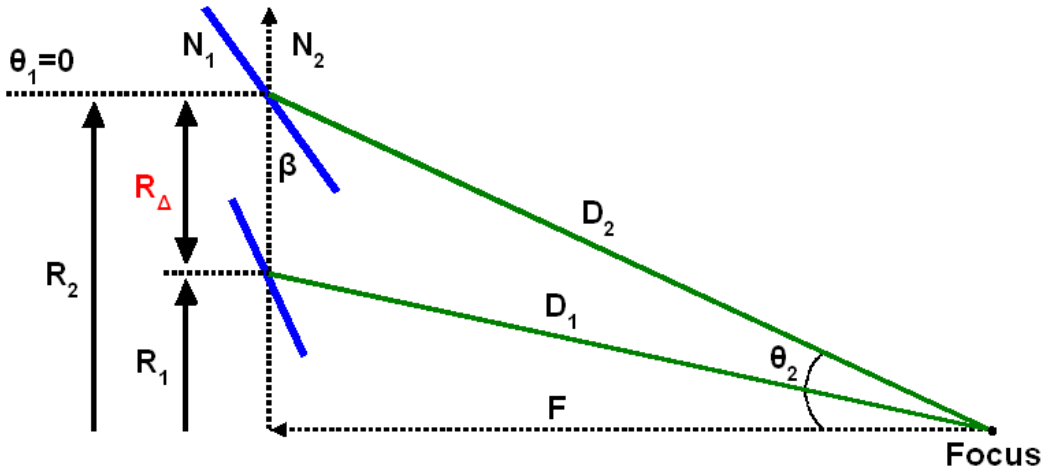

Figure 14. Kinoform phase matching.

Equation 7 relates the optical path length for adjacent zones with the matched phase difference of light waves reaching the focus.

$$M\lambda = D_2 - D_1 = \sqrt{F^2 + R_2^2} - \sqrt{F^2 + R_1^2} = \sqrt{F^2 + R_1^2 + 2R_1R_\Delta + R_\Delta^2} - \sqrt{F^2 + R_1^2} \tag{7}$$

Solving Equation 7 for R_Δ gives the radial distance to the next zone.

$$R_\Delta = \sqrt{R_1^2 + M^2\lambda^2 + 2M\lambda\sqrt{F^2 + R_1^2}} - R_1 \tag{8}$$

Similarly the distance to the previous zone with a smaller radius is given by,

$$R_{\Delta-} = R_1 - \sqrt{R_1^2 + M^2\lambda^2 - 2M\lambda\sqrt{F^2 + R_1^2}} \tag{9}$$

Finally, for any R, F, M and λ, the radial locations of the surrounding zone centers is given by Equation 10,

$$R^{\pm} = \sqrt{R^2 + M^2\lambda^2 \pm 2M\lambda\sqrt{F^2 + R^2}} \tag{10}$$

A Matlab function that designs a kinoform Fresnel lens to focus a parallel incident beam of light to a point has been written and is given in Appendix B. Using Equation 10 it first calculates the locations of the Fresnel zone centers for the desired aperture, wavelength and phase match order. Equation 11 is then used to find the slope of the lens surface at those center locations that refracts an incident ray to the focus. The geometry associated with Equation 11 is shown in Figure 14. η is the ratio of the refractive indices on opposite sides of the aperture, N_1 over N_2.

$$\tan\beta = \frac{\sin\theta_1 + \sin\theta_2}{\sqrt{\eta^2 - \sin^2\theta_1} - \cos\theta_2} \tag{11}$$

Multiple rays are traced to the focal point from each zone and the diffraction pattern at the image plane is calculated using the function in Appendix A.

Kinoform Lens Design Code

Figure 15 shows a plot from the kinoform design code. The plot shows the lens aperture, the incident beam, the diffraction pattern at the image plane and a ray trace from the lens to the focus. Output vectors containing (x,y,z) coordinates of the aperture, surface slopes, zone boundary locations and depths, ray surface intersections, and the diffraction intensity distribution

are also produced. The plot title information includes both the refraction spot location and width at the image plane and the diffraction peak center location and size (full width at half max).

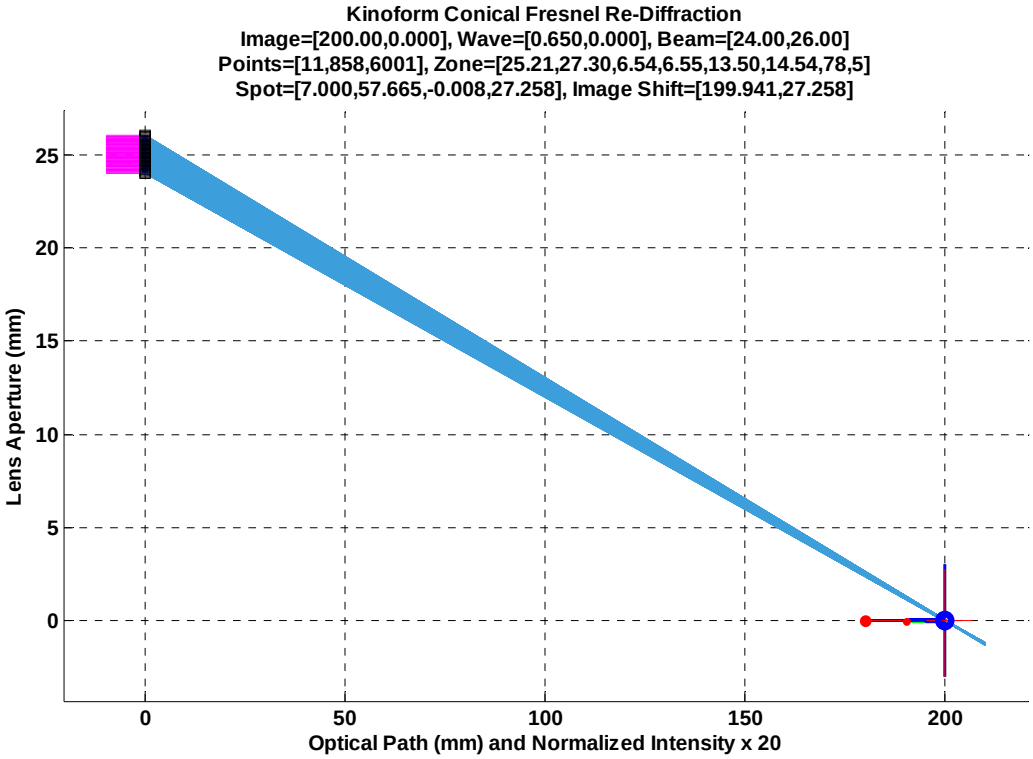

Figure 15. Kinoform lens ray trace and diffraction analysis.

Zooming into the plot in Figure 15 reveals the structure of the conical zone kinoform lens surface. A small portion of the lens and ray trace is shown in Figure 16. Three complete zones near the center of the aperture are shown. The difference in zone depth and width is very small and is not apparent in the plot because the wavelength (650 nm) is relatively small and the focal length is relatively large (200 mm), requiring a very small change in zone spacing to produce phase matched optical path lengths from the central ray (thick magenta lines) of each zone. For this lens there are 78 zones over a 2 mm aperture that range in depth from 6.54 to 6.55 µm and in width from 25.21 to 27.30 µm. The slope of each zones ranges from 13.50° to 14.54° and is calculated with Equation 11 so that the central rays converge exactly at the focus. The thinner rays (light blue lines) that start at the lens surface are traced past the image plane to show the spread of refracted light that will result from using a conical instead of aspheric zone profile.

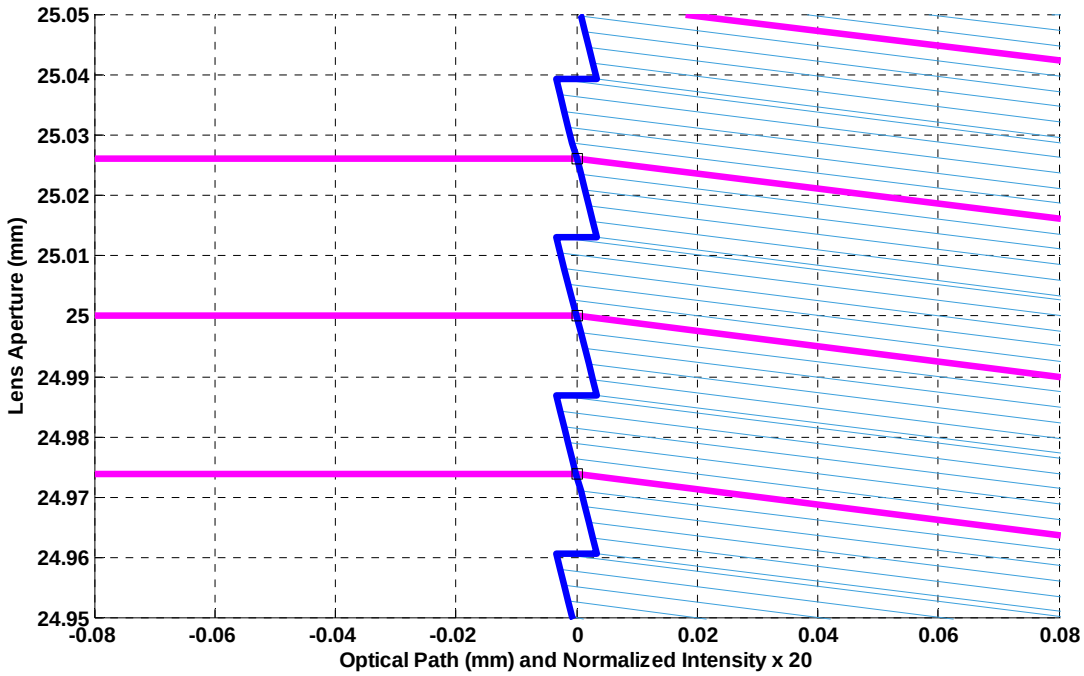

Figure 16. Kinoform zone structure.

The diffraction pattern as observed at the image plane is shown in Figure 17. By matching the phase of refracted rays from the lens to the image, the maximum intensity from each zone occurs at the same location, very close to the focus. The plot shows the diffraction distribution (green line) with a marker at its peak (7 μm from the focus) and a bar indicating its width (58 μm) at half the maximum value. The ray trace intersection with the image plane near the focus is shown in Figure 18. Since the slope of each zone is constant, rays that are not incident at the center of the zone do not converge exactly at the focus. The width of the region of the image plane where the ray cross the image plane is 27.26 μm and the geometric center of this region is 8 nm from the intended focal point. The figure shows both the center of the refracted rays (green square) and the center of the diffraction pattern (blue circle). The small offset between the refraction and diffraction patterns cannot be removed by focusing. That is, shifting the image plane to the center of the original diffraction pattern (green curve) only slightly increases the width of the refraction spot, however a new diffraction pattern calculated at this new focus is also shifted (blue curve).

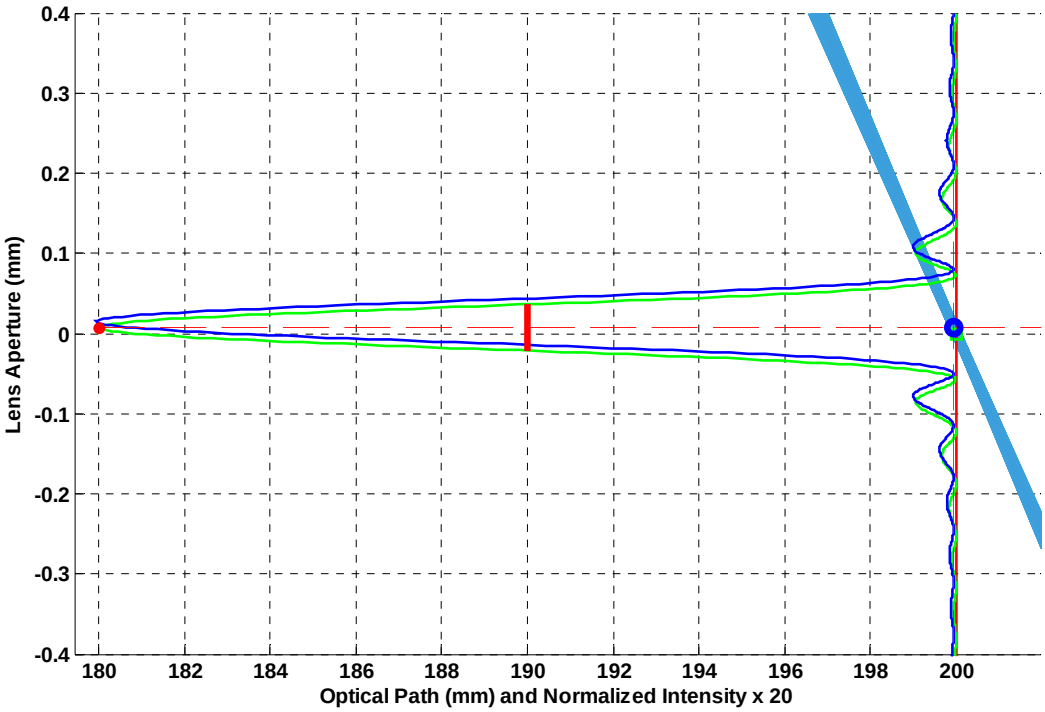

Figure 17. Kinoform diffraction pattern and ray trace at the image plane.

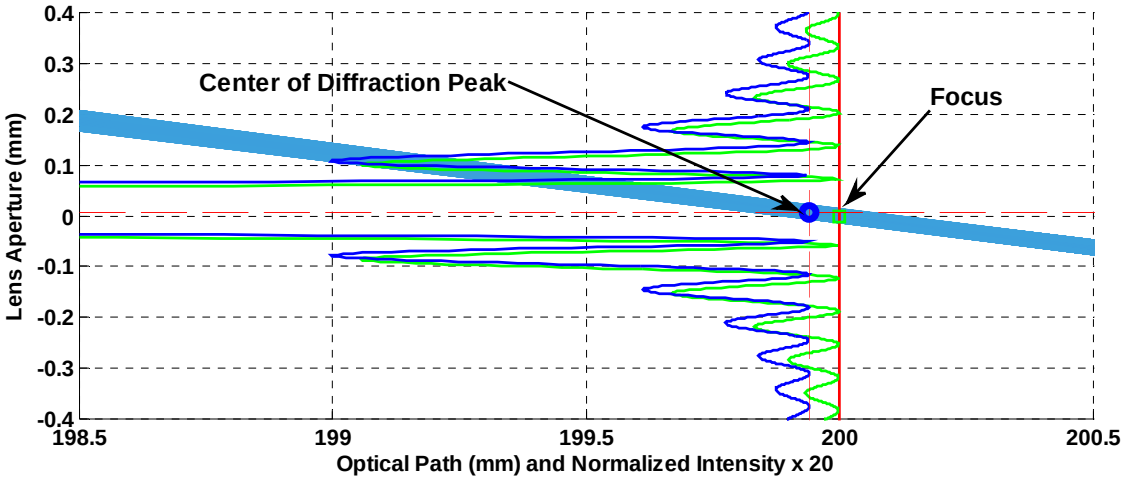

Figure 18. Kinoform ray trace at the image plane.

In Figure 19, the diffraction pattern at the image plane is plotted for a 2 mm beam with its center at five aperture locations. As shown in the plot, the diffraction patterns almost exactly overlay one another.

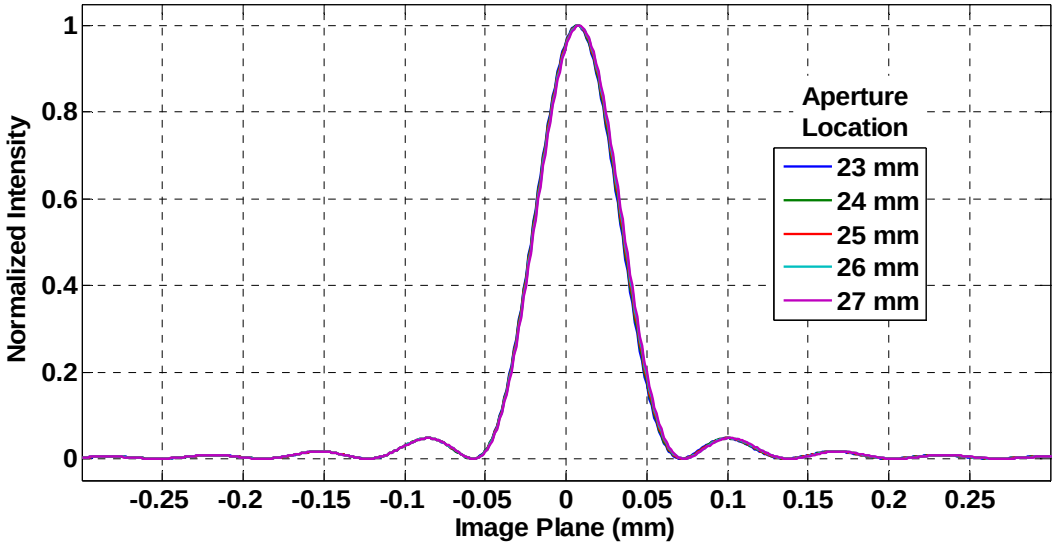

Figure 19. Kinoform lens diffraction at multiple beam locations on lens aperture.

Sensitivity Analysis

The kinoform lens is relatively insensitive to focus errors. Shifting the image plane from the design location does not have a great impact on the location of the diffraction energy. Figure 20 shows that even with a large focus error of 4 mm the diffraction spot center and refraction ray fan are closely aligned. The diffraction spot width has increased very little to 59 µm and the refraction spot has more than doubled to 66.6 µm. In this figure, the lens was designed for a focal length of 200 mm, but the image plane was located 204 mm along the optical axis for the diffraction analysis.

On the other hand, the location of the diffraction peak is impacted by a shift in wavelength. In Figure 21, the wavelength was changed from 650 to 651 nm for the diffraction analysis. This one nanometer shifts causes the location of the peak to shift 25 µm on the image plane. The spot width has only increased about 100 nm. Even a large wavelength shift of 10 nm increases the diffraction spot width by only a few micrometers, but moves the peak location 380 µm. The refraction ray trace is unaffected by a wavelength shift.

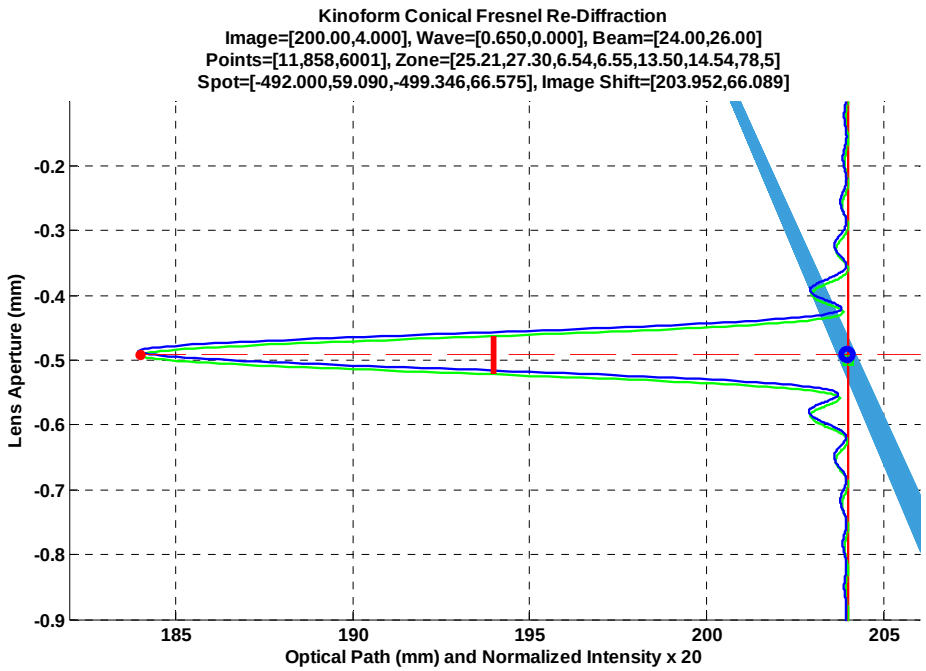

Figure 20. Kinoform diffraction and ray trace with a 4 mm focus error.

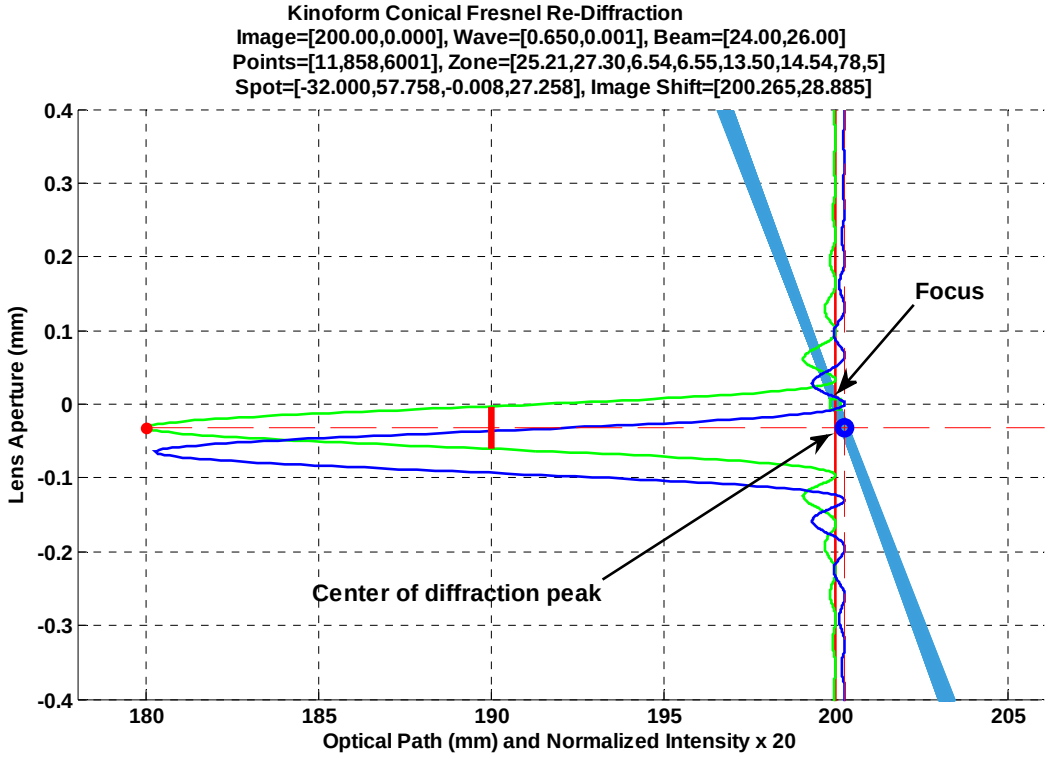

Figure 21. Kinoform diffraction and ray trace with a 1 nm wavelength shift.

1.5 CONCLUSIONS

An iterative aspheric zone Fresnel lens design code has been developed. The code includes toolpath generation and ray tracing through a simulated as-machined surface. Additional code to support the ray trace operations is given in the appendices to [1] and includes a vector solution to Snell's law in 3D and a general purpose, robust 2D curve intersection routine. Extension of the ray trace code to arbitrary 2D input shapes is current being implemented. Future work includes a 3D implementation of the aspheric design code that optimizes surface curvature to focus a scanning laser beam.

A numerical diffraction analysis code for an arbitrary lens shape has been implemented. The code is general purpose in that aperture size, focal length and wavelength are not constrained. Extension of the routine to implement both refraction and diffraction through multiple surfaces is being implemented.

A kinoform design code that matches the phase from adjacent Fresnel zones by varying the zone width as a function of optical path length and wavelength has been written. The resulting lens directs both the diffracted and refracted light to the same locations, the focus. However the kinoform lens is very sensitive to wavelength changes. Other degrees of freedom for the Fresnel lens design are the zone depth, zone offset (i.e., all zone centers do not have to lie along a line parallel to the image plane) and non-uniform phase match order. Exploiting these may reduce wavelength sensitivity. Also, the closely related notion of a multi-wavelength harmonic lens is being studied [4,5].

REFERENCES

1. Dow, T., K. Garrard and A. Sohn. Final Report – Phase I, Fresnel Scanning Lens Design. Precision Engineering Center, North Carolina State University (2007).
2. Sohn, A., K. Garrard and T. Dow. Fresnel Lenses for Scanning Systems. Precision Engineering Center Annual Report, 24, 229-248, (2006).
3. Rossi. M., R. Kunz and H. Herzig. Refractive and diffractive properties of planar micro-optical elements. Applied Optics, 34, 26, 5996-6007, (1995).
4. Sweeney, D. and G. Sommargren. Harmonic diffractive lenses. Applied Optics, 34, 14, 2469-2475, (1995).
5. Vannucci, G. A tuned Fresnel lens. Applied Optics, 25, 16, 2831-2834, (1986).
6. Born M. and E. Wolf. Principles of Optics, 7th Ed. Cambridge University Press, (1999).
7. Fowles, G. Introduction to Modern Optics. Dover, (1975).
8. Hecht, E. and A. Zajac. Optics, Addison-Wesley, (1976).

APPENDIX A – NUMERIC DIFFRACTION SIMULATION

```
% Calculate intensity distribution of diffracted light
%   [intensity,h] = diffract(screen,lens,normals,mask,lambda,Rx,Mx,tstr)
% Input
%   screen       points on the screen,       m x 3
%   lens         points on the lens surface, n x 3
%   normals      lens surface normals,       n x 3
%   mask         boolean lens mask,          default = n x 1 (all 1s)
%   lambda       wavelength,                 default = 6.328e-4 mm
%   Rx           refractive index of lens,   default = 1.4893    (pmma)
%   Mx           refractive index of medium, default = 1.0002926 (air)
%   tstr         plot title,                 default = 'Diffraction Pattern'
% Output
%   intensity    normalized intensity distribution at the screen
%   h            handle to plotted results
%
% The normalized intensity distribution of a parallel wavefront inside a lens
% is calculated at a distant screen surface.  The magnitude and phase of light
% reaching a point on the screen is a weighted complex summation of the light
% diffracted from every point on the lens.  This sum include the phase of the
% light as reaches the lens-air interface and the spherical wavefront produced
% by diffraction from each point on the lens.  The diffraction intensity from
% every lens point to every screen point is weighted by the cosine of the angle
% between the lens surface normal and a vector between the lens and the screen.

function [intensity,h] = diffract(screen,lens,normals,mask,lambda,Rx,Mx,tstr)

% check input parameters
error(nargchk(3,8,nargin));
screen_np = length(screen);
lens_np   = length(lens);

% supply defaults for optional parameters
if nargin < 4 || isempty(mask),   mask   = true(lens_np,1);       end
if nargin < 5 || isempty(lambda), lambda = 6.328e-4;              end
if nargin < 6 || isempty(Rx),     Rx     = 1.4893;                end
if nargin < 7 || isempty(Mx),     Mx     = 1.0002926;             end
if nargin < 8,                    tstr   = 'Diffraction Pattern'; end

% there must be a surface normal for each lens point
if lens_np ~= length(normals)
   error('normals vector length must equal number of lens points');
end

% there must be a mask value for each lens point
if lens_np ~= length(mask)
   error('mask vector length must equal number of lens points');
end

wavenum = 2*pi/lambda;             % wave number (1/mm)

lens    = lens(mask==true,:);      % apply mask to lens surface
normals = normals(mask==true,:);   %        and to normals
lens_np = length(lens);            % update number of data points

% find the intensity at each point on the screen from every point on the lens

% allocate space for results, screen intenstity distribution
amp = zeros(screen_np,1);

% phase of the light leaving the lens
lens_phase = exp(i * lens(:,1) * Rx * wavenum);

% iterate for each point on the screen
for k = 1:screen_np
   % form vectors from the kth point on screen to each point on the lens
   V  = repmat(screen(k,:),lens_np,1) - lens;        % cols are (x,y,z)
```

```
   L  = sqrt(sum(V.^2,2));         % length            of each vector in V
   dc = V ./ repmat(L,1,3);        % direction cosines of each vector in V

   % find angles between normals and vector to screen point
   % robust calculation uses atan(norm(cross(a,b)),dot(a,b))
   % builtin norm is not vectorized, use sqrt of sum-of-squares for 2-norm
   inclinationF = atan2(sqrt(sum(cross(normals,dc,2).^2,2)), ...
                                dot  (normals,dc,2));

   % amplitude and phase of light at kth point on the screen
   amp(k) = sum(lens_phase           .* ...          % phase through the lens
                cos(inclinationF)    .* ...          % weight based on normals
                exp(i * Mx * wavenum .* L) ./ L );   % phase of spherical wave
end

% intensity distribution of light on the screen
intensity = abs(amp).^2;                             % == amp .* conj(amp)
intensity = intensity / max(intensity);

% plot results
if nargout ~= 1
   h = figure;
   fontprops = {'FontName','Arial','FontSize',12,'FontWeight','Bold'};
   plot(screen(:,2),intensity,'LineWidth',4);
   title(tstr,fontprops{:});
   xlabel('Screen Position (mm)',fontprops{:});
   ylabel('Normalized Intensity',fontprops{:});
   set(gca,fontprops{:});
   set(gcf,'Units','Pixels','Position',[420 347 953 601]);
   grid on;
   xl = xlim;
   yl = ylim;
   xlim(xl + xl(2).*[-.05 .05]);
   ylim(yl + yl(2).*[-.05 .05]);
end
```

APPENDIX B – KINOFORM LENS DESIGN AND ANALYSIS

```
% Kinoform Fresnel lens design and diffraction analysis
%   [info,intensity,lens,lightP,lensP,imageP,g] = kinodiff(lightP,lensP,imageP)
% Input
%   lightP     light parameters structure
%                .lambda         incident wavelength
%                .waveF          wavelength perturbation (diffraction analysis)
%                .center         center position of beam
%                .width          beam width
%   lensP      lens  parameters structure
%                .Fl             focal length
%                .ar             full aperture radius
%                .Rx             refractive index of lens
%                .Mx             refractive index of medium
%                .pmo            phase match order
%                .znpts          number of points in each zone
%   imageP     image parameters
%                .center         center position of image plane
%                .width          width of image plane
%                .np             number of points on image plane
%                .shiftF         image plane shift (diffraction analysis)
% Output
%   info       results information structure
%                .nz             number of zones
%                .zone_depth     vector of zone depths (info.nz x 1)
%                .zone_width     vector of zone widths (info.nz x 1)
%                .zone_tau       vector of zone slopes (info.nz x 1)
%                .zone_dc        vector of zone direction cosines (nz x 3)
%                .diffractspot   spot location (peak) and size (width at max/2)
%                .refractspot    spot location (peak) and size (width at max/2)
%                .imageshift     image plane shift (OPL) to diffraction peak
%   intensity  normalized intensity distribution, yI (imageP.np x 2)
%   lens       lens surface data, xyz (lensP.znpts*info.nz x 3)
%   lightP     light parameters structure
%   lensP      lens  parameters structure
%   imageP     image parameters structure
%   g          handle to plot object
%
% A kinoform conical Fresnel lens is designed and analyzed.  The kinoform lens
% has optical path lengths from the center of each zone to the focal point that
% differ by an integer multiple of the incident wavelength.  This integer
% multiple is the phase match order, pmo.  The resulting lens both focuses a
% parallel beam of light to the focal point and directs the diffraction order
% equal to pmo from each zone to the focus.  The diffracted intensity
% distribution is calculated over a specified region of the image plane and both
% the refractive and diffracted spot sizes and locations are returned.  A plot
% of the lens and image plane is produced along with a ray trace of the beam
% to the image and the diffraction pattern overlaid on the image plane.
%
% Ken Garrard
% 2008.02.12

function [info,intensity,lens,lightP,lensP,imageP,g] = kinodiff(lightP,lensP,imageP)

% check number of input args
error(nargchk(0,3,nargin));

% inputs must be structures
if nargin < 1 || ~isstruct(lightP), lightP = struct(); end   % light parameters
if nargin < 2 || ~isstruct(lensP),  lensP  = struct(); end   % lens  parameters
if nargin < 3 || ~isstruct(imageP), imageP = struct(); end   % image parameters

% check parameter structures, fill in missing fields with defaults
lightP = sfldchk(lightP,           ...  % light (mm)
   struct('lambda',    0.000650,  ...  %    wavelength           (mm)
          'waveF',     0,         ...  %    wavelenght shift     (mm)
          'center',   25,         ...  %    beam center location (y,mm)
          'width',     2));            %    beam width           (y,mm)
```

```
lensP = sfldchk(lensP,            ...  % lens
   struct('Fl',      200.0,       ...  %    focal length         (x,mm)
          'ar',       50.1,       ...  %    aperture radius      (y,mm)
          'Rx',        1.4893,    ...  %    refractive index     (pmma)
          'Mx',        1.0002926, ...  %    refractive index     (air)
          'pmo',       5,         ...  %    kinoform phase match order
          'znpts',    11));            %    number of data point in each zone

imageP = sfldchk(imageP,          ...  % image plane
   struct('center',    0,         ...  %    center location      (y,mm)
          'width',     2,         ...  %    image plane size     (mm)
          'np',     6001,         ...  %    number of observation points
          'shiftF',    0));            %    image plane shift    (x,mm)

% adjust focal length to nearest integer multiple of the wavelength
lensP.Fl = round(lensP.Fl/lightP.lambda)*lightP.lambda;

% adjust image plane shift to compensate for wavelength shift
if strcmpi(imageP.shiftF,'auto')
   imageP.shiftF = ...
      lensP.Fl/lightP.lambda*(lightP.lambda+lightP.waveF)-lensP.Fl;
end

% image plane parameters
image_offset = imageP.center - imageP.width/2;

% kinoform design factor
kinoF = 2 * lensP.pmo * lightP.lambda;

% kinoform phase match functions for zone midpoint location
pm_nextR = @(r) sqrt(r^2 + (kinoF/2)^2 + kinoF*sqrt(lensP.Fl^2+r^2));
pm_prevR = @(r) sqrt(r^2 + (kinoF/2)^2 - kinoF*sqrt(lensP.Fl^2+r^2));

% find zone midpoints from center to largest radius
k   = 2;
zbn = lightP.center;
while zbn(k-1) < lightP.center + lightP.width/2,
   zbn(k) = pm_nextR(zbn(k-1));
   k = k + 1;
end
zbn(k) = pm_nextR(zbn(k-1));       % need extra midpoint to find last boundary

% find zone midpoints from center to smallest radius
k   = 2;
zbp = lightP.center;
while zbp(k-1) > lightP.center - lightP.width/2,
   zbp(k) = pm_prevR(zbp(k-1));
   k = k + 1;
end
zbp(k) = pm_prevR(zbp(k-1));       % need extra midpoint to find last boundary

% construct zone midpoint and zone boundary vectors
zone_midpoint = [fliplr(zbp) zbn(2:end)];
zone_boundary = diff(zone_midpoint)/2 + zone_midpoint(1:end-1);

zone_midpoint([1,end]) = [];       % delete zone midpoints outside of aperture

% estimate groove angle for incident zone Fresnel facets
t1 = 0;
t2 = atan2(zone_midpoint,lensP.Fl);
zone_tau = atan2((sin(t1)+sin(t2)), ...
                 (sqrt((lensP.Rx/lensP.Mx)^2-(sin(t1)^2))-cos(t2)));

% setup zone data for lens
nzones  = length(zone_midpoint);
zone_np = ones(1,nzones) * lensP.znpts;  % # points in each lens zone
zone_X  = zeros(1,nzones);               % zone centers are aligned at x=0

% total number of data points on lens
```

```
lens np = sum(zone np);

% direction cosines of refracted ray for each zone
zone_ra = asin(lensP.Rx/lensP.Mx*sin(zone_tau))-zone_tau;
zone_dc = [cos(zone_ra); -sin(zone_ra); zeros(1,nzones)].';

% setup image position vector, three columns (x,y,z), constant x, z==0
image = zeros(imageP.np,3);
image(:,1) = lensP.Fl + imageP.shiftF;
image(:,2) = linspace(image_offset,image_offset+imageP.width,imageP.np);

% setup lens position vector, three columns (x,y,z), z==0
lens    = zeros(lens_np,3);        % allocate space for lens data points
dircos  = zeros(lens_np,3);        % allocate space for dirction vectors
refangl = zeros(lens_np,1);        % allocate space for refraction angles
p = 1;                             % index of first point in a zone

for k = 1:nzones                   % fill up lens data one zone at a time
   e = p+zone_np(k)-1;             % index of last point in kth zone

   % fill in y coordinates first
   lens(p:e,2) = linspace(zone_boundary(k),zone_boundary(k+1),zone_np(k));

   % calculate x coordinates using y's and slope for this zone
   lens(p:e,1) = zone_X(k)   + (lens(p,2)-lens(p:e,2))*tan(zone_tau(k));
   lens(p:e,1) = lens(p:e,1) + (lens(p,1)-lens(e,1))/2;

   % fill refracted ray direction vector and angle vector for this zone
   dircos(p:e,:) = repmat(zone_dc(k,:),e-p+1,1);
   refangl(p:e)  = repmat(zone_ra(k),e-p+1,1);

   p = e+1;                        % increment index for next zone
end

% calculate diffraction pattern
intensity = diffract(image,lens,dircos,true(lens_np,1), ...
                     lightP.lambda+lightP.waveF,lensP.Rx,lensP.Mx);

% find image location of peak intensity
[one,mxI] = max(intensity);

% find the full width at half max
[x1,y1] = curve_intersections(image(:,2),intensity, ...
                              [image(1,2) image(end,2)],[.5 .5]);

% find endpoints of refracted rays
traceF = hypot((lensP.Fl+imageP.shiftF)*1.05,max(lens(:,2)));
xp = cos(refangl)*traceF;
yp = sin(refangl)*traceF;

% find refracted ray spot size
u = [lens(:,1) xp           NaN(size(xp))]';
v = [lens(:,2) lens(:,2)-yp NaN(size(yp))]';
[x2,y2] = curve_intersections(u(:),v(:),[image(1,1) image(end,1)], ...
                                        [image(1,2) image(end,2)]);
rfspot = max(y2)/2 + min(y2)/2;

% find shifted focal point (x center of ray intersection with image plane)
[x3,y3] = curve_intersections(u(:),v(:),[image(1,1)-1 traceF], ...
                                        [image(mxI,2) image(mxI,2)]);
image_shift = max(x3)/2 + min(x3)/2;

% find spot width of shifted focal spot
[x4,y4] = curve_intersections(u(:),v(:),[image_shift image_shift], ...
                                        [image(1,2)  image(end,2)]);

% diffraction intensity at shifted image plane
imageS      = image;
imageS(:,1) = image_shift;
intensityS  = diffract(imageS,lens,dircos,true(lens_np,1), ...
```

```
                        lightP.lambda+lightP.waveF,lensP.Rx,lensP.Mx);

% fill results info structure
info.nz           = nzones;
info.zone_depth   = lens(1          :lensP.znpts:lens_np-1,1) - ...
                    lens(lensP.znpts:lensP.znpts:lens_np,  1);
info.zone_width   = diff(zone_boundary)';
info.zone_tau     = zone_tau';
info.zone_dc      = zone_dc;
info.diffractspot = [image(mxI,2) range(x1)];
info.refractspot  = [rfspot range(y2)];
info.imageshift   = [image_shift range(y4)];

% plot refraction raytrace from lens to image and diffraction spot
g  = figure;
ax = axes;
hold(ax,'on');
grid(ax,'on');
set(ax,'Color',[160 160 160]/256);
set(g,'Units','Pixels','Position',[420 347 953 601]);
magF  = round(ceil(lensP.Fl/10)/2)*2;
brdF  = 0.05;
Xbeam = -lensP.Fl*brdF;

% plot incident beam
plot(ax,[Xbeam*ones(1,nzones); zeros(1,nzones)], ...
        [zone_midpoint; zone_midpoint],'m-');

% plot refracted rays from midpoint of each zone
plot(ax,[zeros(1,nzones);               cos(zone_ra)*traceF], ...
        [zone_midpoint;   zone_midpoint-sin(zone_ra)*traceF],'m-');

% plot refracted rays from all other lens points
lp = lens;                                      % copy lens data
lp(floor(lensP.znpts/2)+1:lensP.znpts:end,:) = []; % remove zone midpoints

% find endpoints of refracted rays
xp = cos(refangl)*traceF;
yp = sin(refangl)*traceF;
xp(floor(lensP.znpts/2)+1:lensP.znpts:end,:) = [];
yp(floor(lensP.znpts/2)+1:lensP.znpts:end,:) = [];
plot(ax,[lp(:,1) xp]',[lp(:,2) lp(:,2)-yp]','y-');

% plot image and focal point (midpoint of ray intersection with image plane)
plot(ax,image(:,1),image(:,2),'r-','LineWidth',2);
plot(ax,image(1,1),rfspot,'gs','MarkerSize',6,'LineWidth',2);

% plot lens
plot(ax,lens(:,1),lens(:,2),'b-','LineWidth',4);

% plot zone midpoints
plot(ax,zeros(nzones,1),zone_midpoint,'ks','MarkerSize',6);

% plot diffraction intensity
plot(ax,image(1,1)-magF*intensity,image(:,2),'g-','LineWidth',2);

% plot diffraction intensity at shifted focal point
plot(ax,imageS(1,1)-magF*intensityS,imageS(:,2),'b-','LineWidth',2);

% add red line at half max
plot(ax,image(1,1)-magF*y1,x1,'r-','LineWidth',4);

% add a dot at peak intensity
plot(ax,image(1,1)-magF*intensity(mxI),image(mxI,2),'r.','MarkerSize',20);

% add shifted focal point cross hair markers
plot(ax,[image(1,1)-magF*intensity(mxI) image_shift; max(xp) image_shift], ...
        [image(mxI,2) image(1,2); image(mxI,2) image(end,2)],'r--');

% add shifted focal point
```

```
plot(ax,image shift,y3(1),'bo','MarkerSize',8,'LineWidth',4);

% add axis labels and title info
set(ax,'FontName','Arial','FontSize',12,'FontWeight','Bold');
xlabel(ax,sprintf('Optical Path (mm) and Normalized Intensity x %d',magF));
ylabel(ax,'Lens Aperture (mm)');

if numel(x1) > 2, c = '*';         % indicate multiple peaks in plot title info
else c = '';
end

% print result in title string
title(ax,sprintf(                                                    ...
   ['Kinoform Conical Fresnel Re-Diffraction\n'                      ...
    'Image=[%.2f,%.3f], Wave=[%.3f,%.3f], Beam=[%.2f,%.2f]\n'       ...
    'Points=[%d,%d,%d], Zone=[%.2f,%.2f,%.2f,%.2f,%.2f,%.2f,%d,%d]\n' ...
    'Spot=[%.3f,%.3f%c,%.3f,%.3f], Image Shift=[%.3f,%.3f]'],       ...
    lensP.Fl,imageP.shiftF,[lightP.lambda lightP.waveF]*1000,       ...
    lightP.center-lightP.width/2,lightP.center+lightP.width/2,      ...
    lensP.znpts,lens_np,imageP.np,                                  ...
    [min(info.zone_width) max(info.zone_width)]*1000,               ...
    [min(info.zone_depth) max(info.zone_depth)]*1000,               ...
    [min(zone_tau) max(zone_tau)]*180/pi,nzones,lensP.pmo,          ...
    info.diffractspot*1000,c,info.refractspot*1000,                 ...
    [info.imageshift].*[1 1000]));

% set axis limits
axis(ax,'tight');
xl = xlim;  xlim(xl + xl(2).*[-brdF brdF]);
yl = ylim;  ylim(yl + yl(2).*[-brdF brdF]);

% return intensity vector as [image plane locations, intensity values]
intensity(:,2) = intensity;
intensity(:,1) = image(:,2);
```

APPENDIX C – MULTIPLE CURVE INTERSECTIONS

```
% Find the locations where two curves intersect
%   [xi,yi,Ia,Ib,Sa,Sb] = curve_intersections(xa,ya,xb,yb)
% Input
%   xa,ya    data points on curve one
%   xb,yb    data points on curve two
% Output
%   xi,yi    intersection points
%   Ia       location of intersection points in curve one
%   Ib       location of intersection points in curve two
%   Sa       slopes of intersecting segments on curve one
%   Sb       slopes of intersecting segments on curve two
%
% The intersections of curve one and curve two are computed. The vectors Ia
% and Ib contain indices into xa,ya and xb,yb of the points prior to (or
% exactly at) the points of intersection.  The curves may have vertical
% segments, overlapping segments or be broken into sections with NaNs.  The
% curves may intersect exactly at an endpoint.  The vectors Sa and Sb contain
% the slopes (in radians) of the pairs of intersecting segments.
%
% Based on 'intersections' version 1.6b2 and 1.7 by D. Schwarz
% 2007.11.13

% Given two line segments, L1 and L2 with endpoints,
%
%    xa(1),ya(1) and xa(2),ya(2)
%    xb(1),ya(1) and xb(2),yb(2)
%
% four equations in four unknowns (t1,t2,xi and yi) can be written.  If the
% lines intersect, then the point of intersection is xi,yi and t1 and t2 are
% the relative distances from the start of each line to xi,yi.
%
% The four equations are,
%
%    t1 * (xa(2) - xa(1))  =  xi - xa(1)
%    t2 * (xb(2) - xb(1))  =  xi - xb(1)
%    t1 * (ya(2) - ya(1))  =  yi - ya(1)
%    t2 * (yb(2) - yb(1))  =  yi - yb(1)
%
% These equations can be expressed in matrix form as A*T = B or,
%
%  [ xa(2)-xa(1)       0       -1   0;      [ t1;      [ -xa(1);
%        0       xb(2)-xb(1)  -1   0;   *    t2;   =    -xb(1);
%    ya(2)-ya(1)       0        0  -1;        xi;        -ya(1);
%        0       yb(2)-yb(1)   0  -1 ]       yi ]       -yb(1) ]
%
% Solving for T gives both the intersection point and its location on each
% line segment.  If 0 <= t1 <= 1 and 0 <= t2 <= 1, then L1 and L2 intersect
% at xi,yi.  In the case of t1=1 or t2=1, the intersection is at a segment
% endpoint.  A is singular for collinear or parallel segment pairs.
%
% The number of lines segment pairs for which T = A \ B has to be solved is
% reduced by considering the smallest enclosing rectangle with sides parallel
% to the x and y axes for each line pair.  Only the line segment pairs bound
% by overlapping rectangles need to be considered.  Other line segment pairs
% cannot intersect.

function [xi,yi,Ia,Ib,Sa,Sb] = curve_intersections(xa,ya,xb,yb)

% Check input vectors
error(nargchk(4,4,nargin))

% Force column vector inputs
xa = xa(:);
ya = ya(:);
xb = xb(:);
yb = yb(:);
```

```
% Vectors xa and ya must be equal length with at least two points
al = length(xa);
if al < 2 || length(ya) < 2 || al ~= length(ya)
   error('xa and ya must be equal length vectors with at least two points')
end

% Vectors xb and yb must be equal length  with at least two points
bl = length(xb);
if bl < 2 || length(yb) < 2 || bl ~= length(yb)
   error('xb and yb must be equal length vectors with at least two points')
end

% Find all combinations where a rectangle enclosing a line segment from curve
% one overlaps with a rectangle enclosing a line segment from curve two
overlap = ...
          (repmat(min(xa(1:end-1),xa(2:end)),     1,bl-1) <= ...
           repmat(max(xb(1:end-1),xb(2:end)).',al-1,   1));

overlap = overlap & ...
          (repmat(max(xa(1:end-1),xa(2:end)),     1,bl-1) >= ...
           repmat(min(xb(1:end-1),xb(2:end)).',al-1,   1));

overlap = overlap & ...
          (repmat(min(ya(1:end-1),ya(2:end)),     1,bl-1) <= ...
           repmat(max(yb(1:end-1),yb(2:end)).',al-1,   1));

overlap = overlap & ...
          (repmat(max(ya(1:end-1),ya(2:end)),     1,bl-1) >= ...
           repmat(min(yb(1:end-1),yb(2:end)).',al-1,   1));

[i,j] = find(overlap);             % indices of candidate segment pairs

% Find all line segment pairs that have at least one NaN vertex
xya  = [xa ya];                    % curve one [x y]
xyb  = [xb yb];                    % curve two [x y]
dxya = diff(xya);                  % first finite differences for curve one
dxyb = diff(xyb);                  % first finite differences for curve two
% NaNs propagate through all calculations
remove = isnan(sum(dxya(i,:) + dxyb(j,:),2));

% Remove NaN elements from candidate pairs
i(remove) = [];
j(remove) = [];

% Initialize A and T as matrices
% use one column of T and one page (ie, 3rd dimension) of A for each pair
% of candidate line segments
n = length(i);
T = NaN(4,n);                      % T is a 4 element column vector
A = zeros(4,4,n);                  % A contains n 4x4 matrices
A([1 2],3,:) = -1;                 %    delta_xa     0       -1  0
A([3 4],4,:) = -1;                 %       0      delta_xb   -1  0
A([1 3],1,:) = dxya(i,:).';        %    delta_ya     0        0 -1
A([2 4],2,:) = dxyb(j,:).';        %       0      delta_yb    0 -1

% Initialize the right hand side vector, B
B = -[xa(i) xb(j) ya(i) yb(j)].';

% Solve A*T=B for each pair of candidate line segment pairs by finding the
% LU decomposition of A and then solving U*T=L\B with linsolve.  Linsolve
% is much faster if the system is known to be upper-triangular.
%
% Linsolve returns the solution vector T and the reciprocal of the condition
% number of A.  There is no solution when A is singular and 1/cond of A is
% zero.  In this case the lines are parallel and may be collinear
% (overlapping or joined end-to-end).
rc = zeros(1,n);
opts.UT = true;
for k = 1:n
   [L,U] = lu(A(:,:,k));
```

```
   [T(:,k),rc(k)] = linsolve(U,L\B(:,k),opts);
end

% The line segment pairs for which 1/cond is zero or nearly zero includes
% parallel lines that do not intersect.  Such anomalous intersections are
% distinguished by testing for collinearity of a point from one line with
% both points from the other line.  Three points are collinear if and only if
% the cross product (x2-x1) x (x1-x3) is zero, which is equivalent to testing
% the 2x2 matrix [xa(2)-xa(1) ya(2)-ya(1); xb(1)-xa(1) yb(1)-ya(1)] for
% singularity.  This is reliably done by finding the reciprocal condition
% number of the matrix and testing for a value very close to zero.  Segment
% pairs that fail this test are parallel and do not overlap.
tol = 1e-10;
collinear = false(1,n);
for k = find(rc < tol)
   T(1,k) = NaN;
   collinear(k) = rcond([dxya(i(k),:); xyb(j(k),:) - xya(i(k),:)]) < tol;
end

% Find intersections from the candidate set of line segment pairs
% parallel and collinear pairs will not be included since T(1,:) = NaN
% For an intersection at a segment endpoint the values of T(1:2,:) will be zero
% or one.  Test with a tolerance to allow for imperfect floating point results.
in_range = T(1,:) >=  -tol & T(2,:) >=  -tol & ...
           T(1,:) <= 1+tol & T(2,:) <= 1+tol;

% Process collinear segments
if any(collinear)
   ia = i(collinear);
   ja = j(collinear);

   % set xi and yi to midpoint of overlapping regions
   T(3,collinear) = (max(min(xa(ia),xa(ia+1)),min(xb(ja),xb(ja+1))) + ...
                     min(max(xa(ia),xa(ia+1)),max(xb(ja),xb(ja+1)))).' / 2;
   T(4,collinear) = (max(min(ya(ia),ya(ia+1)),min(yb(ja),yb(ja+1))) + ...
                     min(max(ya(ia),ya(ia+1)),max(yb(ja),yb(ja+1)))).' / 2;

   % include repaired collinear intersections
   in_range = in_range | collinear;
end

% Extract intersection points from solution matrix
xi = T(3,in_range).';
yi = T(4,in_range).';

% Remove duplicate intersection points
[xyi,r] = unique([xi yi],'rows');  % find duplicate rows
xi = xyi(:,1);                     % keep unique points
yi = xyi(:,2);

% Find index into input lines of the point prior to each intersection
% (or the exact intersection if the point is on either line segment)
Ia = i(r);                         % curve one, xa(Ia),ya(Ia) are prior points
Ib = j(r);                         % curve two, xb(Ib),yb(Ib) are prior points

% Find slopes of line segments containing intersection points
if nargout > 4
   xa(end+1) = xa(end);            % duplicate last point on curve one
   ya(end+1) = ya(end);
   xb(end+1) = xb(end);            % duplicate last point on curve two
   yb(end+1) = yb(end);

   % calculate slopes
   Sa = atan2(ya(Ia+1)-ya(Ia),xa(Ia+1)-xa(Ia));
   Sb = atan2(yb(Ib+1)-yb(Ib),xb(Ib+1)-xb(Ib));
end
```

2 FAST LONG RANGE ACTUATOR - *FLORA*

Qunyi Chen
Graduate Student
Thomas A. Dow
Dean F. Duncan Distinguished Professor
Department of Mechanical and Aerospace Engineering
Kenneth Garrard and Alex Sohn
Precision Engineering Center Staff

The goal of this project is to develop a Fast Long Range Actuator (FLORA) to produce optical quality freeform surfaces. The target range of motion of ±2 mm at 20 Hz creates a challenging problem and will require innovation in design, fabrication and control. This report discusses the performance of the modified prototype (which was initially built in 2003 with Precitech on a small-business grant funded by NASA) over the past year. The prototype uses a 50 mm stroke linear motor, air bearing supported lightweight triangular piston and a glass-scale linear encoder. Changes to the encoder, amplifier and controller and the resulting improvements in performance are reported. Both simulations and experimental results are presented to evaluate the performance of the existing design and determine the direction for a new system design. Significant improvements in following error (10 times) and disturbance rejection (8 times) have resulted in the changes incorporated in improved version of FLORA. In addition, more general design philosophies for this application are discussed in terms of physical design and controller design, the effect of moving mass and physical damping in this dynamic system are also discussed.

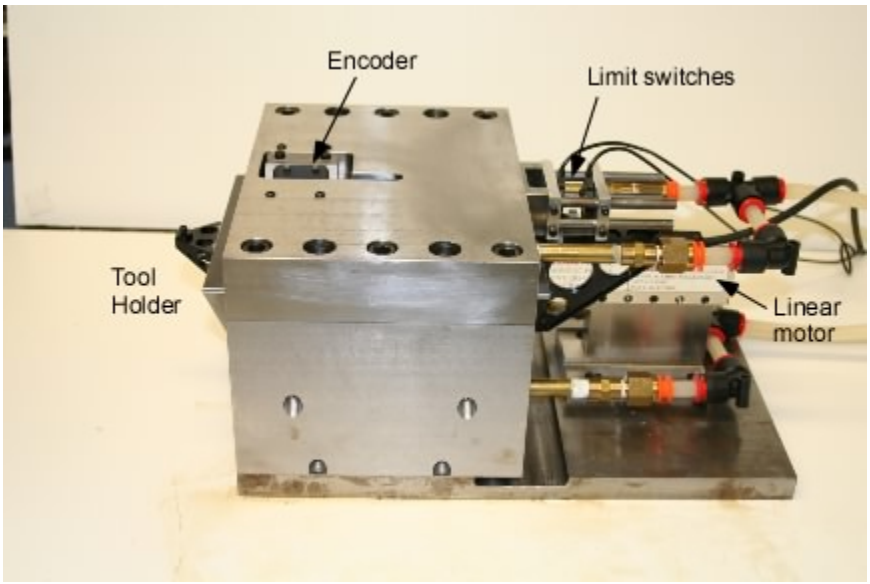

2.1 INTRODUCTION

Diamond turning (DT) has revolutionized the fabrication of optical surfaces for consumer, defense and science applications such as contact lenses, forward-looking infrared radar and infrared spectrometers. It has made this impact not only because it can accurately and rapidly fabricate diffractive, refractive and reflective optical surfaces, but also because it can create reference features tied to the optical surfaces to assist in the assembly process. An emerging trend in optical design is the use of Non-Rotational Symmetric (NRS) surfaces to reduce complexity, bulk and weight while improving optical performance. To create these so-called freeform surfaces, DT machines have been operated at very slow spindle speeds or modified with a piezoelectric Fast Tool Servo (FTS) or a flycutter. The proposed Long Range Actuator (FLORA) integrates existing technologies (air bearings, linear motors, high-resolution encoders and real-time control) into a lightweight, moving tool holder that can be retrofitted onto a conventional DT machine.

The objective of the FLORA is to create optical quality surfaces while moving the tool over a range of ± 2 mm at a frequency of 20 Hz. The technical challenges include:

Form Error Diamond turning machines can create excellent form fidelity because of their stiff, linear slides and air-bearing spindles. This process is ideally suited (and was developed) for rotationally symmetric surfaces such as spheres or rotationally-symmetric aspheres. Moving the slides of these machines to create NRS surfaces at typical spindle speeds would be well beyond the bandwidth limits of the large, heavy axes. Reducing the moving mass will improve the bandwidth of the system but also make it more susceptible to disturbances. The goal is to create a lightweight design that will reduce the machining time while retaining the form accuracy of current DTMs.

Surface Finish Simple theoretical relationships between machining parameters (spindle speed, axis velocity) and tool geometry can be used to predict surface finish; but the actual surface will be degraded by tool imperfections (waviness, wear, damage) and workpiece material properties. For the dynamic conditions envisioned, machine vibrations and dynamic forces can exacerbate the problem and result in unacceptable surfaces.

2.2 SYSTEM DEVELOPMENT

A prototype FLORA was built during 2004 and has continued with support from NSF. The FLORA has a light-weight honeycomb triangular piston, a linear motor and a high-resolution linear encoder. The total range of motion of the motor is 50 mm but the goal is a stroke of 4 mm at 20 Hz. A photograph of the actuator installed on the ASG-2500 DTM is shown in Figure 1.

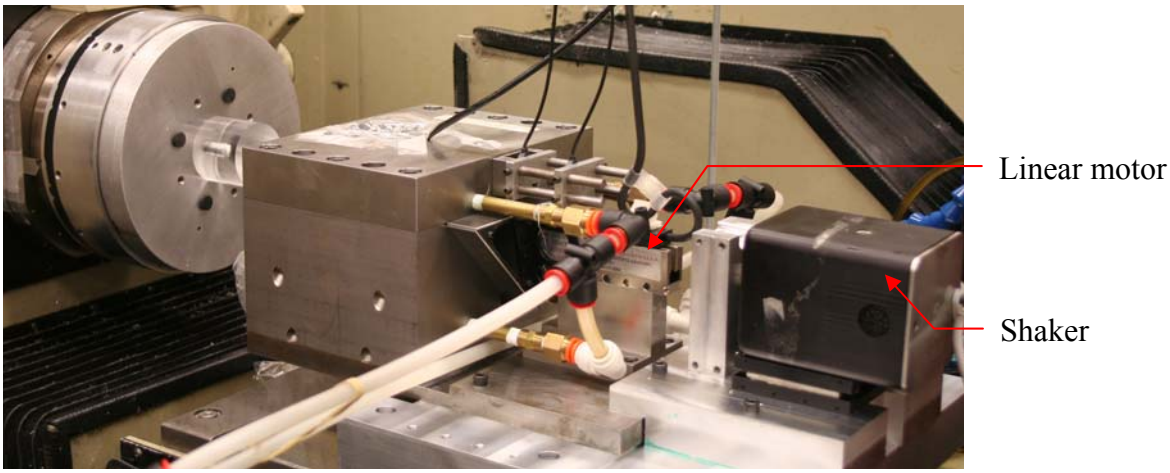

Figure 1. Photograph of the FLORA system mounted on the ASG-2500 DTM.

To improve the surface finish and figure error for this actuator, a number of changes to the electronic components were made over the past year.

- High-resolution encoder – A Sony glass scale encoder was added to provide piston position feedback with 0.25 nm resolution at speeds up to 750 mm/sec.
- Linear Amplifier – An Aerotech linear amplifier BL10-80A is being used to drive the Airex linear motor. The amplifier has a maximum current output of ±10 Amps with a bandwidth of 2000 Hz. The motor can produce a peak force of 81 N.
- Control platform – A PMDi controller has been installed that can provide an update time of 25 µsec or 40 Kz. This system uses an Analog Devices SHARC processor 40 MHz ADSP-21061L. PMDi has provided valuable support and expertise to the PEC.

Figure 2 shows the electrical schematics of the FLORA and its interconnection to the ASG-2500. In this implementation, the tool motion is slaved to the spindle motion and cross-feed motion of x-slide. The data acquisition electronics of the FLORA take the spindle encoder signal and the x-slide quadrature signal to generate the tool motion command. As a safety measure, the FLORA uses the ASG emergency stop switch signal to disable the Aerotech amplifier when the switch is pushed down. The ground lines from the computer to the two separate 5 VDC power supplies are essential to guarantee the proper communication of all motion wire devices.

2.3 OPEN LOOP TRANSFER FUNCTION

The single DOF system shown in Figure 1 consists of moving piston in an air bearing (an undamped mass m), the actuating force F from the linear motor and the tool feeding position $z(t)$ from the linear encoder. The actuating force is a function of the motor force constant K_f and the command current input to the amplifier I. Figure 3(a) shows the measured open loop system

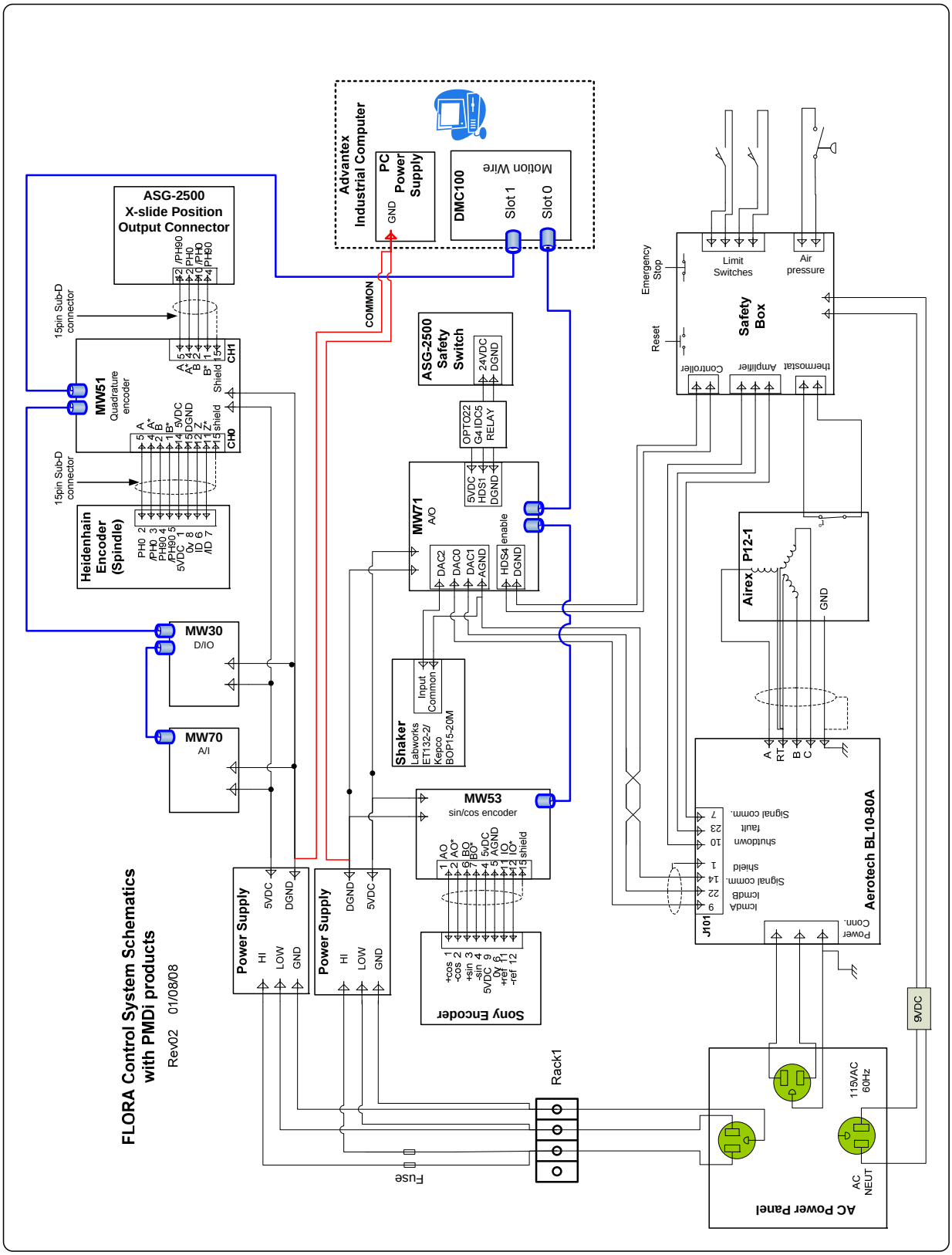

Figure 2. Electrical schematics of the FLORA control system

transfer function between position output in mm to input in current to the amplifier. Figure 3(b) shows the result when the command amplitude is modified based on Equation (1) to remain at the same level. In this case the transfer function is from mm command to mm motion.

$$A = \frac{K_f I}{m\omega^2} \tag{1}$$

The peak in Figure 3(b) at 900 Hz is due to the analog current loop within the amplifier and motor. Additional resonance peaks above 1000 Hz are possibly due to aerodynamic effects in the linear air-bearing or structural dynamics of the encoder read head mounting bracket. The existence of these high frequency dynamics limits the capability of conventional feedback controller design.

Based on the frequency response in Figure 3(a), a MATLAB function ***invfreqz*** is used to identified the open loop transfer function below 1500 Hz with one zero and four poles. The identified discrete function is then converted into continuous form in Equation (2). The zero at *-13448* and the conjugate pole pair at *-2858.5± 5408.7i* in the identified equation are from the analog current loop dynamics within the linear amplifier and the motor. Figure 4 shows a comparison of open-loop frequency response between the measured and the identified discrete model. This is the basic system dynamics equation to be used for controller synthesis.

$$TF_{open}(s) = \frac{51806782\,(s+13448)}{s^2 \cdot (s^2 + 5717s + 37424559)} \tag{2}$$

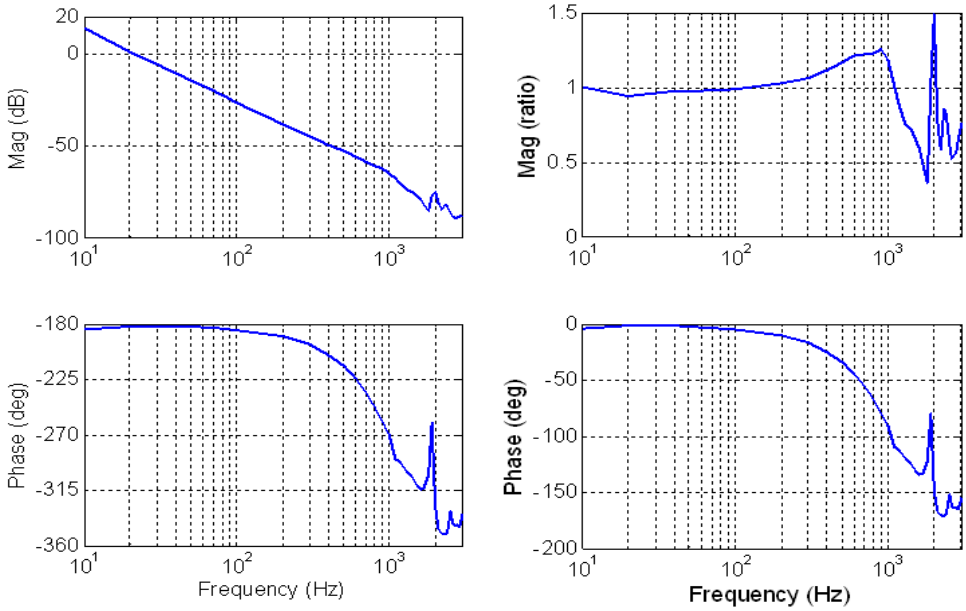

(a) (b)

Figure 3. Commutated open loop system transfer function frequency responses from current command (a) and corrected for system inertia (b) using Equation (1)

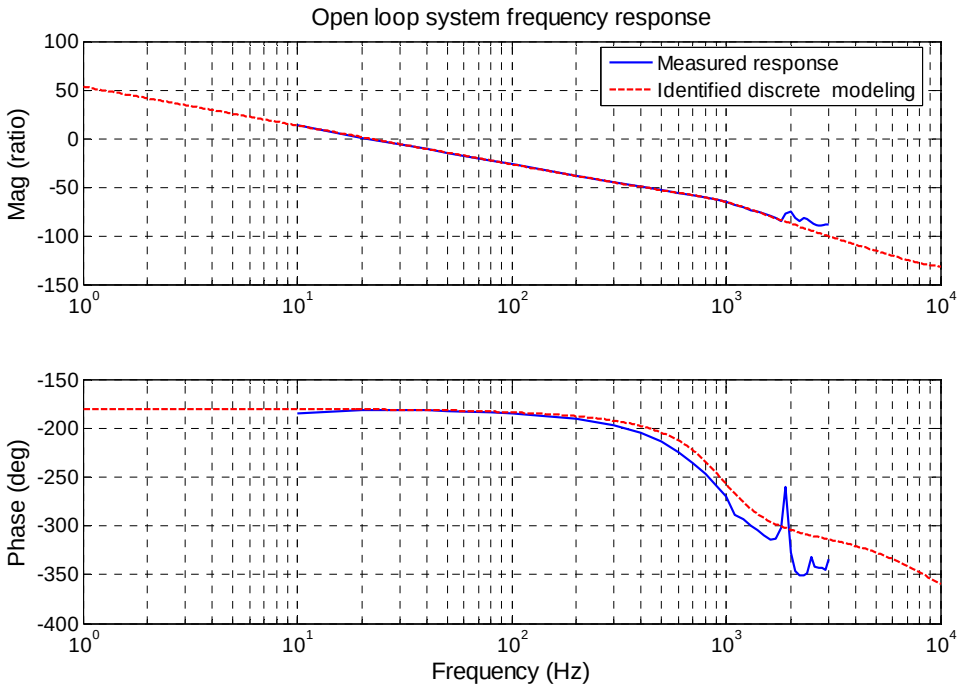

Figure 4. A comparison of open-loop control system frequency response for FLORA

2.4 MOTION SYSTEM DESIGN AND CONTROL

The unique positioning requirement on range, speed and accuracy in the single-point diamond turning process makes the control of FLORA a difficult challenge. Although there is no direct transfer function between the created optical surface quality (form error and surface finish) and FLORA motion control performance at this moment, a combination of air bearings, linear motors, high-resolution encoders and real-time control provides the best possibility to maintain the surface quality from existing DTM while extending the range and frequency of tool motion.

For this low-mass direct-drive motion control system, there are a number of challenges:

- Ultra positioning accuracy requirement for high speed dynamic operation condition and known motion path (i.e. sinusoidal trajectory tracking with slow time varying motion amplitude and frequency). For example, position error within ±20 nm for 2 mm 20 Hz sinusoidal tracking.
- High sensitivity of the low-mass direct-drive to internal/external disturbances/noise/errors and high frequency dynamics (model uncertainties) as well as the dependence of stiffness on the servo controller,
- Reaction force reduction for linear actuation system

The methodologies to tackle these challenges are:

- Optimize the system components selection/design and integration to minimize error, noise and disturbance, and increase the dynamic resonance frequencies as far away from the operation frequency as possible.
- Develop an effective control approach to minimize the influence of error, noise and disturbance on the system performance according to the features of SPDT process.

By combining the physical design and controller design to create a new FLORA, it provides the power to optimize the performance better than either single approach would provide.

2.4.1 MOTION SYSTEM ANALYSIS

The FLORA is a frictionless, force controlled system which consists of a linear motor applying force to a piston supported in a low-friction air bearing. The force of the motor drives the piston with position feedback from a high-resolution linear encoder as illustrated in Figure 5. The acceleration of the piston will be proportional to this force but the displacement will be 180° out of phase. A feedforward acceleration command is used to improve the performance of the system.

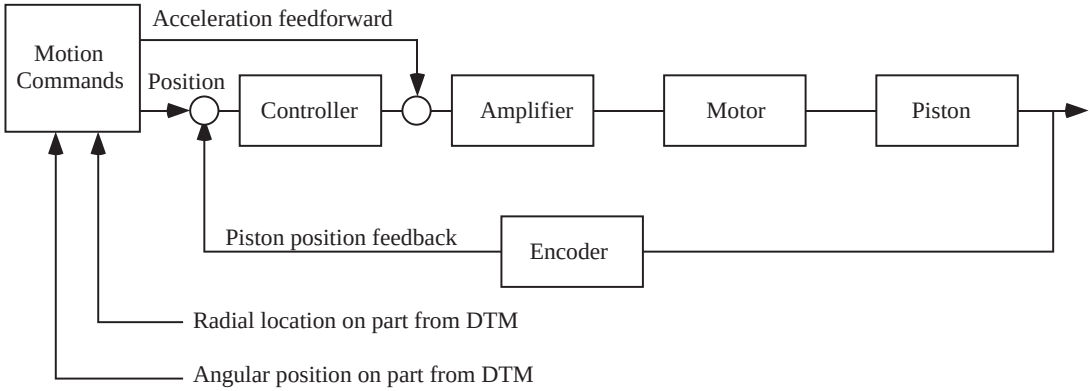

Figure 5. Controller layout for FLORA

Feedforward controller design

The feedback control discussed next maintains the stability and robustness of the system but it needs to be combined with other control approaches to create acceptable control performance. For example, feedforward controller in Equation (3) is designed as the inverse of the dominant linear model for fast response and reduce profile tracking error, where K_f is the motor force constant and $\ddot{z}_d$ for the profile acceleration.

$$K_{FF}(z) = \frac{m}{K_f}\ddot{z}_d \tag{3}$$

Closed Loop Controller Design

The closed-loop block diagram is shown in Figure 6, where *C* contains the dynamics of actuator and controller together and *P* contains the dynamic of the tool holder. *n*(t) is the encoder position feedback error or noise, *r*(t) is the position command for the tool, and *z*(t) is the resulted tool position.

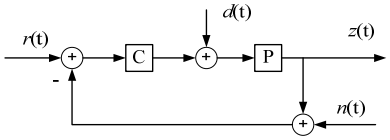

Figure 6. FLORA control system diagram

The functional requirement for the FLORA is to track a commanded trajectory while confronted by disturbances, measurement noise, plant uncertainty, actuator saturation and bandwidth limitations.

Position command *R*(s) There are a few different operation conditions in the diamond turning process.

(1) Actively hold the tool to touch-off the part surface to determine the zero reference position of the tool motion.
(2) Point-to-point positioning to move the tool to a specified location.
(3) Sinusoidal motion with slowly varying amplitude and fixed frequency to cut a tilted flat. In this case, the tool can achieve 2 mm sinusoidal motion up to 20 Hz.
(4) Sinusoidal motion with slowly varying amplitude and frequency to cut freeform surface.

In typical machining process (items 3 & 4), the motion control system is continuously in transient state, never reaches a steady state as in the stand alone testing.

Disturbance *D*(s) Disturbance rejection is an important characteristic of a motion control system. During the machining operation, small changes in the depth of cut will change the force on the tool and introduce a disturbance to the positioning system. The disturbance is not only from physical sources but also from electrical noise in the controller and the amplifier. These disturbances result in poor surface finish. Although the disturbances originate from different sources, they can be taken as lumped disturbance forces acting on the tool holder in addition to the motor actuation force.

- 63 Hz disturbance force is produced due to the natural frequency of the ASG-2500 z-slide
- The electronic noise with 60 Hz odd harmonic contents in the linear amplifier produce 60 Hz harmonics disturbance forces due to the non-linear electromagnetic force generation process
- The fundamental operation frequency of the tool motion also produces the disturbance forces at its harmonic frequencies due to the non-linearities
- Thrust force disturbance in the cutting process, mainly in the frequency range below 400 Hz

Encoder noise/error *N*(*s*) The measurement error is the difference between the measured tool position and the true position. The Sony BH25 encoder measurement has resolution quantization error, the scale grating error and interpolation error. The current achievable frequency limit in the encoder measurement using the PMDi interpolator board is 325 KHz. Below this limit, the interpolation of the 0.25 μm encoder signal pitch could be programmed up to a factor of 8096 (31 pm resolution). Beyond this limit, the resolution degrades to the half of the signal pitch (125 nm). Collaborative efforts with PMDi are underway to increase the frequency limit of interpolation process up to 1 MHz, which is needed to measure position up to 250 mm/sec. Section 4.4.3 shows the effect of this frequency limit on the motion control performance.

.

2.4.2 POSITION FEEDBACK CONTROLLER DESIGN

The ultraprecision positioning requirement in the diamond turning process presents a challenge that any basic position feedback controller can not handle. It is planned to take two steps to design a robust high performance motion controller: First, a classical controller design with a combination of feedforward and PID/lead-lag position feedback has been implemented to achieve reasonable performance over the range of frequencies of interest. Second, advanced control approaches will be developed to further improve the tool positioning performance.

Position feedback controller improves the robustness, profile tracking and disturbance rejection of the control system, and provides a firm foundation to support for other control components. However, due to the inherent limitation of position feedback control approach, it is impossible to obtain ideal response across all frequencies while maintaining the stability of the closed-loop system. For example, to have 1 nm position error magnitude for 2 mm 20 Hz sinusoidal tracking, a high controller gain is required that would destabilize the closed-loop system due to the actuator saturation and high frequency dynamics in the system. As a result, only reasonable overall performance can be achieved by a trading-off between stability/robustness and transient/steady state performance. This trade-off process is illustrated by following design of two controllers.

PID controller

PID controller was first tried due to its intuitive nature. The gains are determined by trial-and-error tuning process. Equation (6) and Equation (7) show the continuous form and the discrete form of the controller with T_s as the sampling period.

$$K_{PID}(s) = K_P + \frac{K_I}{s} + K_D s \tag{4}$$

$$K_{PID}(z) = \frac{\left(K_P + \frac{K_I T_s}{2} + \frac{K_D}{T_s}\right)z^2 - \left(K_P - \frac{K_I T_s}{2} + \frac{2K_D}{T_s}\right)z + \frac{K_D}{T_s}}{z^2 - z} \tag{5}$$

Lag-lead controller

The lag-lead controller uses frequency design approach to obtain desired frequency response. In general, a lead compensator is designed for fast response and a lag compensator for small steady state error.

Lead compensation

$$K_{lead}(s) = \frac{\alpha\tau s + 1}{\tau s + 1} \tag{6}$$

Lag compensation

$$K_{lag}(s) = \frac{\tau s + 1}{\tau s} \tag{7}$$

$$K_{lag}(z) = \frac{(T_s\omega_{lag} + 2)z + (T_s\omega_{lag} - 2)}{2(z-1)} \tag{8}$$

The overall controller gain K_c is selected to make the loop gain equal to one at the crossover frequency ω_c.

$$\left|K_c \cdot K_{lead}(z)K_{lag}(z)P(z)\right| = 1 \tag{9}$$

Comparison of two controllers

The transfer functions for controllers are defined between the position error input (mm) and current command output to the amplifier (amp). Equation (10) is for PID controller and Equation (11) for Lag-lead controller.

$$K_{PID}(z) = \frac{3321.1z^2 - 6518.9z + 3200}{z^2 - z} \tag{10}$$

$$K_{LL2}(z) = \frac{4355z^3 - 11928z^2 + 10878z - 3303}{2z^3 - 4.4197z^2 + 3.1516z - 0.73186} \tag{11}$$

A comparison of the theoretical closed-loop system frequency response for the two controllers is shown in Figure 7. They behave similarly in the frequency domain; that is, they increase loop gain at low frequency, add phase lead to obtain phase margin at the crossover frequency and lower the gain at high frequency. The transfer function in Figure 7(a) is from position command to the output position. It shows the closed-loop system has a bandwidth of 1122 Hz with the PID controller and 1594 Hz with the lag-lead controller. As a result, the closed-loop response

for the lag-lead will be faster but with slightly larger overshoot. The sensitivity function in Figure 7(b) is a measure of the error in tracking commands and rejecting disturbances. The unit of magnitude in this graph is in *dB* and it shows results that would not be visible in Figure 7(a) especially at low frequencies. For example, a sine wave command using the PID controller at 20 Hz, the magnitude is -52 dB in Figure 6(b), the error is 0.25% and the amplitude ratio in Figure 7(a) is 0.9975.

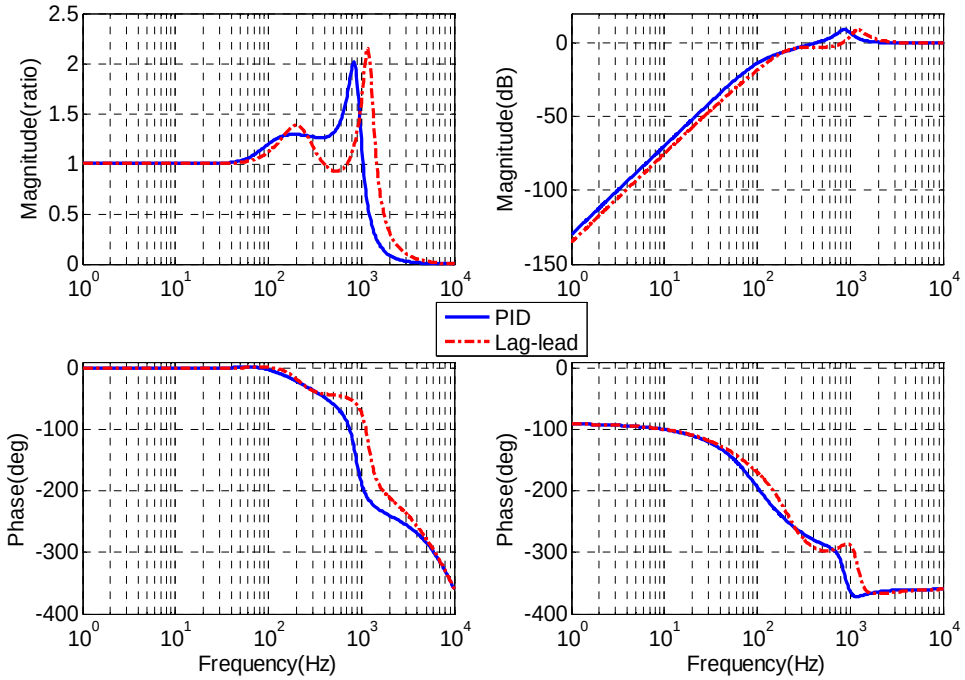

(a) Complementary sensitivity function (b) Sensitivity function

Figure 7. Closed loop simulations for PID and Lag-lead controllers

It is important to make the sensitivity magnitude small, and Figure 7(b) shows the typical trade-offs involved in feedback control design.

1. The lag-lead controller will minimize tracking errors and disturbance forces at frequencies lower than 1000 Hz. Below 100 Hz, the sensitivity magnitude from the lag-lead controller is about half that of the PID controller. This simulation result has been verified by the experiments with a disturbance force at 60 Hz.
2. Both controllers have nearly the same peak sensitivity magnitude but the lag-lead controller peaks at a higher frequency (1200 Hz) than the PID (800 Hz). This behavior will amplify disturbances above 1000 Hz.

The design process involves a compromise between reducing low frequency error magnitude and improving disturbance rejection at high frequency as shown in Figure 7(b).

With these two controllers design, additional studies on sensitivity function have been performed regarding the need for physical damping and most desirable piston mass.

1) Physical damping is not needed for the FLORA. At high frequencies the amplitudes and thus the forces are too small to make any appreciable difference. At low frequency and high amplitude, the damping forces are high but are not needed and only lead to higher motor force.
2) When the closed-loop system sensitivity magnitude frequency response exceeds 0 dB, the system relies totally on the mass to reject disturbances and noise. The controller actually amplifies the disturbances at frequencies higher than crossover frequency (430 Hz for the PID controller, 830 Hz for the lag-lead controller in Figure 7(b)). As a result of the high frequency disturbance with current FLORA design and achievable controller design, a smaller piston mass will reduce the system disturbance rejection capability. In other words, the high frequency disturbance shall be eliminated in the next generation FLORA design if the mass is to be further reduced.

2.4.3 POSITION HOLDING TEST

Figure 8 shows the frequency spectrum of the piston motion when holding position. Error for the PID controller is ±40 nm PP (10.8 nm RMS) and ±30 nm PP (8.0 nm RMS) for the Lag-lead. It is clear from Figure 8 that the amplitudes are smaller for frequencies less than 1000 Hz in the case of lag-lead controller.

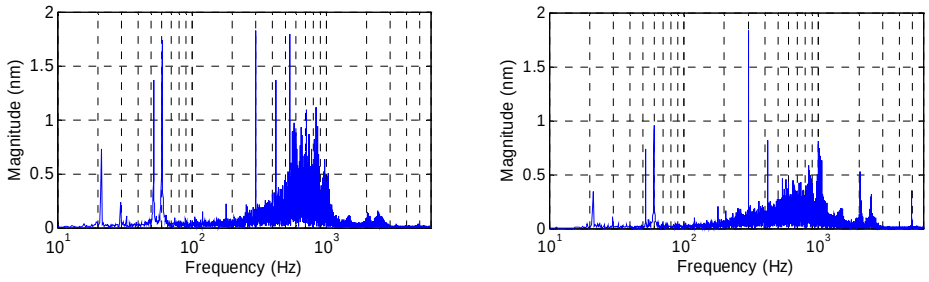

(a) PID controller (b) Lag-lead controller

Figure 8. Frequency spectrum of position data when holding position

2.4.4 MOTION TRACKING TEST

Figure 9 and 10 shows the positioning error in a test of sinusoidal profile tracking at 2 mm amplitude and 20 Hz. The error for both cases is about ±200 nm PP. The frequency limit of the encoder measurement has significant impact on the motion control performance. With 100 KHz limit, the high frequency position error glitches due to 125 nm measurement resolution exists in almost 100% of motion cycle, while 325 KHz limit make about 21 % of motion cycle free of this error glitch. The frequency spectrum in both figures only shows the section of magnitude from 0

to 4 nm to compare these two cases. It can be seen that, the magnitudes for frequencies above 1 KHz in Figure 10 is only half of those in Figure 9.

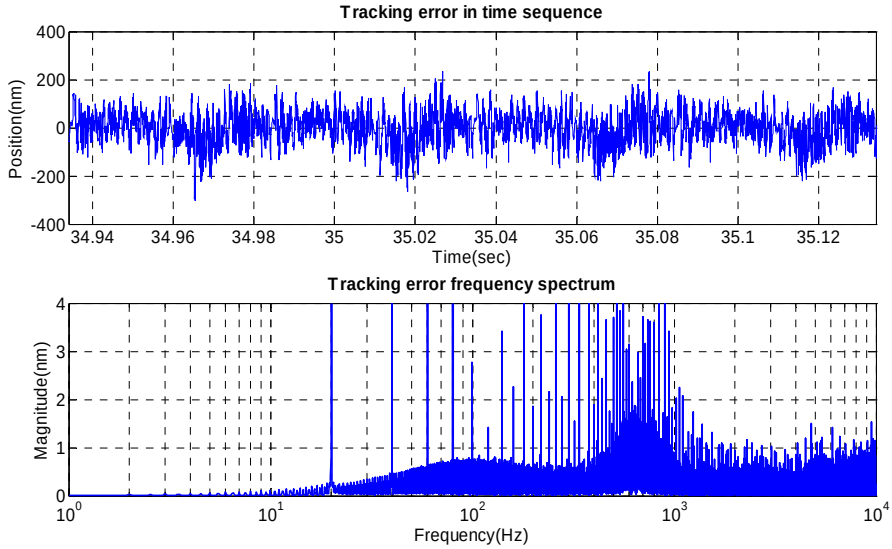

Figure 9. 2 mm 20 Hz sinusoidal tracking test with 100 KHz encoder measurement limit

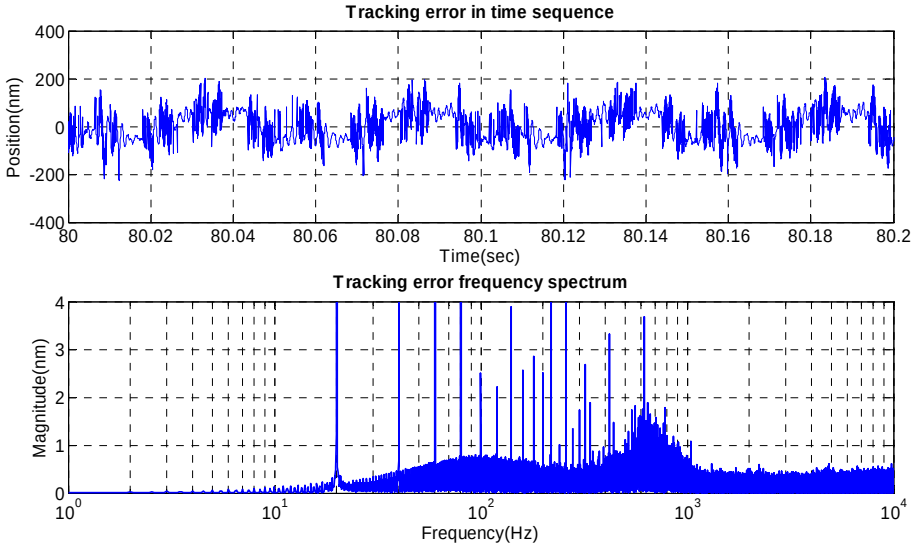

Figure 10. 2 mm 20 Hz sinusoidal tracking test with 325 KHz encoder measurement limit

2.4.5 MOTION PLANNING

To minimize the motion range of the FLORA piston, the freeform surface should be decomposed into a best-fit rotationally symmetric surface for the DTM axes and the residual non-rotationally symmetric shape for the FLORA. The position of the FLORA is synchronized to the position of the DTM axes by generating its motion command ($\boldsymbol{Z}$) as a function of DTM spindle angular position (θ) and the cross-feed slide position ($\boldsymbol{X}$) for a general freeform surface in Equation (12).

The measurement resolutions of spindle and X-slide position introduce errors to the tool motion command. For the case of the tilted flat, the motion command is shown in Equation (13) where *A* is the slope of the surface.

$$Z = f(X, \theta) \tag{12}$$

$$Z = A \cdot X \cdot \sin(\theta) \tag{13}$$

The X position is from the laser interferometer on the ASG controller. However, there was no easy access to this information so a pseudo quadrature signal was generated in the ASG to provide the PMDi controller with relative position of the slide from the center of rotation; that is, the radius. For the slide speed chosen for the machining the ± 2 mm tilted part with a 50 mm diameter, the measurement resolution of X position was 638 nm and this will produce quantization step size of 51 nm in the tool motion command to the FLORA piston. The second input from the ASG is angular position from the 20000 count/rev spindle encoder. At the maximum stroke, 1 count will produce a quantization step size of 628 nm in the tool motion command. To resolve these quantization error issues, a command stream smoothing technique has been developed to reduce the quantization step size due to the finite resolution of spindle encoder. In addition, a new laser interferometer (Zygo ZMI 501A) will be installed on the ASG-2500 to provide measurement resolution up to a few nanometers for x-slide position.

Spindle encoder feedback smoothing technique

The output of the spindle encoder is a quadrature signal producing 20,000 counts/revolution. The controller reads this input at the clock rate of 20 KHz so the number of counts is related to the spindle speed. At a spindle speed of 20 Hz, the counter will see a change of 20 counts per controller cycle but at slightly faster speed (1250 rpm for example), the digitized counter reading will change by 20 or 21 counts. When this integer difference changes by one full count, it will generate a small disturbance in tool position. To reduce the magnitude of this change, a smoothing algorithm has been designed and implemented on the PMDi digital signal processor.

The algorithm uses the fact that while the spindle speed may not be the exact set value, the average will stay constant. Therefore, using the average change in counts at the actual spindle speed will smooth steps and provide a higher resolution estimate of the angular position of the tool. The change in counts per controller cycle and the average of some time interval can be written as:

$$\Delta_{count} = counter(t) - counter(t-1)$$

$$count_{avg} = \Sigma counts / number\ of\ cycles \tag{14}$$

Based on the average count, the position of the spindle in counts can be estimated as

$$position(t) = position(t-1) + count_{avg} \tag{15}$$

The error (e) from this estimation of position can be determined and driven to zero by a adding or subtracting a fixed correction (0.1 count for example) depending on the sign of the error.

$$e(t) = \Delta_{count} - count_{avg} + e(t-1) \tag{16}$$

For e > 0

$$\begin{aligned} position(t) &= position(t) + correction \\ e(t) &= e(t) - correction \end{aligned} \tag{17}$$

For e < 0

$$\begin{aligned} position(t) &= position(t) - correction \\ e(t) &= e(t) + correction \end{aligned} \tag{18}$$

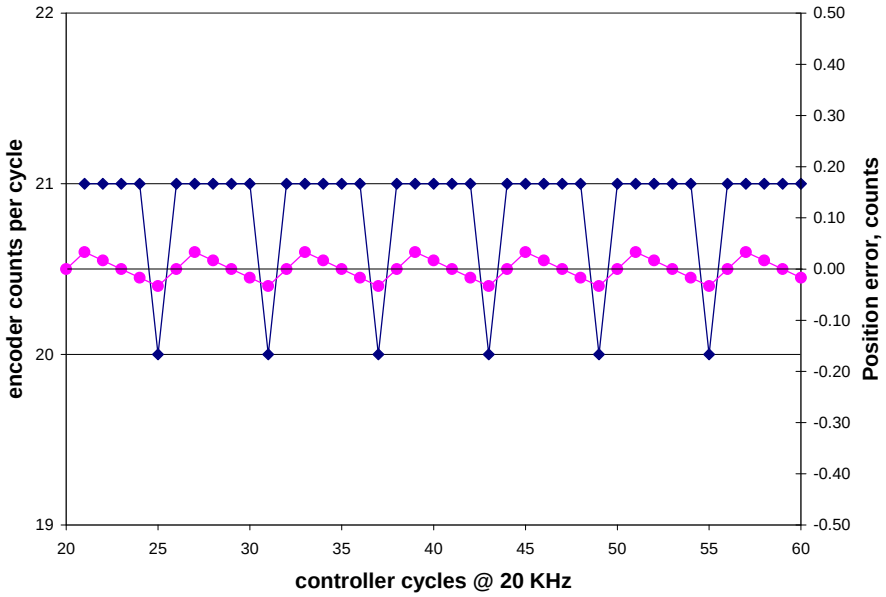

Figure 11. Spindle encoder quantization and the reduction in step size from 1 to 0.03 counts

A theoretical example of the application of this smoothing algorithm to the spindle speed slightly above 20 Hz (20.833 Hz or 1250 rpm) is shown in Figure 11. This graph shows that the digitized number of counts per controller cycle changes from 20 to 21 because the spindle speed is not an exact multiple of the controller cycle time. This change would produce a small step in the command due to the quantization. If the algorithm discussed above is applied, the averaging effectively increases the resolution of the encoder and the one step change is divided evenly in the time between steps.

2.5 CUTTING PERFORMANCE

2.5.1 FLAT SURFACE

A flat surface was machined to test the ability of the FLORA piston to hold position while being excited by the machining forces. The flat was machined with a 0.5 mm radius diamond tool at 500 rpm with a 1 mm/min feedrate (2 µm/rev) and 2 µm depth of cut on the finish pass. The theoretical finish is 1 nm PP. The Zygo NewView measurement in Figure 12 shows a 144×108 µm patch on this surface that represents approximately 72 tool passes and has an average surface finish of 9.0 nm (RMS).

Table 1 compares the RMS of flat surface finish when the tool is locked or positioned by the control system. For the locked case, the air bearing was locked down by removing the air from the lower sides of the triangular piston. Comparing to the case of the locked tool, the two controllers added surface roughness. The active closed-loop control adds 5.6 nm RMS error for the PID controller and 2.3 nm RMS error for the Lag-lead controller.

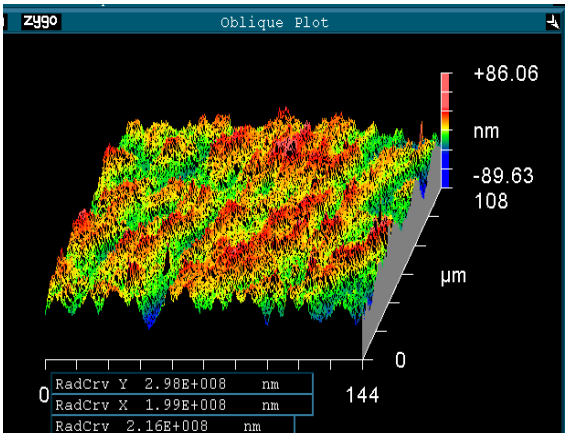

Figure 12. ZYGO image of surface finish (RMS=9.0 nm) of a half inch diameter brass flat

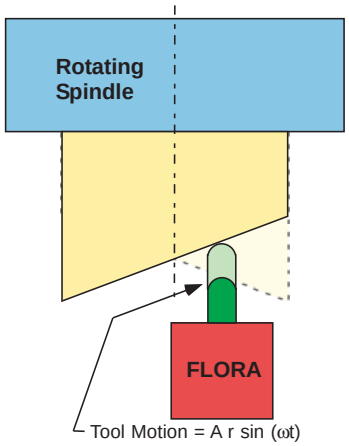

Figure 13. Tilted flat for measuring non-rotationally symmetric actuator performance

Table 1. Comparison of RMS error with a locked and position controlled tool holder

	Tool holding method		
	Piston Locked	**Lag-lead controller**	**PID controller**
Surface finish, nm RMS	6.7	9.0	12.3
Piston Motion, nm RMS	1	8.0	13.1

2.5.2 TILTED FLAT

A tilted flat was machined to evaluate the ability of the servo to create non-rotationally symmetric optical surfaces. The tilted flat requires a sine wave motion of the tool with the amplitude changing linearly with the radius. This part is a good test of the performance of the actuator as the amplitude changes but the frequency remains constant. The machined surface should be a flat and thus easy to measure in a laser interferometer.

Figure 13 shows the arrangement of the experiment. The tool is mounted on the X-axis which moves in the horizontal (radial) direction starting at the center and moving to the OD of the part. The amplitude is the highest at this point. The spindle is on the Z-axis and remains stationary during the cut. The commanded motion to the tool is as shown in the equation in Figure 6 where *A* is the slope of the tilted flat, *r* is the radius of the part at the tool contact point and ω is the angular speed of the spindle.

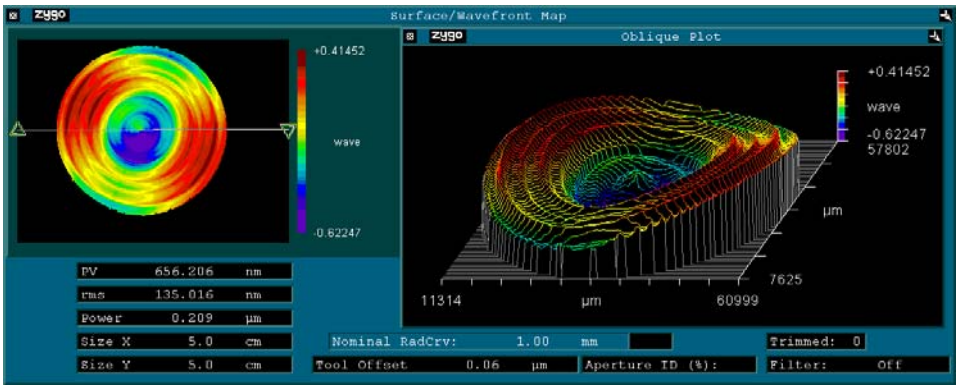

Figure 14. Measured flatness of the 50 mm diameter tilted flat using laser interferometer. Maximum amplitude of actuator was ±0.2 mm at 10 Hz.

One additional correction to the tool path is to compensate for the radius of the tool. Notice from Figure 13 that the tool will touch the part on the left of its centerline at its longest extension and a half-cycle later to the right of its centerline at its shortest extension. Half way in between, it will touch at the tool centerline. This change in contact position results in a small change in part radius (depending on the radius of the tool) and therefore height at the location where the cutting occurs. The solution is to modify the tool commanded position to account for the tool radius. The command is approximately a small sine wave which is twice the frequency of the spindle rotation. Figure 14 shows the shape of the tilted flat measured on the Zygo GPI laser interferometer. The diameter of the part is 50 mm and it was rotating at 600 rpm (10 Hz). The flatness of the machined plastic part was excellent, 135 nm RMS, or 0.2 waves. This means the surface is flat to 1 part in 3000. Note that the surface has astigmatism (two highs and two lows

on the surface) and the center is low compared to the edges. There is also a cyclic variation in height with a 4 mm wavelength and a magnitude less than 100 nm.

2.6 REACTION FORCE REDUCTION

The force created by starting and stopping the FLORA piston (0.65 Kg mass) results in a significant disturbance to the DTM. An active reaction force attenuation approach using a commercial shaker[1] supported by a linear ball bearing slide placed on the base of the FLORA is shown in Figure 1. When the FLORA and reaction force act in opposite directions, there will be little net force or torque on the machine base if the two actuation forces are properly aligned and tuned. The disadvantage of this design is that the second actuator requires additional cost and is only used for reaction force attenuation. Reducing the mass of the FLORA and the amplitude or frequency of actuation will reduce the force.

Calibration process: To properly tune the control signal to the shaker, an accelerometer[2] was used to measure the structure vibration level either at the actuators base plate and encoder read head. The steps to find the proper signal to the counterbalance mass were:

(1) Actuate the shaker alone, take the phase lag (*PH1*) of control signal to the Kepco amplifier and accelerometer signal in position output mode, and the peak-peak amplitude (*VA1*) of accelerometer output signal in voltage,
(2) Actuate the piston alone, take the phase lag (*PH2*) of control signal to the Kepco amplifier and accelerometer voltage output, and the peak-peak amplitude (*VA2*) of accelerometer output signal in voltage,
(3) The final phase correction for the voltage command to the Kepco amplifier is *PH1-180-PH2*
(4) The final magnitude correction ratio for the voltage command to the Kepco amplifier: *VA2/VA1*.

It is impossible to completely eliminate reaction force, especially when the linear motor and the shaker have different dynamic characteristics. However, Table 2 shows the performance of the reaction force reduction when the piston is commanded to move in 2 mm 20 Hz sine wave motion. In these tests, the accelerometer was attached to the side surface of encoder read head in-line with the piston actuation direction.

The reaction force resulted from 2 mm 20 Hz sinusoidal piston motion is 21 N, the shaker can effectively attenuate most of the reaction force from the linear motor. The measured vibration level is reduced by 37 times. However, it can also be seen that from Table 2, there is some

[1] Labworks shaker ET 132-2, driven by Kepco amplifier BOP 15-20M

[2] Charge accelerometer Bruel & Kjar 4393 with charge amplifier 2635

amount of increase for the magnitude of 40 Hz and 80 Hz motion components. This is due to differences between the dynamic characteristics of the shaker and linear motor. Ideally, two actuators with exactly the same properties should be used for reaction force management.

Table 2. Reaction force reduction with voice coil motor in 2 mm 20 Hz sinusoidal piston motion

Shaker actuation state	**Accelerometer output signal** (volt)				
	Peak-peak value in time domain	Change of harmonics magnitude in frequency domain when the shaker is activated			
		20 Hz	40 Hz	60 Hz	80 Hz
Not activated	0.630	-35 dB	15 dB	0dB	10dB
Activated	0.017				

For operation at a lower frequency (2 mm 5 Hz) sinusoidal piston motion, the reaction force is about 1 N and there is little change of accelerometer measurement signal under three scenarios: no piston motion, piston activated, both the piston and the shaker activated. This measurement result shows that 1 N 5 Hz reaction force exerts little impact on the rest of the system.

2.7 CONCLUSIONS AND FUTURE WORK

The goal of this project is to develop a design and control methodology to create a Fast Long Range Actuator that can machine non-rotationally symmetric (freeform) optical surfaces. The form error should be less than 150 nm (λ/4) and a surface finish less than 5 nm RMS. But speed is also an important issue and the design must have a bandwidth to produce these freeform surfaces with minimum deviation from current processing time for spherical or aspheric parts.

The FLORA control system has been upgraded with a high-resolution encoder, a linear amplifier and a high-speed DSP based controller. The key conclusions are as follows:

- High controller gain in the frequency range below 1000 Hz is needed to reduce tracking error at 20 Hz and reject disturbance forces in cutting process. Improved performance could be achieved if the high frequency (>1000 Hz) dynamics within the FLORA can be minimized physically.
- The feedback control design approach achieved reasonable performance over the range of frequencies of interest. It will be combined with feed-forward control and other more advanced control approaches to improve the tool positioning performance.
- The system changes discussed in this paper improved the position holding capability by 85% over the system described in 2006 [1].

Over the next few months, several significant changes to the system will take place and a second prototype design will evolve.

Encoder and Data Acquisition System The key issues are to improve the analog signals quality and digital signal processing so that position interpolation process can handle signal up to 1 MHz.

Motor The linear motor will be retained for the new controller/encoder experiments and then evaluated to see if a voice coil motor is preferable.

Linear Amplifier Increase the nominal bandwidth up to 4~5 KHz, modify the analog current control loop to remove the frequency response peak around 900 Hz.

New Piston and Air Bearing Design A new design is being proposed to reduce the width of current FLORA by half while maintaining the air bearing stiffness and structural stiffness. The dynamics of the piston under the support of the air bearing will be optimized to minimize the micro scale motion in other 5-DOF when the piston moves in the tool feed direction.

Advanced Controller Design A composite controller is proposed with three main foci.

(1) Optimal control, robust control or other non-linear control approach will be explored in addition to basic PID control and Lag-lead control to push the limit of the position feedback control.
(2) A wide-band control approach called disturbance observer [2, 3] can further increase the controller gain in the low frequency range without compromising the system stability and robustness by implementing it within velocity loop.
(3) A narrow-band control approach called adaptive feedforward controller [4] can be used to increase controller gain at selected frequencies.

All these different approaches can be integrated into a composite controller to achieve robust high performance motion control system.

REFERENCES

1. Buescher, N., Dow, T and Sohn, A., *Live Axis Turning*, Proceedings of ASPE, Vol 37, 2006, pg 25-28.
2. Lee, Ho Seong and Tomizuka, M., *Robust motion controller design for high-accuracy positioning systems,* IEEE Transactions on Industrial Electronics, v43, n1, Feb.1996, p48-55.
3. Elfizy, A. T., Bone, G. M. and Elbestawi, M. A., *Model-based controller design for machine tool direct feed drives*, *International Journal of Machine Tools and Manufacture*, Volume 44, Issue 5, April 2004, Pages 465-477.
4. Byl, Marten F., Ludwick, Stephen J. and Trumper, David L., *A loop shaping perspective for tuning controllers with adaptive feedforward cancellation*, Precision Engineering, Volume 29, Issue 1, January 2005, Pages 27-40.

3 FRESNEL LENS TESTING AND FABRICATION

Alex Sohn
Precision Engineering Center Staff
Thomas A. Dow
Dean F. Duncan Distinguished Professor
Department of Mechanical and Aerospace Engineering
Kenneth Garrard
Precision Engineering Center Staff

To reduce the cost of manufacturing the optical components in laser print engines, the PEC is working to design and fabricate Fresnel lenses that perform as well or better than existing components. Fresnel lenses are typically thinner than conventional lenses and are potentially easier and quicker to mold. This report describes the challenges in measuring and fabricating these lenses. The effort began with the evaluation of commercial, conical groove Fresnel lens using a CMOS array digital camera as the sensor. The results revealed poor surface features and performance that was not acceptable for the scanning system. However, part of the problem was in the measurement process and the technique needed to be modified. The breakthrough in measuring spot sizes was calibration of the intensity response of the CMOS camera used in the measurements. After initial tests of a commercially available conical Fresnel lens revealed too much diffraction, an aspheric lens was machined for testing. Finally, progress in designing lenses for diffraction made it necessary to machine conical groove "kinoform" lenses with groove spacing on the order of only a few micrometers. A special apparatus has been designed and tested to achieve this fine groove structure.

3.1 INTRODUCTION

Laser scanning systems

A simplified schematic of a laser scanning system using a Fresnel lens is shown in Figure 1. The laser, collimating optics and scan mirror are as in a conventional system. The scan lenses, however would be replaced by one or two Fresnel lenses. Since the beam must be scanned over a large distance (usually around 200 mm), the scanning lens is usually long in the scan direction. The orthogonal or "process" direction (out of the plane of the page in Figure 1) usually has different focusing requirements so that the lens is typically anamorphic or non-rotationally symmetric.

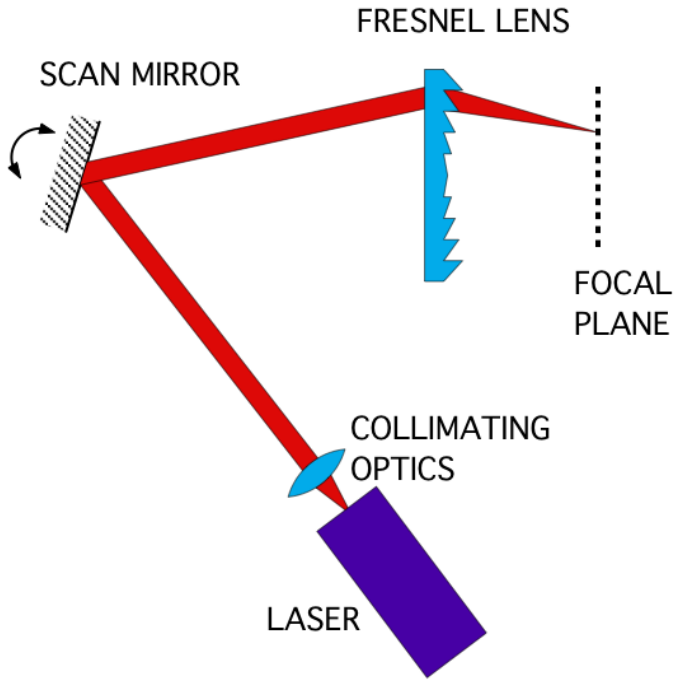

Figure 1. A simplified laser scanning system using one Fresnel lens for the scanning optics.

The key aim of this research is to develop a Fresnel lens to focus the scanning laser beam onto the rotating drum at the focal plane in Figure 1 such that a fixed relationship exists between the scan angle and axial position of the beam on the drum face. The conventional, multi-element refractive lenses currently used for the scanners follow the so called "*f*-θ" relationship; that is,

$$h = f\theta$$

where h is the axial location of the spot across the face of the drum, f is the focal length of the lens and θ is the input beam angle. Fresnel lenses can also be made to follow the *f*-θ condition but because of the discontinuous shape, diffraction effects cannot be ignored.

To develop Fresnel lenses for scanning systems, examples have been purchased, designed and fabricated. A few structures were commercially available and but the shapes are limited. To study shapes such as constant-depth aspheric Fresnels and anamorphic surfaces, it is necessary to fabricate the lenses. Initial testing included a Fresnel prism and a conical-groove constant-spacing Fresnel lens. A true aspheric profile and constant-depth groove lens was designed following the design approach of Section 1 of this Annual Report. This report describes the measurement and fabrication of Fresnel lenses.

3.2 LENS METROLOGY

3.2.1 TEST SETUP

Measuring the performance of various lenses and, ultimately a well-performing Fresnel scanning lens, was accomplished with the setup shown in Figure 2. The setup has been through several revisions beginning with a helium-neon laser and coarse focusing and translation mechanisms. In the current setup, a collimated diode laser beam is focused by a test lens onto a CMOS camera array. A 200 mm focal length lens focuses the beam to the location of the focal plane of the camera – a Canon Digital Rebel XT camera. Early experiments revealed that the 1 mW source was too intense and caused saturation of the camera array. Using silicon mirrors with a much lower reflectance in the visible spectrum as fold mirrors and/or neutral density filters accomplished this attenuation without unduly affecting the profile of the beam. For measurements as a function of aperture position, a translation stage allows the sample lens to be translated together with the camera at precisely spaced intervals.

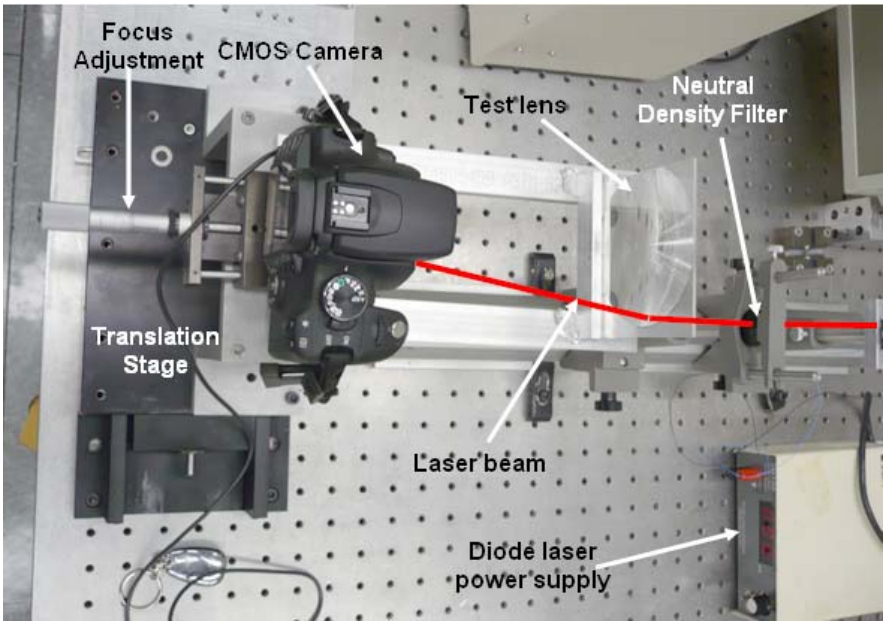

Figure 2. Experimental test setup.

3.2.2 DIGITAL CAMERA

The digital camera is an ideal device to measure spot size because of its low cost, USB interface for transferring data to the computer and the available software to analyze the image. Ironically, its drawbacks are also related to the onboard image processing software that the manufacturer uses to produce a satisfying picture quality for the typical user. The Center for Electron Microscopy at NC State does not use digital cameras but instead uses black-and-white film that is processed and then scanned on a calibrated scanner to produce a digital image. Finding a way to relate the output data from the digital camera to the intensity of the size of the spot from the lens has been difficult.

A typical color detector array in a digital camera detector is a large array of photodetectors arranged in tiles that each have 4 detectors with red, green and blue filters arranged in square pattern. The CMOS detector on the Canon camera has 8 million photodetectors spread over an area of 22.2 x 14.8 mm or an average spacing of 6.5 µm between detectors. The following description of a typical CMOS chip was taken from the Olympus web site [1].

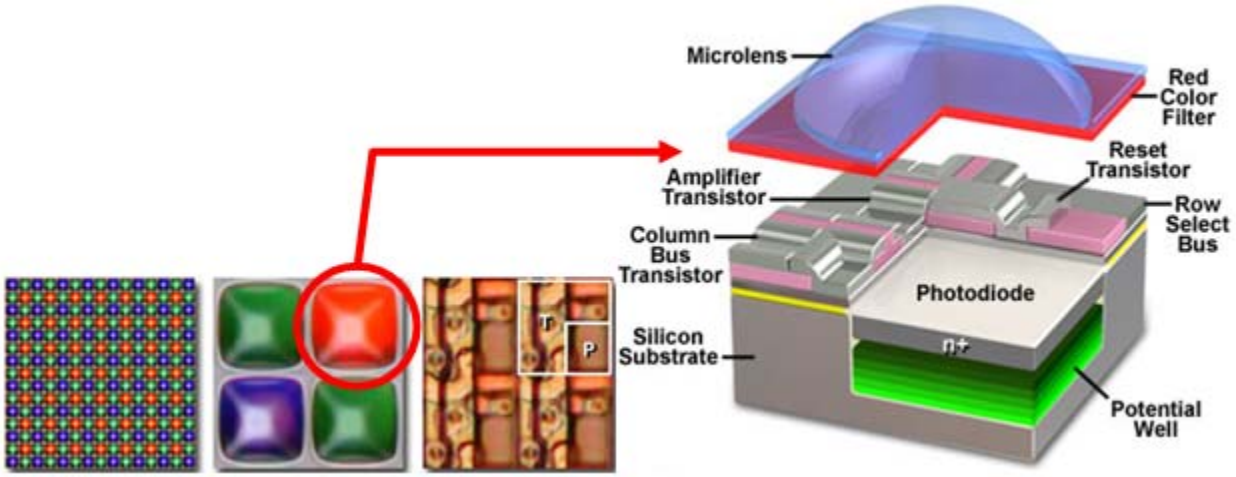

Figure 3. Photodiode detector array (left) is made up of single pixels (right) arranged in a basic tile (center) of four filtered photodiodes; one red, one blue and two green. The size of this 4 element tile is 13 x 13 µm in the Canon CMOS array.

A quartet of detectors with different filters is shown in Figure 3 along with the details of each photodetector. To concentrate incident photons into the photodiode electron collection wells, each of the filtered photodiodes are housed beneath a miniature positive meniscus lens. The inset in Figure 3 reveals a high magnification view of the filters and microlens array. Included on the integrated circuit is analog signal processing circuitry that collects and interprets signals generated by the photodiode array. These signals are sent to the analog-to-digital conversion

circuits, located adjacent to the photodiode array on the upper portion of the chip. Among the other duties performed by the CMOS image sensor are clock timing for the stepwise charge generation, voltage collection, transfer, and measurement duties, as well as image processing and output of the accumulated signals.

The photodiode array in Figure 3 reveals a sequential pattern of red, green, and blue filters that are arranged in a mosaic pattern named after Kodak engineer Bryce E. Bayer. This color filter array (a Bayer filter pattern) is designed to capture color information from broad bandwidth incident illumination arriving from an optical lens system. The filters are arranged in a quartet ordered in successive rows that alternate either red and green or blue and green filters. Figure 3 illustrates the alternating filter rows. Each red filter is surrounded by four green and four blue filters, while each blue filter is surrounded by four red and four green filters. In contrast, each green filter is surrounded by two red, four green, and two blue filters. The total number of green filters in the array is equal to the number of red and blue filters combined. The heavy emphasis placed upon green filters is due to human visual response, which reaches a maximum sensitivity in the 550-nanometer (green) wavelength region of the visible spectrum.

The unbalanced nature of Bayer filter mosaic arrays, having twice as many green filters as blue or red, would also appear to present a problem with regards to accurate color reproduction for individual pixels. Typical transmission spectral profiles of the common dyes utilized in the construction of Bayer filters are presented in Figure 4. The quantum efficiency of the red filters is significantly greater than that of the green and blue filters, which are close to each other in overall efficiency. Note the relatively large degree of spectral overlap between the filters, especially in the 520 to 620 nanometer (green, yellow, and orange) region.

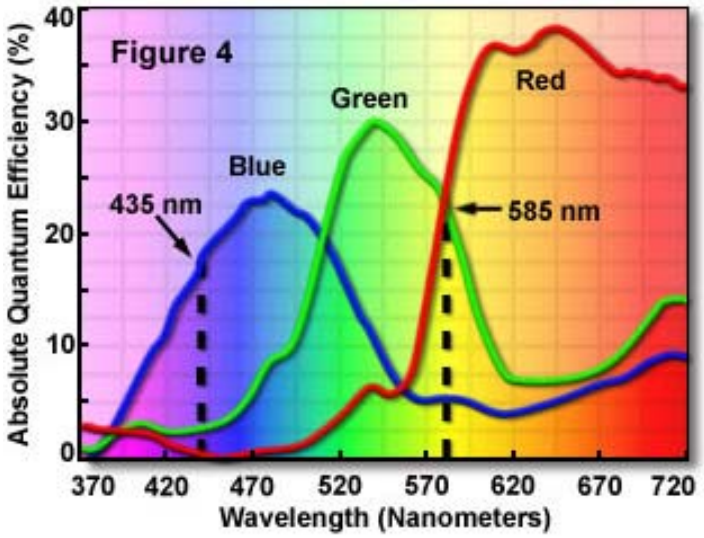

Figure 4. Transmission spectral profile of common dyes in a Bayer filter.

*After a raw image has been obtained from a CMOS photodiode array blanketed by a Bayer pattern of color filters, it must be converted into standard red, green, and blue (**RGB**) format through interpolation methodology. This important step is necessary to produce an image that accurately represents the scene imaged by the electronic sensor. A variety of sophisticated and well-established image processing algorithms are available to perform this task (directly on the integrated circuit after image capture), including **nearest neighbor**, **linear**, **cubic**, and **cubic spline** techniques. To determine the correct color for each pixel in the array, the algorithms average color values of selected neighboring pixels and produce an estimate of the color (chromaticity) and intensity (luminosity) for each pixel in the array. Figure 5(a) is the raw Bayer pattern image before reconstruction by interpolation and Figure 5(b) is the results obtained after processing with a correlation-adjusted version of the linear interpolation algorithm.*

Figure 5. Raw Bayer pattern image (left) and interpolated image (right) of the same scene.

The complexity of the image processing performed by a digital camera was not anticipated when it was chosen as the sensor for these tests. However as the project has evolved, calibration techniques have been developed to create an image useful for the lens development.

3.2.3 INCIDENT BEAM

Initially, a HeNe laser (632.8 nm wavelength) from a length-measuring interferometer was used as the source beam. This instrument has an adjustable aperture stop with two positions that create a 1.4 or a 2.8 mm diameter beam. The large aperture beam was used for the illumination and the intensity of the beam as measured through diamond-turned PMMA flat shown in Figure 6. The diameter of the beam is 2.8 mm Full Width Half Maximum (FWHM). Clearly, the beam is not the ideal Gaussian form but has some lobing and structure. Later in the development, this

HeNe laser was replaced with a diode laser used in commercial print engines. The wavelength was longer (650 nm) and the beam diameter was larger, 5 mm.

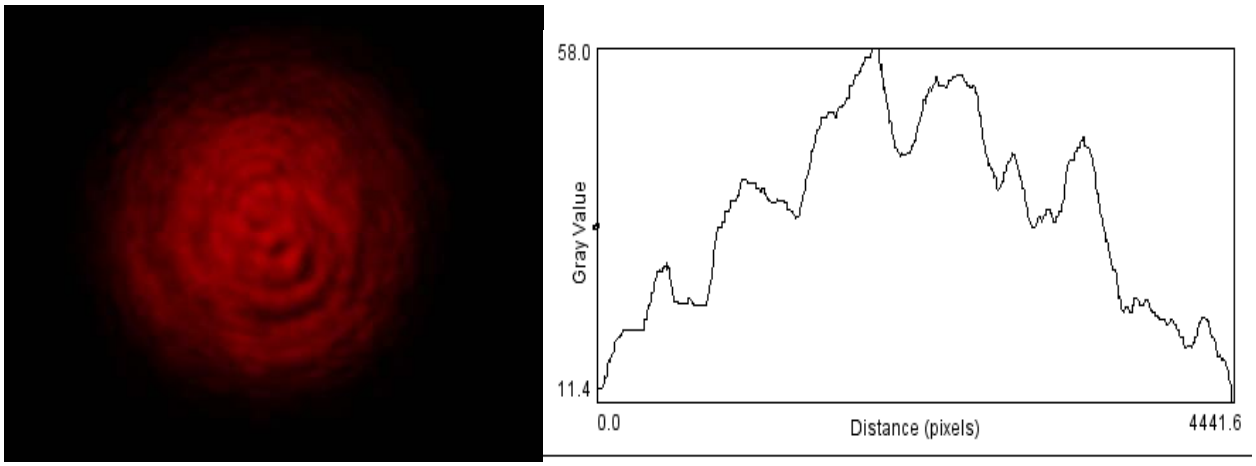

Figure 6. Incident HeNe beam with large aperture (FWHM =2.8 mm).

3.2.4 FOCUSING TEST

As part of the initial setup, the spot size from a glass biconvex focusing lens (FL = 200 mm) was measured to establish a baseline for the focusing experiments. The tests were carried out by focusing the beam on the shutter surface of the camera and one result is shown in Figure 7. This figure shows the image of the focused spot and a horizontal scan through the center of the spot with the grey scale value from each detector plotted as a function of distance along the array. This resulting spot size is estimated to be 80 µm FWHM.

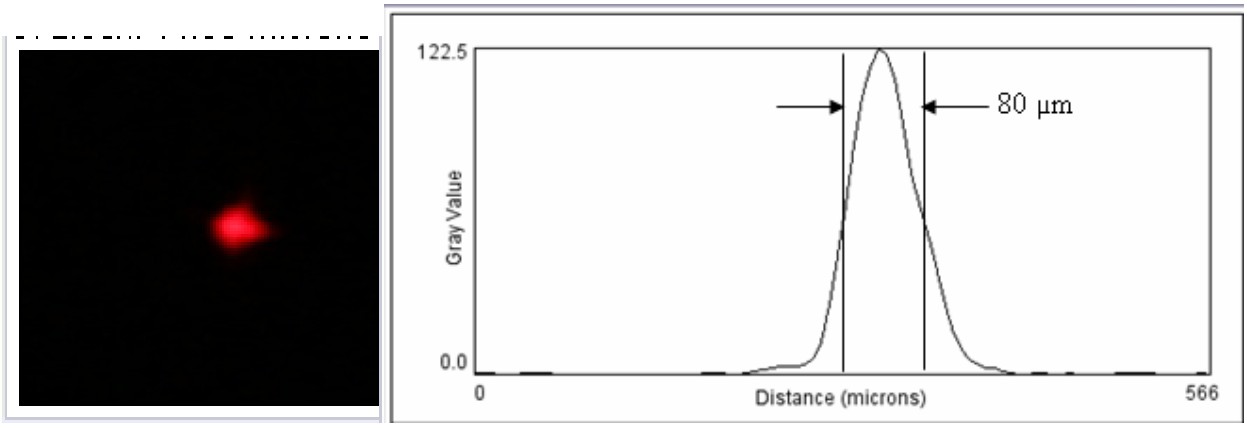

Figure 7. Image spot from 200 mm f/1 lens with attenuated beam (left) and intensity plot (right). FWHM is 80 µm.

Note in Figure 7 that the grayscale value is 122. As explained above, the camera takes the intensity from each filtered photodiode (also considering the value of the neighboring photodiodes) and creates a RGB digital word with a maximum value of 255 for that virtual pixel. Thus the maximum value for a single color with equal weighing for each color is 85. However, because the laser light is mostly red, a value of 122 means that the red intensity has been saturated and increased intensity of light is the result of exposing adjacent photodetectors whose intensity is added to that virtual pixel as a result of the interpolation scheme in the firmware. As shown in Figure 4, the filters are not perfectly selective, that is, red light passes through both the green and blue filters with lower efficiency. Thus, the interpolation algorithm uses light levels from a neighborhood of adjacent photodetectors in a proprietary algorithm to arrive at the RGB color value for a single virtual pixel.

3.2.5 CONICAL GROOVE LENS MEASUREMENTS

The first Fresnel lens to be measured was a 10.4" diameter, 8.00” focal length (f# =0.76), 0.06” thick, 200 grooves/inch (0.127mm spacing) conical groove contoured to aspheric profile designed to operate with grooves facing out. A 1.5” wide section was cut from the center and the lens was measured with the beam both on-axis and off-axis. The lens was illuminated by the 2.8 mm diameter HeNe beam. The on-axis spot measurement is shown in Figure 9, with a cross section in Figure 10. The central spot is surrounded by annular rings that cause large amounts of what appeared to be diffraction. The FWHM spot size was large (0.9 mm) and this diffractive structure would have to be removed if this type of lens were to perform adequately in a scanning application. The poor performance of this lens may be due to the poor surface quality illustrated in Figure 8 but the measurement technique was also to blame because the overall intensity measured vastly exceeded the red channel saturation level of 85. As a result, an effort to calibrate the camera sensor was begun.

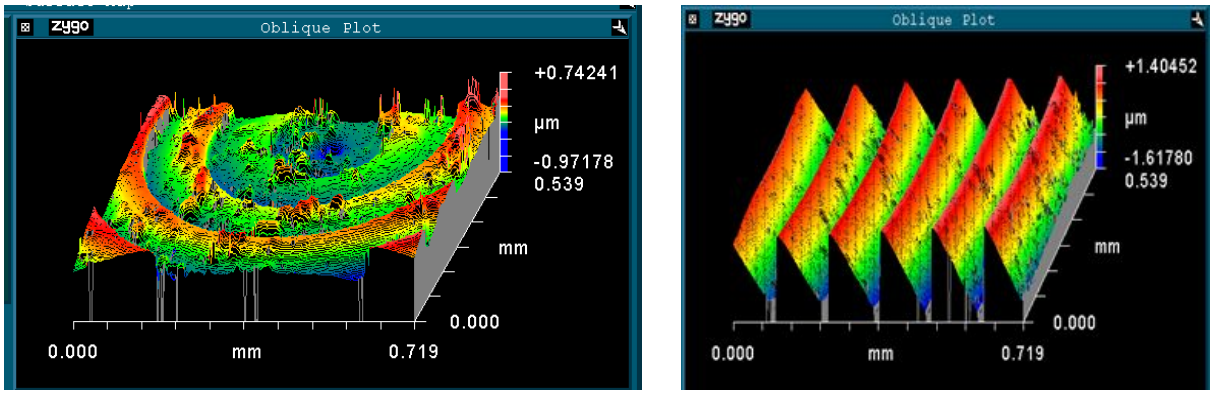

Figure 8. Optical profilometer measurement of center (left) and outside edge of a commercial conical-groove Fresnel lens. Note the poor surface quality near the center.

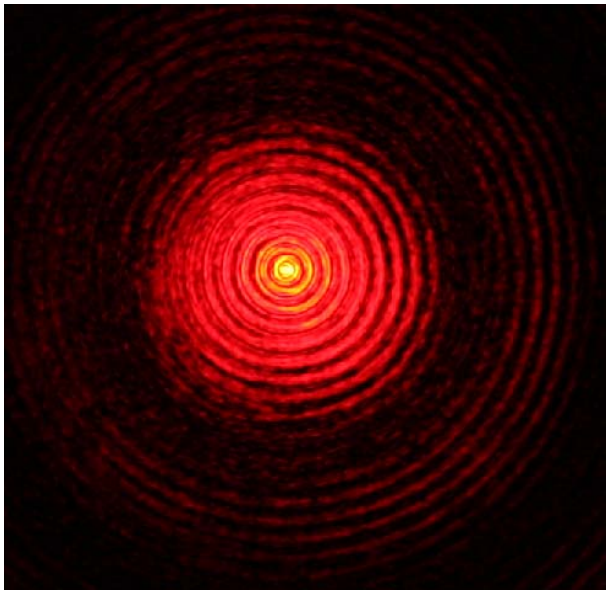

Figure 9. Conical groove Fresnel intensity on-axis. The image size is approximately 4 x 4 mm.

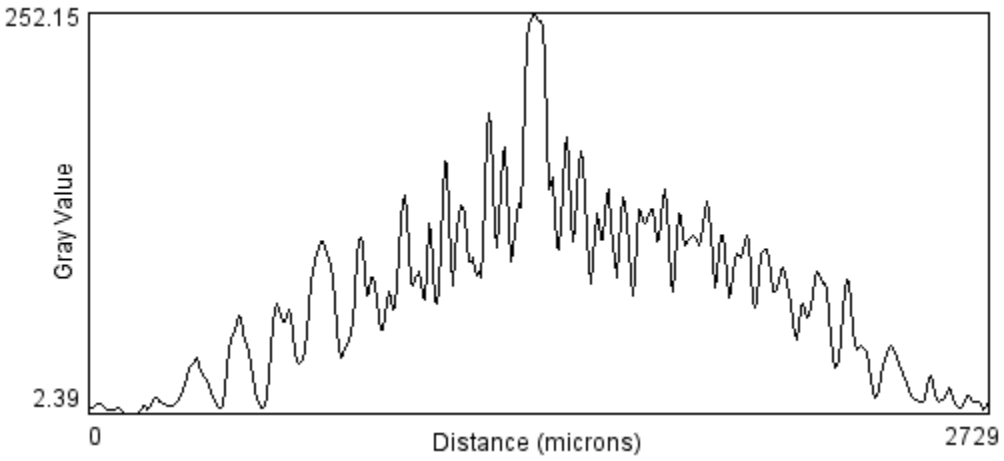

Figure 10. Section of irradiance plot shown in Figure 9. The vertical scale is the RGB 8-bit digital value that the camera assigns to each pixel on the array.

3.2.6 SINGLE-SLIT MEASUREMENTS

The results of the conical groove experiments pointed to the detailed knowledge of the operation of the digital camera and the relationship between light intensity into it and the resulting digital output. A simple test was needed that had a known theoretical result to show the difference between the measured and predicted illumination. To this end, a single slit was made with two

razor blades spaced at 0.100 mm. The result of measuring the diffraction pattern from this slit is shown in Figure 11 along with the theoretical model of diffraction from a slit.

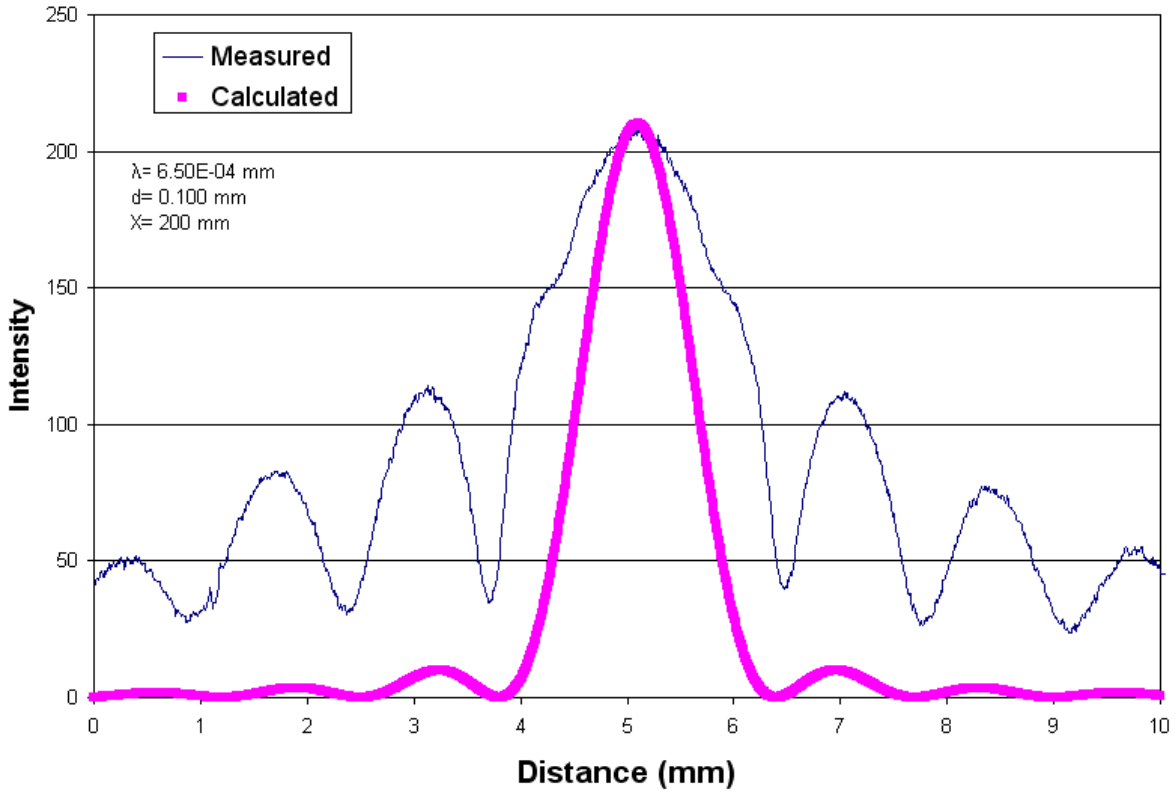

Figure 11. Intensity plot of the diffraction from a single slit. The measured profile does not match the calculated intensity but th, though the spacing of the diffraction peaks is correct.

The diffracted intensity pattern was calculated using the Fraunhofer approximation [2] with the diffracted intensity can be written as:

$$I = C^2 \frac{\sin^2\left[\pi(d/\lambda)(Y/X)\right]}{\left[\pi(d/\lambda)(Y/X)\right]^2} \tag{1}$$

where C is a normalization constant, d is the slit spacing, λ is the incident wavelength, Y is the distance from the slit to the screen and X is the distance on the screen. While the spacing of the diffraction orders in Figure 11 was close to the predicted values, the result showed the diffracted orders to have a much higher intensity than expected. In this case, the scenario was so simple that it had to be the measurement that was flawed. This observation led to the development of a calibration technique for the camera CMOS detector.

3.2.7 INTENSITY CALIBRATION

Based on the results of the single slit measurements, it became clear that it was important to reduce the intensity of the light to avoid saturating the detectors but in addition, the detector response may not be linear. To relate the spot size from a lens to the camera output, the response must be linearized with respect to incoming intensity.

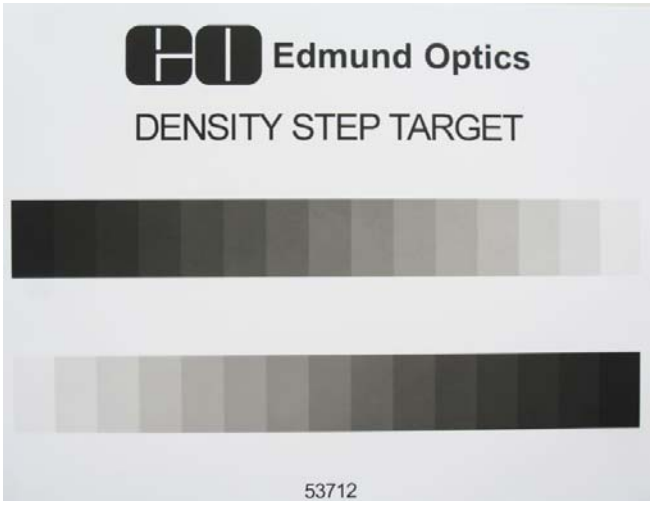

FIGURE 12. Density step target used in the first attempt to calibrate the CMOS camera.

The first attempt to calibrate the CMOS detector used the density step target in Figure 12. An image of this target was made with the camera and lens at different light levels to vary the intensity on the detector and the response was fit to a curve shown in Figure 13. Two problems arose with this technique: 1.) then non-linear nature of the target and 2.) heavy dependence on lighting of the target's response. The density target is calibrated in terms of optical density (O.D.).

$$O.D. = -\log_{10}\left(\frac{I}{I_0}\right), \tag{2}$$

Where I_0 is the incident and I is the reflected or transmitted intensity. Since this is a logarithmic scale, the density range of 0.09 to 1.5 in the target covers only a small portion of the response

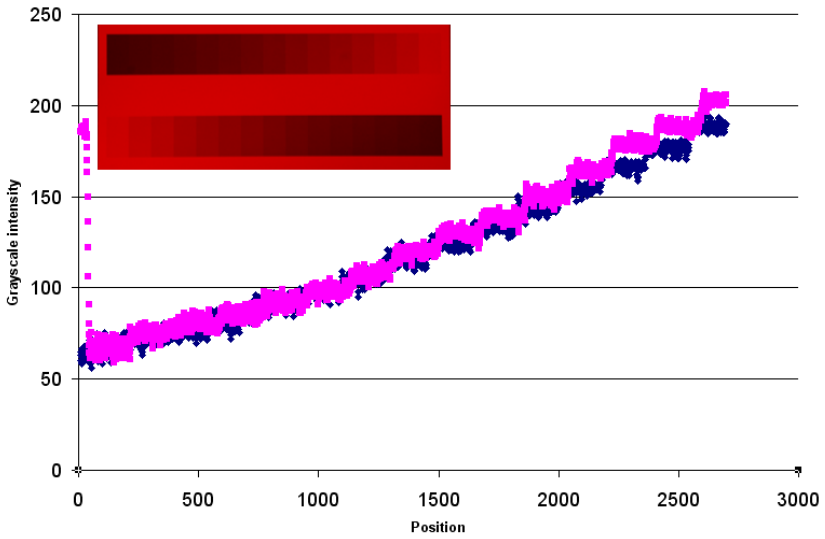

Figure 13. Calibration of the greyscale output from the Canon camera/lens as a function of optical density of target (in terms of position along target).

range of the camera. The density step target was thus abandoned in favor of a more direct technique.

The second technique to calibrate the detector was to use the laser itself. Since intensity increases linearly with exposure, if the same source is captured at multiple exposures, the intensity of the images can be used to calibrate the detector. To calibrate the full range of the detector, different points on the same image with different relative intensities were sampled. Figure 14 is an example of a spot measurement. Multiple points on the intensity profile can be monitored. If the profiles are plotted as a function of exposure time as in Figure 15, the change in intensity can be determined.

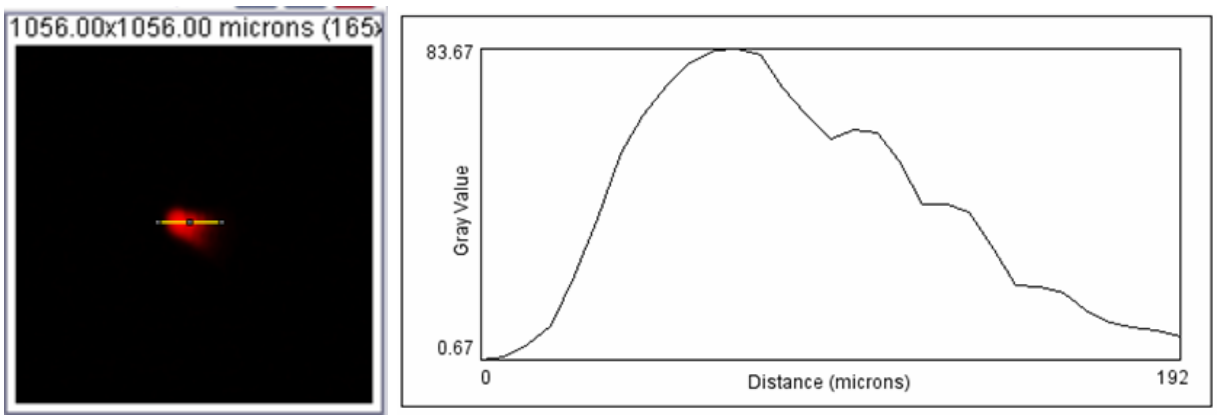

Figure 14. Sample spot measurement used in calibration showing intensity of red output (maximum value 85) vs. position.

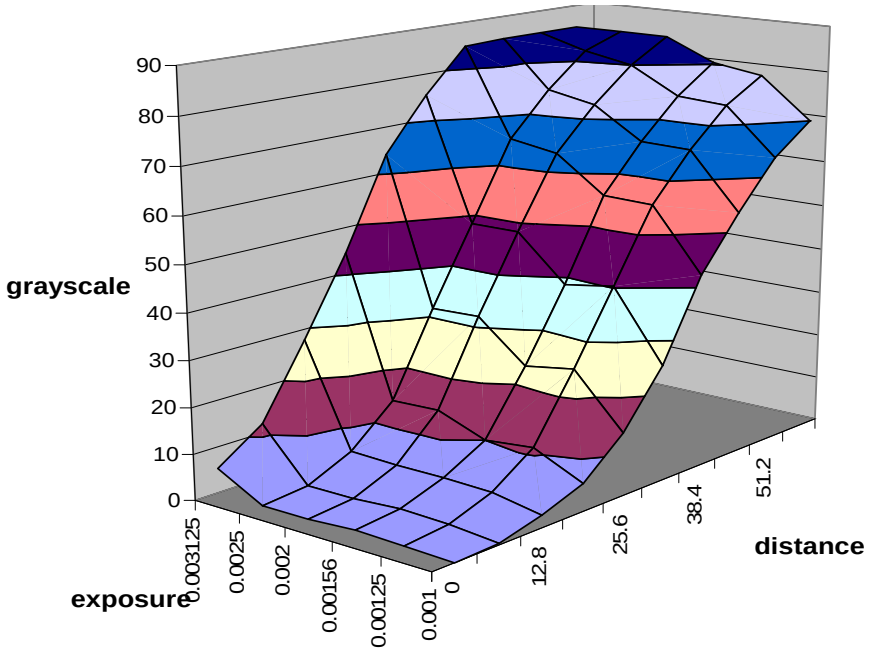

Figure 15. 3-D intensity plot of multiple spots from Figure 14 as a function of exposure time.

If the individual points are plotted on the exposure time axis shown in Figure 16, the different intensities and exposure times can be correlated. Take, for example, the lowermost curve in Figure 16. The last data point at 0.003125 sec. exposure has approximately the same intensity as the second point of the second curve at 0.001 sec. exposure. A similar condition occurs for the second data point at 0.002 sec. exposure on the brightest curve and the last data point on the middle curve at 0.003125 sec. exposure. In this manner, several locations at different exposures can be tied together with only the knowledge that intensity increases linearly with exposure time.

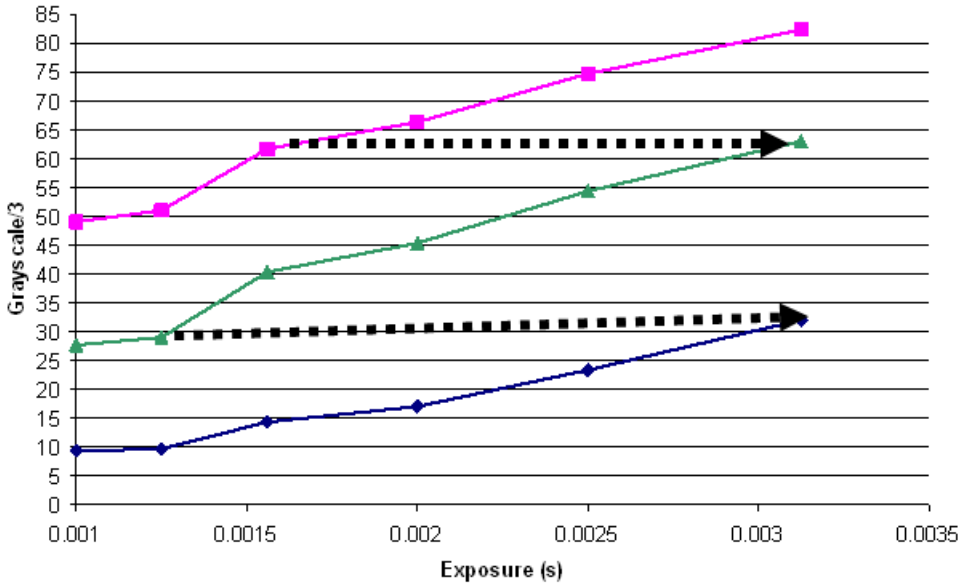

Figure 16. Several data locations from Figure 15 plotted on the exposure time axis.

Unfortunately, local variations and beam fluctuations possibly due to the setup being disturbed between measurements have a significant impact on this method and the final results were not very repeatable. If, however, the same principle of linearizing the response with the exposure is applied to an area as opposed to individual points, much of the variability is removed. The final method used the raw, collimated laser beam, adjusted to an output of 1.0 mW and attenuated through a series of neutral density filters (total optical density = 2.5). A sample image is shown in Figure 17, with the area used for calibration circled. The intensities of the 200 pixels in this area were averaged, reducing local variations in intensity. Images were generated in RAW format files on the camera and the Canon software was used to generate uncompressed TIFF files. The logarithmic fit is then normalized to yield a relative intensity of 1 at the maximum red intensity value of 85, yielding the calibration curve shown in Figure 18.

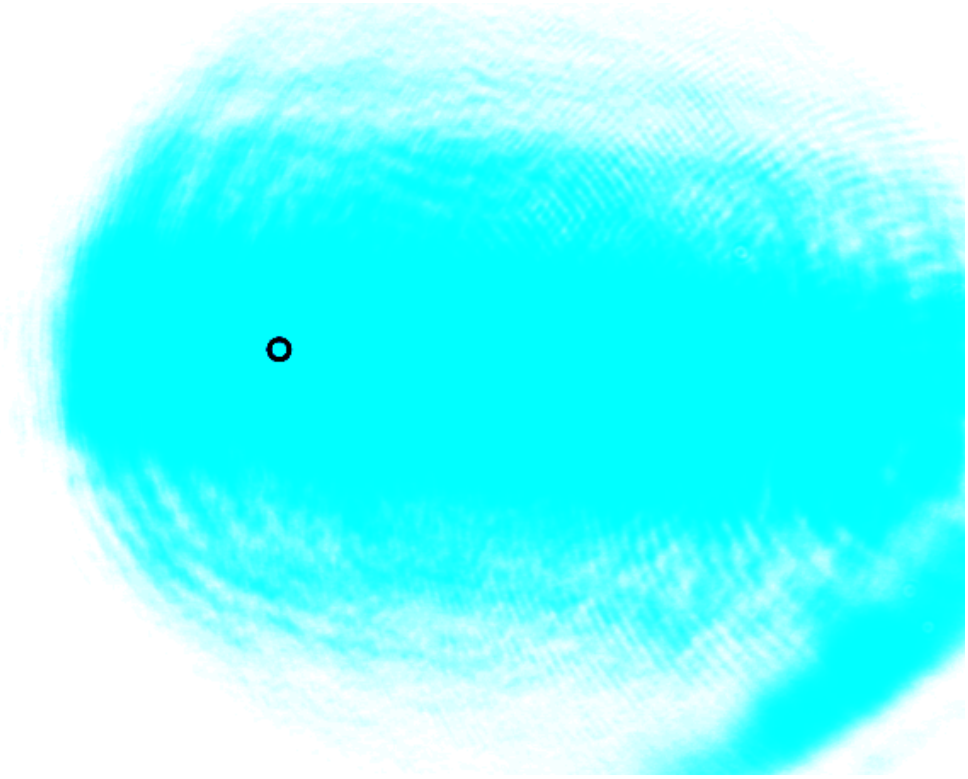

Figure 17. Raw laser beam used in calibration. The circle indicates the area used in calibration. The circle is approximately 100 μm in diameter and represents 200 photodetectors.

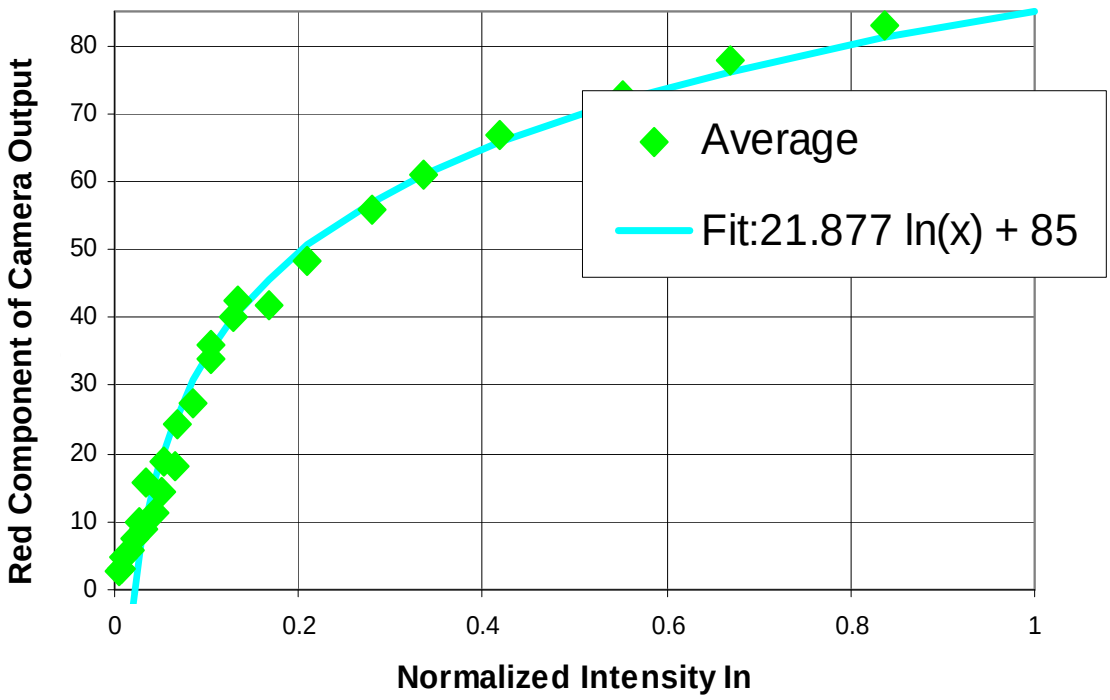

Figure 18. Plot of normalized input intensity (determined by shutter speed) versus the red component of grayscale output of the CMOS camera. Data yields a logarithmic curve.

From the curve fit to the collected data shown in Figure 18, a linearization function that can be applied to all subsequent data is can be expressed as:

$$I = \exp\left(\frac{R-85}{21.877}\right) \tag{3}$$

where the intensity I of light falling on the detector is calculated as a function of the magnitude of the red component of the greyscale value, R.

3.2.8 MEASUREMENTS WITH CALIBRATED DETECTOR

Now that the Canon CMOS detector has been calibrated to determine the intensity of the light falling on the detector based on the grayscale value, the light measurement experiments can be repeated to see if they follow the expected response. These measurements were carried out on the slit and the conical Fresnel lens.

Single Slit Measurement

Based on the calibration Equation (5), the grayscale data from the camera was converted to intensity and compared with the theoretical model for slit diffraction in Figure 19. By equating

the peaks in the measured and predicted intensity, the calibrated intensity matches the predicted extremely well. Compare this result to Figure 11 before the calibration expression was applied.

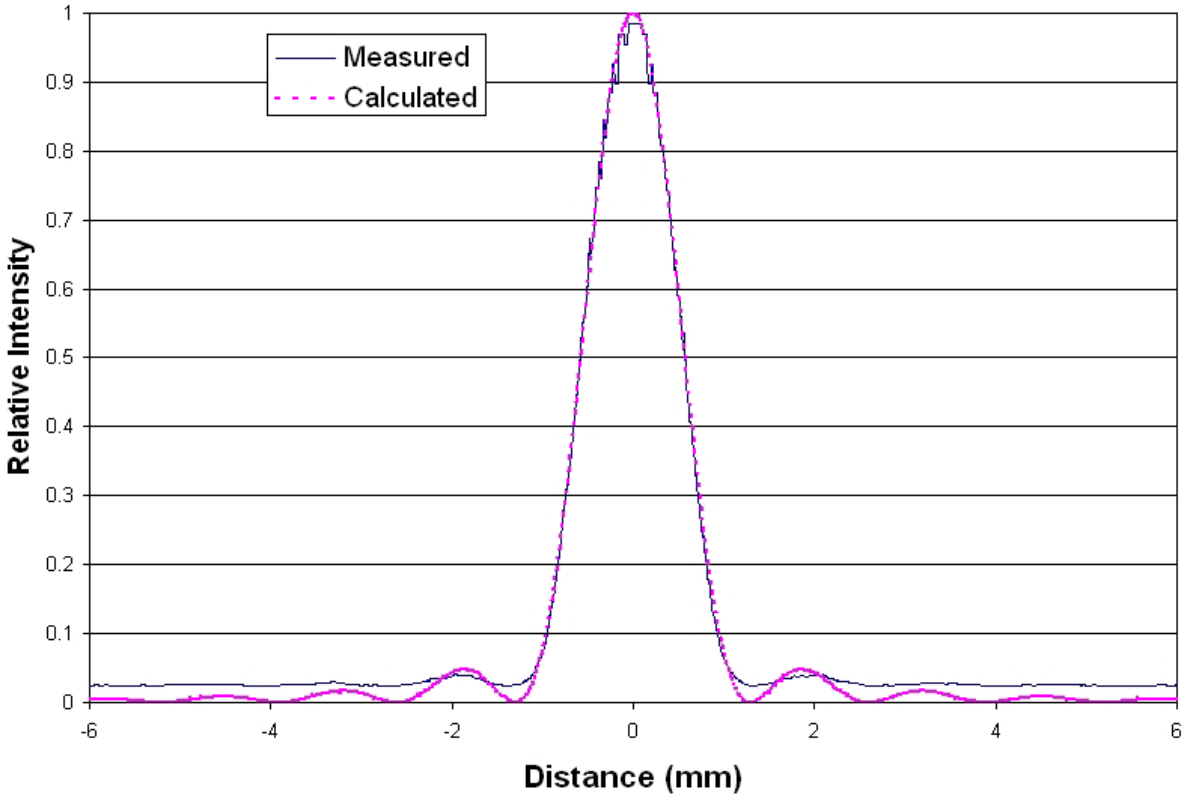

Figure 19. Measured and predicted light from a 0.100 mm slit at a distance of 200 mm from screen. Vertical amplitudes of measured and predicted are set equal.

Conical-groove Fresnel Lens

The conical groove lens (discussed in Section 3.2.5) was measured again with the calibration applied to the camera output. The results are shown in Figure 20 and 21 along with the expected spot from the diffraction analysis. Because this lens is a focusing lens, the resulting spot will be combination of the light that is refracted toward the focus due to the different slope on each facet of the lens and the diffraction that occurs due to the segmented nature of the lens. The magnitudes of both the measured (dotted line) and the predicted (solid line) spots have been normalized to one. However, the analysis does not take into account the magnitude of the refracted and diffracted intensity. The relative shape of the measured and predicted beams is all that can be compared. Clearly there is a major difference in the magnitude of the predicted high-spatial frequency diffractive peaks and the measured spot.

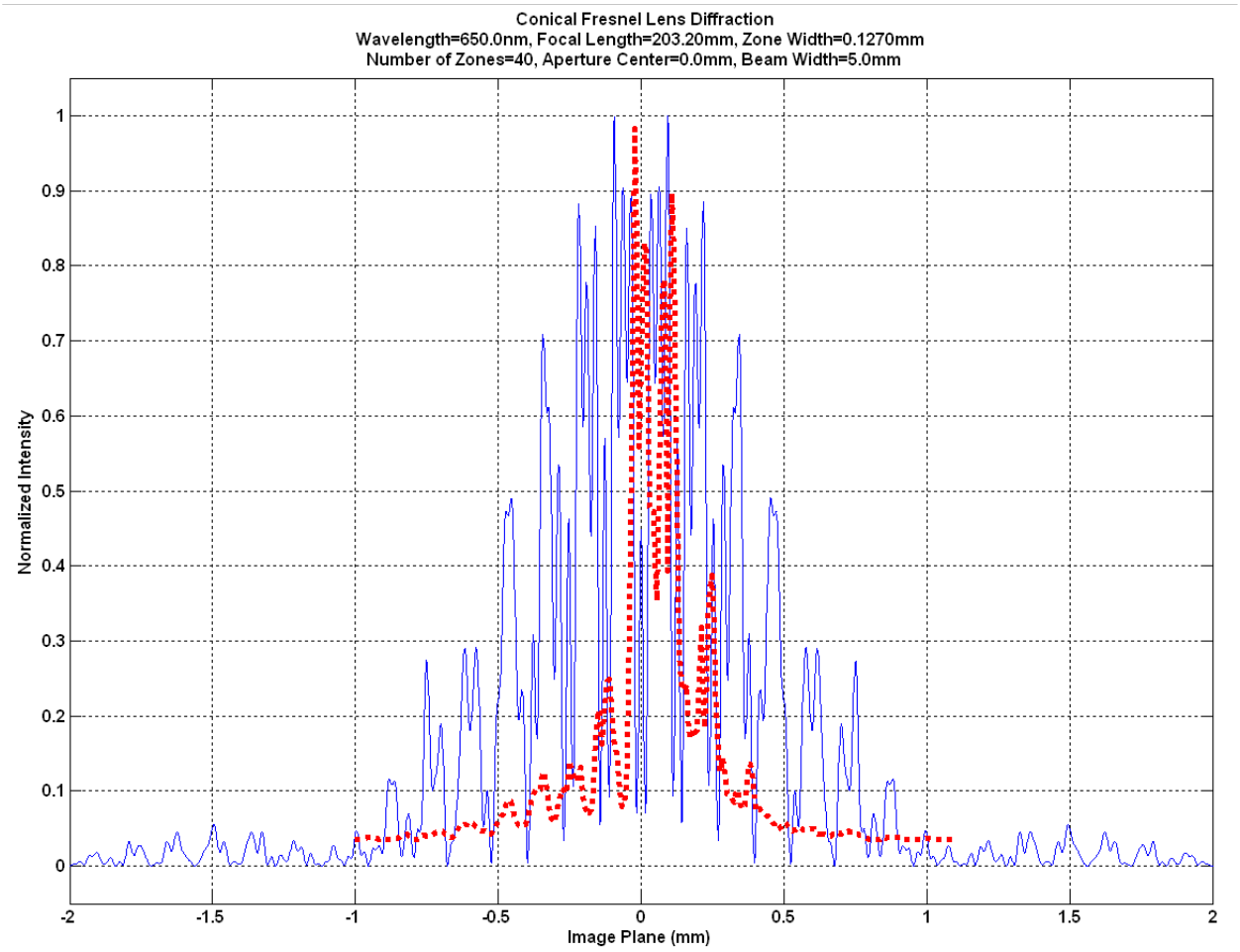

Figure 20. Measurement of the spot size for the 5 mm diameter beam of the conical groove Fresnel lens on axis. This beam illuminates 40 segments of the lens.

Figure 21 shows the results of the same Fresnel lens but illuminated 25 mm off-axis with a 5 mm diameter laser source. As with the previous comparisons, the peak of the measured intensity and predicted diffraction pattern have been normalized to one. This does not take into account any difference in refracted and diffracted beam intensity. However, the general form and width of the measured beam intensity and the diffraction pattern is similar.

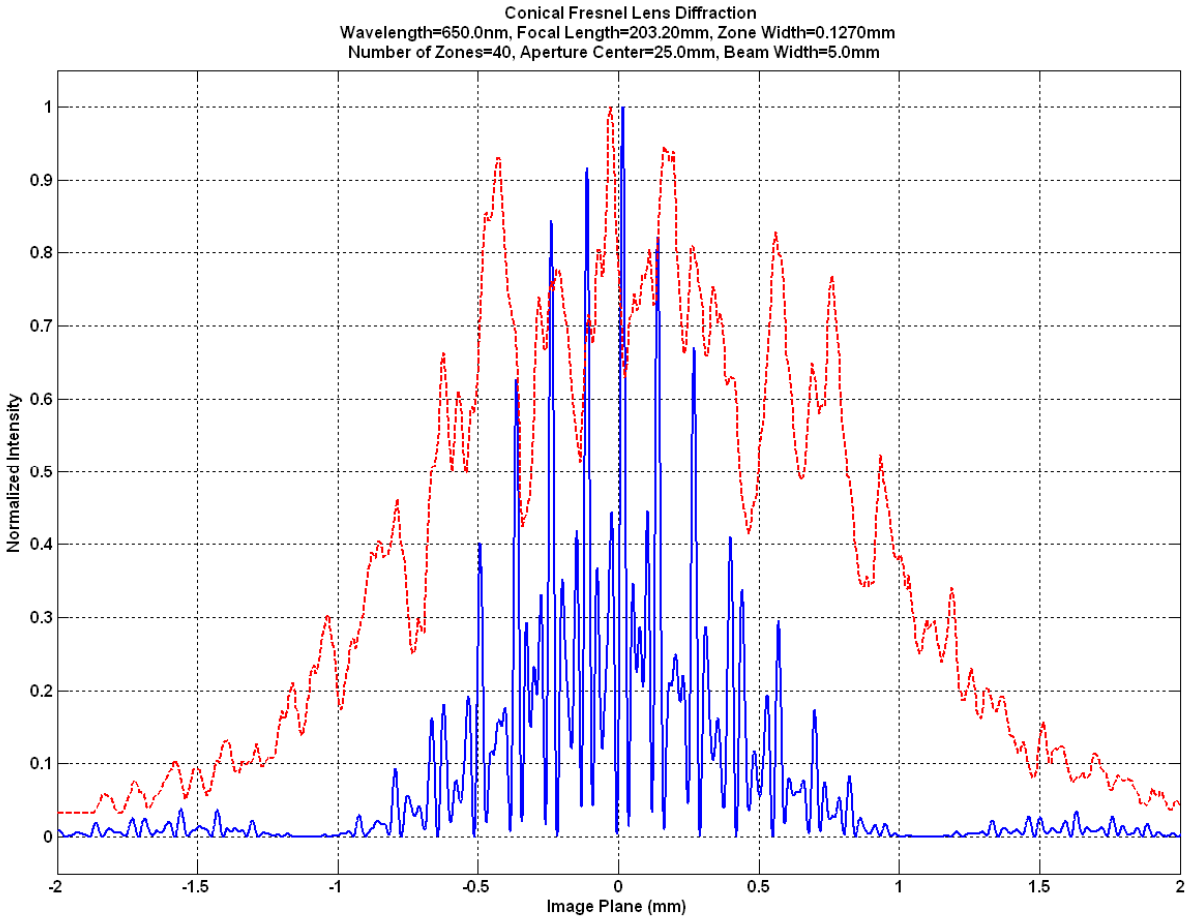

Figure 21. Measurement (dotted line) and prediction (solid line) of the diffraction pattern at the focus of the conical Fresnel lens with a 25 mm off-axis input beam of 5 mm diameter illuminating 40 zones.

3.3 FABRICATION OF PLASTIC LENSES

3.3.1 ASPHERIC GROOVE FRESNEL LENS

Given the poor results obtained with the conical-groove lens, an aspheric-groove Fresnel lens was designed using software developed by Garrard (see Section 1). As shown in Figure 22, aspheric groove Fresnel lenses have constant-depth grooves as opposed to conical groove Fresnel lenses, which have constant groove spacing. The main advantage this gives the aspheric groove lens is that there is an overall decrease in the number of grooves and, hence less diffraction.

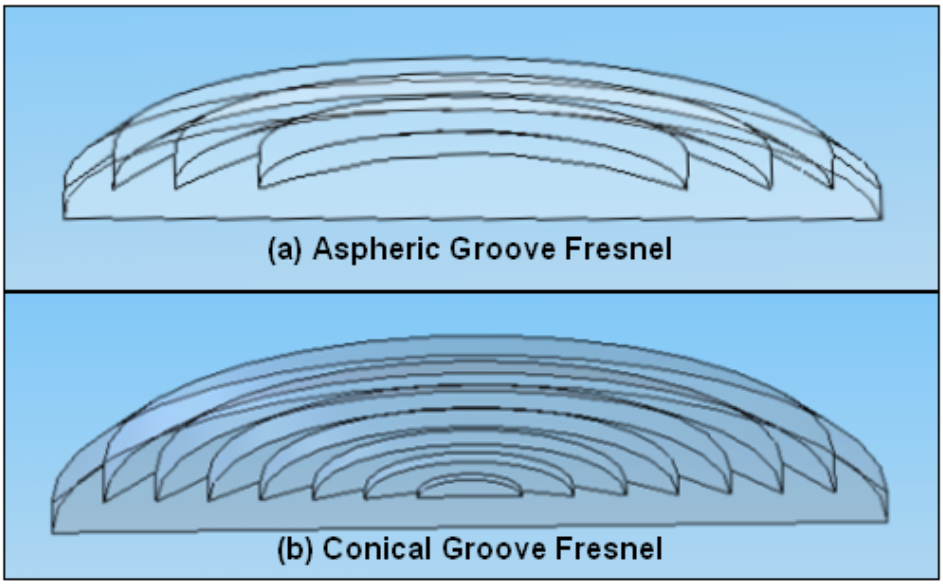

Figure 22. Aspheric groove Fresnel lens (a) showing fewer overall groove number than the conical groove Fresnel lens (b).

3.3.2 MACHINING

The aspheric lens has a 100 mm diameter with 100µm groove depth and is designed for a 200 mm focal length. A 97 µm radius diamond tool was used to turn this lens in Cast Acrylic Plexiglas® (PMMA). Final feedrates of 2.5 µm per revolution were used to obtain a theoretical finish of 10 nm P-V. As the Figure 23 shows, an air ionizer was used to prevent static from binding chips or damaging the tool through electrostatic discharge. Figure 24 shows the machined lens.

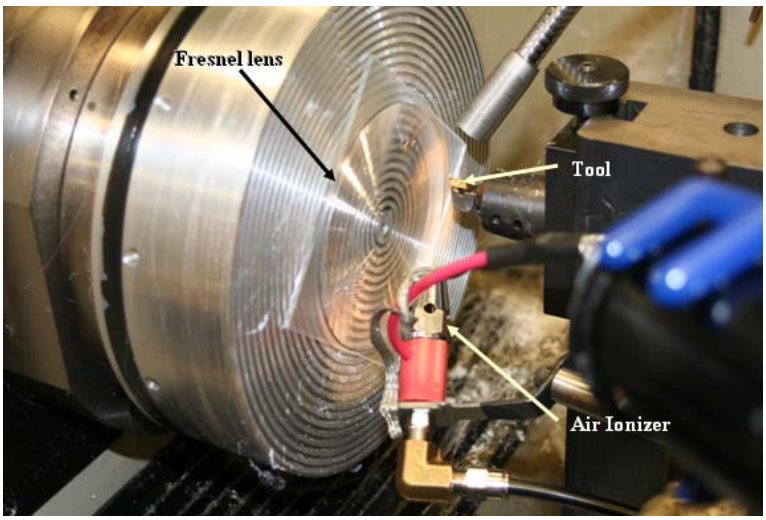

Figure 23. Diamond turning the aspheric Fresnel lens.

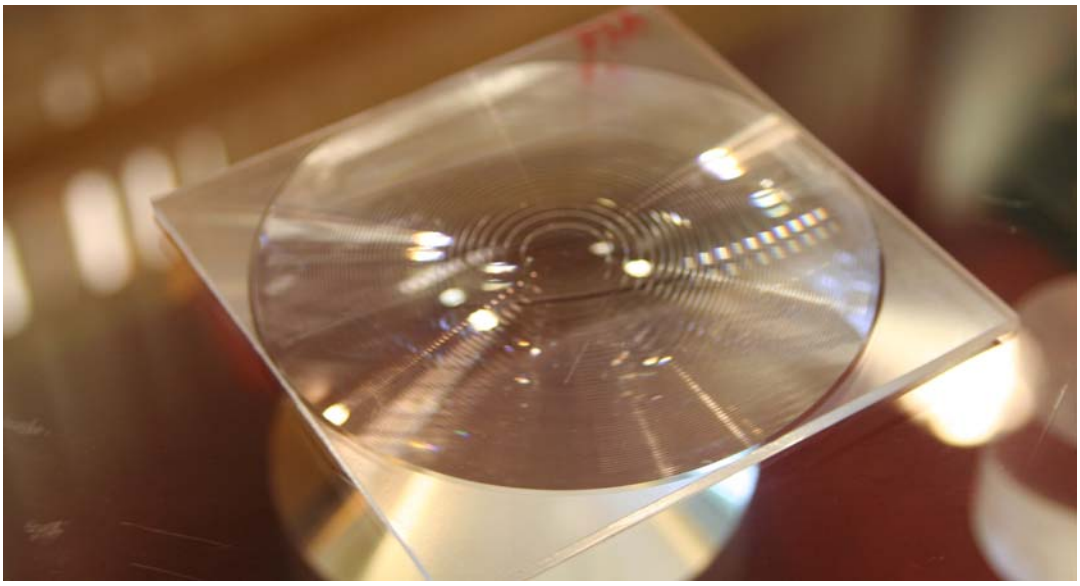

Figure 24. Finished aspheric groove PMMA Fresnel lens.

Surface deflection during machining

The aspheric groove Fresnel lens was machined from acrylic sheet with a 3mm thickness. One concern with machining a thin plastic part on a grooved vacuum chuck is that the pattern of the chuck could generate an error in the part. The vacuum chuck of the PEC's ASG 2500 diamond turning machine (DTM) has concentric grooves every 0.100" (2.54mm) with a width of 0.050"(1.37 mm). With a vacuum of 20 in of mercury (p=10 psi), the deflection of 1/8" sheet of acrylic plastic can be calculated. By approximating the plastic sheet between grooves as a pressure loaded beam that has fixed ends, the expression for maximum deflection (y) in the center is:

$$y = \frac{1}{384}\frac{wL^4}{EI} \tag{4}$$

where w is the vacuum pressure (p) per m of length, L is the length of the groove, E is the elastic modulus of the plastic (69 MPa) and I is the area moment of inertia of the cross-section. Since $w=pb$ and

$$I = \frac{bh^3}{12}, \tag{5}$$

the expression for deflection becomes rectangular beam of thickness t, substituting and simplifying gives the deflection.

$$y = -\frac{12}{384}\frac{pL^4}{Et^3}. \tag{6}$$

Given the above parameters for plastic and the dimensions of the beam, the resultant deflection is only 4 nm. Therefore, deflection of the 3 mm thick plastic due to the grooves in the vacuum chuck is not a problem.

3.3.3 SURFACE FINISH

To eliminate the print-through from rough machining passes, the final part was made with two finishing passes: one at 5 µm D.O.C. and the last at 1µm D.O.C. The resulting surface finish as measured with the Zygo white light interferometer is shown in Figure 25. The RMS surface roughness was 16 nm over a length of 143 µm.

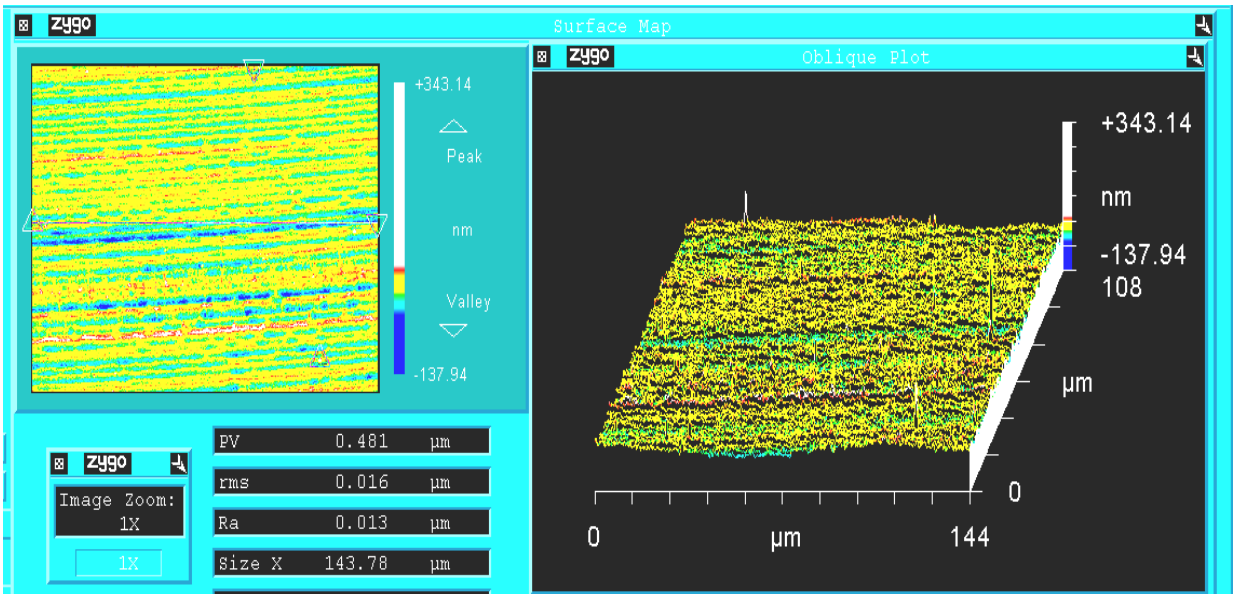

Figure 25. Surface finish of aspheric Fresnel lens is 0.016 µm rms.

3.3.4 ASPHERIC GROOVE LENS

The spot pattern of the aspheric Fresnel lens was measured with the grooves facing away from the camera with a 6 mm diameter solid state laser beam on-axis and at several off-axis positions. Figure 26 shows the spot sizes measured using the calibrated camera data for the different off-axis positions. The small change in location of the focus (< 1.5 mm) with off-axis beam position could be due to setup the camera and lens or related to the shape or flatness of the lens. The spot sizes for the measurements shown in Figure 26 are 38, 115, 80, and 170 µm FWHM for 0, 12.7, 25.4 and 38.1 mm off-axis beams respectively. The number of illuminated facets for these spots are 1, 3, 5 and 10 respectively. A hypothesis for the widening of the spot as the beam moves off-

axis is the increased number of groove transitions (0.14 mm each) in the beam path as the off-axis distance is increased and consequent increase in diffraction.

The drop in peak intensity is largely due to the larger spot size as the beam moves farther off axis. Note that the 2D relative flux (area under each curve) is 100, 100, 85 and 58% for the four positions. Contributions from groove radius and relief angle (24% for the 1.5 in spot) and Fresnel reflections (8% for the1.5 in spot) make up most of the deficit in flux. The remaining 10% of losses are most likely due to diffraction. The 24% figure for masking by the tool radius and relief angle are illustrated in Figure 27.

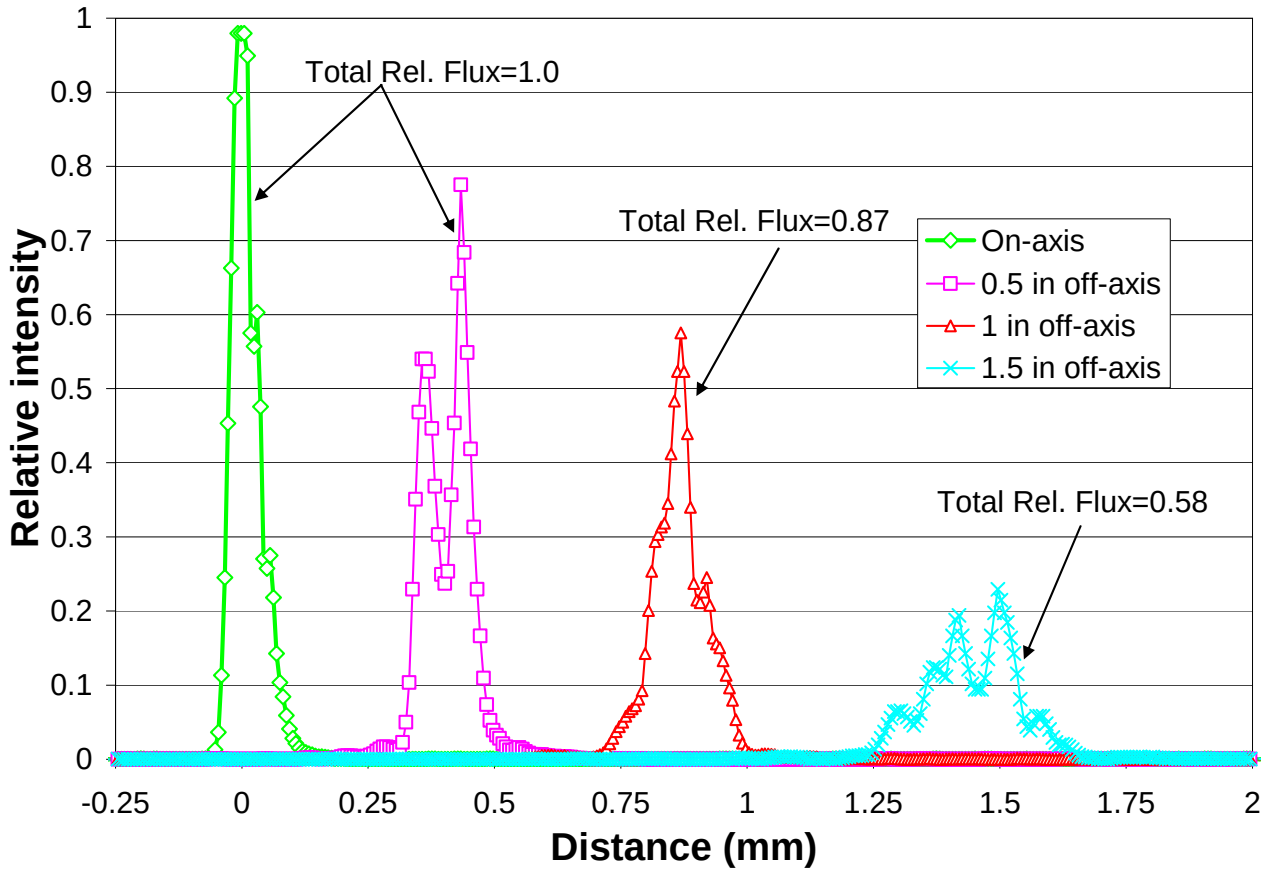

Figure 26. Linearized beam profiles for Aspheric Fresnel Lens using a 6 mm dia. beam. At the center of the lens the beam is within one facet but at 38.1 mm it covers 16 facets.

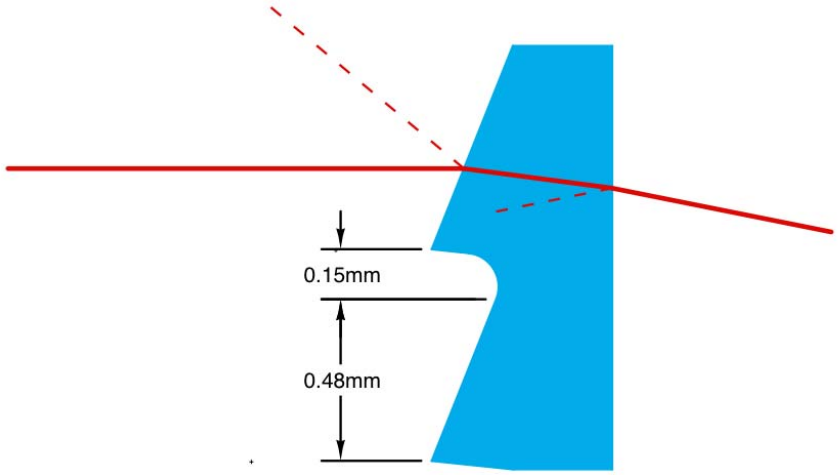

Figure 27. Section of two grooves of the aspheric Fresnel lens at 38 mm. Note the 0.15 mm obscured region formed by the 0.1 mm radius tool and the relief angle.

While the regularly spaced peaks in Figure 26 hint that diffraction is present for the off-axis measurements, it becomes more apparent if the spots are viewed at a different scale as in Figure 28. The periodic peaks characteristic of diffraction are amplified in this view and diffraction is shown even for the 12.7 and 25.4 mm off axis beams.

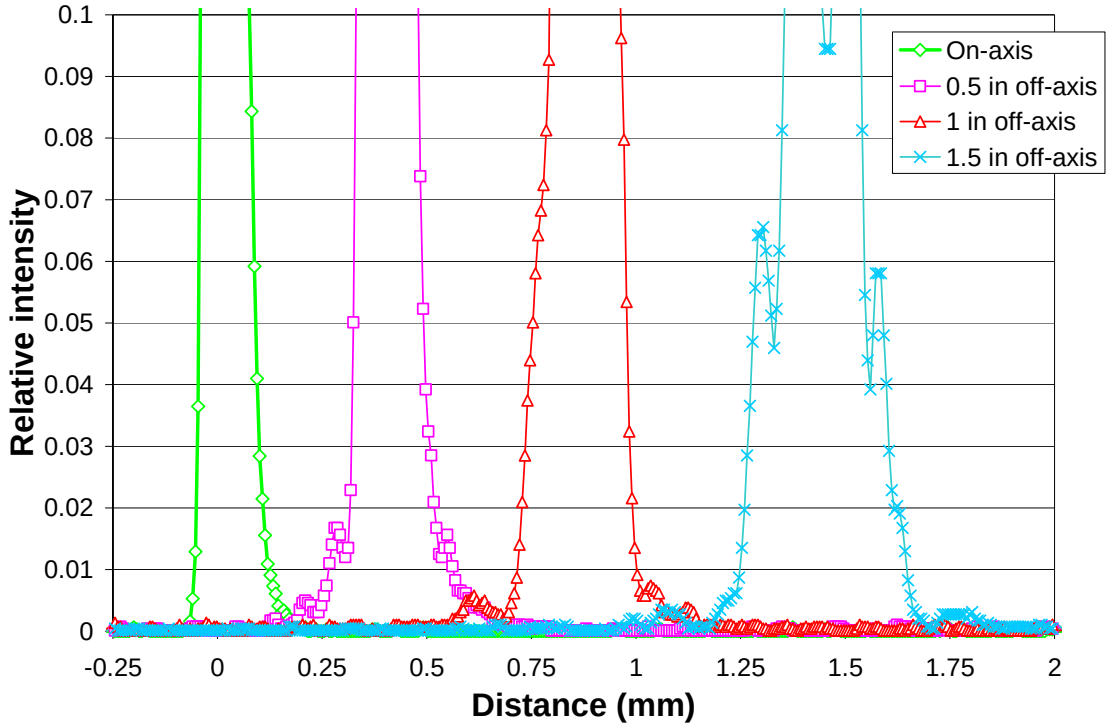

Figure 28. Plot of Figure 26 with amplified vertical scale. Note the peaks or lobes on the sides of the beams characteristic of diffraction.

Even more telling is Figure 29, which shows a comparison of the measured beam spot and the calculated diffraction pattern near the center of the target for a 6 mm diameter beam that passes through the lens 38.1 mm from the center. The calculation stems from the Fraunhofer diffraction [2] of a multi-slit grating. The groove spacing of 650 μm slit width of 450 μm representing the clear area of each groove as shown in Figure 29 and a total of 10 illuminated grooves was used in the calculations.

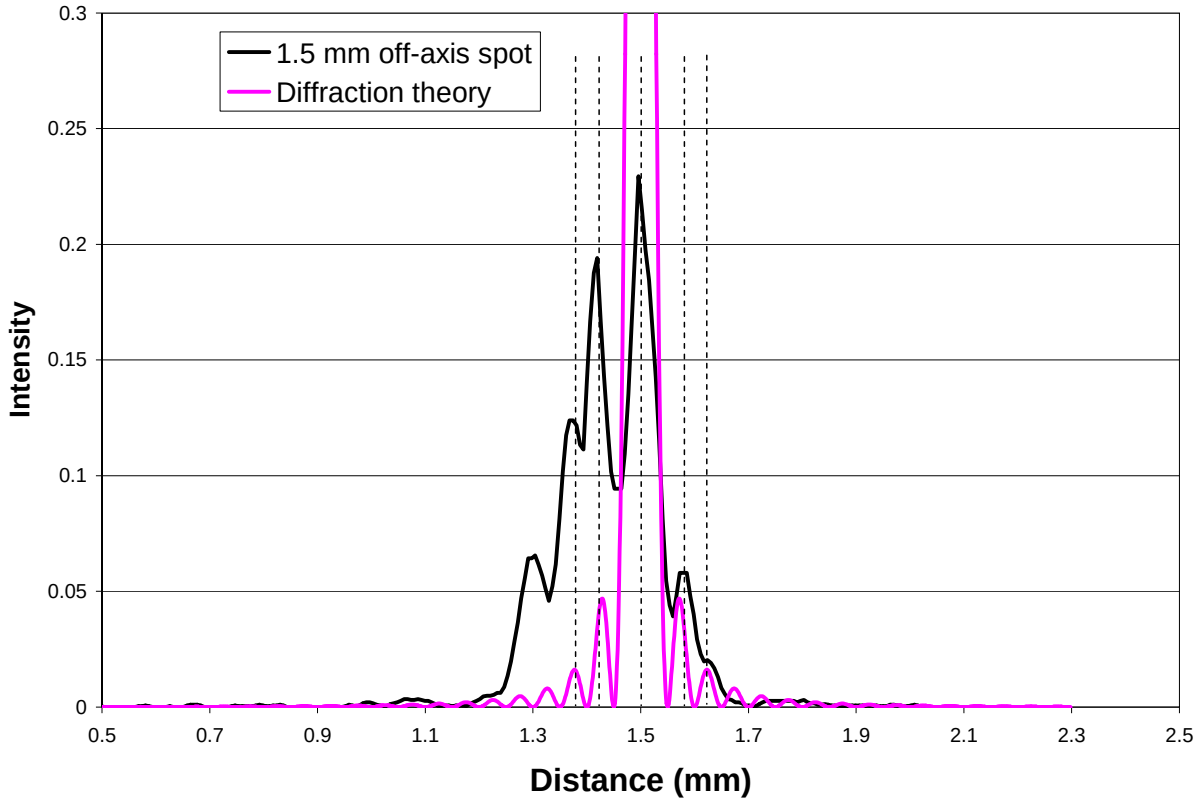

Figure 29. Comparison of measured spot size and predicted diffraction for the aspheric Fresnel lens illuminated with an 6 mm diameter beam that is 38.1 mm off-axis. The dotted lines show the approximate alignment of the diffraction peaks in the measured spot and the calculated pattern.

3.3.5 KINOFORM LENS FABRICATION

The purpose of the lens system for a scanner is to focus the source laser beam into a small spot on the image plane. The ideal spot location is a linear function of scan angle (i.e., the f-θ condition). The size and shape of the spot is determined by both refraction and diffraction. Even if the lens surfaces were designed so that all rays converge at the same location on the image plane, the spot size will not be zero due to diffraction. Each zone of a Fresnel lens both redirects incident light toward a focal point and produces a diffraction pattern due to the discontinuous boundaries with adjacent zones. However it is possible for the diffraction peaks to all be

directed to the same point on the image plane. This is done by varying the width and depth of the zones to ensure that the optical path length from the center of each zone is an integer multiple of the incident light wavelength. This apodization process (i.e., aperture tuning), matches the phase of the refracted light so that the location of constructive interference can be controlled and produces a Kinoform lens. See Section 1 for more details on the type of lens.

The spacing and angle of the facets on the Kinoform lens determine the location of the refractive and diffractive beams. For a phase match order of M = 1, the groove spacing must be very small at larger apertures and the lens becomes difficult to fabricate; for example, 6 µm spacing for a 200 mm f/l. lens at r=11.5 mm. Even when the phase match order is increased to M=5, the groove spacing is still very small and many grooves have to be made with a dead sharp tool. The lens cannot be contoured with a radiused tool as was done for the aspheric lens but rather must be machined as a series of plunge cuts. The side of the dead sharp tool forms the flat refractive portion of the lens and must be rotated at each plunge to change the angle as the groove radius is changed. Ideally, a rotary axis (oriented perpendicular to the X-and Z- axes of the diamond turning machine) would be used to rotate the tool. Unfortunately, neither of the diamond turning machines at the PEC has such a rotary axes, so a temporary solution was devised to machine small segments of Kinoform lenses.

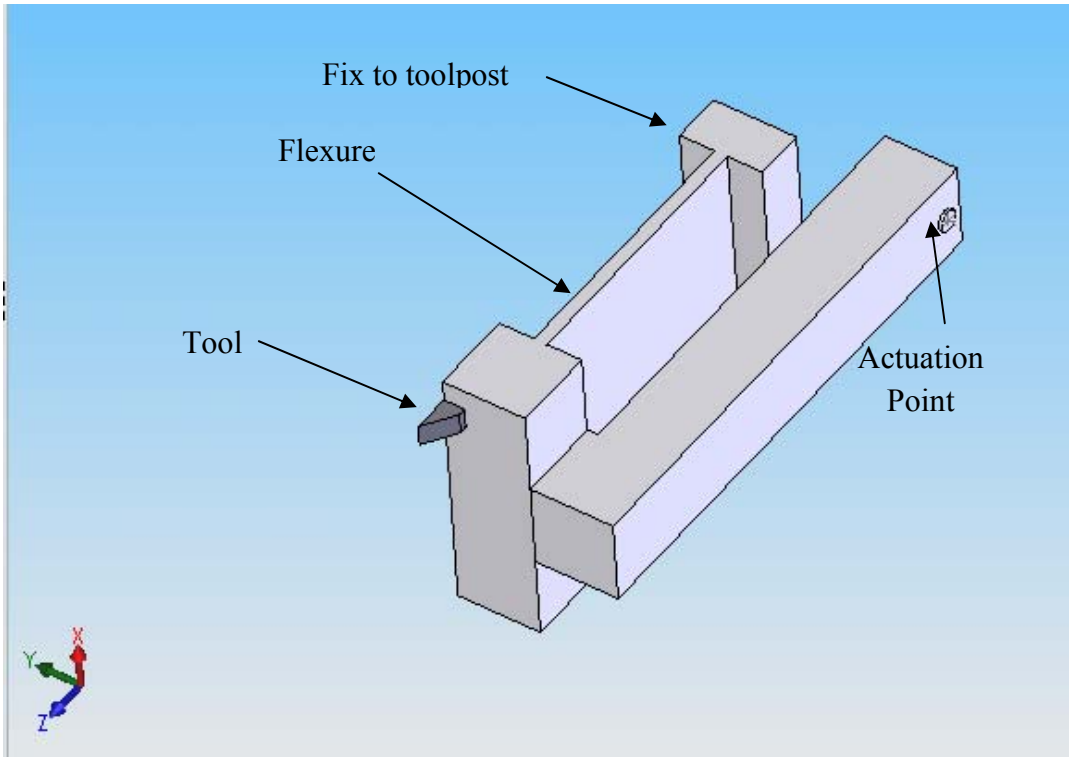

Figure 30. Tool rotation mechanism. A flexure that is very stiff in the vertical direction allows the tool to rotate in the Y-Z plane.

The tool rotation device is based on a flexure mechanism that is mounted on the X-axis of the DTM and a linear stepper motor axis that is used to push on the actuation point to rotate the tool as shown in Figure 30. The force at the actuation point produces a force and a moment at the tool. The moment rotates the tool and the force moves it in the y-direction creating a small motion in the z-direction (depth of cut). The flexure was designed to allow actuation at reasonable forces without exceeding the yield strength of the aluminum flexure. COSMOS finite element analysis was used to evaluate the stress vs. deflection for different flexure designs. Figure 31 shows the result of one analysis with the stress distribution in the flexure highlighted. The peak stress shown is only 56 MPa which is 20 % the yield stress of 6061-T6 aluminum.

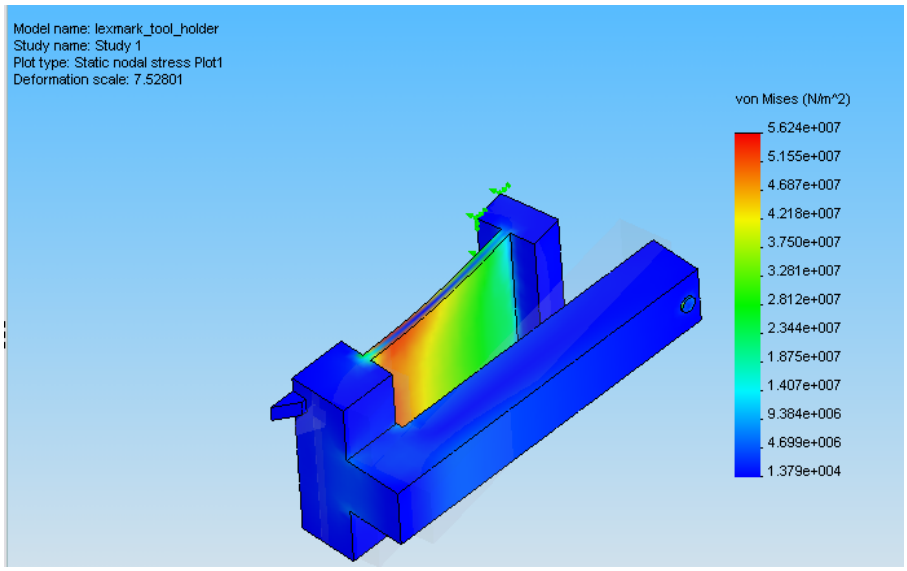

Figure 31. COSMOS FEA of stresses in the flexure mechanism

The flexure bends predictably and causes deflections of the tool that can be modeled. Parameters of interest are 1.) position at the actuation point 2.) deflection angle, 3.) position of the tool tip. After modeling, the same parameters were measured on the mechanism and the comparison in Figure 32 shows the excellent agreement between model and measurements. While the measured results show slightly lower angular and linear displacements than the model, the displacements are linear and the measured values can be used to move the tool. Higher tilt displacement is possible by extending the load arm.

To machine the lens, the groove angle is set by the motion of the stepper motor and the x and z slides of the DTM are programmed to compensate the tool motion caused by the rotation. A Dspace DSP controller will be used to send the stepper motor commands to position the tool rotation as a function of X-axis position. The mechanism was constructed and tested as shown in Figure 33.

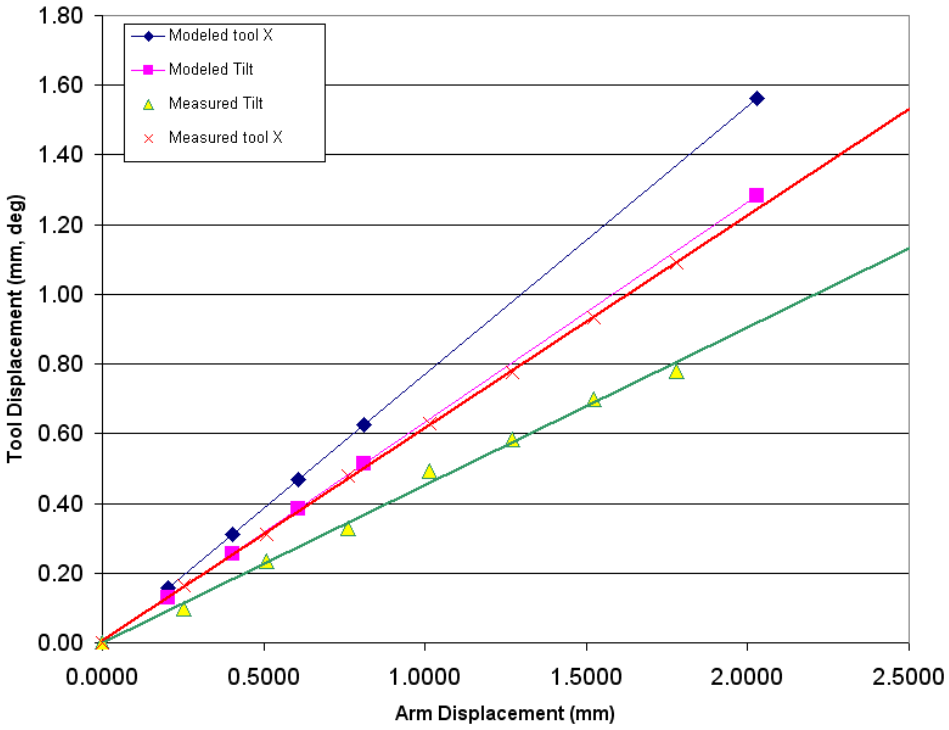

Figure 32. Plot showing modeled and measured deflections of the tool rotating mechanism. Since the tool tip is translated significantly, the DTM axes will be programmed to compensate.

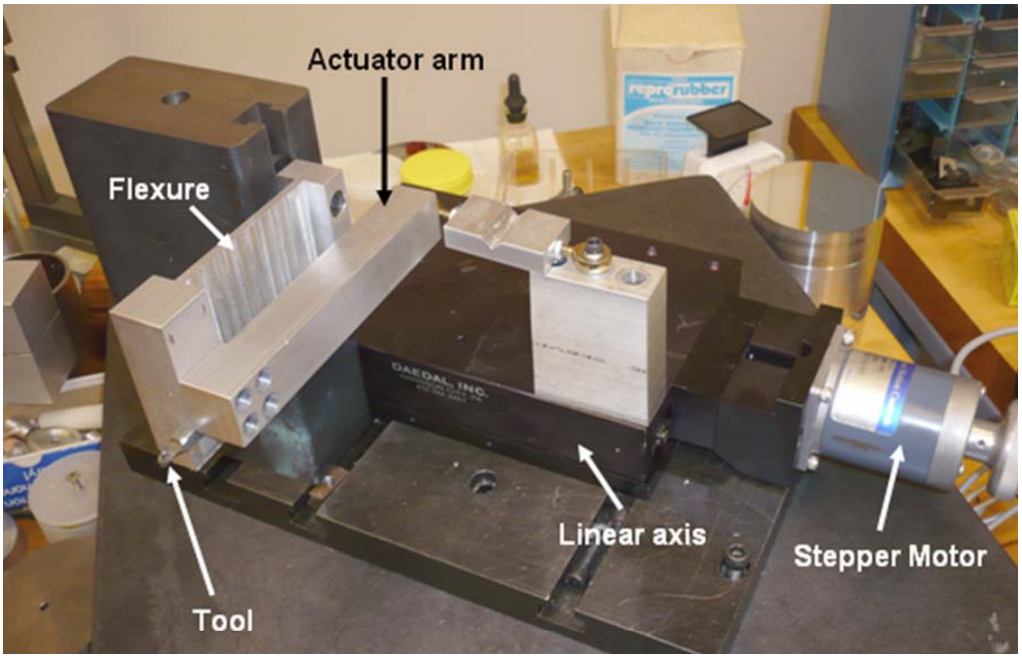

Figure 33. Tool rotation apparatus showing the flexure, linear axis and stepper motor.

3.4 CONCLUSIONS

The testing of Fresnel lenses at the PEC has progressed from simply taking photographs of spots to producing calibrated, linearized spot sections. While acquiring an understanding of the process needed to generate useable data from the digital camera, a powerful tool for image analysis is now available for subsequent experiments and development. The linearization procedure has been shown to be repeatable and to show excellent agreement with theoretical diffraction patterns such as that from a single slit diffraction. These techniques have been used to analyze the performance of a constant-groove-depth aspheric Fresnel lens fabricated at the PEC. The results show great potential for using Fresnel lenses to focus millimeter-size beams. With additional improvements to the diffraction behavior of Fresnel lenses based on design process described in Section 1 and the measurement and fabrication techniques described here, spot sizes of less than 80 μm will be obtained with subsequent lenses. These lenses will likely be a Kinoform (diffractive/refractive) design and the fabrication principles are now being developed. The lenses made so far are focusing lens and the next step will be to develop a scanning lens based on the lessons learned thus far. These lenses will be applied to the scanning system of a laser printer to create more economical lenses in laser printers.

REFERENCES

1. Olympus web page on imaging detectors http://www.olympusmicro.com/primer/digitalimaging/cmosimagesensors.html
2. Möller, K.D. Optics. University Science Books, 1988, pp 129-130.

4 RAKE ANGLE VARIATION IN DIAMOND TURNING

Alex Sohn
Precision Engineering Center Staff
Thomas A. Dow
Dean F. Duncan Distinguished Professor
Department of Mechanical and Aerospace Engineering
Kenneth Garrard
Precision Engineering Center Staff

The PEC has a long history studying cutting mechanics in single-point diamond turning (SPDT). The latest installment in this ongoing investigation is looking at the effect of rake angle on the forces in SPDT. In certain scenarios, the change in rake angle can be significant and have a profound effect on the finished part. One of these scenarios is examined here as is the measurement of cutting forces and the results of these measurements.

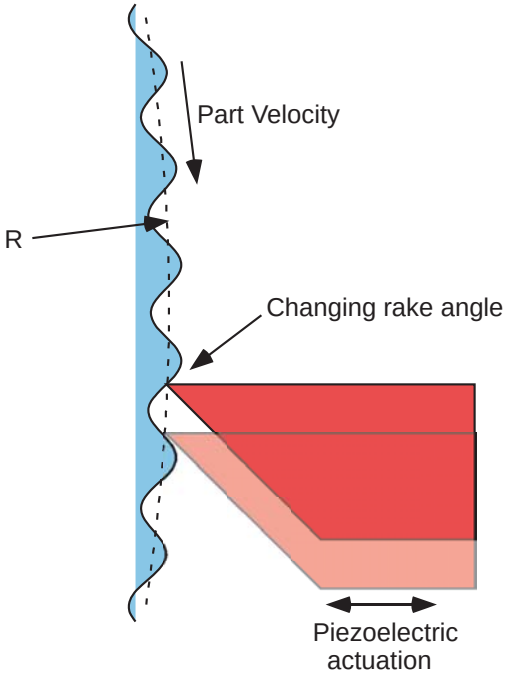

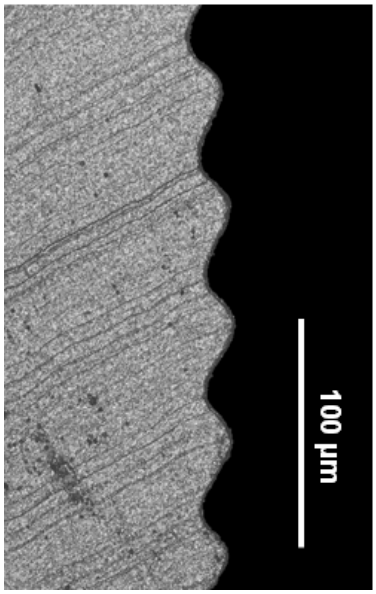

4.1 INTRODUCTION

When turning non-rotationally symmetric (NRS) surfaces using a fast-tool servo (FTS), the rake angle of the tool effectively changes as a function of the surface slope. As fast tool servos find ever more applications and are pushed to higher slopes, larger strokes and higher operating frequencies, the diamond tools used on them tend to encounter larger variations in rake angle. Recent experiments at the Precision Engineering Center (PEC) have pushed this envelope to variations in rake angle of up to 90 degrees. The effect on figure, finish and tool life is substantial, so a quantization of the errors is needed. The varying tool forces are the main contributor to rapidly changing cutting conditions. These tool forces have been measured in various cutting experiments with the goal of determining optimum rake angles for machining. Large negative rake angles produce large thrust forces whereas large positive rake angles require large clearance angles and, hence, fragile tools. With advance knowledge of the tool forces and the material being cut, an optimum initial rake angle may be found.

The example case studied here involves a 6 mm diameter cylinder with sine waves machined around the periphery. This part was machined at the PEC with a piezoelectric fast tool servo of 20 μm range and 1 kHz bandwidth. A magnified cross-section is shown in Figure 1. Two observations in making these parts led to this investigation of tool forces: 1) significant distortion in the shape of the sine waves and 2) abnormally high tool wear given the short cutting distances and small depths of cut.

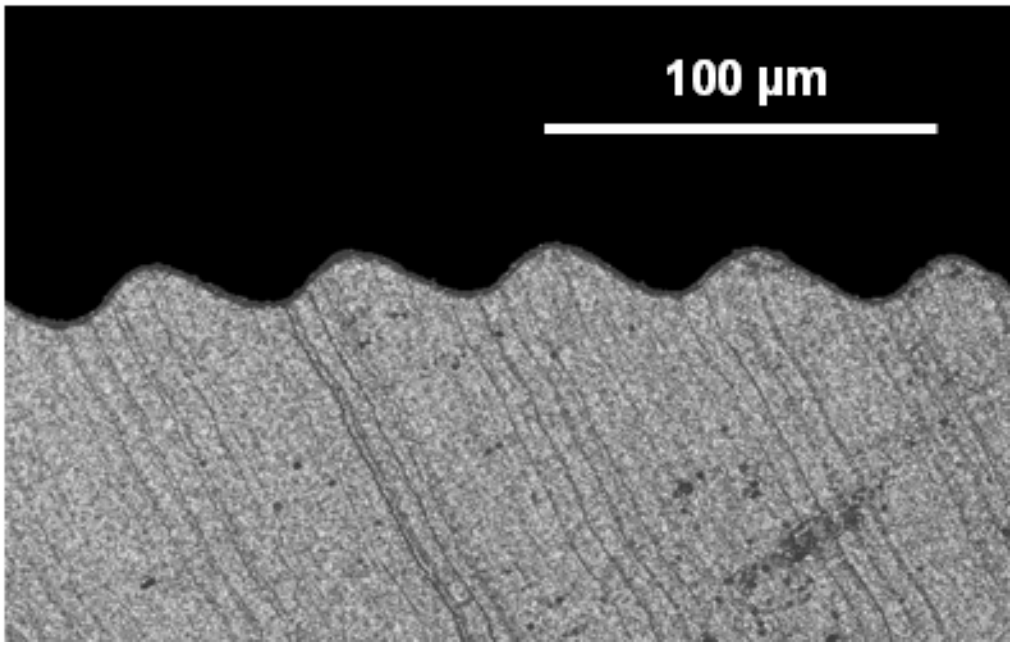

Figure 1. Cross-section of 360 periods of a 17 μm sine waves on a 6 mm diameter cylinder.

4.2 TOOL FORCE AS A FUNCTION OF RAKE ANGLE

To get an idea of the force variation involved in cutting these sinusoidally figured parts, the forces had to be measured. Previous investigations into tool forces at the PEC [1, 2] by Arcona and Drescher did not measure the effect of varying rake angles, though efforts to assess tool forces at normal (0º rake) incidence were successful.

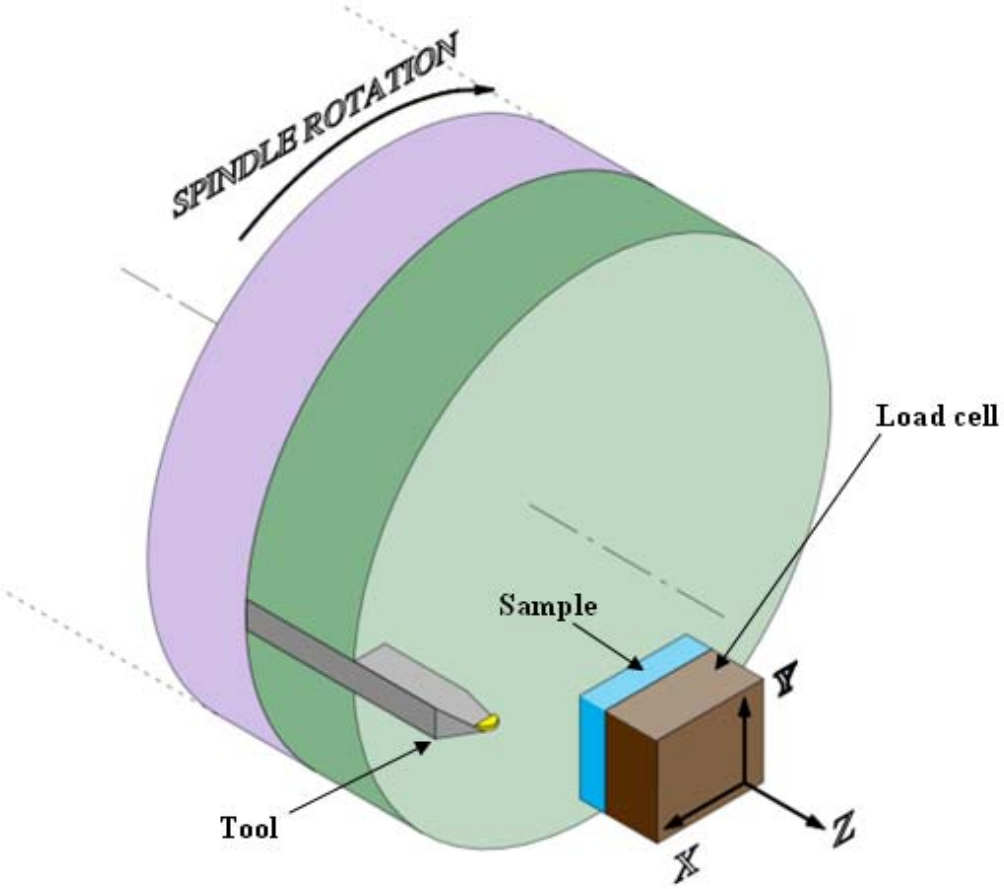

Figure 2. Schematic showing setup for tool force measurements.

The experimental setup used for measuring forces (Figure 2) involved placing a sample on a Kistler 9251A piezoelectric load cell and collecting force data while the sample was flycut. The interrupted cut avoided the problem of charge loss in the piezoelectric load cell, though some ringing at the beginning of each cut had to be truncated from the data. The sample was electroless nickel plated copper and was fixed while the rotating tool could be repositioned at varying rake angles. The tool clearance angle of 12º, however, limited positive rake angle measurements to 10º. The measured cutting and thrust force orientations are shown in Figure 3.

The force directions are fixed with respect to the surface of. the workpiece as the tool is rotated through different rake angles. A sample measurement is shown in Figure 4. The plot shows one pass over the sample at 0º rake angle. Data was collected at 5 kHz. Cuts were made with the tool positioned at 0º, 10º, -10º, -20º and finally 0º again. The freshly lapped tool had a conical nose radius of 0.5 mm. Each cut was performed with a 20 µm upfeed and a 10 µm depth of cut at 120 rpm spindle rotation. The final results for force measurements are tabulated in Figure 5. Each data point represents an average of 20 passes over the workpiece. A least-squares 2nd-order polynomial curve fit allows extrapolation to larger rake angles. Future experiments using large-clearance tools and a larger adjustment range of tool angle will actually allow data collection at rake angles larger than 20º.

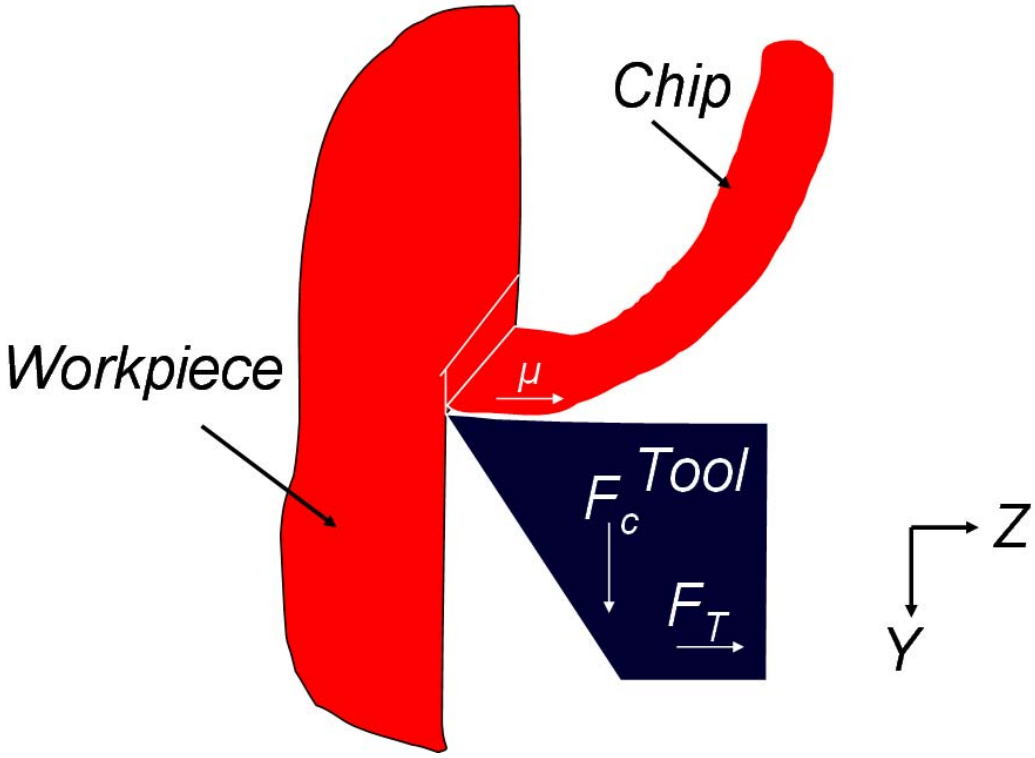

Figure 3. The cutting force (F_c) and the thrust force (F_t) are measured with respect to the axis orientations of the machine.

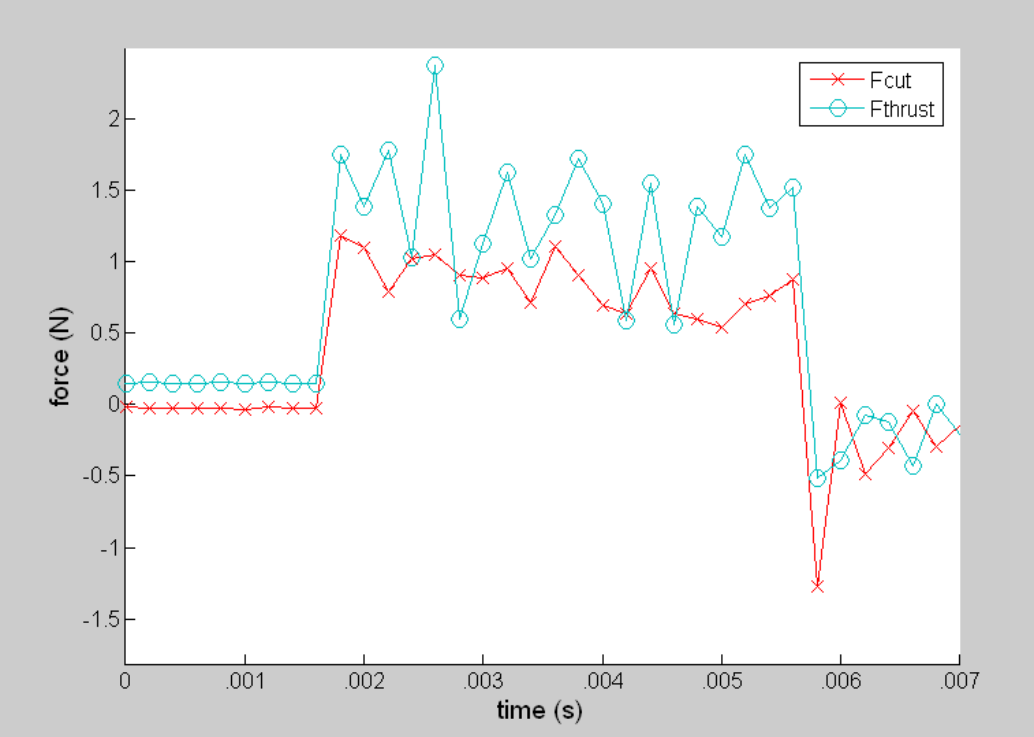

Figure 4. Sample force measurement at 0º rake angle.

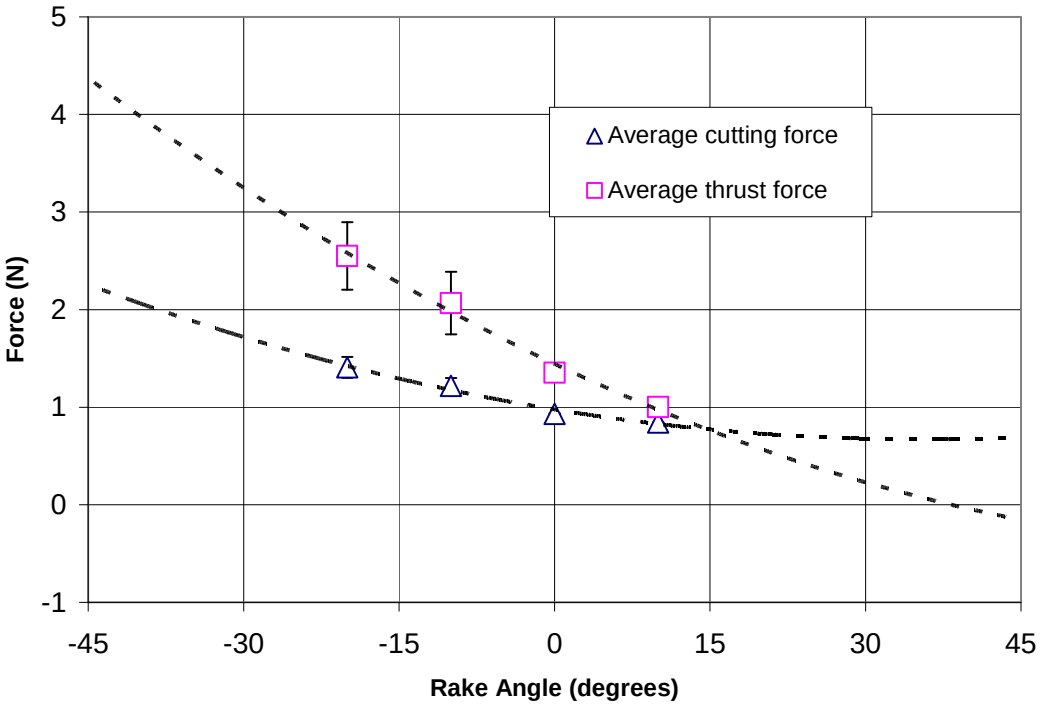

Figure 5. Force variation as a function of rake angle. The dashed lines are least-squares polynomial fits to the data and are extrapolated to ±45 º.

4.2.1 IMPACT ON FIGURE ERROR

While tool forces are always present in machining, constant forces usually have little impact on figure error, particularly in ordinary turning applications when stiff toolposts are used. Fast-tool servos typically are limited in their static stiffness, however, and varying forces can cause them and the workpiece to deflect. Particularly on small parts, compliance in the material can be significant, causing a figure error. Test parts were structured with a 16µm sine wave with ±45° rake angle variation. The part was a 6 mm diameter electroless Nickel plated brass cylinder. Modeling the cylinder as a cantilever beam with a length of 20 mm, the deflection can be calculated from the experimentally obtained tool forces. Calculating deflection from this and correlating to the measured forces yields a perturbed sine wave as shown in Figure 6. This distorted sinusoidal shape is very similar to that shown in Figure 1 and when superimposed onto the measured data follows the shape of the actual part. This is illustrated in Figure 7.

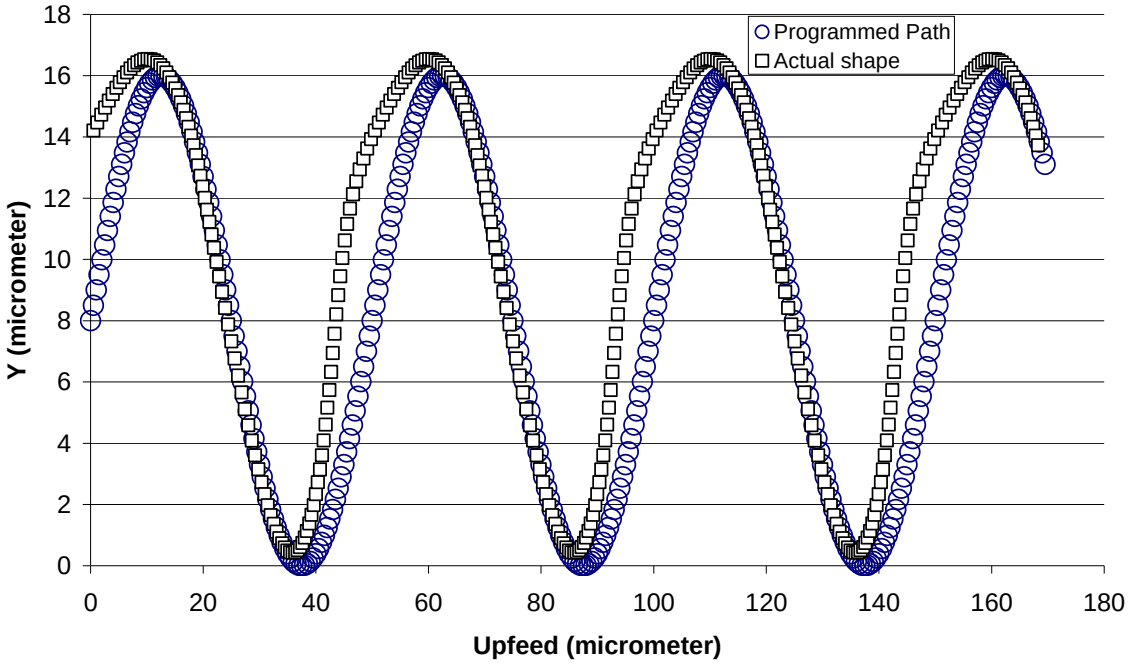

Figure 6. Perturbed shape of the sine waves machined on a 6 mm diameter, 20 mm long brass cylinder. The programmed ideal path is shown for reference.

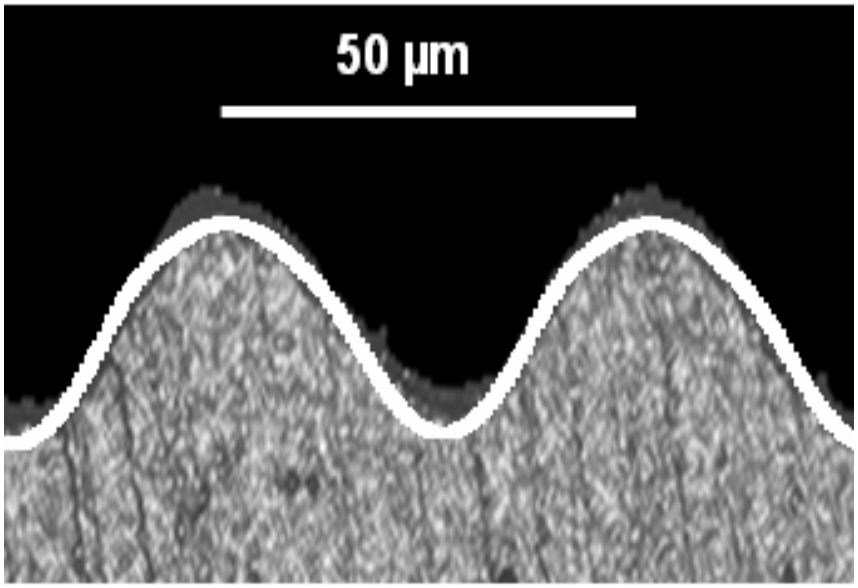

Figure 7. The calculated perturbed tool path from Figure 7 superimposed on a section of Figure 1

4.2.2 TOOL LIFE

Significant wear was noted on the tool used to machine the sine wave parts. The distance cut was less than 500 m but the tool surface showed signs of wear. Ordinarily, this sort of cutting distance in nickel would not lead to appreciable wear or chipping of the tool, but with a zero rake angle and the extreme clearance angle of 50° used, the edge becomes quite fragile. This geometry was based on the conventional non-ferrous metal turning practice of using a 0° rake angle tool. Hence, the included angle on the tool is only 40° whereas most conventional tools have included angles around 80°.

The change in rake angle for this application will be ±45° but the initial rake angle is not specified. The clearance angle must be at least 45° but the initial rake angle could be anywhere from 0 to something less than –45°. If the initial rake angle is made negative, the forces will go up throughout the sine wave motion of the tool but the included angle of the tool can be increased leading to a more robust tool with potentially longer life. So a compromise between cutting forces and tool shape must be made for this non-rotationally symmetric fabrication process.

The optimum geometry can be determined by applying tool force data to different tool geometries and evaluating the internal stresses in the diamond. Initial assessments using COSMOS finite element software and the experimental force values of Figure 5 are shown in Figure 8 and 9. Figure 8 shows the results when the forces measured for 0º rake angle are applied to the tool. In this case, the peak stress in the tool is 2.9 GPa. Figure 9 is a result of

applying the forces measured with a negative rake angle of -20º. The maximum stress in this case occurs at a distance equal to the depth of cut away from the edge of the tool and is 5 GPa or twice the value for 0º rake. The vector sum of the normal and thrust forces at the two rake angles studied and the stress on the tool are proportional; that is, the force doubles and the stress in the tool doubles for the same tool geometry.

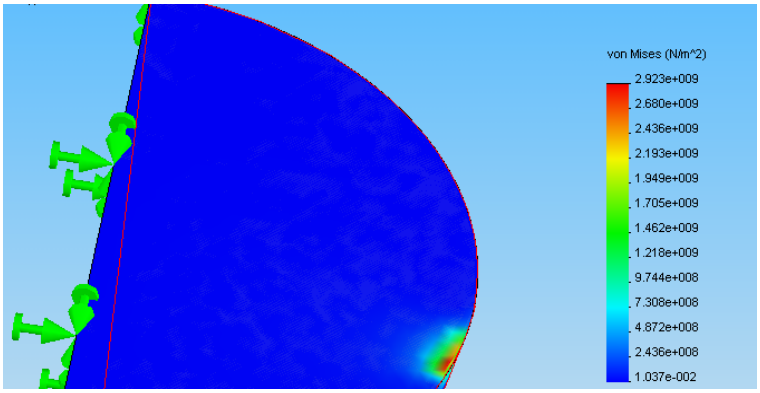

Figure 8. Simulated stresses in the diamond tool calculated using FEA and measured forces. Maximum stress at 0º is 2.9 GPa

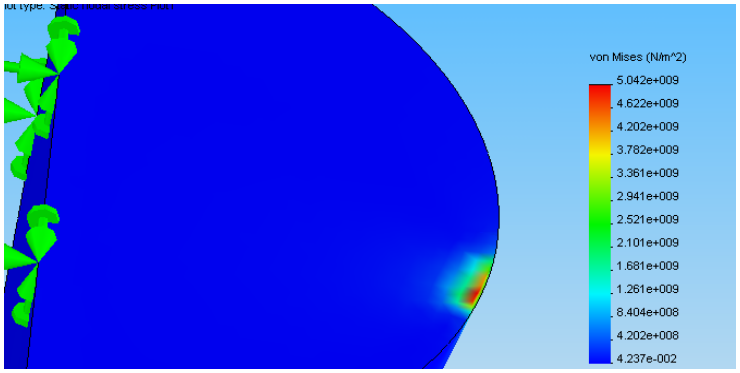

Figure 9. FEA as in Figure 8 performed at -20º rake angle. Maximum stress is 5 GPa.

4.3 CONCLUSIONS

The role of a changing rake angle in machining free-form optics is rarely addressed. However, as tool excursions and, hence, surface slopes increase, the impact of rake angle variation cannot be ignored. This will be true both from the standpoint of static deflection of the workpiece and tool as well as the impact on the life of the tool. The preliminary results presented here represent the first step in an effort to understand the effect of varying rake angles in diamond turning. The resulting knowledge will lead to methods for combating the negative effects of this phenomenon, and ultimately, better more cost effective free-form optics.

REFERENCES

1. Arcona, C., “Chip Formation and Surface Finish in Diamond Turning”. PhD Dissertation 1996.
2. Drescher, J. P, “Tool Force, Tool Edge and Surface Finish Relationships in Diamond Turning”, PhD Dissertation 1992.

5 HIGH PRESSURE PHASE TRANSFORMATION OF SILICON

Timothy Kennedy
Graduate Student
Ronald Scattergood
Professor
Department of Materials Science and Engineering

Single point diamond turning was performed on (100) Si along the <011> direction using both -30° and -45° diamond tools with feedrates of 1 and 5 µm/rev. Machining was performed using a t-lathe and a parallel fly cutting setup. All samples were analyzed with Raman spectroscopy, and cross sectional Transmission Electron Microscopy (TEM). Dislocation loops and slip planes were found at depths up to 250 nm below the surface of both feedrates of the t-lathe machined samples. In the fly cut samples no dislocations were found, and the a-Si Fly cut samples were machined with two separate set of tools, and using Raman spectroscopy it was found that depending on tool edge design an amorphous layer was not always created. This was contradicting by the TEM images showing a thin a-Si layer. A correlation between the Raman spectra and cross sectional TEM images of the diamond turned silicon was not able to be determined. TEM analysis is still needed to analyze subsurface damage, and to determine the deformation mode (i.e. high pressure phase transformation (HPPT) or dislocation movement). Recent results have provided more insight into the lack of dependence between feed rate and the depth of the amorphous layer.

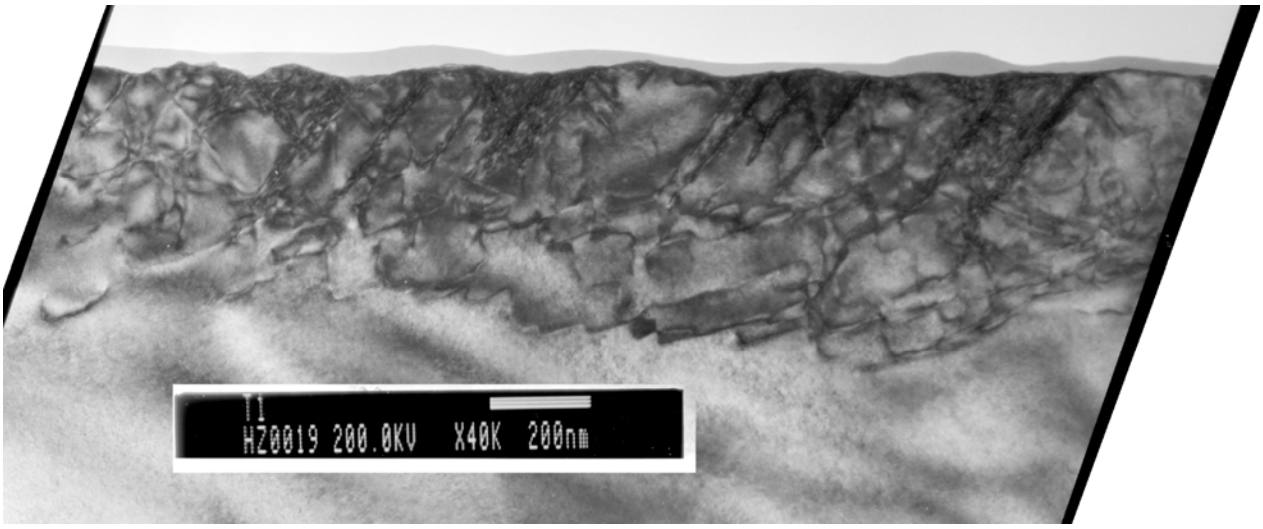

5.1 INTRODUCTION

Diamond cubic silicon (Si-I) is a brittle material under standard temperature and pressure, but when exposed to a high pressure environment the crystal structure transforms into a ductile β-tin metallic phase (Si-II). Once the Si-II is unconstrained it back transforms into multiple forms of Si, mainly amorphous Si (a-Si) and Si-I. The total transformation of silicon depends on loading, unloading, and temperature. This is shown in the transformation schedule in Figure 1. This transformation allows silicon to be machined without brittle fracture occurring, but the back transformation alters the subsurface (~500 nm in depth). This alteration can be divided into two layers: an amorphous layer and a damage layer. The amorphous layer can extend from the surface down as far as 200 nm; this is the byproduct of the back transformation process which creates amorphous silicon (a-Si). Below the amorphous layer a damage layer extends another 300 nm; this layer is comprised of dislocation structures. In situ analysis of this transformation during the manufacturing process is impractical. Using transmission electron microscopy (TEM) and Raman spectroscopy a portrait can be formed of the deformation mechanism in diamond turned silicon.

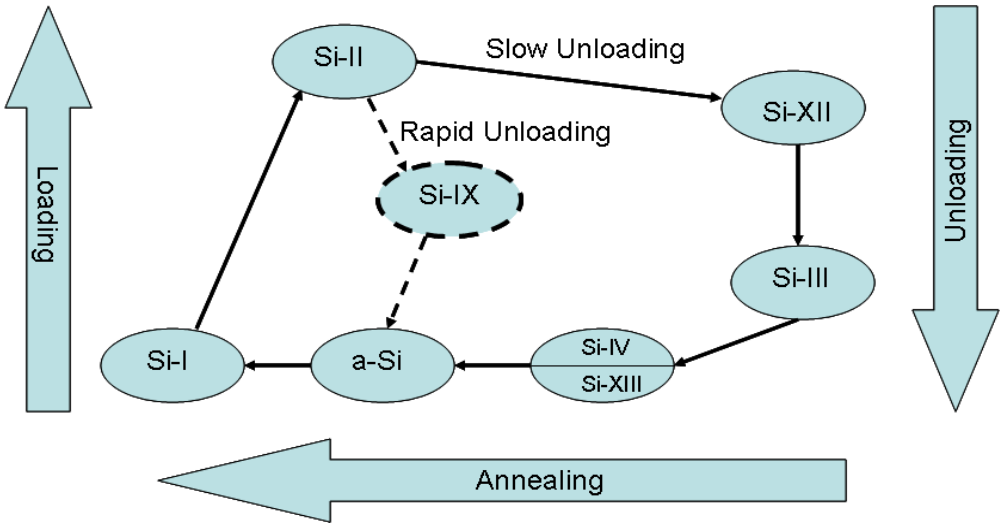

Figure 1. Silicon transformation schedule. [1]

5.2 PROJECT DETAILS

TEM and Raman data was collected from (100) oriented silicon that was diamond point turned along the <110> type direction. Different crystal orientations are available but it has been shown that (100) oriented silicon provides the best ductility.[2] Samples were machined at 1 and 5 μm/rev using a t-lathe diamond turning setup and a parallel fly cutting technique, the latter using two sets of tools consisting of a -30° and -45° rake angle round nose diamond tool. A tool force model was created using the Merchant Model, and tool force measurements were collected using a three axis load cell while fly cutting.

5.2.1 EXPERIMENTAL SETUP

A Rank Pneumo ASG 2500 Diamond Turning Machine was used to create the samples for this study. Two diamond turning setups were used; the first a traditional T-lathe setup and the next a parallel fly cutting setup. The fly cutting samples were 10 mm wide by 20 mm long, and are oriented so that the cutting direction follows the <110> type direction across the 10 mm width; as compared to an entire wafer for the lathe operation. Two sets of tools were used; one set sharpened by IMT and the other manufactured by Edge Technologies. The tools used were 3 mm radius round nosed diamond with rake angles of -30° and -45°. Unlike the traditional T-lathe setup where the tool is on the x-axis and the sample in on the spindle; parallel fly cutting places the tool on the spindle while the sample is on the x axis parallel to the tool so that a flat cut can be produced. Since carbon reacts with silicon, the latter technique reduces the diamond tool wear since the diamond is not always in contact with the silicon. Spindle speed and feed rate need to be optimized so that the layered structure can be controlled and possibly eliminated through machining, instead of other processes such as thermal annealing. Samples have been prepared with feed rates between 1 and 5 μm/rev, since previous research has shown a possible transition in the subsurface through Raman spectroscopy.[2]

5.2.2 MATERIAL CHARACTERIZATION

To characterize the machined silicon two techniques will be used; Raman spectroscopy and transmission electron microscopy (TEM). Raman spectroscopy measures the intensity and wavelength of inelastically scattered light from molecules. The scattered light is shifted by the molecular vibrational energy, which is directly controlled by the interatomic bond length of the atoms in the sample. In the case of silicon each crystalline phase has its own interatomic bond length, thus each phase would have a unique and sharp Raman spectrum. In the case of a-Si, the interatomic bond lengths vary so the Raman spectrum from a-Si is broadened. For this study it is important to know crystalline silicon (Si-I) has a peak at around 520 cm^{-1} while amorphous silicon (a-Si) centers around 470 cm^{-1}.

A different Raman technique known as polarized Raman (non-polarized Raman was described previously) was also used to analyze the machined silicon. In polarized Raman different structures have different Raman active modes, which will scatter photons with energy (cm^{-1}) different from the incident wave. The scattering intensity *I* is given by

$$I = C\sum_{j}\left|e_i \cdot R_j \cdot e_s\right|^2$$

Where C is a constant, e_i and e_s are the incident and scattered polarization vectors, respectively, and R_j is the Raman tensor, determined from group theory for the different crystal structures. Linear polarizers were used to fix the directions of e_i and e_s, and the Si wafer was on a rotating sample stage. Rotating the stage by an angle θ changes R_j such that

$$I \propto \sin^2 2\theta$$

for single crystal Si cut along the (100) plane. Amorphous Si has no directional dependence, so the intensity for its peak should remain constant as θ varies. Scans were done on wafers machined at different rates and with different tool tip rake angles. The incident polarization was set vertical, and the scattered was set horizontal. The [110] direction of the sample initially pointed vertically. The angle θ with the vertical was increased in increments of 10° for each scan. Data was taken for the first quadrant, and the values of the others were extrapolated by symmetry. Intensities of the peaks at 470 cm^{-1} (a-Si) and 520 cm^{-1} (Si-I) were plotted on polar graphs as a function of θ[1]. Even though Raman spectroscopy is a useful tool for its qualitative information it does not provide quantitative data like TEM.

TEM can provide high resolution micrographs through the use of a high energy electron beam (200 kV) that is transmitted and diffracted through the electron transparent sample. Cross-sectional TEM (XTEM), selected area diffraction (SAD), and bright field-dark field (BFDF) imaging were utilized for this study. XTEM provides the proper view of the subsurface layers compared to the more traditional planar view. To help corroborate the Raman spectroscopic data SAD was used to determine the phases present in the subsurface. SAD involves the use of an aperture to reduce the intensity and the area of the incoming beam, and then viewing the insuing diffraction pattern. A diffuse halo pattern indicates an amorphous material, while evenly spaced spots would indicate a crystalline phase. Bright field images result from the selection and viewing of the transmitted spot, while dark field images are created by selecting the diffracted spot that appears to the left of right of the transmitted spot. BFDF can show differences in phases in the sample, the presence of dislocations, and strain fields.

5.3 RESULTS

5.3.1 T-LATHE MACHINING RAMAN RESULTS

Previous research at the NCSU Precision Engineering Center used samples that were lathe machined using the IMT tools with -30° and -45° rake angle tools at feed rates of 15, 7, 3, 2, and 1 μm/rev, and then analyzed through non-polarized Raman spectroscopy.[2] A possible

[1] All Raman spectroscopy data and information provided by Benjamin Gilbert, Masters Student, Department of Physics, NCSU

dependence between feed rate and the thickness of the a-Si layer can be seen in Figure 2 when machined with a -30° rake angle tool. This dependence is based on the decreasing Si-I peak at 520 cm^{-1} as feed rate lowers until it is consumed by the shoulder of the a-Si peak at 1 µm/rev.

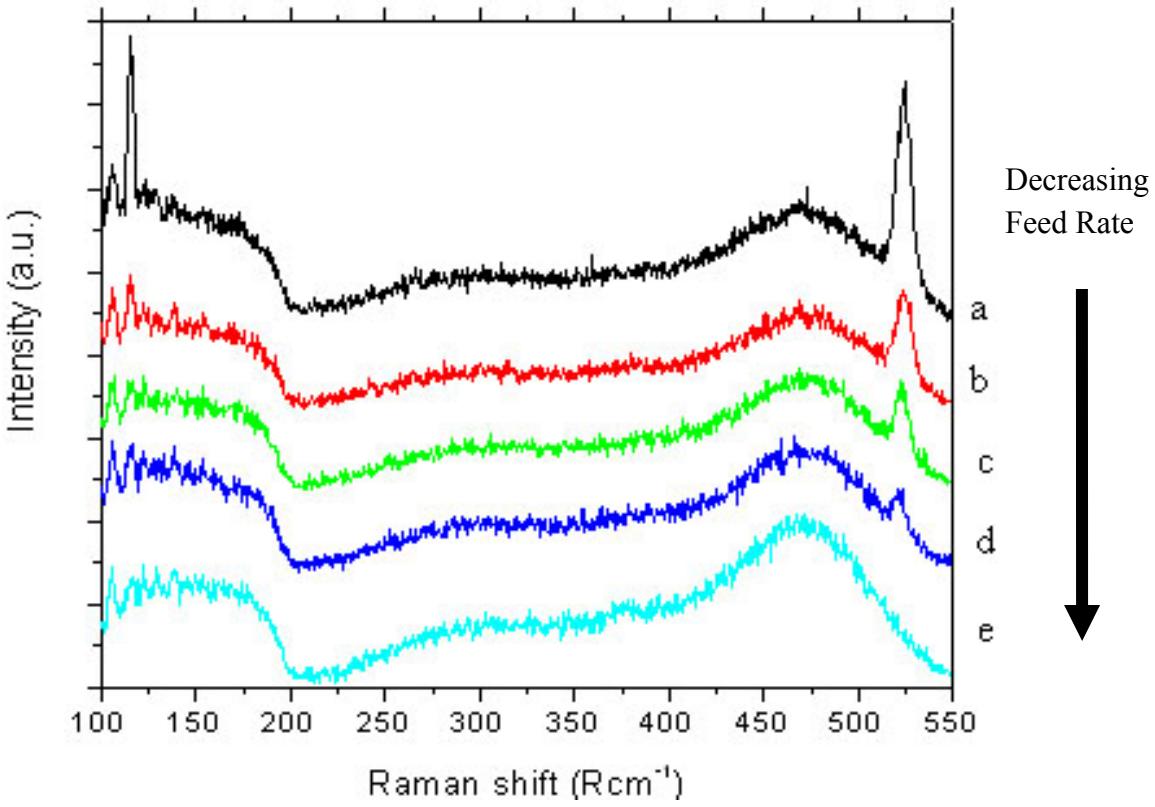

Figure 2. Raman spectra at feed rates a) 15, b) 7, c) 3, d) 2, and e) 1 µm/rev IMT -30° tool, showing a possible dependence on feed rate and a-Si thickness. [2]

Samples that were machined with a -45° rake angle tool did not show the same feedrate dependence as seen in the spectra in the Figure 3. The Si-I peak does not disappear into the a-Si shoulder as in Figure 2. A comparison between the results of the two tools is impractical due to the various factors. Tool forces, tool wear, and stress states at the tip are all dependent on the rake angle and initial tool condition.

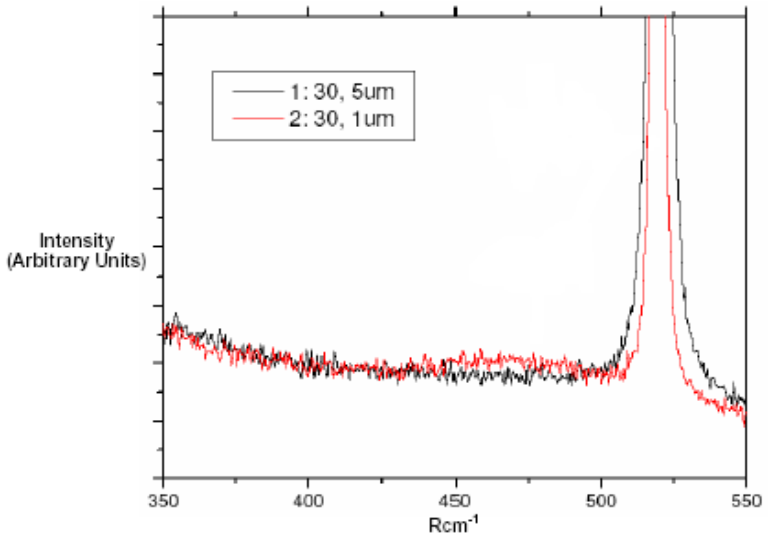

Figure 3. Raman spectra showing no dependence between feed rate and a-Si layer thickness with a -45° rake angle tool. [2]

5.3.2 T-LATHE MACHINING TEM RESULTS

Once the Raman spectra were recorded the silicon samples were made into TEM samples. It was determined that only the samples machined with the -30° IMT tool at 5 and 1 µm/rev would be viewed since the Raman spectra showed that these parameters would provide the best view of the differing thickness of the a-Si layer. The micrograph in Figure 4 provides the best view of the subsurface layers for silicon machined at 5 µm/rev. Starting from the bottom up the following layers are present; undisturbed silicon, then a layer of dislocations 400 nm thick, above the dislocations is the a-Si layer which is on average 44 nm thick. Inside the dislocation layer slip planes and dislocation loops exist. The slip planes lie at a 54° from the (100) surface, signifying a (111) slip system. The (111) slip system is the most common in plastic deformation in diamond cubic materials. Figure 5 shows that the a-Si and the beginning of the dislocation layer do not have the same topography which is somewhat unexpected. SAD indicated a diffuse halo, showing that he top layer was indeed amorphous silicon.

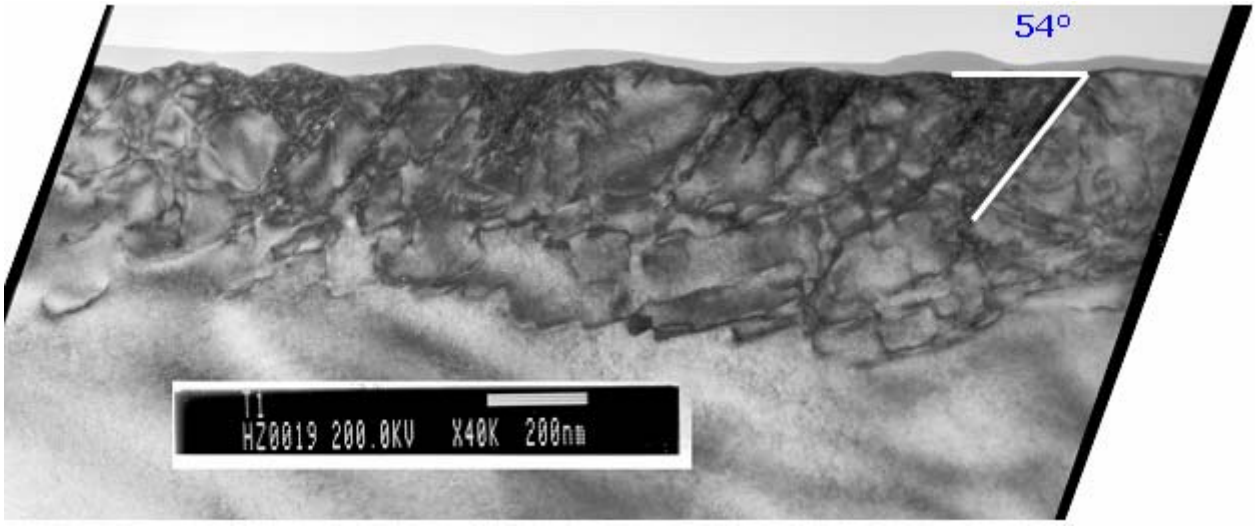

Figure 4. TEM micrograph machined 5 μm/rev with a IMT -30° tool at 40,000x. The (111) slip system angle is shown along with the a-Si layer and the dislocation microstructure.

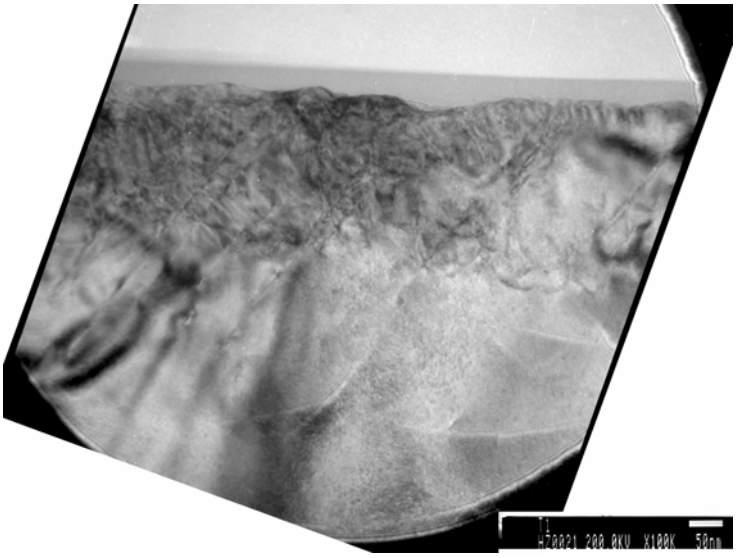

Figure 5. TEM micrograph machined 5 μm/rev with a IMT -30° tool at 100,000x.

The use of bright field/dark field (BFDF) pairs helps to view the dislocation structures, any phase contrast, and the strain fields that are present in the silicon. Strain fields and dislocation loops are present in the BFDF pair in Figure 6, 7, and 8. When the lattice of a crystalline material is strain, it changes the way electrons are transmitted through the structure. This change is usually seen by contrast change. It is another way to help indicated a strained lattice, view dislocations, and view alloying elements or precipitates.

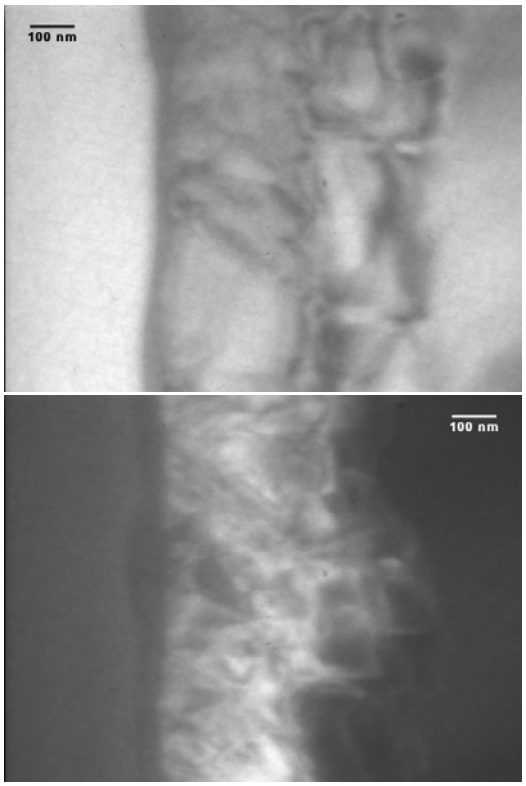

Figure 6. BFDF pair, machined at 5 μm/rev with a IMT -30° tool, 196,764x. Notice the strain induced contrast change in the dislocation layer.

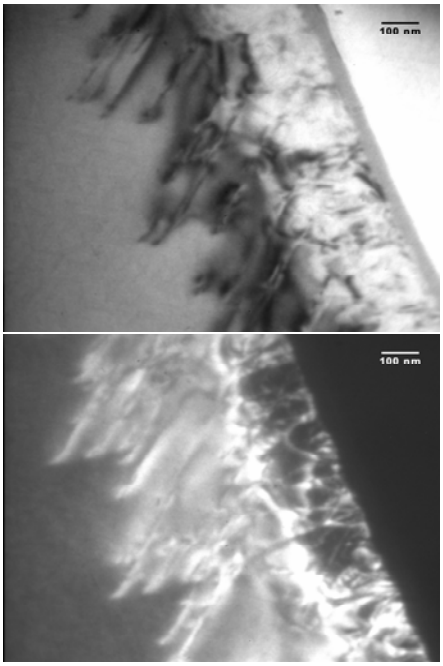

Figure 7. BFDF pair, machined at 1 μm/rev with a IMT -30° tool, 196,764x. Notice the slip planes going deep into the undisturbed silicon.

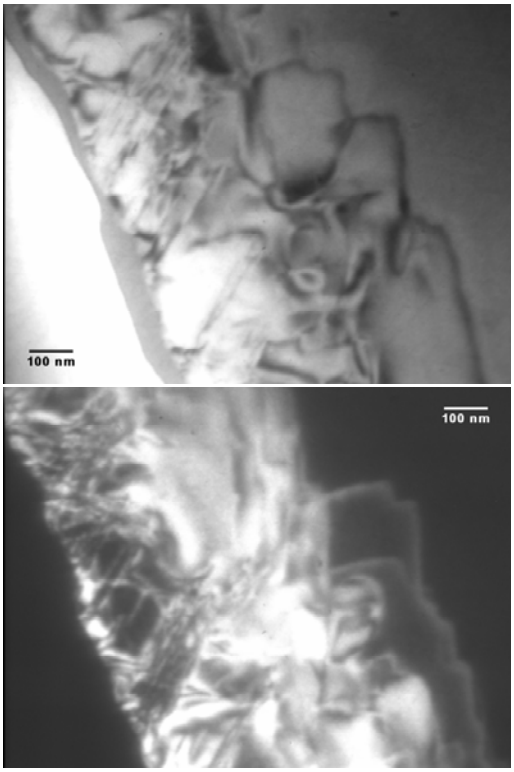

Figure 8. BFDF pair, machined at 1 μm/rev with a IMT -30° tool, 196,764x. Notice the dislocation loops going in and out of the undisturbed silicon.

The machining parameters in Figure 7 and 8 are the same, 1 μm/rev with a IMT -30° tool. Even though one does not see the same structure in the subsurface, it all depends on the angle of the sample and the angle of the diffracted electron beam. So in Figure 7 slip planes penetrate deeply (400nm) into the undisturbed silicon. While Figure 8 shows dislocation loops and a highly strain dislocation layer.

5.3.3 LATHE RAMAN SPECTRA AND TEM COMPARISON

It is important to try to compare the TEM and Raman spectroscopy results. The Raman results indicate that the a-Si layer at a feed rate of 1 μm/rev should be thicker than the a-Si at a feed rate of 5 μm/rev. To compare the TEM results, the a-Si layer is measured and then plotted versus feed rate, Figure 9. The result form this comparison is surprising. There is no statistical difference between the thicknesses of the a-Si layer at the two feed rates. Only 4 nm separate the layers, and this is contradictory to the Raman spectroscopy results. Due to time constraints no fly cutting samples were imaged in the TEM. The reason for this discrepancy will be discussed in a later section.

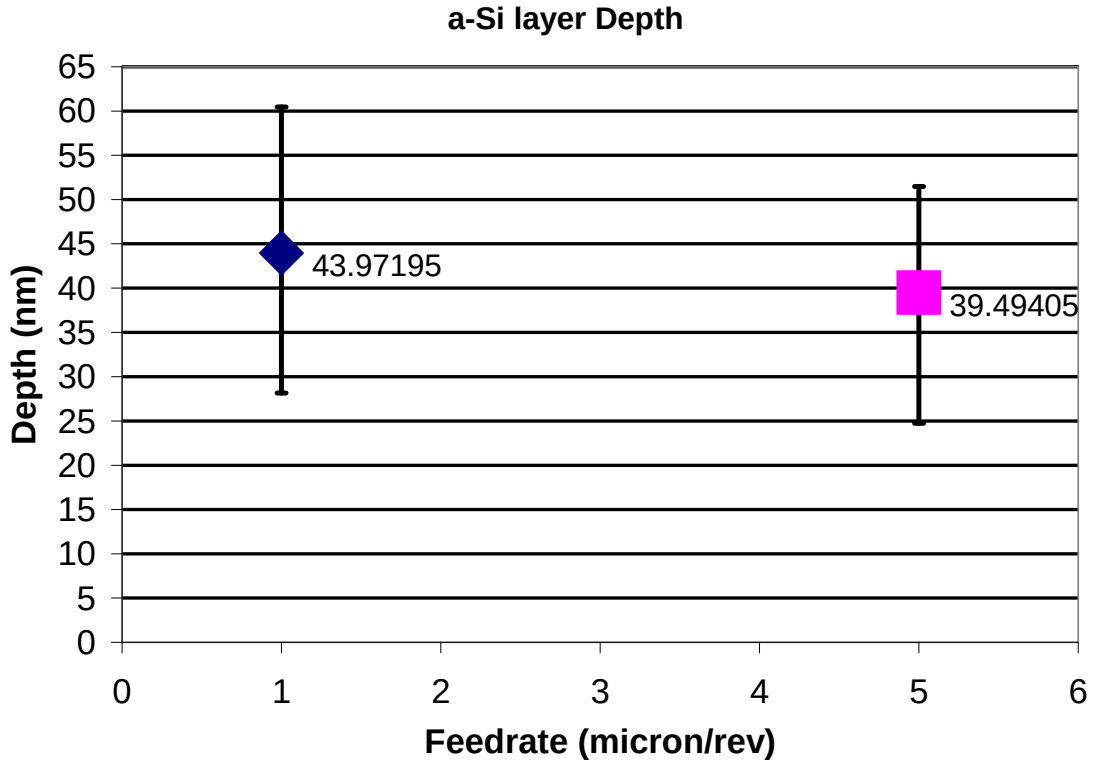

Figure 9. Depth of the a-Si layer versus feed rate. There is no statistical difference between the to feedrates, which counters the Raman spectra for those feed rates.

5.3.4 FLY CUTTING RAMAN RESULTS

It was important to make sure that the t-lathe machining and fly cutting created the same Raman spectra. None of the fly cutting Raman spectra matched the lathe machining spectra. Figure 10 is a representative spectra for the fly cut silicon. It is apparent that the a-Si peak is missing from the spectra as compared to the Raman spectra from the t-lathe set up. Both sets of tool were used in fly cutting and neither set showed no sign of any amorphous material, only a sharp Si-I peak at 520 cm^{-1}. This is troublesome since the surface showed no signs of brittle fracture. When machining silicon it is usually assumed that when brittle fracture occurs on the surface that no amorphous material is created. One of the ideas behind ductile machining of brittle materials is that a second phase is formed through a high pressure phase transformation to facilitate the plastic deformation of the machining process. The Raman spectra of both the -30° and -45° rake angle tools, regardless of feed rate, showed the same lack of an a-Si peak at 470 cm^{-1} . All of the tool parameters are the same between the two machining parameters, so it is unclear to why there should be a difference between the two sets of Raman spectra. So to ensure that the Raman spectra were accurate from both tool sets, polarized Raman was utilized. The results that come from the polarized Raman help to clear the picture of the characterization of the subsurface.

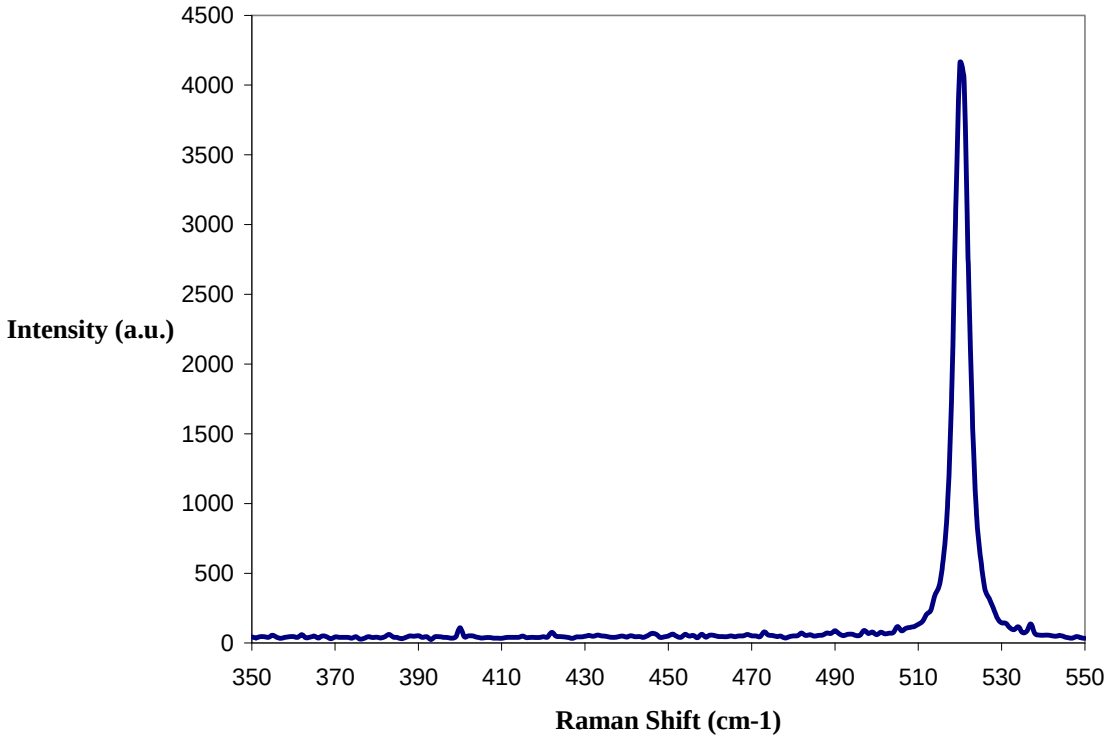

Figure 10. Raman spectrum of silicon machined at 1 µm/rev using a -30° Edge tool showing lack of a-Si at 470 cm^{-1} .

As mentioned in a previous section to create a polar Raman spectra the intensities of the a-Si and Si-I were plotted as a function of polarization angle. The a-Si peak has no dependence on angle since it has no crystal structure. Si-I follows a clover leaf pattern that is expected from the physics of Raman and the direction <110> as can be seen in Figure 11 and 12. Once again there appears to be no correlation between feedrate and the a-Si layer. The layer thicknesses shown in Figure 9 can now be considered valid knowing that there could be no dependence.

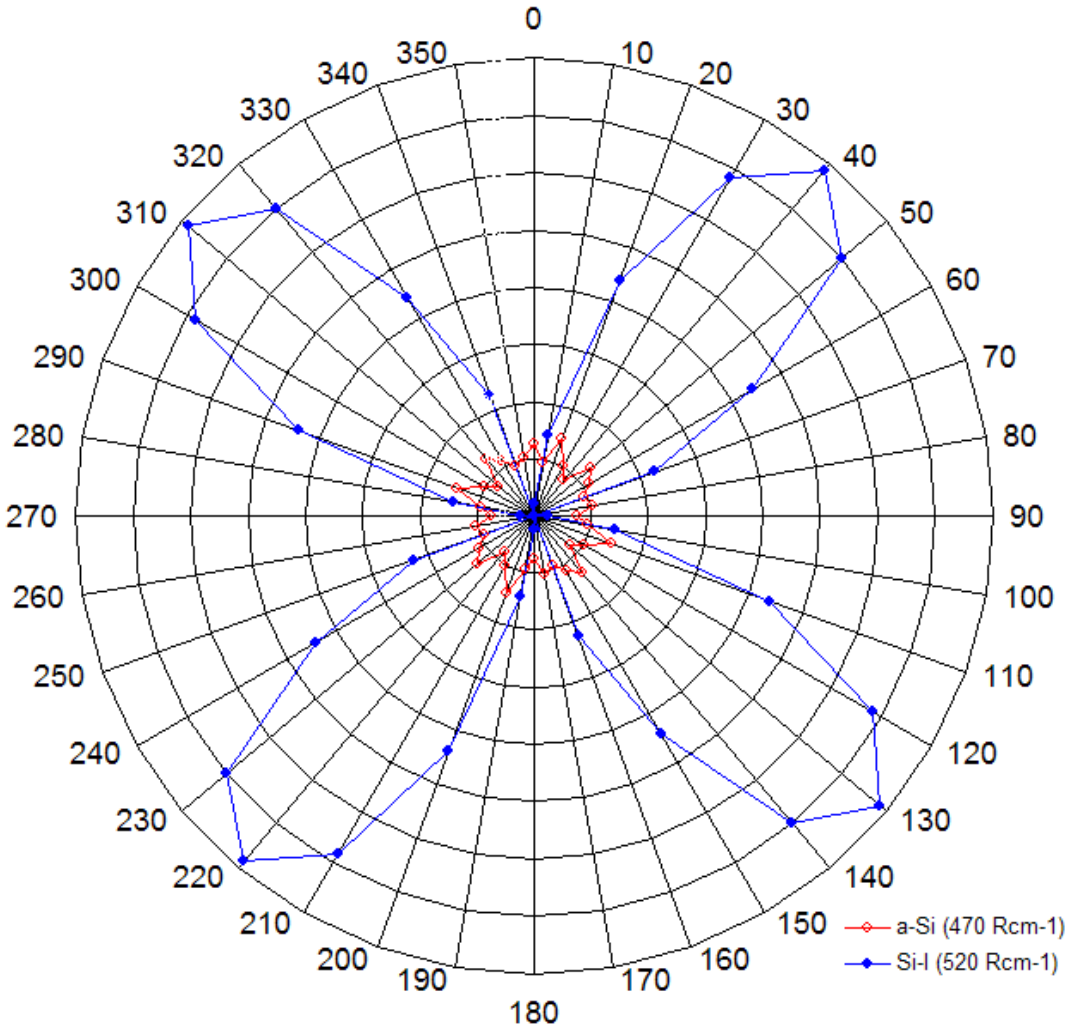

Figure 11. Polar Raman plot of silicon machined at 1 μm/rev with a IMT -30° tool.

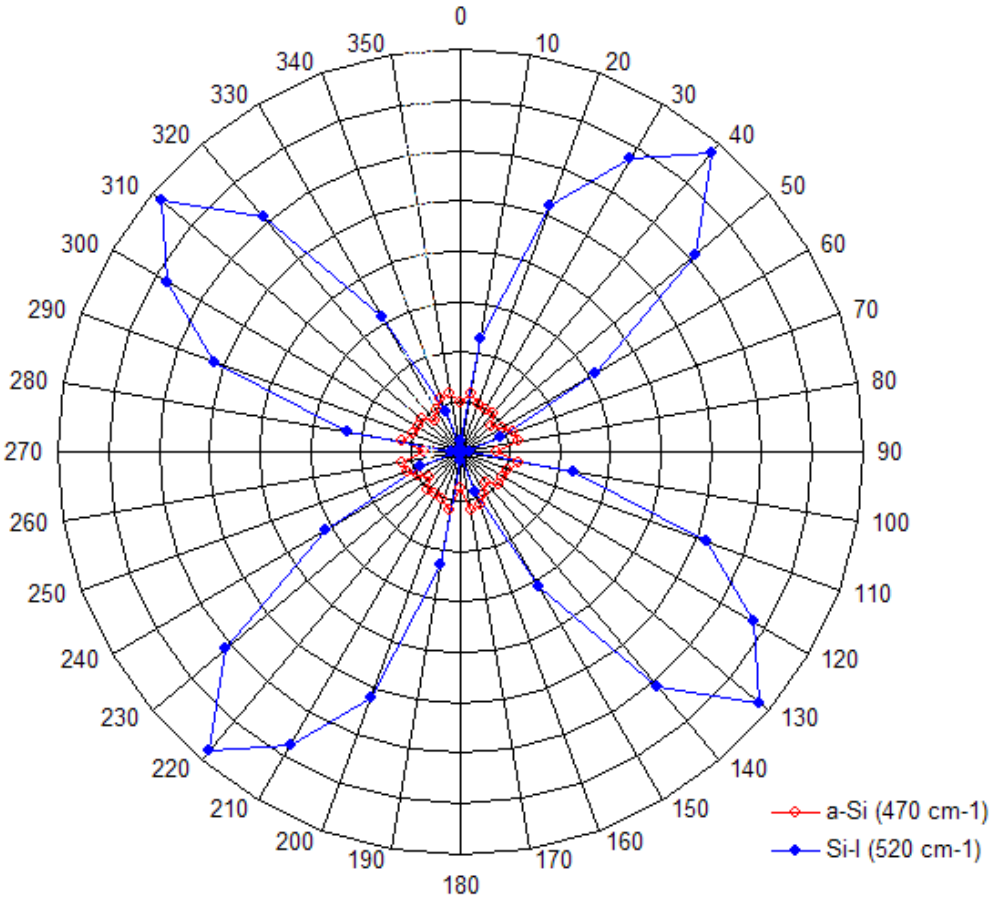

Figure 12. Polar Raman plot of silicon machined at 5 µm/rev with a IMT -30° tool.

5.3.5 FLY CUTTING TEM RESULTS

When the machining technique is switched to parallel fly cutting a change in the subsurface is evident. Figures 13 and 14 were fly cut at 5 µm/rev with an IMT -30° tool, and there is no damage layer beneath the a-Si layer when compared to Figure 2. Even the a-Si layer is dramatically thinner than previously measured. When the tool vendor is changed to Edge Technologies the same microstructure is seen. Figures 15 and 16 were fly cut at 5 µm/rev with an Edge Tech -30° tool, and the same lack of dislocations and a thin a-Si layer is apparent.

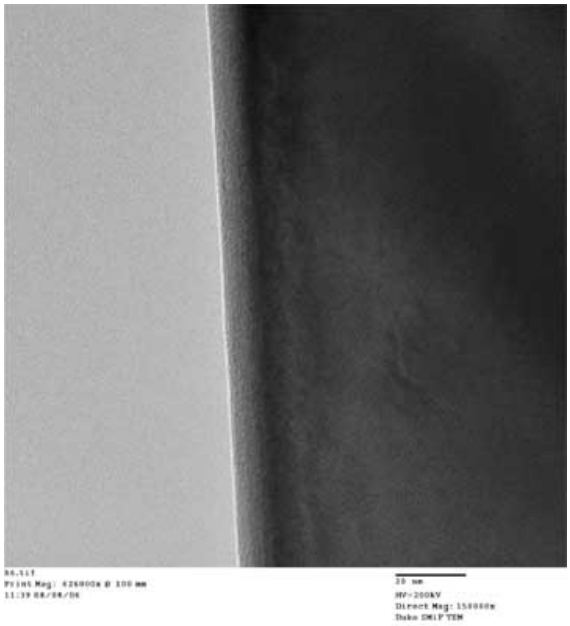

Figure 13. TEM micrograph fly cut at 5 μm/rev with an IMT -30° tool. Notice the lack of a damage layer.

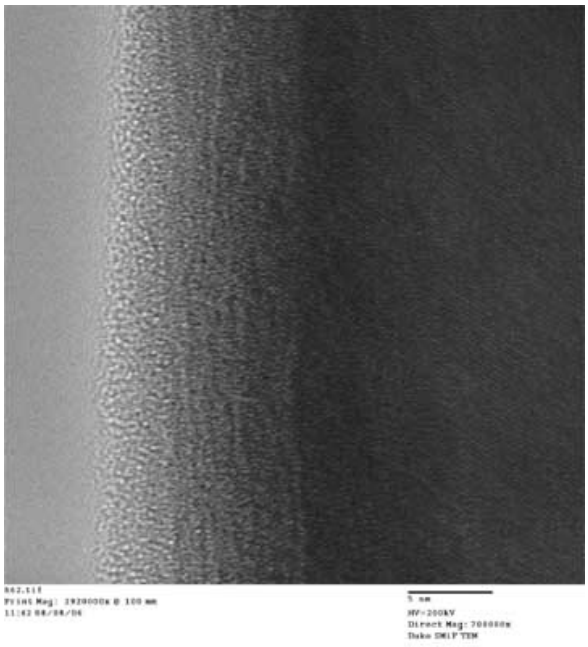

Figure 14. TEM micrograph fly cut at 5 μm/rev with an IMT -30° tool showing a higher magnification of the a-Si layer at the surface.

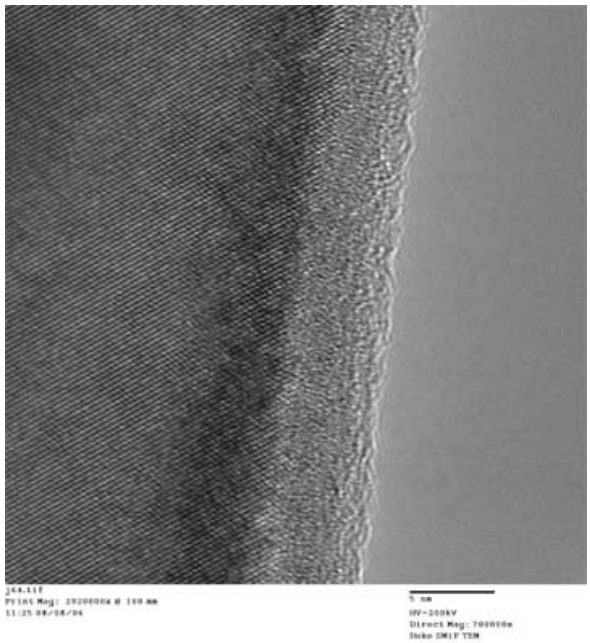

Figure 15. TEM micrograph fly cut at 5 μm/rev with an Edge Tech -30° tool showing a higher magnification of the a-Si layer at the surface.

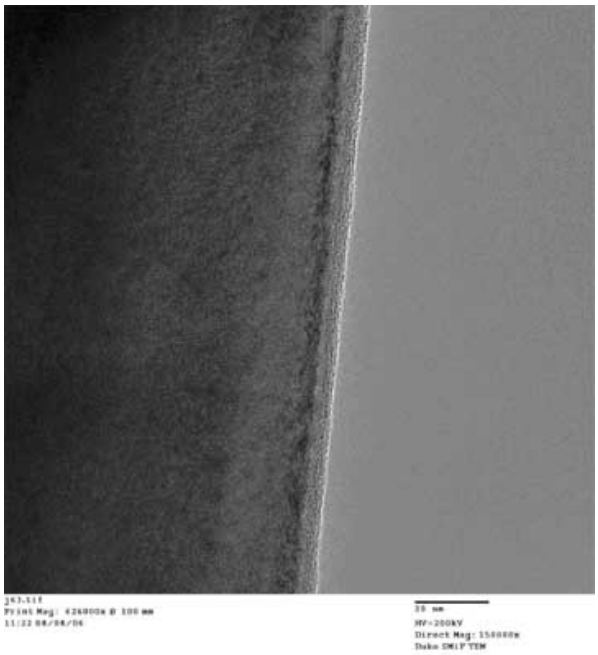

Figure 16. TEM micrograph fly cut at 5 μm/rev with an Edge Tech -30° tool. Notice the lack of a damage layer.

5.3.6 TOOL FORCE

Analyzing tool force measurements is an excellent method to help determine what may be happening to the silicon where other techniques cannot observe the machining process. To do this, a three axis load cell was used. Three axis load cells are able to collect force data on the x, y, and z axis simultaneously, and can be easily adapted to the fly cutting process. The two important forces that come from the load cell are the thrust force and cutting force. The thrust force is the force being applied perpendicular to the sample surface, while the cutting force is parallel to the surface and inline with the tool motion. Figure 17 shows the forces colleted on a 5 µm/rev sample cut with a -30° CP tool. The reason the lines do not plateau is that the sample was not perpendicular to the machining x-axis.

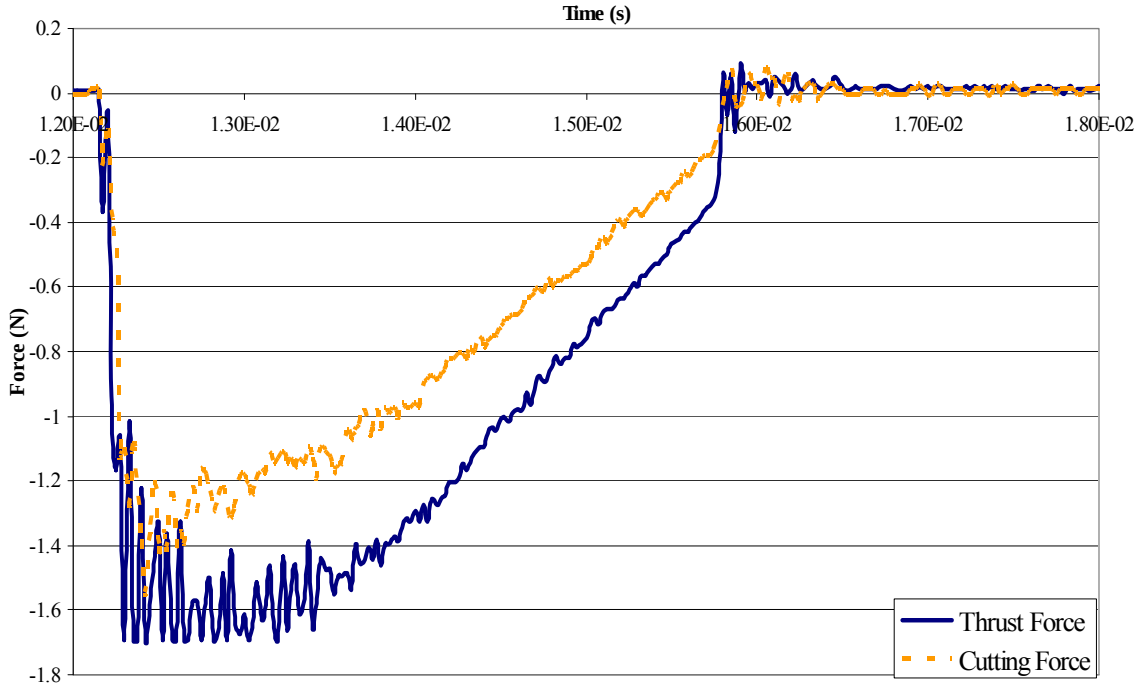

Figure 17. Tool force data for a 5 µm/rev sample cut with a -30° CP tool

The force values obtained are similar to those found in the literature. But when these forces are placed in the Merchant machining g model the calculated pressures do not match the pressure needed for silicon HPPT (~12 GPa). The reason for this is shearing. Shearing has been shown to reduce the HPPT in silicon by as much as forty percent, down to around 5 GPa. [5] So when the values obtained through the Merchant machining model now make sense when viewed through the idea of shear reduction.

5.4 MACHING TECHNIQUE COMPARISON

Beyond comparing t-lathe machining and fly cutting, it is important to compare these results with the results found from CMP processing. It is interesting to compare these new TEM results to the as received CMP silicon wafer in Figure 18, which shows a nominal a-Si layer thickness of around 2 nm. It was previously thought that CMP was the only way to achieve optical surface finish with very little subsurface damage, but that has been proven not to be the case.

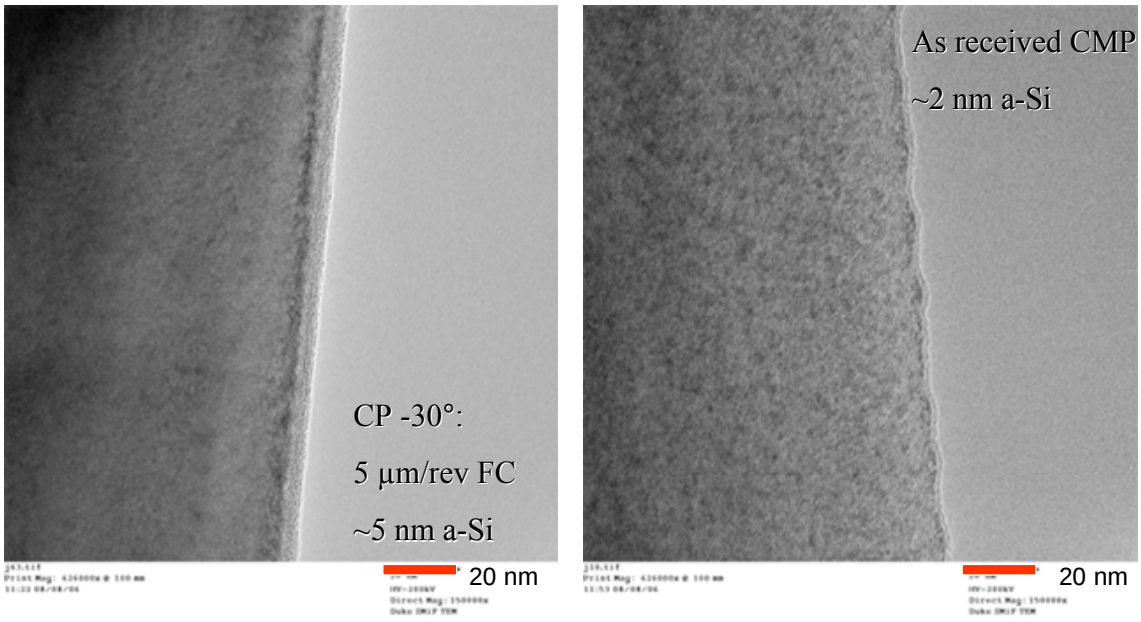

Figure 18. Comparison between a 5 µm/rev sample and an as received silicon sample cut with a -30° CP tool

.

Figure 19 shows the comparison of a-Si layer depth versus the machining feed rate and technique. Due to the fact that lathe machining and fly cutting are equivalent machining techniques, the various tool parameters seem to have an affect on the a-Si layer depth.

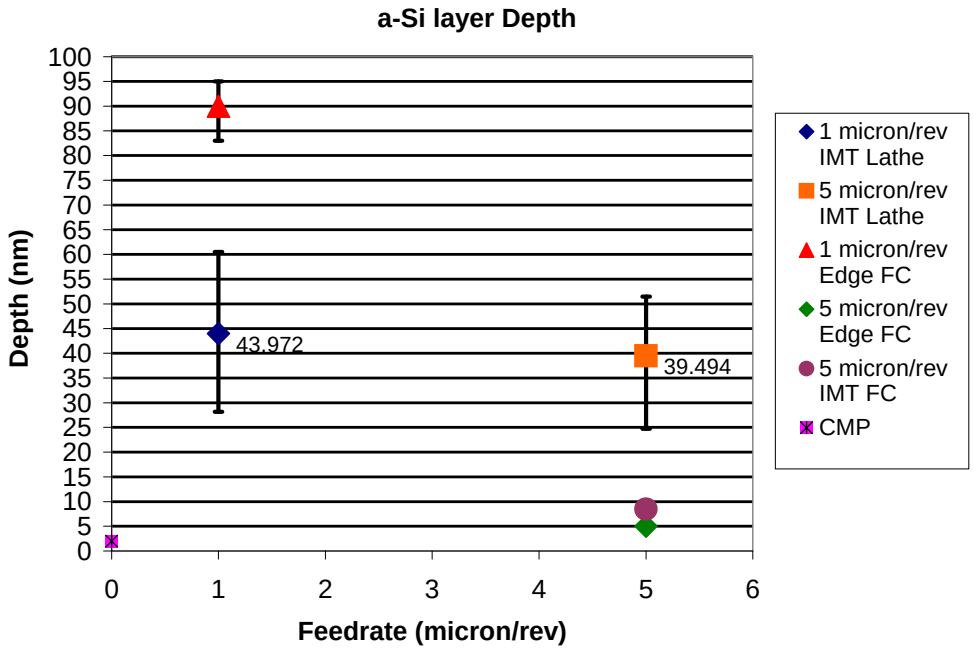

Figure 19. TEM micrograph fly cut at 5 µm/rev with an Edge Tech -30° tool. Notice the lack of a damage layer.

5.5 COMPARISONS AND CONCLUSIONS

To make sure that the TEM results are on par with what other research groups have seen a comparison is need. Other groups [3, 4] have reported dislocations, dislocation loops, and slip planes. If an HPPT is occurring then the loops and slips planes indicate a normal metallic deformation mode when the silicon transforms into ductile Si-II. Another point is the existence of the amorphous layer. Once again there is evidence for either an HPPT or other deformation mode. The theory in silicon HPPT is that upon unloading the Si-II will back transform through various phases until it reaches the amorphous stage, at which time it does not have enough energy to recrystallize into Si-I leaving a metastable a-Si, as illustrated in Figure 2. If viewed through a traditional deformation mode, the amorphous layer exists due solely to the extreme high pressure at the surface under the diamond tool, and the dislocations underneath follow traditional silicon slip mechanisms. More in depth studies will need to be performed to pin point the true deformation mechanism.

From the TEM data it is clear that the back transformed material contains an amorphous layer and a deeper damage layer. Multiple research groups have also seen this structure, but it is

important to note that there has been no in depth evaluation of the damage layer before. Before the polar plots were recorded the Raman spectra and TEM images were contradictory to each other, due to the lack of a statistical difference in a-Si layer thicknesses. Now taking into account the polar plots the TEM data and Raman data can now be seen in good comparison to each other. As shown the samples machined with fly cutting showed no a-Si peak in the Raman spectra. This is due to the fact that the resolution limit of Raman spectroscopy is around 10 nm. The resolution limit is larger than the a-Si layers seen in the TEM images. At this point, the existence of an HPPT in silicon during diamond turning is looking more probably, and any mode or mechanisms set forth in future research are only theoretical.

5.6 FUTURE WORK

Upcoming research will not use Raman spectroscopy due to the resolution limit, but will rely on additional TEM imaging and tool force measurements. Beyond silicon, lithium niobate will be examined due to the lack of research on the subsurface created during single point diamond turning of this important optical material.

REFERENCES

1. Domnich, V. and Y. Gogotsi. “Phase Transformations in Silicon Under Contact
2. Loading”, Rev. Adv. Mater. Sci. 3(2002) 1-36
3. Randall, T., M.S. Thesis, *Characterizing the Ductile Response of Brittle Semiconductors to Dynamic Contact Processes*, North Carolina State University, 2004. http://www.lib.ncsu.edu/theses/available/etd-06182004-104005/
4. Shibata, T. “Cross-section transmission electron microscope observations of diamond-turned single-crystal Si surfaces”. Appl. Phys. Lett. 65 (20), 14 November 1994. 2553
5. Kunz, R. “High Resolution studies of crystalline damage induced by lapping and single-point diamond machining of Si(100)”. J. Mater. Res., Vol. 11, No. 5, May 1996. 1228
6. Aleksandrova, M. “Phase transitions in Ge and Si subjected to shear under pressures up to 12 GPa and the P-T-shear diagrams of these elements”. Phys. Solid State, Vol. 35, No. 5, May 1993. 663

6 ELLIPTICAL VIBRATION-ASSISTED MACHINING

David Brehl
Graduate Student
Thomas A. Dow
Dean F. Duncan Distinguished Professor
Department of Mechanical and Aerospace Engineering

The Ultramill EVAM tool has been used to machine millimeter-scale optical surfaces. Simple spherical reflectors were made first to evaluate the types and sources of surface errors which can occur when making optical parts of this size. Several spherical surfaces were machined and errors removed on successive parts, reducing the figure error to 62 nm RMS. Next a fiber-optic beam splitter was designed which features high-sag off-axis ellipsoidal reflecting surfaces to be machined using the Ultramill. This beam splitter eliminates additional refracting elements, such as ball lenses, used for collimation in existing designs. A test reflector was made with sculpted 3-D geometry representative of that required by the beam splitter. Initial performance test and metrology results are presented for this reflector. As a preliminary to the optical surface experiments, thermal stability of the Ultramill was investigated for the original open-circulation cooling arrangement as well as for a closed-circulation scheme. Closed-circulation cooling is determined to have considerably greater temperature stability leading to reduction in form error caused by thermal variations. However pressure pulsations from the existing diaphragm-type coolant circulation pump limit the achievable surface roughness to 20 nm RMS when using closed-circulation cooling.

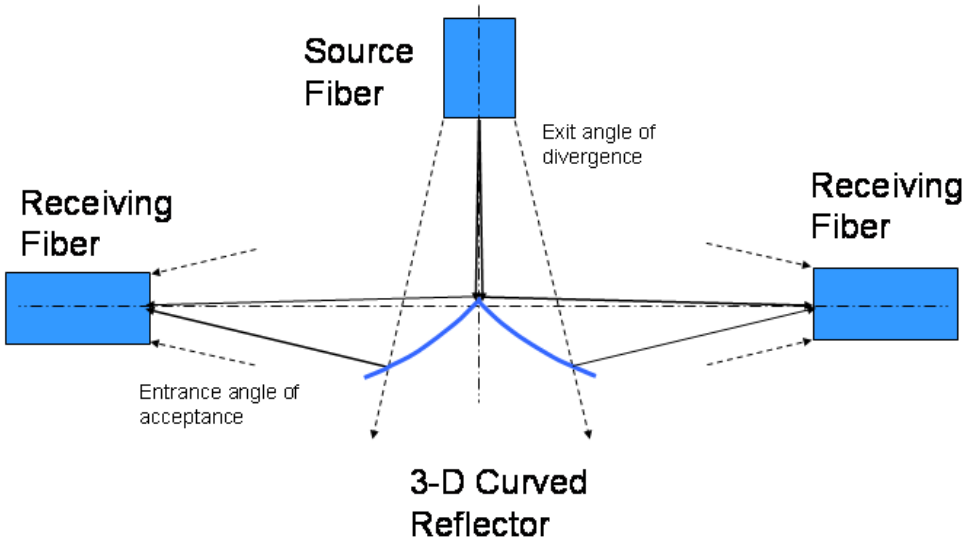

6.1 INTRODUCTION

The Ultramill is a precision cutting tool using "elliptical vibration-assisted machining" (EVAM). It avoids many of the issues associated with other methods for micro-device fabrication. In EVAM, a piezoelectrically-driven toolholder moves the tip of a diamond cutting tool in a tiny elliptical path at frequencies of 1 to 4 kHz. This elliptical tool motion is superimposed on the feed motion of the workpiece. Advantages of the Ultramill EVAM process are:

- Optical quality surface finish
- 3-D features at a scale of 10's of micrometers, with sub-micrometer tolerance
- Near-zero burr at the edges of cuts
- Large range of materials that can be machined
- Extended diamond tool life when used to machine ferrous materials

Previously the Ultramill was used to create micro-structures in materials such as copper and stainless steel [1]. These included binary microstructures such as the PEC Angstrom symbol logo at sizes of 1mm square and 200 μm square (hard-plated copper) [2], and the Sandia thunderbird logo (17-4 PH stainless steel) [3]; trihedron structures in which 3-D geometry was created by the cross-section of a dead-sharp tool [4]; and features with complex sculpted 3-D geometry. These last included a convex cylinder segment (Figure 1) and a grooved "potato chip" part with sinusoidal cross-sections in both the upfeed and crossfeed directions (Figure 2). These examples illustrate the potential for the Ultramill to machine parts with arbitrary 3-D non-rotationally symmetric geometry. These parts have overall sizes ranging from approximately 1 mm to smaller than 200 μm with individual feature resolution smaller than 10 μm, and surface finishes of less than 15 nm RMS. When making sculpted 3-D surfaces, aspect ratios of 0.04 and vertical dimensions up to 20 μm have been achieved.

In the current research the Ultramill is used to machine functional millimeter-scale optical elements including spherical reflectors and a new type of fiber-optic beam splitter needing fewer optical components. This latter project requires making a part with an off-axis aspherical surface that also lacks rotational symmetry. Making such parts requires a capability to machine high-sag surfaces with a maximum depth greater than 100 μm equivalent to a vertical aspect ratio of 0.1, while achieving optical quality surface roughness and figure error.

Before undertaking these optical fabrication projects, thermal stability of the Ultramill during operation was investigated in some detail. This was motivated by concern that temperature fluctuations could cause dimensional changes in the Ultramill structure, resulting in form error in the machined part due to changes in the tool tip position in the depth of cut direction. A closed-circulation cooling scheme was investigated as a means of minimizing thermal variations compared to the original open-circulation cooling arrangement.

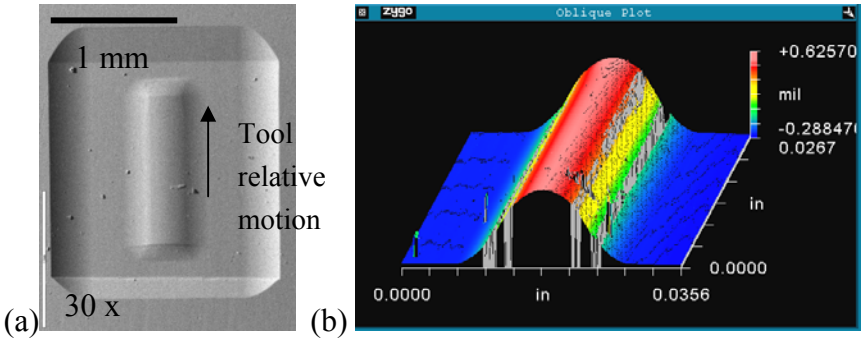

Figure 1. Convex cylinder feature machined in hard-plated copper with 1 mm nose-radius tool. Radius of curvature is 1 mm, height 20 µm and aspect ratio is 0.04. (a) SEM image. (b) White-light interferometer image.

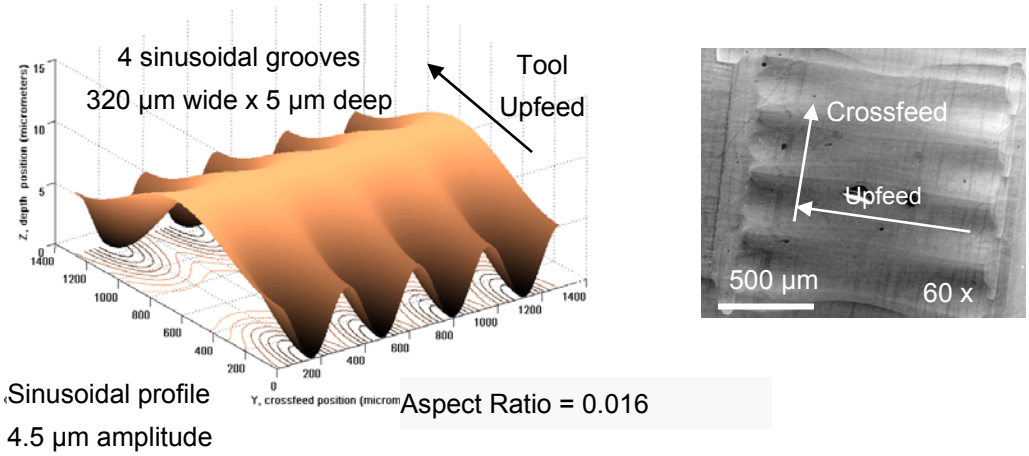

Figure 2. "Potato chip" part consisting of grooves with sinusoidal profile in the upfeed direction and sinusoidal groove cross sections. (*left*) Part design (*right*) SEM image of part made in hard-plated copper using 1 mm nose-radius tool.

6.2 PROCESS AND EQUIPMENT

Figure 3 depicts the Ultramill's elliptical tool-tip motion generated by a pair of piezoelectric actuators. Sinusoidal voltage signals, 90 degrees out of phase, are supplied to the two parallel actuators. The linear motion of the actuators is converted to an elliptical tool motion by means of a mechanical linkage that is part of the toolholder design. The ellipse dimensions can be varied by changing the amplitude and relative phase of the voltage signals applied to the actuators.

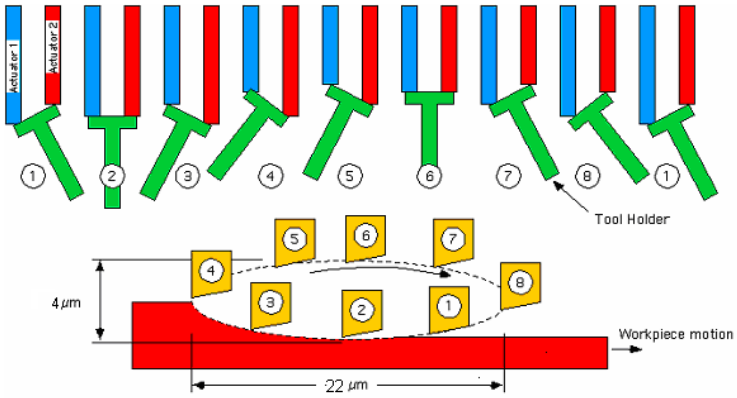

Figure 3. Ultramill Vibration-Assisted Machining Concept.

The elliptical tool motion is superimposed on the upfeed motion of the workpiece producing a toolpath in the form of overlapping ellipses. This geometry results in chips with a maximum thickness that is less than the conventional machining chip thickness (depth of cut) leading to significantly smaller tool forces. The reduced tool forces mean that in EVAM vibration and chatter are suppressed, resulting in improved surface finish and permitting smaller features to be made with smaller tolerances. The periodic entry and exit of the tool from the work creates cusp-like features regularly spaced in the upfeed direction. Short, discontinuous chips are created when the depth of cut (DOC) is smaller than the semi-minor axis of the toolpath ellipse. This is because the tool tip exits the workpiece before its motion reverses relative to the work feed and the tool cuts the chip from the work material.

Figure 4 shows the Ultramill installed on a Nanoform diamond turning machine (DTM) which provides 3-axis X-Y-Z motion for raster machining. The spindle was locked using the Ultramill for the experiments described in this report but could be used as a fourth axis (C-axis) for making more complex surface shapes. All three linear axes possess hydrostatic oil bearings and nanometer-accuracy positioning ability. Laser interferometers give position feedback information for the X and Z axes, while a linear encoder is used by the Y-axis. A UMAC controller provides motion and control commands to the Nanoform axes, with the capability to execute motion programs written using standard CNC 'G'and 'M' codes. A vacuum chuck on the spindle face holds the workpiece during machining. A side-mounted video microscope camera affords a view of the tool rake face and the work surface, to facilitate touchoff. A second video microscope camera is mounted on the Y-axis adjacent to the Ultramill. This gives a magnified aerial view of the workpiece surface and can be used to position the tool tip at a desired X-Y location.

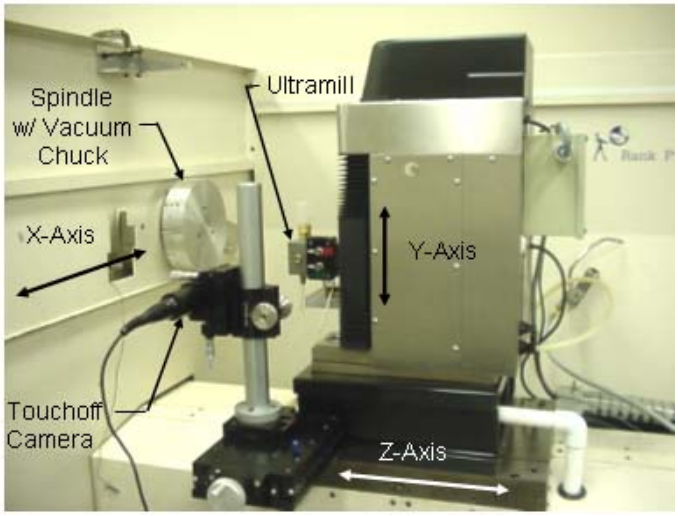

Figure 4. Ultramill installed on Nanoform 3-axis diamond turning machine (DTM). Y-axis camera for plan view of workpiece surface is not installed in this in picture.

6.3 THERMAL STABILITY INVESTIGATION

6.3.1 BACKGROUND

The Ultramill is driven by piezoelectric actuators which produce waste heat as a result of hysteresis during their expansion/contraction cycle. The heat generation in the Ultramill is sufficiently large that the actuators need to be actively cooled by a circulating dielectric fluid, to achieve a safe operating temperature below 100 °C. The Thermocube temperature control unit contains a solid-state thermoelectric heat exchanger that adds or removes heat as required to keep the coolant at a programmed setpoint temperature. Pressure to move the coolant through the system is generated by a positive-displacement diaphragm pump in the Thermocube.

Physically connecting the coolant supply line to the Ultramill might cause its structure to vibrate due to pump-induced pressure pulsations, which in turn would cause error in machined surfaces. Therefore from its initial installation until May 2007, the Ultramill used an open-circulation cooling scheme. In April 2007 an investigation of closed-circulation cooling was initiated to compare the quality of the surfaces produced. The goal of these investigations was to:

1. Reduce the temperature of the Ultramill by increasing the effectiveness of the heat transfer process.
2. Improve the temporal stability of the Ultramill temperature.
3. Minimize Ultramill vibration induced by the diaphragm pump.

6.3.2 COOLING SYSTEM CONFIGURATIONS

Figure 5 shows the original open-circulation configuration of the Ultramill cooling system and the closed-circulation configuration that were investigated.

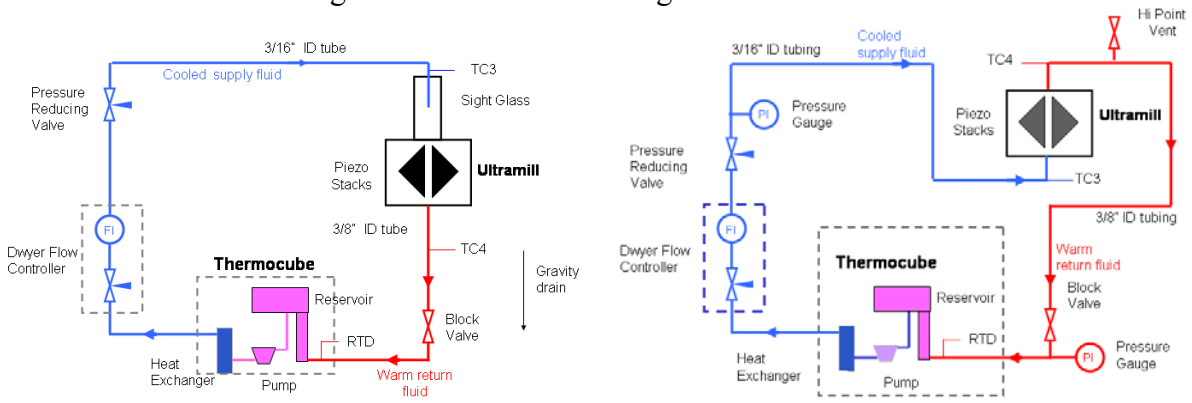

Figure 5. Open-circulation cooling arrangement (left) and closed-circulation (right).

In the open-circulation arrangement, the coolant was supplied from the Thermocube by the diaphragm pump. During steady-state operation, coolant leaving the Thermocube was cooled below the setpoint (return) temperature at the Thermocube inlet, and increased in temperature as it passed over the actuator stacks. The volumetric flow rate was adjusted using a Dwyer Instruments ball-float flow controller. A downstream pressure reducing valve was used to improve the resolution of the flow controller by taking up most of the pressure difference between ambient and the pressure provided by the diaphragm pump. The coolant discharged into a sight glass mounted atop the Ultramill cooling chamber. It then flowed by gravity into the coolant return line. Since the liquid level in the sight glass is only 80 mm above the centerline of the cooling chamber, the liquid pressure at the preload diaphragm-toolholder interface was 1.5 KPa (0.2 psi). At this low pressure, little if any fluid leaked from the coolant chamber. To facilitate gravity-driven flow, the Thermocube was located on the floor, about 1.2 m below the center line of the Ultramill.

Figure 5 also shows the closed-circulation cooling arrangement with the coolant supply line connected to the bottom port of the Ultramill cooling chamber. The volumetric flow rate of the coolant is still controlled by the ball-float flow controller and pressure reducing valve. The coolant return connection is on the top of the Ultramill. The coolant return line contains a high-point vent which is used to evacuate air from the system when it is first filled with fluid. In the closed-circulation configuration, the Thermocube is located above the Ultramill to help any air bubbles in the coolant circuit flow away from the Ultramill. In closed-circulation cooling, the pressure in the Ultramill cooling chamber is 30 to 150 KPa (5 – 15 psi) above ambient. This

high pressure causes some coolant leakage from the joint between the toolholder and preload diaphragm. The fluid leakage is captured in a container for reuse.

6.3.3 EXPERIMENT RESULTS

Three types of experiments were conducted to evaluate the differences between the open- and closed-circulation cooling schemes:

1. Temperature measurements from thermocouples placed throughout the coolant path
2. Capacitance gage measurements of the tool location as a function of time
3. Surface finish results from machining experiments

Temperature Measurement Tests

Figures 6 and 7 show temperature data recorded during Ultramill operation driven with 400 V_{PP} at 1 KHz. Figure 6 shows data for the gravity-driven open-circulation configuration. The coolant flow rate varied between 0.30 and 0.40 L/min as adjustments were made to keep a constant liquid level in the sight glass. Figure 7 shows temperature data for the closed-circulation configuration with coolant flow maintained at approximately 0.40 L/min for the first part of the run, then reduced to a low flow rate of 0.16 L/min.

The top plot in each figure shows the temperature measured by a thermocouple on the piezoelectric actuator. The middle plots show the temperature of the Ultramill's solid steel base block, at a location on the centerline 10 mm behind the piezo stacks ("block core") and also at the end farthest away from the piezo stacks ("block end") where it attaches to the DTM. The bottom plots show the temperature of coolant at the inlet and outlet of the Ultramill cooling chamber.

With open-circulation cooling the indicated stack temperature is seen to fluctuate across a range of several degrees, with abrupt changes observed. In contrast, in Figure 7 the stack temperature for closed-circulation cooling is nearly constant when the coolant flow is 0.40 L/min. It is also at a lower temperature indicative of a larger convection heat transfer coefficient between the stack surfaces and the circulating coolant. At 0.40 L/min flow rate the indicated stack temperature actually fluctuates cyclically with a period of approximately 3.3 minutes and a 0.4˚C peak-to-peak magnitude. The coolant temperatures cycles practically in phase with the stack temperature, again with a period of about 3.3 minutes. This period is believed to reflect the natural frequency for the installed cooling system arrangement (i.e. the length and volume of the coolant hoses, Ultramill volume, and Thermocube heat rejection capability have a fundamental response characteristic). When the closed-circulation coolant rate is reduced to 0.16 L/min this cyclic behavior of the coolant temperature becomes more pronounced: the range of coolant

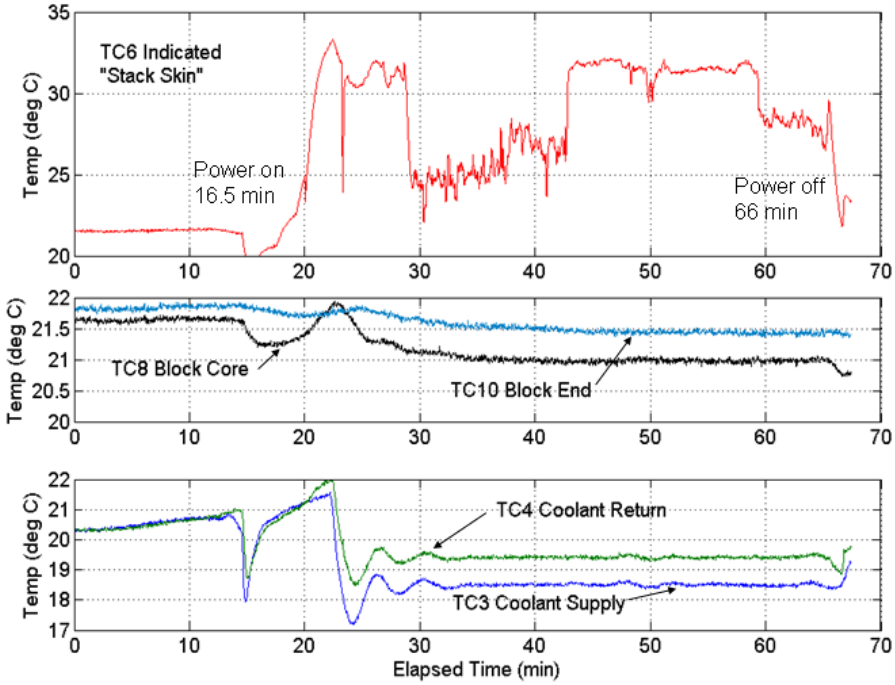

Figure 6. Ultramill temperatures during operation with open-circulation cooling configuration. Coolant flow varied from 0.30 to 0.40 L/min to maintain liquid level in the sight glass. "Block core temperature" is measured near the face of base block in contact with circulating coolant, and is therefore lower than at the "block end" which is adjacent to Y-axis.

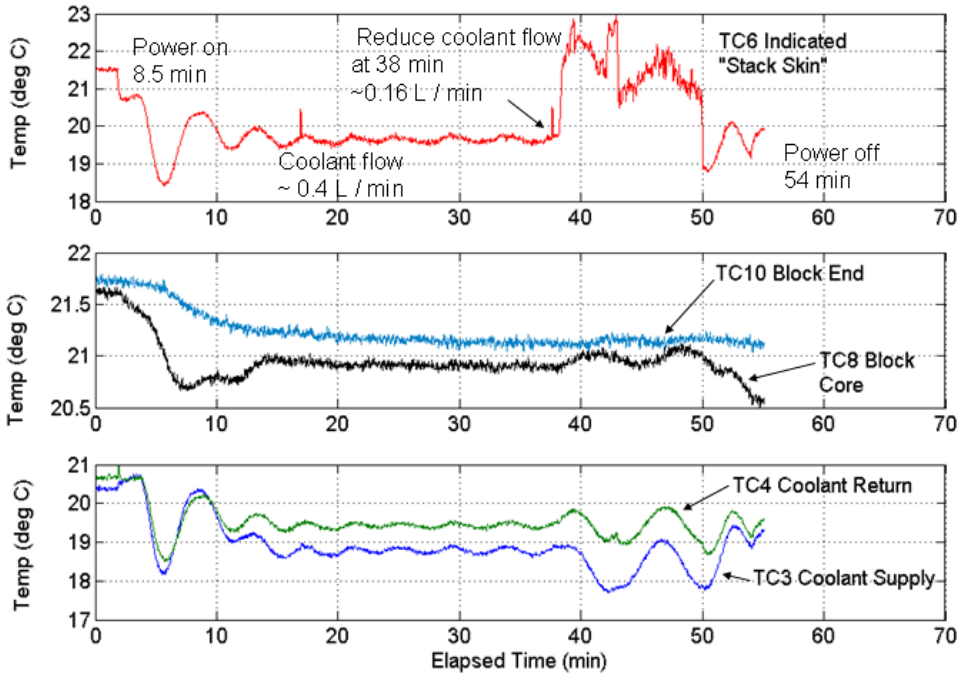

Figure 7. Ultramill temperatures for typical machining test using closed-circulation cooling. Coolant flow was reduced from 0.40 L / min to 0.16 L / min at elapsed time of 38 minutes.

temperature variation increases to 1.1 °C and the period grows to about 7 minutes. Although the indicated stack temperature at the smaller coolant rate still appears to be cyclic it also shows greater irregularity and a larger range of fluctuation. For the low flow case, the base block temperature can be seen to be varying cyclically at the same period as the stack and coolant temperatures, but with a noticeable phase lag. This indicates there is significant thermal interaction between the base block and the circulating coolant and also possibly with the actuator stacks. Temperature variation in the base block is undesirable since it is a source of thermal expansion/contraction in the depth of cut direction. These results show that a significant coolant flow rate of approximately 0.40 L/min is needed to maintain temperature stability in the Ultramill structure.

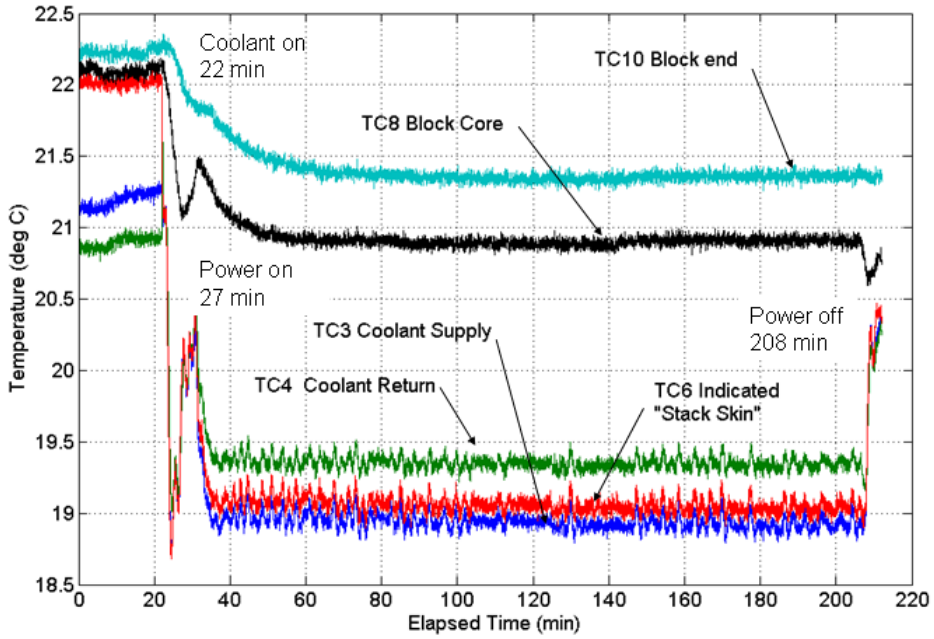

Figure 8. Ultramill temperature performance during a machining run of more than 2 hours duration, showing long-term temperature stability achieved using closed-circulation cooling.

Figure 8 shows Ultramill temperature data recorded during a 2.5-hour long machining run, for the closed-circulation configuration at a coolant rate of 0.40 L/min. After the Ultramill reached thermal equilibrium at approximately 50 minutes elapsed time, the temperature measured at all locations showed fluctuations of less than 0.4 ˚C, demonstrating the long-term temperature stability which can be achieved by the closed-circulation cooling mode.

Figure 9 presents the results of another significant temperature test. The Y-axis, to which the Ultramill is attached, is driven by a linear electric motor. At the start of the test in Figure 9 the Y-axis motor had been energized for several days. The motor was turned off and temperatures

of the Ultramill structural components decayed exponentially until they reached ambient room temperature after about 17 hours. The tool tip position changed by more than 1.5 μm as a result of thermal contraction by the Ultramill. The Y-axis motor was then reenergized and it can be seen that the Ultramill temperatures began to increase once more. This significant thermal interaction between the Y-axis and the Ultramill means there should be a delay of 18 to 24 hours after the Y-axis motor is powered up, to allow the Ultramill to achieve thermal and dimensional equilibrium before starting machining.

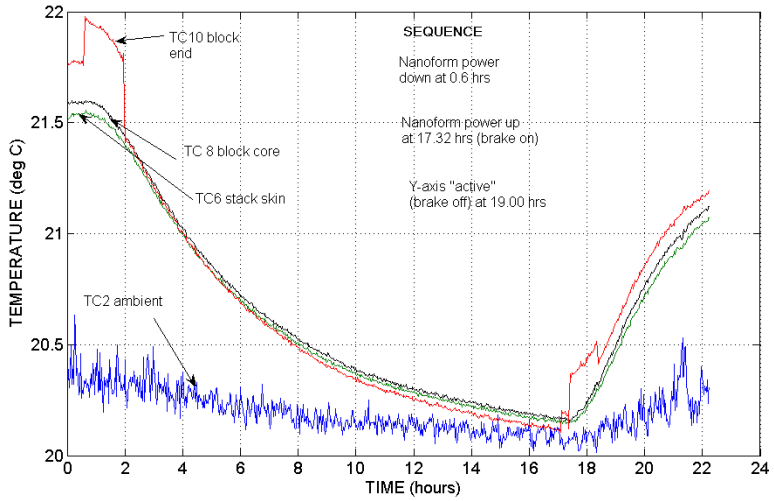

Figure 9. Ultramill temperature variation after shutdown and subsequent restart of Y-axis linear motor, confirming thermal interaction between the Ultramill and the Y-axis.

Capacitance Gauge Tests

For capacitance gauge measurement of variation in nominal tool-tip position caused by thermal expansion/contraction, the diamond tool was replaced by an aluminum target of approximately the same mass. The capacitance gauge was fixed to the X-axis of the diamond turning machine. The average distance between the target and the cap gage (after the elliptical vibration motion is removed) was used to track the toolholder position in the depth of cut direction as a function of time. Cap gauge testing has two advantages over cutting flats: 1) the test duration can be set independent of the part size and 2) the capacitance gauge data is continuous in time rather than compromised by the raster scan pattern that may partially obliterate one pass by subsequent crossfeed passes.

Figure 10 shows results for an open-circulation test of approximately 50 minutes duration. The top panel shows Ultramill temperatures including the stack temperature while the bottom panel shows the cap gauge target position relative to its location when the Ultramill is powered down.

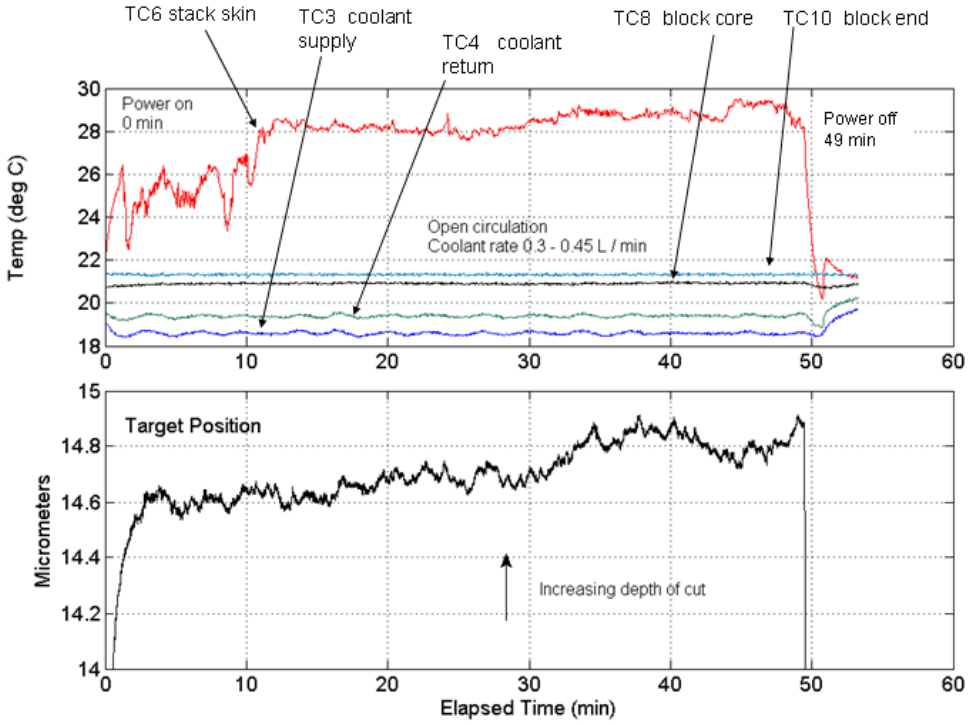

Figure 10. Capacitance gauge test for open-circulation cooling configuration.

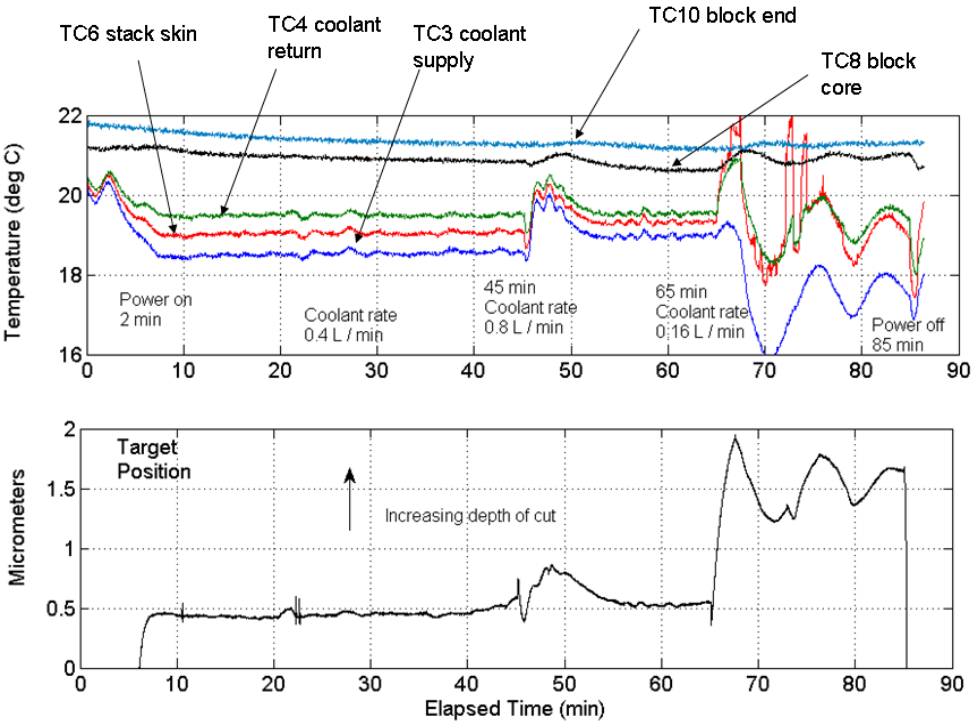

Figure 11. Capacitance gauge data for closed-circulation cooling test. Coolant flow rate was varied between three different level ranging from 0.16 to 0.80 L/min.

An increasing value for target position reflects motion toward the capacitance gauge probe, equivalent to thermal expansion of the tool in the direction of greater depth of cut. The stack temperature reached an approximate steady state at an elapsed time of approximately 12 minutes and then followed the stack temperature. The total expansion of the tool is on the order of 15 μm so it is essential that the system reach equilibrium before a cutting experiment is started.

Figure 11 shows results for a closed-circulation cooling test. In this test the coolant rate was initially the normal rate of 0.40 L/min, but was later changed to a high rate of 0.80 L/min and then reduced to a low rate of 0.16 L/min. The temperature and cap gauge position plots in Figure 11 show how the Thermocube takes several minutes to respond to a large change in coolant rate, with adverse effect on coolant and Ultramill structure temperatures, and consequently on tool tip position. Therefore coolant flow rate should be kept constant when using closed-circulation cooling.

Table 1 summarizes the variation in stack skin temperature and cap gauge target position for the tests shown in Figures 10 and 11. The PV and RMS variation in each case was based on the latter portion of each test segment, after steady-state was achieved following a change in conditions (e.g. application of power to the Ultramill, or change to coolant flow rate). In closed-circulation cooling, variation in stack temperature and cap gauge position both decrease with increasing coolant flow rate. At the normal (0.4 L/min) and high (0.8 L/min) flow rates the RMS cap gauge variation is smaller than for the open-circulation cooling configuration. This suggests that parts machined using closed-circulation cooling will have a smaller amount of form error caused by temperature variation.

Table 1. Temperature and Target Position Variation for Capacitance Gauge Tests.

Case	**Coolant Rate**	**Data Duration**	**Stack Skin Temperature Variation**		**Cap Gauge Position Variation**	
	L / min	min	°C PV	°C RMS	nm PV	nm RMS
Open circulation	0.30 to 0.45	25	1.64	0.36	323	74
Closed circulation "Low" flow	0.16	10	2.31	0.48	420	122
Closed circulation, "Normal" flow	0.40	25	0.32	0.05	324	48
Closed circulation "High" flow	0.80	10	0.31	0.05	98	21

Surface Figure Error

Flat features (1 mm long x 0.5 mm wide) were raster machined into a copper workpiece while collecting Ultramill temperature data. The flats required 100 passes and took 8.2 minutes each to machine. Three flats were cut using open-circulation cooling and 4 flats with closed-circulation cooling: two at the normal flow rate of 0.4 L/min for open-circulation cooling, one at 0.8 L/min and one at 0.16 L/min.

Figure 12 shows the area-based figure error for the flats against RMS variation in stack skin temperature. The figure error was determined for a rectangular area 0.5 mm long x 0.4 mm wide in the central region of the flat, using white-light interferometry to measure the surface. These figure error measurements are non-filtered and cover 80 crossfeed passes or approximately 6.5 minutes of machining time. Therefore they include the effect in the upfeed direction of the elliptical vibration machining process, as well as the effect of Ultramill temperature variations in both upfeed and crossfeed directions. Figure 12 shows that closed-circulation cooling did not improve area-based figure error in these flats. At the normal flow rate of 0.40 L/min the figure error was the same as for open-circulation cooling, although with closed-circulation cooling the temperature variation was much smaller. At a low flow rate of 0.16 L/min the figure error is twice as large as at 0.4 L/min and also for open-circulation cooling. This is due to the greater stack and coolant temperature variation leading to increased dimensional variation of the piezo stacks and base block. The figure error for high coolant flow (0.80 L/min) is also worse than at 0.40 L/min. This differs from the cap gauge results in Table 1 which showed that variation in tool tip position gets progressively smaller with increasing coolant flow. As described below the behavior of figure error in the closed-circulation rastered flats is caused by the surface roughness resulting from pump-induced pressure pulsations, which is believed to grow larger with increasing coolant flow. This offsets the reduction in thermal variation from increasing coolant flow seen in the cap gauge results.

Figure 13 shows area-based surface roughness for the flats. Each data point in the figure is the arithmetic average of 3 surface roughness measurements taken at random locations. The sample areas were .013 mm long x .017 mm wide. The surface roughness values were plotted against the same full-test stack temperature variations as in the figure error plot of Figure 12. In the crossfeed direction the sample areas include 4 successive cutting passes which span 15 seconds of machining In the upfeed direction the samples covered .013 sec. The short time covered by these surface roughness measurements mean they include the effects of the EVAM process and DTM dynamics but not the effect of long-period temperature variations. The results in Figure 13 generally follow the trend of the figure error results in Figure 12, except that the surface roughness values are 6-10 nm RMS smaller than the figure errors. Table 2 shows the difference between the figure error and surface roughness results, for the closed-circulation tests. This

difference between surface roughness and figure error is the magnitude of surface error caused by Ultramill thermal instability. A major difference between Figures 12 and 13 is the surface roughness for low coolant flow (0.16 L/min) is the same as that for normal coolant flow (0.4 L/min). This indicates that the error caused by temperature variation (i.e. difference between Figure 12 and Figure 13) is worse for 0.16 L /min than 0.40 L/min, consistent with the cap gauge results. The differences between Figures 12 and 13 also show that the temperature-induced variation at 0.80 L/min is smaller than at 0.40 L/min, again agreeing with the cap gauge results. The increase in surface roughness between 0.40 L/min and 0.80 L/min is believed to be caused by larger pressure pulsations at the higher coolant rate (10 psi compared to 7 psi at the normal flow rate) which increase the magnitude of Ultramill structural vibration.

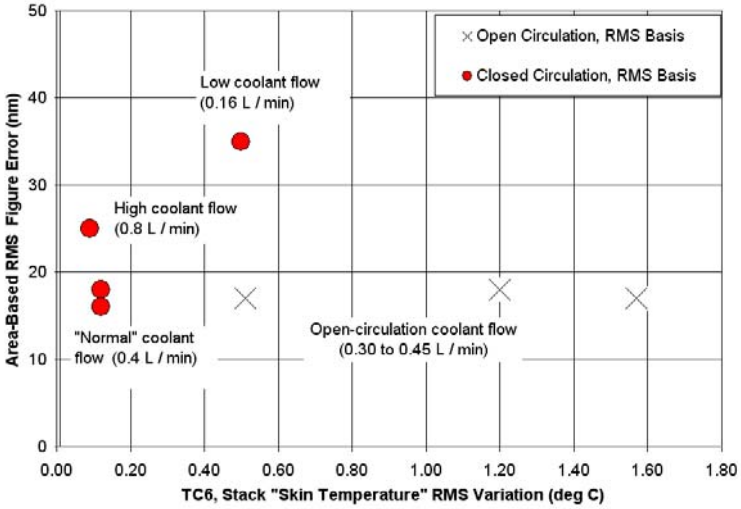

Figure 12. Figure error based on a 0.5 mm long x 0.4 mm wide area in the central region of the rastered flat.

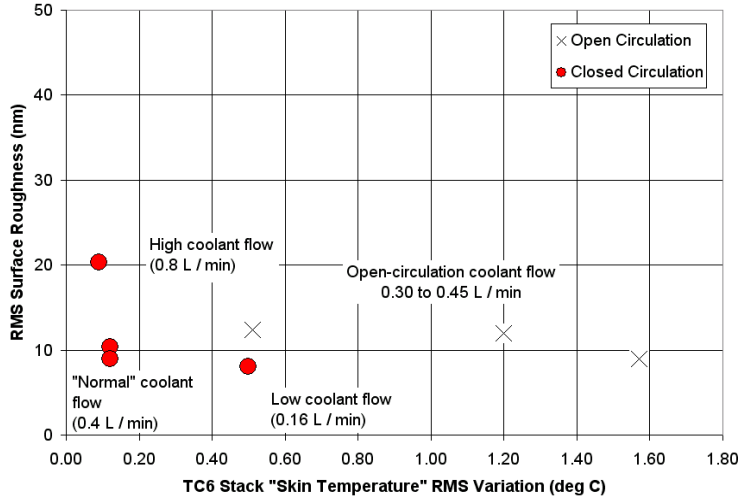

Figure 13. Surface roughness in rastered flats, for test area .013 mm long x .017 mm wide (each point is average of RMS surface roughness at three locations on the flat).

Table 2. Figure Error and Surface Roughness for Flats Cut with Closed-Circulation Cooling.

	Low Flow	**Normal Flow**	**High Flow**
Coolant flow (L/min)	0.16	0.40	0.80
Pressure variation (psi)	5.5	7	10
Area-based figure error[a] (nm RMS)	38	17	25
Surface roughness[b] (nm RMS)	8	10	21
Thermal-induced dimension variation[c] (nm RMS)	30	7	4
Cap gauge variation[d] (nm RMS)	122	48	21
[a] From Figure 12 [b] From Figure 13 [c] Roughness subtracted from figure error [d] From Table 1			

The cap gauge variations are of greater magnitude than those seen in the flats because successive crossfeed passes in raster machining can eliminate high features created during earlier cutting passes.

Figure 14 shows the improvement in form error that can be obtained by using closed-circulation cooling. The figure shows crossfeed profiles obtained by white-light interferometry for the "potato chip" feature shown in Figure 2. This part took approximately 80 minutes to machine, so the crossfeed profiles contain the effects of temperature-induced expansion / contraction of the Ultramill in the direction of depth-of-cut. Open-circulation cooling (left panel) shows considerable variation of up to 500 nm PV from the desired part profile. In contrast, this error is reduced to less than 80 nm PV when closed-circulation cooling is used (right panel).

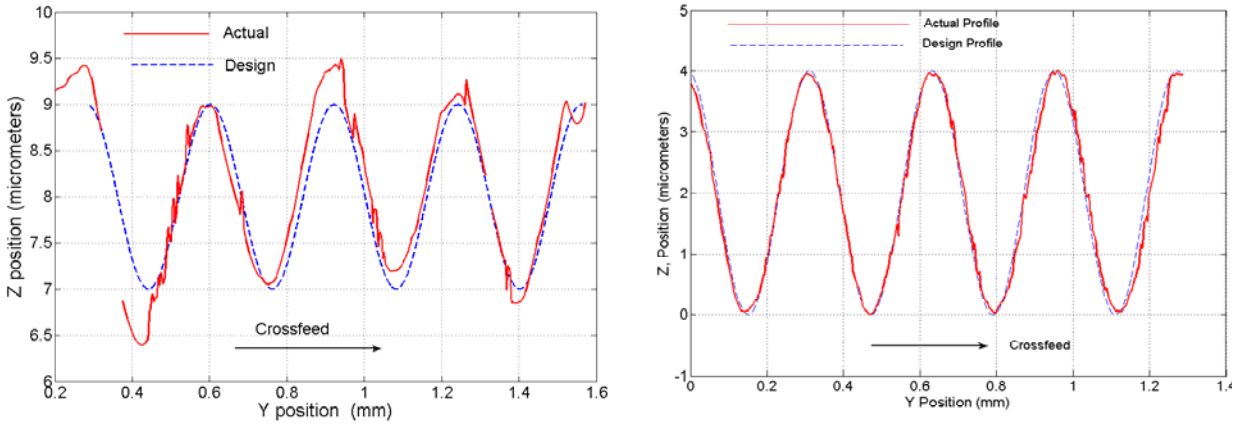

Figure 14. Crossfeed surface profiles for "potato chip" part shown in Figure 2. (*left*) Crossfeed profile for open-circulation cooling showing effects of Ultramill temperature variation. (*right*) Closed-circulation cooling nearly eliminates form error from Ultramill temperature instability.

6.4 SPHERICAL REFLECTOR

6.4.1 PART DESIGN AND FABRICATION

Concave spherical reflectors were machined to identify possible sources of surface error, before using EVAM to make more complex parts. Form error on these parts was easily measured using the PEC's Zygo GPI interferometer (Fizeau interferometer) using a spherical element.

Figure 15 is a MATLAB representation of the design surface. The concave reflector has an aperture diameter of 1.5 mm and a radius of curvature of 4.5 mm, with a maximum sag of 63 µm (depth aspect ratio=0.042). The aperture diameter is a convenient size for imaging with the Zygo GPI interferometer. Once the aperture was selected, the radius of curvature was calculated to assure that maximum downward angle of the surface was smaller than the tool's clearance angle so that the tool flank face would not impact the machined surface.

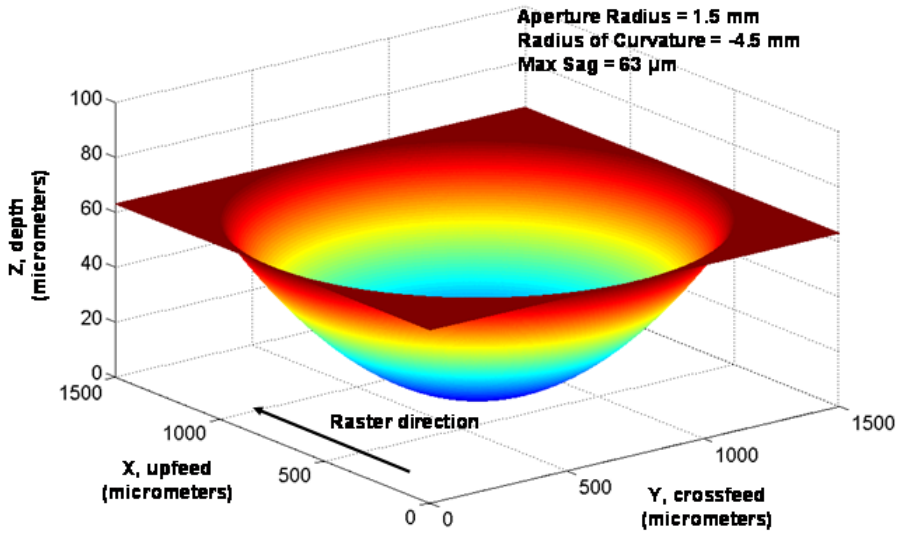

Figure 15. Design dimensions of spherical reflector made by the Ultramill

Several spherical reflectors were machined in hard-plated copper using a1 mm radius round-nosed diamond tool with 0° degree rake angle and 10° degree clearance angle. The toolpath vibration ellipse had nominal dimensions of 22 µm x 4 µm estimated from Ultramill operating conditions of 1000 Hz frequency and 400 $V_{P\text{-}P}$. Maximum programmed upfeed velocity was 200 µm/s. Spacing between individual crossfeed passes was 10 µm, so that 150 raster passes were needed to cover the width of the part. The desired curved profile in the upfeed direction was approximated by blended linear axis moves with a minimum segment length of 10 µm. Along the upfeed centerline there were 50 segments in the upfeed direction, reduced to 2 at the edges. The final required part depth of 63 µm was achieved by six successive roughing cuts

each with a nominal depth of cut of 7 to 11 μm, followed by a final finish cut of 1 μm. To reduce machining time, only the raster passes around the centerline were executed during the first few roughing cuts. Total machining time was initially 68 minutes increasing to 74 minutes after modifying the machining strategy to correct an error caused by Z-axis friction, as described in the next section.

6.4.2 METROLOGY RESULTS

Figure 16 shows part surface error measurements made using the GPI interferometer for two spherical reflectors. Figure 16(a) shows the first part to be machined, while Figure 16(b) is the last part which includes corrective measures for errors discovered in the first part. The interferograms show the departure of the surface from the concave design radius of curvature of 4.5 mm. The initial part had a figure error of 124 nm RMS while on the final part this was reduced to 62 nm RMS.

The first spherical surface machined contained two major errors assignable to the 3-axis diamond turning machine (DTM). The first is astigmatism, which was determined to be due to a squareness error between the DTM's X and Y axes estimated at .004 radians. This was corrected in the motion program by offsetting the programmed starting point of each raster (upfeed) pass from the preceding one. This brought the actual starting point of the tool to the correct location on the part. The corrected part still includes a small amount of astigmatism which may be due to squareness error between the DTM's X and Z axes.

The second major error was a "trench" perpendicular to the upfeed tool motion, bisecting the part at the bottom of the spherical radius. This was caused by friction in the Z-axis ballscrew nut [5] when the Z-axis reverses direction at the bottom of the concave tool path. As shown in the top portion of Figure 17, this friction causes a delay in the start of Z-axis upward motion. The X-axis motion at the bottom of the part is unaffected, so that the actual tool path deviates from the programmed path. To reduce this effect the programmed X-axis velocity was reduced for the movement segment immediately after the point of Z-axis reversal (bottom panel of Figure 17). This allows the Z-axis to "catch up" with the X-axis so that the combined axes motion conforms approximately to the desired toolpath. Figure 18 shows surface profiles in the upfeed direction at the bottom of the reflector, obtained using the New View white light interferometer at high power to give a narrow field of view. These profiles show that slowing the X-axis down during Z-axis reversal reduces the "trench" error from 350 nm PV to 120 nm PV.

Both surface profiles in Figure 18 show periodic features with a peak-to-valley height of 80-100 nm. The spatial frequency of these features corresponds to a time-based frequency of approximately 30 Hz, the same as the diaphragm pump used to circulate the dielectric coolant

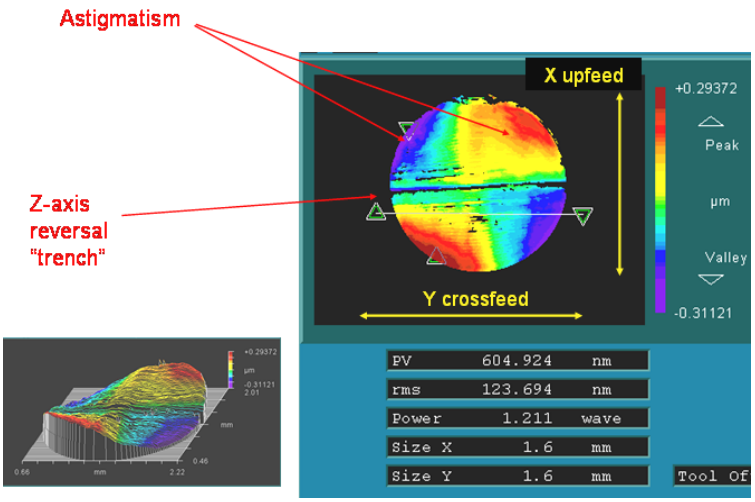

(a) First spherical reflector to be machined, containing astigmatism and crossfeed "trench" errors. Form error is 124 nm RMS .

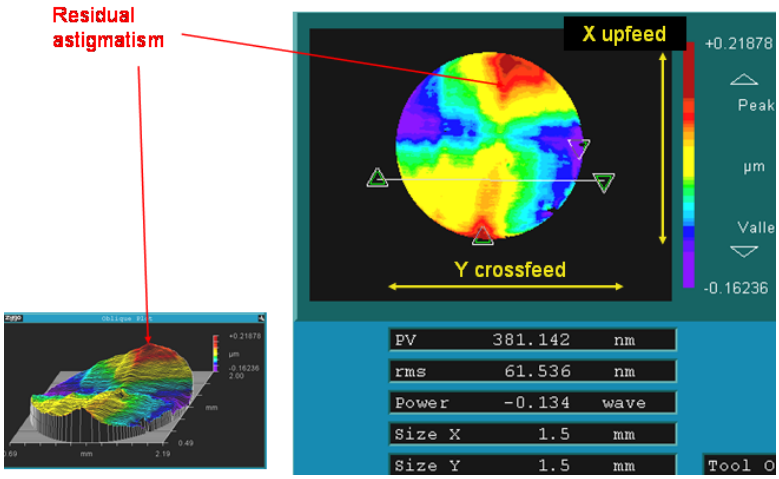

(b) Final spherical reflector, with form error reduced to 62 nm RMS. Residual astigmatism is believed to be from X-Z axis squareness error.

Figure 16. GPI interferograms of spherical reflectors made with the Ultramill. The plots show deviation of the surface from the design radius of curvature (-4.5 mm). .

fluid through the Ultramill. The local surface roughness also was measured at several points on the reflectors using white light interferometery at a narrow field of view, which allowed surface data to be obtained on steep surface slopes. The average surface roughness was 21-23 nm RMS. These results confirm one of the important conclusions of the temperature stability study in Section 6.3, that closed-circulation cooling minimizes figure error caused by Ultramill temperature variations but that the diaphragm pump-pressure pulsation limits the quality of the achievable surface.

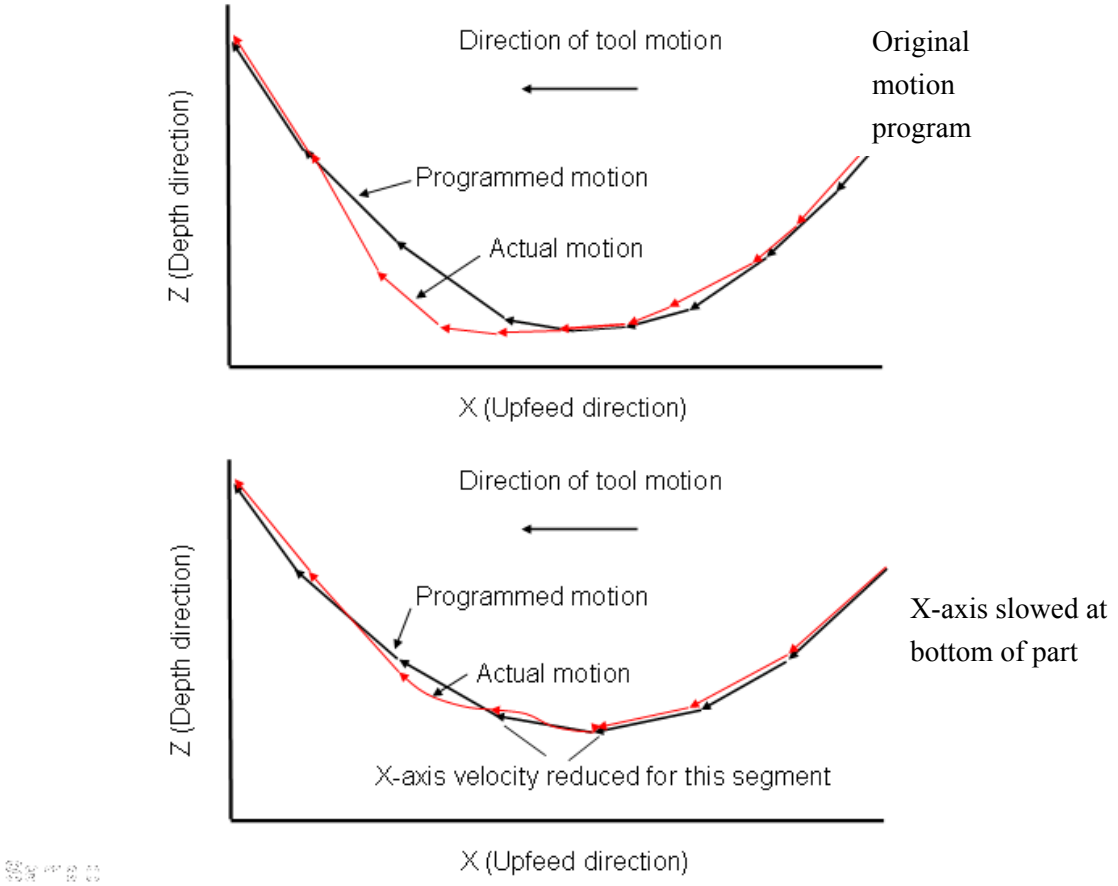

Figure 17. Preventing crossfeed trench at base of concave part. (Top) Stiction in Z-axis ballscrew nut during reversal of direction causes it to lag behind X-axis at bottom of part (Bottom) Slowing down X-axis after Z-axis reversal keeps the two axes synchronized.

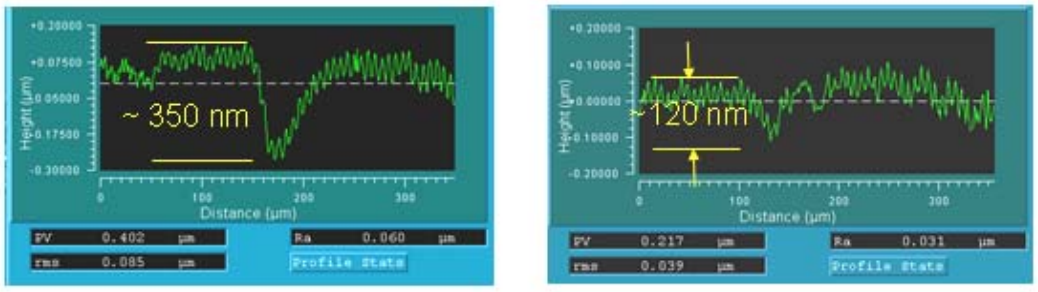

Original motion program

After slowing down X-axis at bottom of profile

Figure 18. White light interferometry profiles at bottom of the concave reflector (best-fit sphere removed). *Left* Effect of Z-axis stiction on machined surface *Right* Suppression of "trench" feature by slowing down X-axis at reversal point. High-frequency features in profiles are caused by Ultramill vibration due to pressure pulsations with closed-circulation cooling.

6.5 FIBER OPTIC BEAM SPLITTER

6.5.1 BACKGROUND

Fiber-optic systems frequently require dividing an input signal into multiple outputs. A simple splitter can be made by fusing branch fibers to an input fiber. This fused splitter is simple to fabricate but has large losses, typically greater than 3 dB attenuation (50% loss) between the input and total of the branch signals. A "free space" splitter as shown in Figure 19 typically has a loss of only 0.15 dB (1.7% loss). It uses a refracting element (ball lenses in Figure19) to collimate the diverging beam from the source fiber ahead of the splitter element. Additional refracting elements are used to couple the branch beams into the receiving fibers. These coupling elements are needed because fiber optics work by repeated total internal reflection, so that light rays that fall outside the fiber's angle of acceptance are not admitted. Beam divergence exiting the fiber is also caused by total internal reflection in the fiber.

Figure 20 shows a new beamsplitter concept, in which the Ultramill is used to fabricate a focusing mirror with complex 3-D geometry that performs both division of the source beam and coupling the branch beams into the receiving fibers.[1] In a 1-to-2 splitter, the mirror replaces 4 optical components used in the existing concept (3 lenses and the splitter). Similarly the number of critical dimensional relationships between components is reduced from 6 to 3. A final advantage of the concept is that EVAM can be used to precision machine a replication master in a material such as steel. Reflectors can then be mass-produced by injection molding, then coated to create a mirror surface.

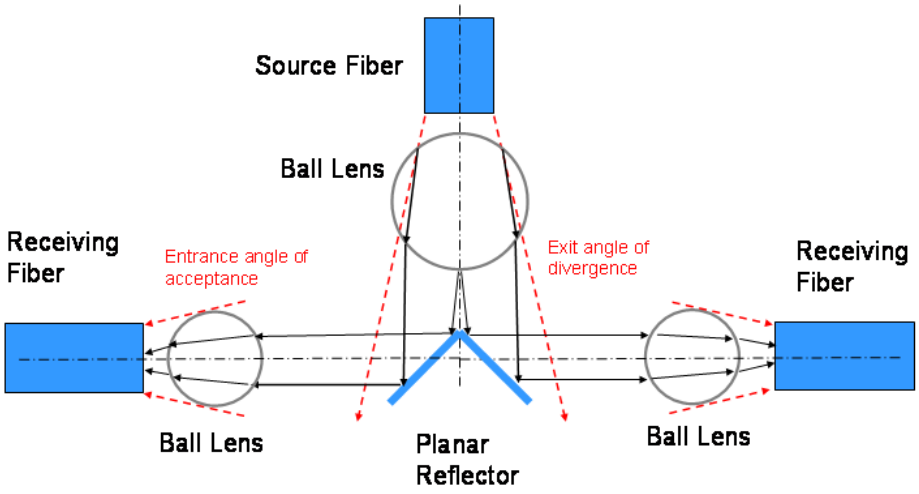

Figure 19. Conventional low-loss free space beam splitter, using ball lenses to collimate source beam and couple branch beams into receiving fibers.

[1] The reflecting beam splitter project was suggested by T. F. Bifano of Boston University.

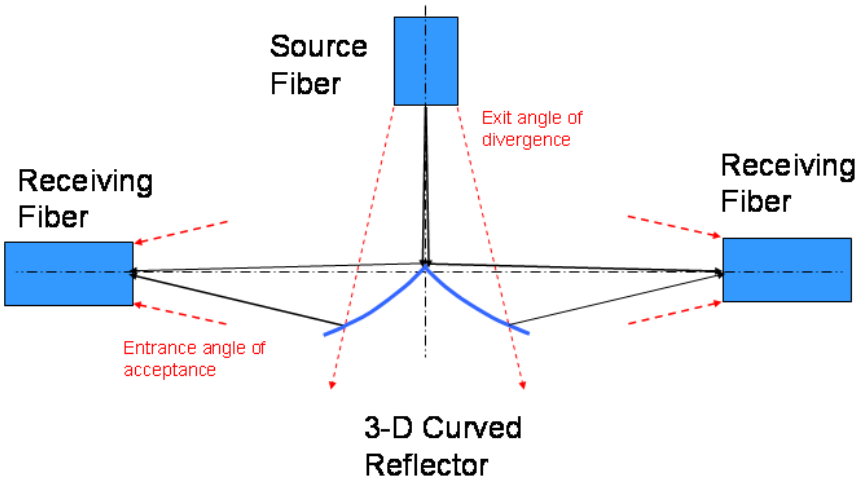

Figure 20. New concept beam splitter replaces the ball lenses with a curved 3-D reflector, made using EVAM

6.5.2 TEST PART DESIGN AND FABRICATION

The Ultramill was used to fabricate a reflecting beam-bender to demonstrate its ability to make complex 3-D optical surfaces. Figure 21 shows development of the design for the test reflector. An elliptical surface is used since all rays emanating from one focus of the ellipse will be reflected through the other focus. The actual surface is formed by revolving the elliptical cross section about its major axis.

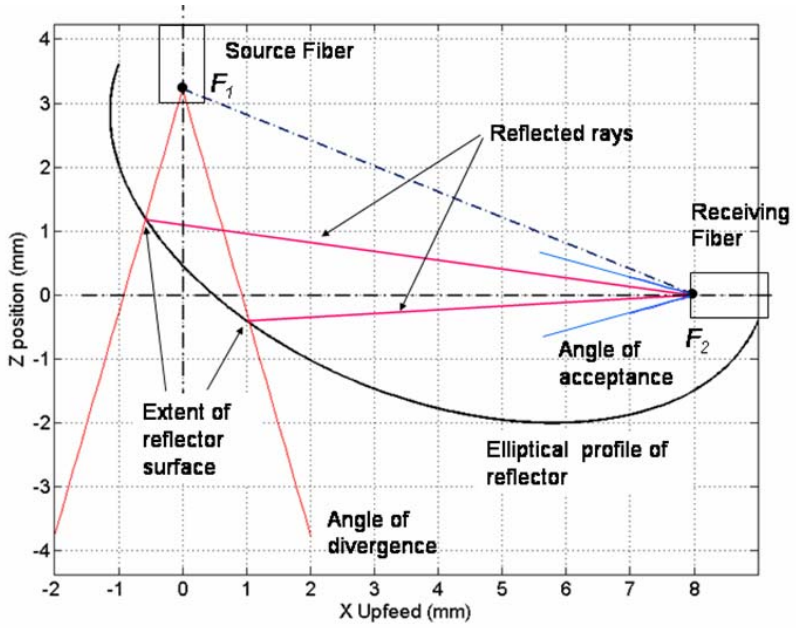

Figure 21. Design of test reflector fabricated with the Ultramill.

The test reflector is designed around a commercially-available optical fiber[2] with an active diameter of 0.062 mm and 32˚ acceptance angle as shown in Figure 21. The elliptical cross section has semi-major axis A = 5.388 mm and semi-minor axis B = 3.23 mm. The figure shows light originating at one focus F_1 behind the exit plane of the source fiber, emanating over the entire divergence angle, and being brought to the other focus F_2 at the entrance plane of the receiving fiber. To fabricate a beam splitter, only the indicated portion of the elliptical profile is needed, extending from the source fiber's centerline to the intercept point of the ray at the divergence half-angle with the ellipse. The required surface makes a circular curve into the plane of the paper, with maximum radius of 3.23 mm.

The Ultramill was used to machine the test reflector in 6061-T6 aluminum. The round-nosed diamond tool had a 1 mm nose radius, 0° degree rake angle and 10° degree clearance angle. In the upfeed direction the surface was extended by 100 µm beyond either end of the source ray intercepts on Figure 21. Figure 22 shows how the surface was tilted in the workholder so that the long axis of the part was brought parallel to the nominal upfeed direction of the tool. This orientation kept the maximum surface angles in the upfeed direction to less than 10 degrees, similar to those used on the spherical surfaces made in Section 6.4. Overall size of the part was 2.51 mm x 1.70 mm. The motion program included the offset calculation derived for the spherical reflector in Section 6.4 to prevent astigmatism. X-axis velocity was slowed down in the region where Z-axis reversal takes place. A crossfeed spacing of 10 µm was used with 170 crossfeed raster passes needed. In the depth direction, nine roughing cuts each of depth 10 to 15 µm were used for bulk material removal followed by a finish cut at 1.4 µm depth to create the final surface. To reduce machining time, only the raster passes around the centerline were executed during the first few roughing cuts. Machining time for the part was 121 minutes, with the finish cut taking 30 minutes.

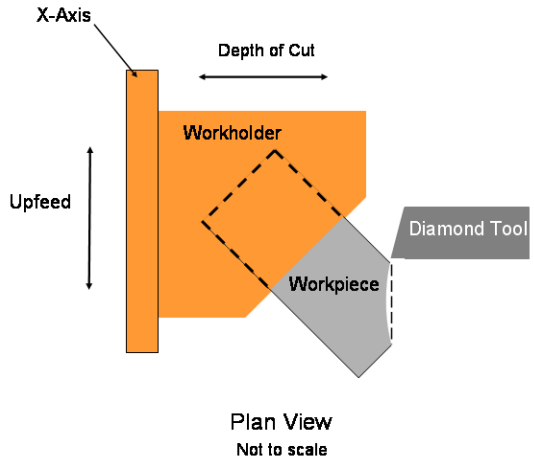

Figure 22. Machining setup for the ellipsoidal test reflector.

[2] Corning "Infini-Cor"®

6.5.3 PERFORMANCE TEST

Figure 23 is a schematic of the test setup used to measure the performance of the test reflector while Figure 24 is a photograph showing the fiber orientation relative to the reflector. A microscope objective was used to couple the beam from a visible-light laser (λ = 632 nm) into the source fiber. The reflector element was used to bend the divergent beam from the source fiber through a right angle while simultaneously coupling it into the receiving fiber. The output from the receiving fiber was measured by a silicon detector optical power meter.

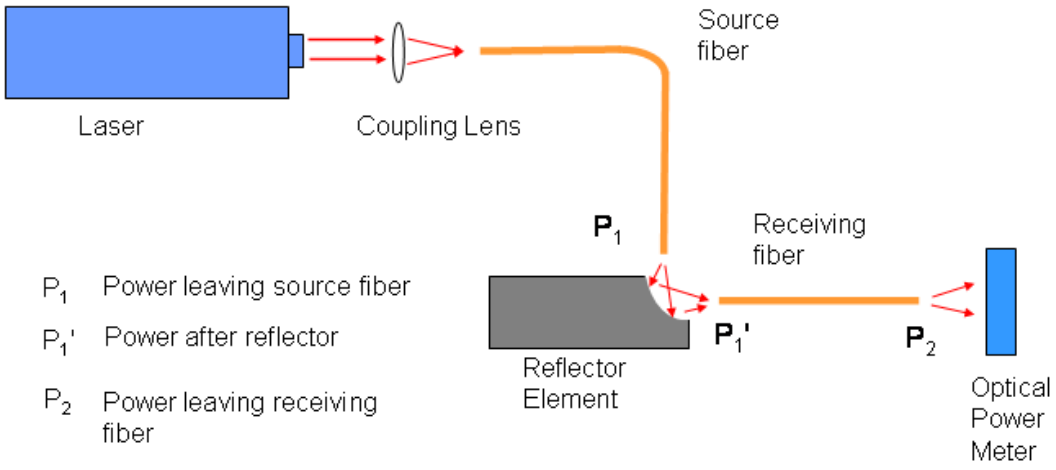

Figure 23. Schematic of setup for performance test of the ellipsoidal reflector.

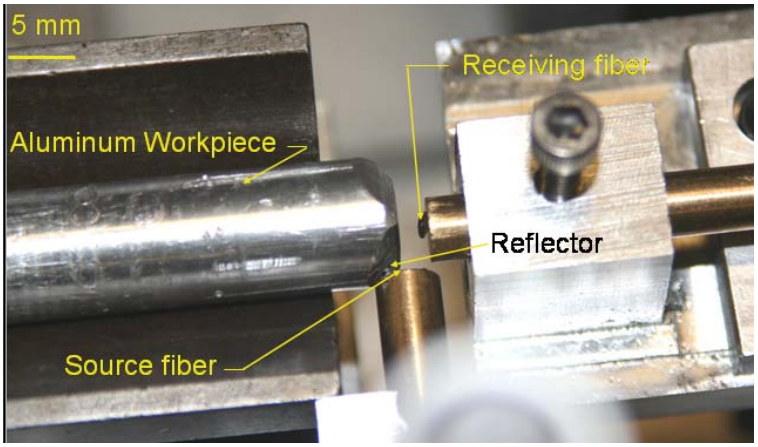

Figure 24. Photograph of beam bender reflector in test setup, showing orientation of reflector, source, and receiving fibers. Optical fibers are held within brass fiber chucks.

The reflecting efficiency E_{REFL} of the reflector is a measure of the incident light that is reflected without regard for focus or optical quality of the image:

$$E_{REFL} = \frac{P_1'}{P_1} \tag{1}$$

where P_1 is the optical power leaving the source fiber and P_1' is the optical power measured after the reflector element. The coupling efficiency E_{CPLG} measures the fraction of the power delivered by the source fiber that leaves the receiving fiber. It is the principal measure of performance for the reflecting system and is given by

$$E_{CPLG} = \frac{P_2}{P_1} \tag{2}$$

where P_1 is as in Equation 1 and P_2 is the power of the beam leaving the receiving fiber. Power readings were made with the silicon detector approximately 8 mm from the fiber end to standardize measurements.

The power emanating from the source fiber was measured by moving the reflector clear of the test setup and projecting the beam directly onto the silicon detector. The average of three tests gave a source beam power (P_1) of approximately 140 μW. The reflector was then placed back into the test set up and the silicon detector used to measure the reflected power from the mirror (P_1'). This gave a three-test average of 122 μW. The reflecting efficiency E_{REFL} for the test part was therefore 87%, compared to a theoretical reflectance for aluminum of 91% at the laser source's wavelength [6].

However when the receiving fiber was installed the output from it (P_2) did not exceed 1.5 μW giving a coupling efficiency E_{CPLG} of approximately 1%. It is not yet known whether this poor performance is caused by limited resolution in the translation stages used to position the fibers relative to the test reflector, or if it is from design or manufacturing errors. The test setup will be evaluated in detail to achieve a more precise positioning of the fibers relative to the reflector. This could include using a collimated source, directed through pinholes, to achieve proper angular alignment of the reflector before using the diverging beam from the source fiber.

6.5.4 METROLOGY

Only limited metrology methods are available for a part such as the ellipsoidal reflector. It can not be measured using the Fizeu-type Zygo GPI interferometer due to its off-axis, aspherical form. White-light interferometry is of limited value because the low-power wide-angle view

required by the large part size results in loss of data over much of the surface due to steep slopes. White-light interferometer data can be obtained from steep surfaces by imaging a narrow region of the part at high power, but this requires stitching multiple data sets together to enable visualization of the entire reflector. Another way to measure the form of the test reflector is by collecting multiple parallel profiles at known crossfeed spacing using the Talysurf contact profilometer. The best-fit ellipsoidal surface for this data set will be determined and which will then be compared to the design surface to assess form error of the test reflector.

Figure 25 shows a single profile along the upfeed direction obtained from the test reflector using the Talysurf. This profile was located near the part centerline, based on visual positioning of the profilometer's stylus. The measured profile is superimposed on the design profile at the part centerline. As there were no reference marks on the part or features suitable for fiducials the alignment between these two profiles is arbitrary. In fact the greater vertical extent of the "design profile" shown in the figure suggests the Talysurf measurement was made at some distance up the shoulder of the surface, away from the centerline in the crossfeed direction. As a result quantitative assessment of the deviation between the design and machined surface is not possible. Except for the divergence on the upfeed side, the machined profile appears to be approximately of the correct shape.

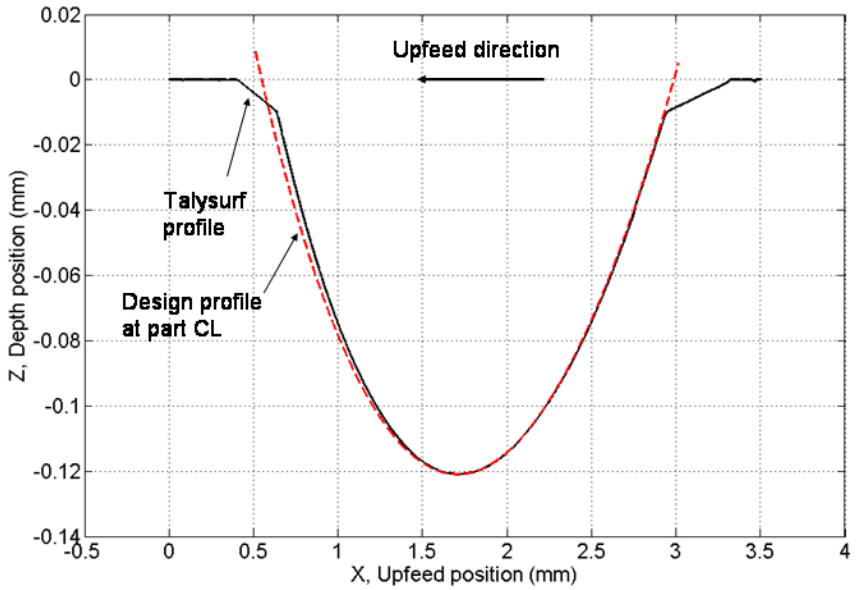

Figure 25. Profile obtained with Talysurf superimposed on design profile at centerline of the test reflector part.

6.6 CONCLUSIONS

1. Open and closed circulation schemes have been studied on the Ultramill. The conclusions were:

- Closed-circulation cooling provides greater stack and coolant temperature stability when the coolant flow rate is maintained at approximately 0.4 L / min or greater.
- Closed-circulation cooling does not change the best-case form error compared to open-circulation, but greater consistency is obtained compared to open-circulation cooling.
- The Thermocube cooler was tuned for a flow rate of 0.4 L/min and that appears to be a reasonable flow rate for cooling the piezoelectric stacks.
- Pressure pulsations from the Thermocube's diaphragm pump limit the surface roughness to approximately 20 nm RMS. The available gear-pump variant might lead to improved surface finishes because it has smaller pressure pulsations at a higher frequency.

2. Millimeter-scale concave reflecting surface with spherical form have been machined by the Ultramill to measure the form errors present. Several surfaces were machined and errors removed on successive parts, reducing the figure error to 62 nm RMS.

- Astigmatism in the first part machined was traced to squareness error in the diamond turning machine's X and Y axes. It was successfully compensated for in the machining program on subsequent parts.
- Friction between the ballscrew and nut causes the Z-axis to lag behind the X-axis when the Z-axis reverses direction at the bottom of the concave part. Slowing down the X-axis at the point of Z-axis reversal was demonstrated to be effective in minimizing errors caused by this characteristic of ballscrew-driven axes.

3. A fiber optic beam splitter been designed which features ellipsoidal reflecting surfaces to be machined using the Ultramill. This concept eliminates additional refracting elements, such as ball lenses, used by existing beam splitter concepts for collimation.

- A test part for a beam bender was fabricated in 6061-T6 aluminum.
- 87 percent of the light incident from the source beam was reflected by the test surface (vs 91 percent reflectivity of aluminum) but the coupling efficiency through the receiving fiber is only 1 percent.
- The reflector geometry limits the available metrology methods. A best-fit ellipsoid based on multiple Talysurf profiles of the test part surface is in progress. A single profile shows approximately the correct surface when compared to the design profile along the part centerline.

6.7 ACKNOWLEDGEMENTS

Primary funding for this work was by National Science Foundation grant DMI-433215 monitored by G. Hazelrigg. Panasonic Boston Laboratory funded the Ultramill thermal stability study. Chardon Tools supplied the diamond tools used in machining experiments.

REFERENCES

1. Brehl, D.E., Dow, T.A., *3-D Microstructure Fabrication Using Elliptical Vibration-Assisted Machining.* Proceedings of the American Society for Precision Engineering, 40, pp.21-25, (2007)
2. Brocato, B.C., Dow, T.A., Sohn, A., *Micro-machining Using Elliptical Vibration Assisted Machining.* Proceedings of the American Society for Precision Engineering, 34, pp.81-85 (2004)
3. Brehl, D.E., Dow, T.A., *Stainless Steel Machining with Vibration-Assisted Diamond Turning*. PEC final report to Sandia National Laboratories (1995)
4. Brehl, D.E., Dow, T.A., *Elliptical Vibration-Assisted Machining.* PEC Annual Report, 24, pp. 149-174 (2007)
5. Cuttino, J. F., *Identification and Compensation of Nonlinear Effects in Precision Actuator Systems.* Ph.D. dissertation, North Carolina State University (1994)
6. Walker, B.H., *Optical Engineering Fundamentals.* R.R. Donnelly & Sons, p.165 (1994)

7 AUTOMATIC MACHINING PROCESS FOR THIN-WALLED HEMISPHERIC SHELLS

Stephen Furst
Graduate Student
Thomas A. Dow
Dean F. Duncan Distinguished Professor
Department of Mechanical and Aerospace Engineering
Kenneth Garrard, Alex Sohn
Precision Engineering Center Staff

At present, the machining of precision hemispheric shells requires substantial human effort. An operator must align a roughly machined shell on the chuck of a diamond turning lathe, where one of the diameters (inner or outer) can be finished. The operator must then transfer the shell to an opposing chuck so that the other diameter can be finished. If the shell is not perfectly centered on the second chuck after transfer, the inner and outer diameters will not be concentric and the resulting hemishell will have a non-uniform wall thickness. This report describes a process that will automate the measurement and transfer of a thin walled hemishell, eliminating the need for human intervention. A complete part measurement and transfer is demonstrated. Measurement errors are tracked through the whole procedure to ensure that the necessary tolerances are maintained. Future work will measure any run-out that may have occurred during the transfer process and automatically realign the part on the second chuck. The entire process will allow a human to place a roughly machined part on either chuck, and then stand by as the machine automatically aligns, machines, measures, transfers, and realigns a complete hemisphere with a tolerance of 3 µm.

7.1 INTRODUCTION

A significant issue in manufacturing thin-walled hemispherical shells is the uniformity of shell thickness after machining. Diamond turning lathes routinely produce spherical parts with form accuracy of 50 nm; however machining both the inner and outer diameters of a shell to a concentricity of 3 µm is a significant challenge. Transfer of the part between fixtures designed for machining the convex outer contour (OC) and concave inner contour (IC) typically requires manual intervention by a skilled operator. One of the surfaces must be machined to its final shape and finish first. That surface is thus at risk of being damaged during the transfer, alignment and machining of the other surface. Eliminating manual part transfer and alignment operations can reduce the likelihood of damaging the part and result in significant cost savings and improved part accuracy.

Figure 1 shows a hemishell on a vacuum chuck designed for OC diamond turning. Figure 1 also shows a probe, which is used to locate the part and surfaces so that the transfer can be completed without human intervention. The goal of this project is to provide industry partners with the capability to produce a full hemispheric shell with concentric IC and OC of the correct radii using new agile, multi-function machining centers (e.g., Mazak Integrex series). The sponsor of this project, BWXT-Y12, is particularly interested in implementing these capabilities.

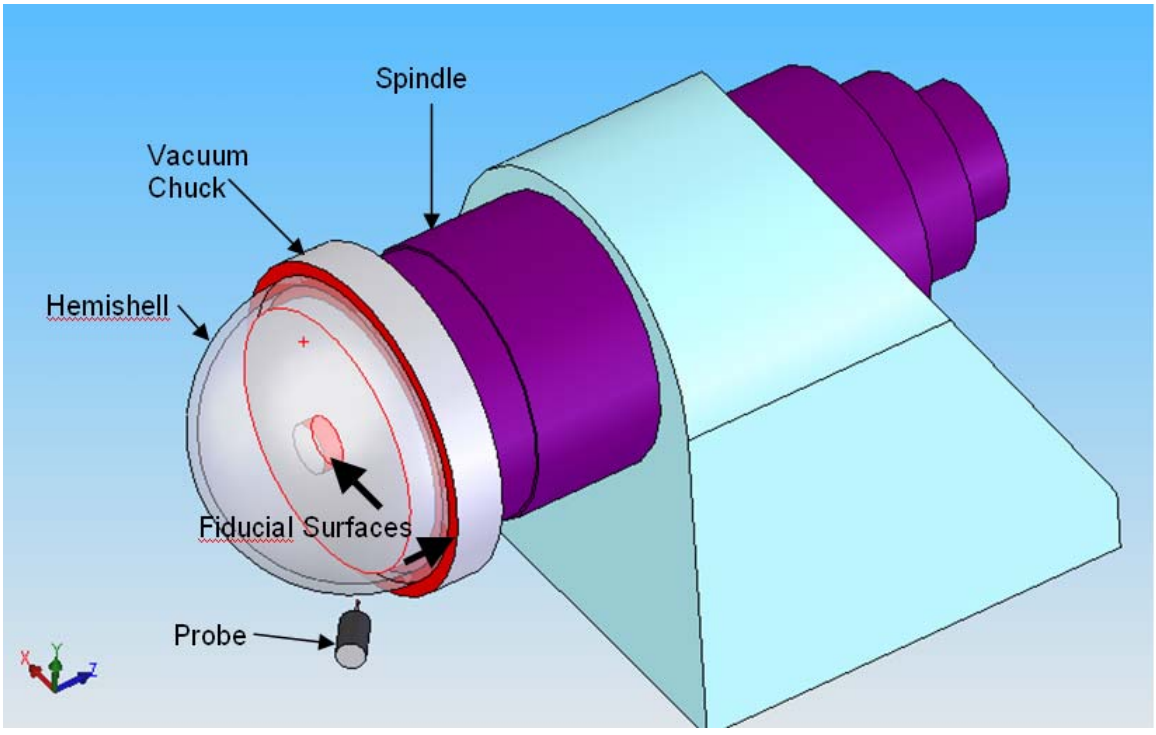

Figure 1: Hemishell on Vacuum Chuck for Diamond Turning

This report includes a summary of the results obtained during the first phase of this project. A transfer procedure has been developed in the context of the PEC machining system. The machining setup at the PEC differs from that at BWXT-Y12, so some of the steps required at the PEC will not be necessary when the process is implemented on BWXT-Y12 machining centers. The transfer procedure describes the steps necessary to measure a part then transfer the part from one chuck to another. The necessary probes have been selected in accordance with the measurements required. Also, an analysis of the probe error sources is provided. The most substantial prior work relevant to this project relates to the characterization of the errors sources in the probes selected [1-3]. The relevant errors are placed into the context of the transfer procedure, so that the transfer move can be made with a known confidence. Errors are reported according to the industry standards [4].

Literature searches have made it apparent that work on an automated shell transfer procedure has not been published before. This report presents the results of the first phase of the project—the sensor selection and the initial transfer procedure. Misalignment, called radial run-out, may occur during the initial transfer due to slipping at the moment the vacuum force is transferred. However, run-out measurement and radial re-alignment will be addressed in future studies.

7.2 PROBE SELECTION

To be able to move a part on a machining setup without human intervention, it is necessary to locate the vital components with probing sensors. For example, the transfer of a thin-walled hemishell from one holding fixture (chuck) to another requires that the positions of both fixtures and the hemishell be known in the same coordinate system. Those positions are determined with probing sensors. Since it is cost efficient to use as few probes as possible in the project, it was also necessary to look ahead to consider the post-transfer run-out measurements.

The sections below describe how a number of sensing probes work. Capacitance gages, LVDT's, and touch probes are considered based on their strengths and weaknesses.

7.2.1 OVERVIEW OF SELECTED PROBES

Each of the probes discussed below can be employed in certain aspects of phase one or this project.

Capacitance Gages

Capacitance gages are ideally suited for non-contact measurements such as spindle run-out. They are available in a number of different geometries as shown in Figure 2. The probes are made with straight and right-angle cabling with different gage areas, stand off distances and sensitivities. Each probe can only measure displacements in one direction.

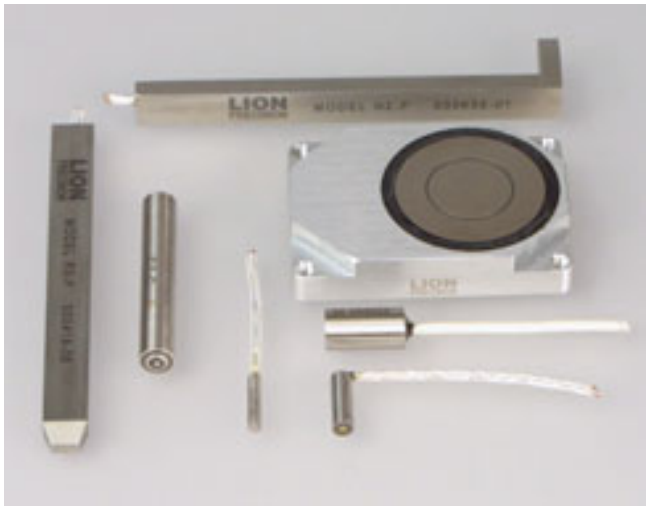

Figure 2: Lion Capacitance Probe Geometries

These probes can also be put together into a cluster so that different directions of interest can be measured. The 5-gage system shown in Figure 3 would cost about $1000 per probe plus $12,900 for the driver box for 5 probes.

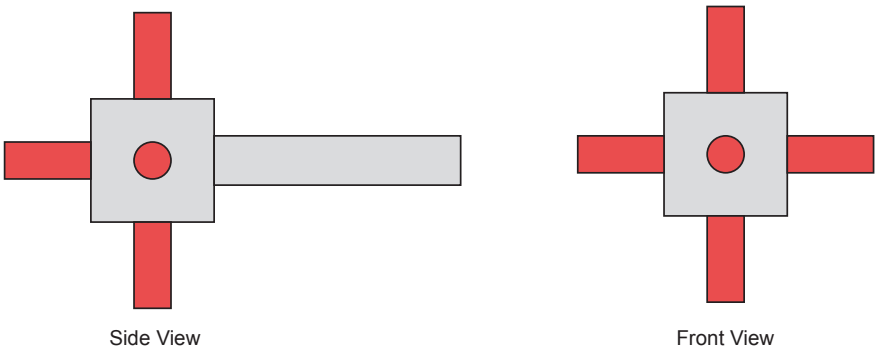

Figure 3: Capacitance Gage Cluster

Another capacitance gage geometry that could be used is a single probe with a spherical end, shown in Figure 4. The cost would be double that of a standard probe ($2000) and, with a single probe driver, the system would cost about $3500. The probe could have a guard ring to drive the probe at the outside and eliminate the capacitance between the conductors.

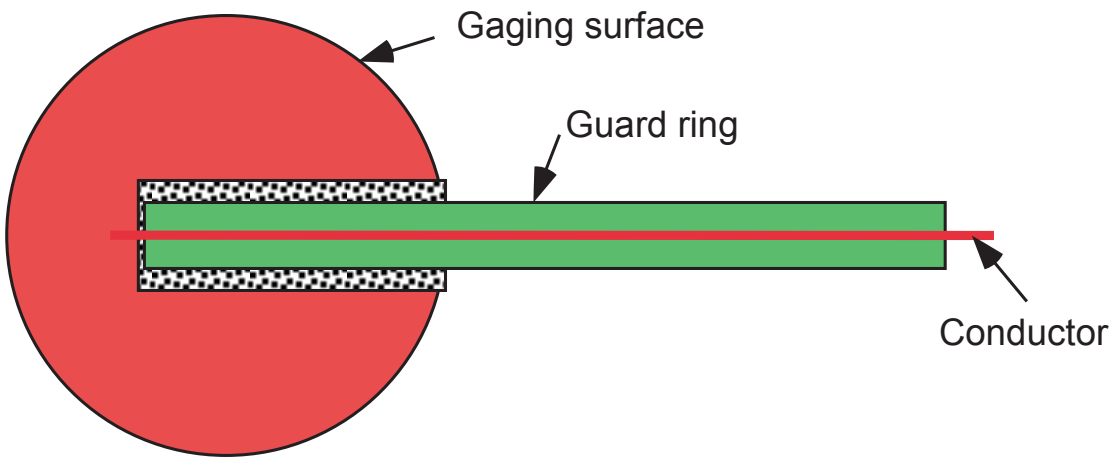

Figure 4: Ball End Cap. Gage for Measuring in Different Directions

This probe could then be used to measure the proximity of a conductor in any orientation but finding a relationship between the location of the part and the probe would be difficult and was deemed infeasible for this project.

LVDT

Linear Variable Differential Transformers have been used extensively to measure run-out for centering parts on spindles and measuring the shape of machined components. They come in a variety of sizes, designs, and costs. A typical design is shown in Figure 5 (a) centering a part on a vacuum chuck. This design uses a shaded-pole inductor (conceptually the same as an LVDT) with the probe on a friction-adjustable pivot which eases the alignment and contact issues. A second design is shown Figure 5 (b) on a polar coordinate measuring machine. In this case the sensor is an LVDT and the probe is guided by an air-bearing to reduce the friction and the load between the probe and the part to be measured.

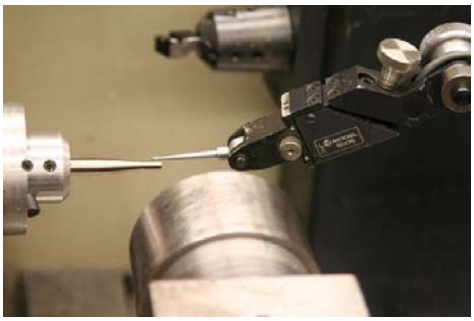
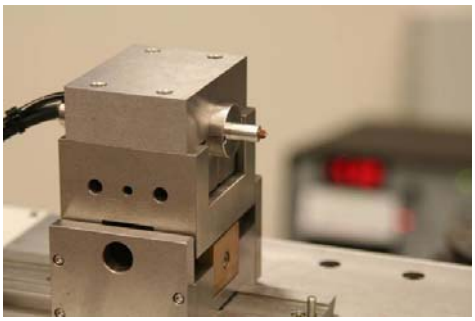

(a) Electronic indicator centering part (b) Air-bearing LVDT on polar measuring machine

Figure 5: LVDT Probe Designs for Measuring the Shape and Run-out of Parts on Spindles

The LVDT probes (like the capacitance gages) produce an output voltage as a linear function of the location of the part with respect to the probe body. For application in this project, the main purpose of the sensing probe is to align the chucks with the spindle centerline and measure the run-out of the shell as the spindle is rotated. An LVDT (or capacitance gage) is ideally suited for the run-out measurement because it measures the change in distance between the part and the fixed probe body. The actual distance is not important, only the change in distance. For the diameter measurements, the probe must be brought within range of the part and then moved to a particular voltage and the machine coordinates measured. The probe is then moved to the opposite side of the part with respect to the spindle axis and new machine coordinates recorded. The difference between these two readings is the diameter. Moving the probe from one side of the part to the other while maintaining knowledge of its position in the machine coordinate system is a significant challenge. As a result LVDTs and Cap gages are poorly suited for measuring diameter by crossing the spindle centerline.

Another problem with the LVDT probe is that it has a single measurement axis. If motion in different directions is needed, the axis of the LVDT will have to be reoriented or multiple actuators will be needed. This will not be acceptable for the measurement of shells at Y-12.

Touch Probes

Kinematic touch probes have been used on coordinate measuring machines since patented [5] by McMurtry in 1979. The typical probe configuration is shown in Figure 6. When a touch probe's ball head contacts the object it is measuring, the triggering force causes the probe's stylus and three pivots to rotate. When one or two of the electrical contacts, labeled 2 in Figure 6, breaks, the electrical circuit is also broken. The breaking of the circuit acts as the triggering signal for the probe. The contacts are preloaded via a spring, labeled 3 in Figure 6. The force on the probe tip that triggers the measurement can come from any direction around a hemisphere above the probe tip. This is a huge improvement over the other probes discussed above, which can only

measure in one direction. The contacting pivot that initially breaks the circuit is dependent upon the direction of the trigger force.

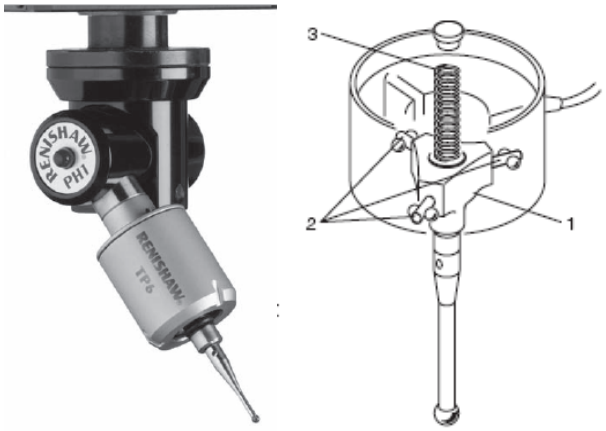

Figure 6: Renishaw Touch Trigger Probe

In trade for their omni-directional detection capabilities, touch probe measurements have substantially larger errors than LVDT's and cap gages. It is essential to recognize that prior to probe triggering, a small rigid body rotation must take place. Additionally, the stylus will bend as a result of the triggering force. The stylus deflection and rigid body rotation combine to form an effect known as pre-travel—the distance the probe head moves before the contacts are broken and the probe triggers. Pre-travel varies with the direction of contact, in an affect known as lobing. Fortunately, a touch probe can be calibrated to remove many of the pre-travel errors. A more detailed discussion of touch probe errors and calibration is given in Section 7.3.4.

7.3 HEMISHELL TRANSFER PROCEDURE

The transfer procedure is designed to find and measure a part on one chuck, then find the opposing chuck within the same coordinate system so that the part can be transferred from one chuck to the other. The radial separation between the part and the opposing chuck must be less than 125 μm for the transfer to be made safely. Additionally, this gap must be uniform to within 8 μm. To make the required measurements, it is necessary to provide a frame of reference, then locate all of the parts and probes with respect to that frame of reference. All of the relevant components are shown in Figure 7. As pictured, the part is located on the chuck where its outer diameter is machined (the OD chuck). The ID chuck and touch probe oppose the OD chuck and hemishell part. The touch probe is rigidly mounted to the ID chuck. The points labeled 1 through 5 represent the locations where the touch probe should contact the hemishell and fixture to fully define the part's location. The significance of these points is discussed below. The LVDT is rigidly mounted to the OD chuck and is used for the initial alignment.

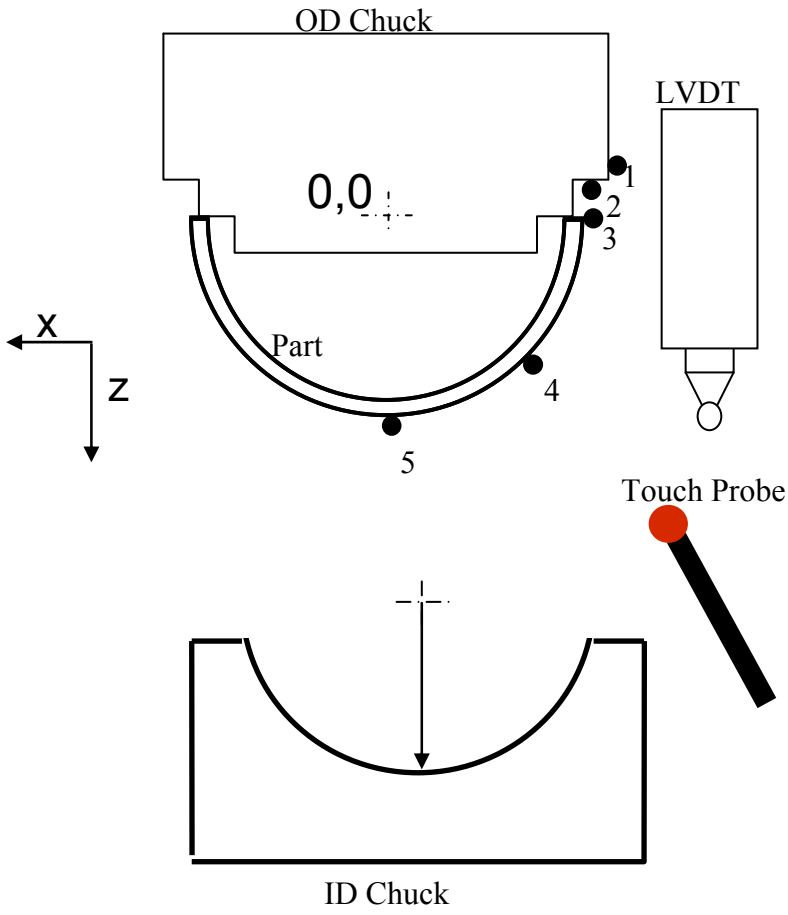

Figure 7: Layout, Top View

7.3.1 INITIAL ALIGNMENT

In reality, the reference location can be chosen anywhere, because it is the position of one component with respect to another that is important for the transfer. However, for simplicity of discussion, the z origin is taken as the point where the probe head center is in the same plane as the equator face of the part. This point is found by touching the fiducial face of the OD Chuck, point 2 in Figure 7. The thickness of the ledge separating point 2 and the face that contacts the part equator is known from previous repeated measurement. Since the probe head radius is also known, a probe touch on point 2 can be used to place the center of the touch probe head in z and set the relative coordinate system to zero.

A caliper is used to set the location of the touch probe in y by measuring the height of the probe head off of the stage. The y position of the spindle centerline is known. Although calipers are

relatively inaccurate, y centering error is well insulated from the more critical x and z errors. This is discussed further in Section 7.4.2.

The x origin is set when the OD Chuck and ID Chuck are radially aligned. Therefore, it is necessary to carefully align the spindle, which holds the OD Chuck, with the ID Chuck, which sits on the x stage. This is done by attaching a federal gage to the spindle, and setting it in contact with one of the radial surfaces of the ID Chuck, as pictured in Figure 8. Then the spindle is rotated; the federal gage will deflect at certain rotational angles if the spindle and the ID Chuck are not aligned.

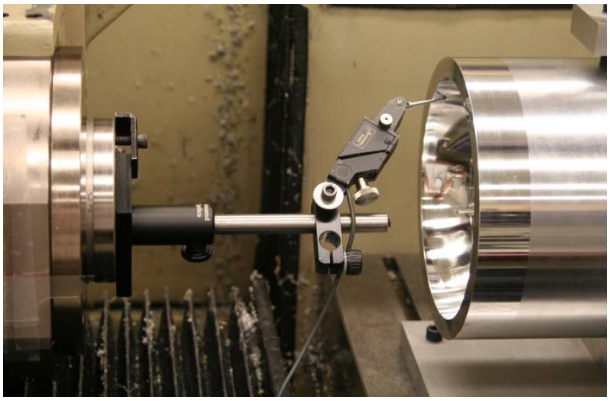

Figure 8: Radial Alignment of ID Chuck and Spindle

A similar process is used to set the front face of the IC Chuck perpendicular to the x-y plane, but the federal gage is reoriented to measure the face run-out instead of the radial run-out, as shown in Figure 9. Once the chucks are aligned to within approximately ±1.5 μm, the relative x coordinate system is set to zero in the DTM controller. The x alignment need only be performed once for any machine setup, so long as the chucks are secured.

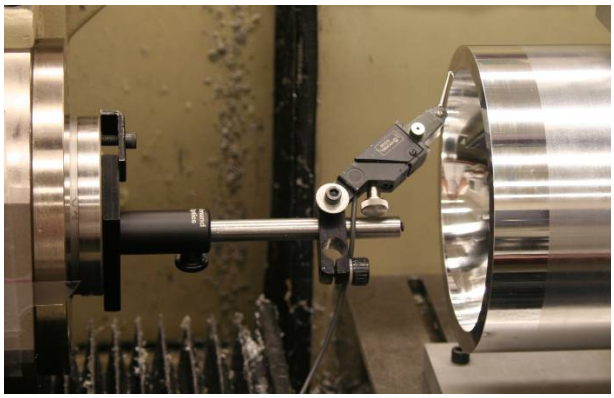

Figure 9: Alignment of ID Chuck Face

7.3.2 LOCATING PROBES

After the z origin is set as described above, the location of the touch probe with respect to the OD Chuck is known. To locate the probe with respect to the spindle centerline, all that is needed is a probe touch at point 1 in Figure 1, because the radius of the OD Chuck is known.

At this point the location of the ID Chuck with respect to the OD Chuck in x is known, as is the location of the touch probe with respect to the OD Chuck in both x and z. To determine the relative locations of the two chucks in z, it is necessary to find the location of the touch probe with respect to the ID Chuck in z. That is, the offset between the touch probe head and the ID Chuck face, shown in Figure 10, must be determined. This is done using an air-bearing Linear Variable Differential Transformer (LVDT).

The air bearing LVDT is aligned with the touch probe in x and y by sweeping the touch probe with the LVDT along both axis. When the LVDT's displacement is at a maximum, the spherical heads of the LVDT and touch probe are aligned. This maximum displacement value is then recorded, along with the z axis position of the LVDT body, labeled Z_{probe} in Figure 10, below. The LVDT body is then moved until the gage is in contact with the ID Chuck face, and the LVDT's displacement matches the maximum displacement previously recorded. The z position of the body, now Z_{chuck}, is then recorded again. The difference between Z_{probe} and Z_{chuck} is the z separation between the probe head and the ID Chuck.

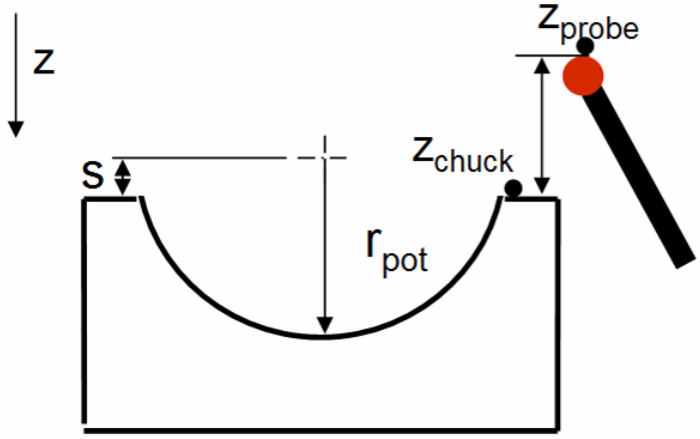

Figure 10: Touch Probe/ID Chuck Location in Z

With the touch probe located with respect to the ID Chuck, it is now possible to locate the part with respect to the ID Chuck by simply touching the OD Chuck or the part apex with the touch probe.

Also note that the touch probe was only subjected to a small force when located by the LVDT; however, when the touch probe is triggered on the part apex is undergoes pre-travel prior to triggering. This pre-travel distance, discussed in Section 2.2.1, must be added back into the z-separation dimension.

7.3.3 PART MEASUREMENT/LOCATION

After the touch probe and chuck are aligned and located, the LVDT may be removed. At this point, the system is ready to measure a hemispherical part that has recently been machined on the OD Chuck. After a part is diamond turned on the OD Chuck, the touch probe touches it at its equator, its apex, and a point halfway between, denoted by points 3, 5, and 4 in Figure 1. Using these three points, it is possible to determine the radius and center point of the sphere using the method described in Section 7.4.1. If the measurements prove that the part will fit in the spherical ID Chuck (pot chuck), then the transfer can proceed. In using this method, it is necessary to assume that the shape of the recently machined part is close to a sphere.

Part Transfer Coordinates

If the part is determined to be of proper size, the transfer coordinates can be determined from the z location of the hemishell apex, point 5. The x coordinate for transfer is 0, set during the initial spindle centerline alignment, and the z coordinate is determined from Equation 1, below. With the exception of Z_5 and pretravel, the terms in Equation 1 are identified in Figure 10. Z_5 is the z location of the part apex, and pretravel is the distance that the probe must move before triggering, as determined in the calibration procedure.

$$Z_{transfer} = Z_5 - \left(Z_{probe} - Z_{chuck}\right) - r_{pot} + S + pretravel \tag{1}$$

Using these transfer coordinates will place the apex of the shell in contact with the bottom of the pot chuck. If a small gap is desired, then the size of the gap must be added to the $Z_{transfer}$ coordinate. The final transfer is made by moving the part to the transfer coordinates, then turning on the vacuum to the pot chuck and turning off the vacuum to the OD Chuck.

Equation 1 shows that the pot chuck must be measured as a setup step for the automated transfer. The pot chuck was measured using the Brown and Sharpe Coordinate Measuring Machine (CMM) at the PEC. The pot's radius and center point were determined by touching 15 points on

the pot's radius with the touch probe, then using the CMM's software to calculate the dimensions. The pot chuck's planar face was then touched at 5 places, and the CMM software used to calculate the position of the plane with respect to the pot's center point. Each measurement was repeated 10 times. The pot's radius was found to be 76.1666 mm with a 2σ uncertainty of 1.9 μm, and the pot was found to be short of a full sphere by 6.1062 mm with a 2σ uncertainty of 2.1 μm, as shown in Figure 11. Note that 2σ uncertainty represents a 96% confidence interval, while σ, the standard deviation, is defined as Type A Standard Uncertainty by the U.S. Guide of the Uncertainty in Measurement [4].

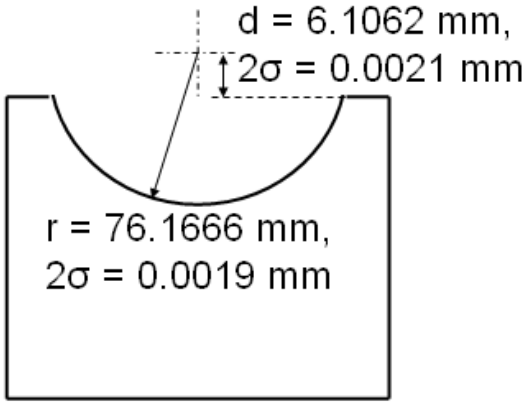

Figure 11: ID (Pot) Chuck Dimensions

7.3.4 TOUCH PROBE ERROR CALIBRATION

The errors associated with measurement taken by a touch trigger probe will be discussed presently, with reference to the coordinate system shown in Figure 12.

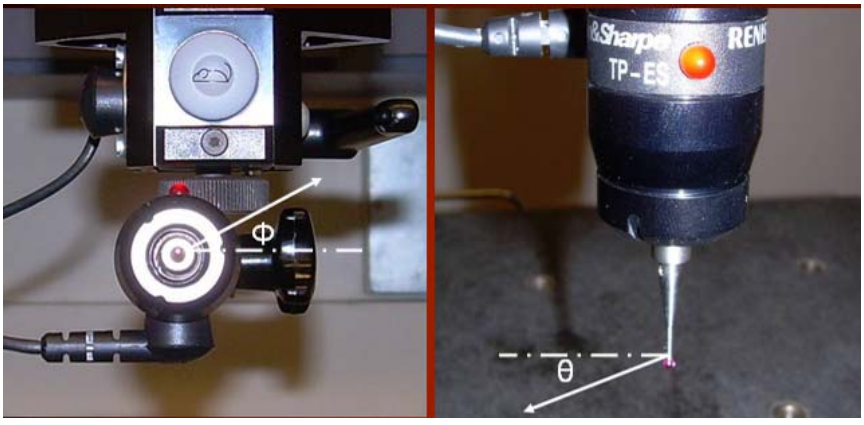

Figure 12: Touch Probe Coordinate System

Three Dimensional Lobing

When the direction of the trigger force varies in the Φ direction, the pre-travel distance varies predictably. This is because the magnitude of the rigid body rotation required to break one of the electrical contacts varies depending on the location of the pivots. For example, if a trigger force F_2 in Figure 13 is applied, the stylus will pivot about the bottom two supports, and the moment arm that will break the contact at the top support is very long, as shown in Figure 13 and Figure 14. As a result, only a small rotation is required to trigger the probe. The opposite is true for F_1.

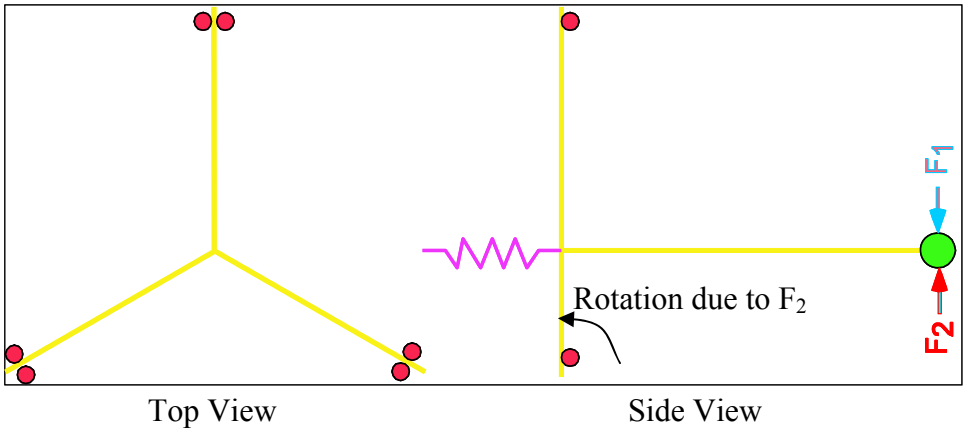

Figure 13: Touch Probe Pivots

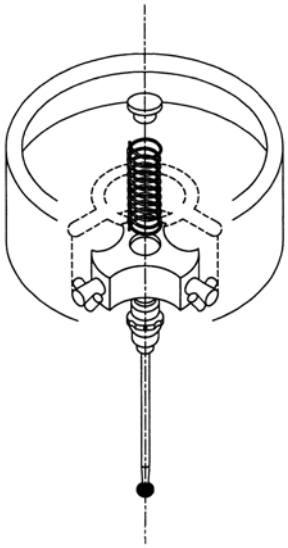

Figure 14: Schematic of Touch Probe Seating

Figure 15, below, shows the variation of pre-travel with Φ, as determined by Dobosz and Wozniak [1]. A trigger from the direction of F_1 requires a greater rotation and thus a greater force, so a larger stylus deflection will result. The diagram in Figure 15 captures all of these errors, along with errors caused by the probe ball having geometry that differs slightly from a perfect sphere.

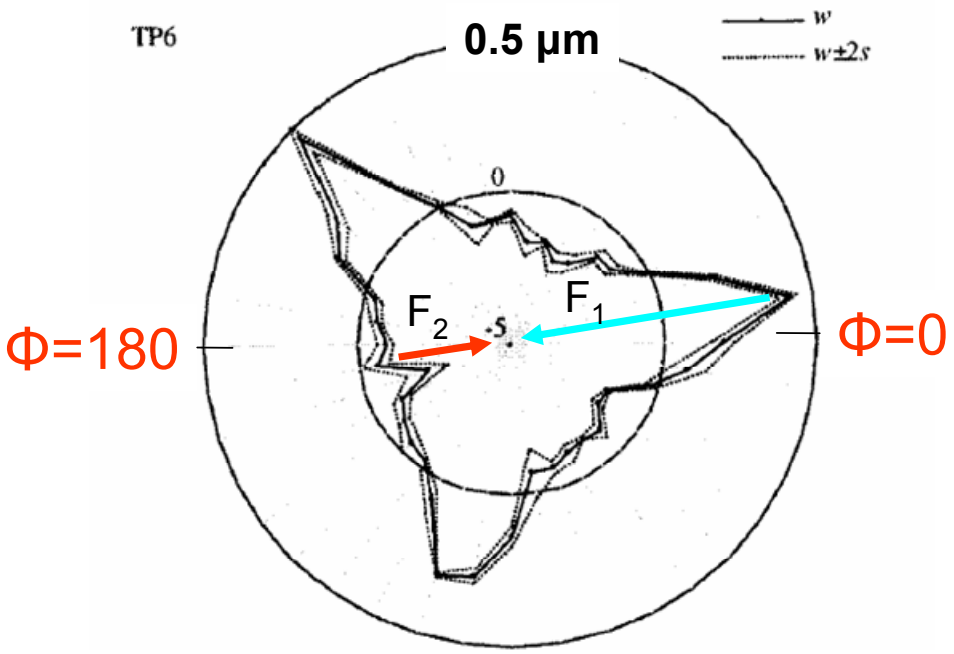

Figure 15: 2-D Touch Probe Lobing

For the measurements in the transfer, the effects of traditional lobing only partly describe the errors. In reality, for this project the trigger force direction will vary exclusively in the θ direction. Prior study on the 3-D error compensation for touch probes has been done by Estler [2, 3]. Estler's model and measured pre-travel are shown in Figure 16. Estler used a precision calibration sphere to determine his measured pre-travel data. In Figure 16, each block of 120 on the "Point Index" represents a full rotation of 360 degrees in Φ. The different 120 point blocks then represent an interval of 10 degrees in the θ direction. The block of point indices between 360 and 480 represents the lobing around the equator of the probe head; this data, although plotted differently, contains the same information as the data in Figure 15. The data between point index of 1440 and 1560 represents repeated touches on the "South Pole" of the probe head (ie. θ = 90 degrees from Figure 12).

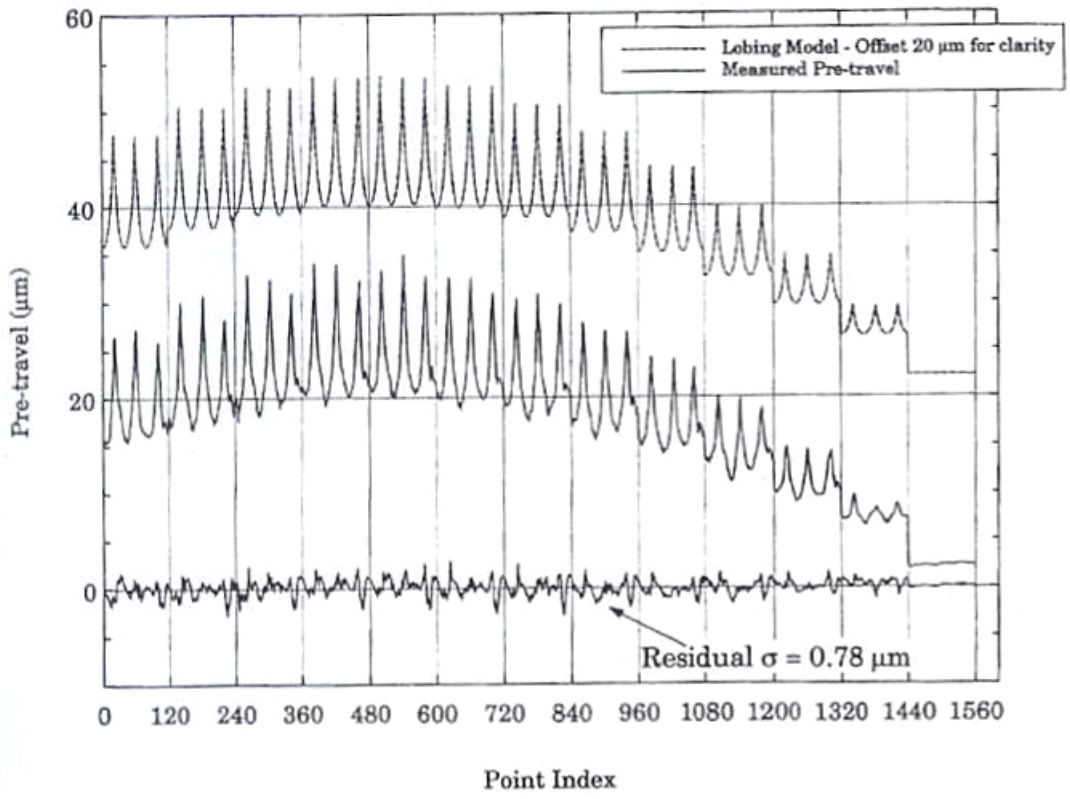

Figure 16: Pre-Travel for TP-2 Touch Probe [3]

Trigger Signal Noise

If a 5V input voltage is applied to the touch probe, the untriggered probe will produce an output voltage of 5V. Ideally, once an electrical contact is broken, the output voltage goes immediately to zero and stays there. However, in reality, the probe's output voltage takes time to equilibrate after a change. The machine axis will be constantly in motion while the probe is triggered, so it is important for the machine coordinates to be recorded at the exact moment that the probe is triggered. The servo speed on the DTM controller, which records both the axis positions and the probe output, is 800 Hz. Therefore, if the axis and probe are moving at a rate of 0.2 mm/min when the probe is triggered, there will be an uncertainty of 4 nm—the distance the probe head moves between controller cycles. This is shown in Equation 2, below

$$\frac{0.2\text{mm}}{60\,\text{sec}} * \frac{1\text{sec}}{800\text{cycles}} \Rightarrow 4\frac{\text{nm}}{\text{cycle}} \tag{2}$$

This ideal level of precision will not be attainable if the probe triggers erratically or repeatedly at a single point. Therefore, a signal conditioning unit is used to smooth the output of the touch probe into a clean square wave. The signal conditioner used is the Renishaw MI-9. The MI-9 inputs and outputs are labeled in the block diagram in Figure 17, below [6].

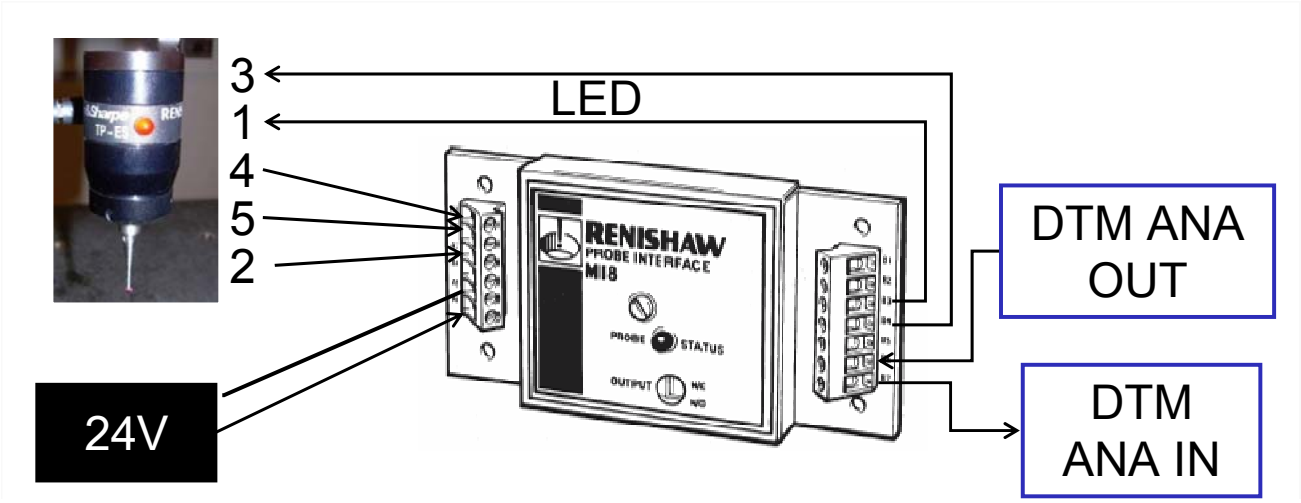

Figure 17: Signal Conditioner Block Diagram

Touch Probe Calibration

When the touch probe is calibrated using a precision sphere, all of the errors from pre-travel variation probe head ball geometry are lumped together. Those errors are then exchanged for the precision sphere geometry variation, which is listed at 63.5 nm in the product specs, and trigger repeatability. Trigger repeatability is hence forth taken as 2σ of the trigger location for multiple touches at the same angle on the same object. Since a centered calibration sphere can be touched for reference prior to any measurements, the primary error source becomes trigger repeatability.

The trigger repeatability is found by touching the calibration sphere from 13 different radial vectors, shown in Figure 18, below. These vectors represent a change in the angle θ only, where θ is defined in Figure 12.

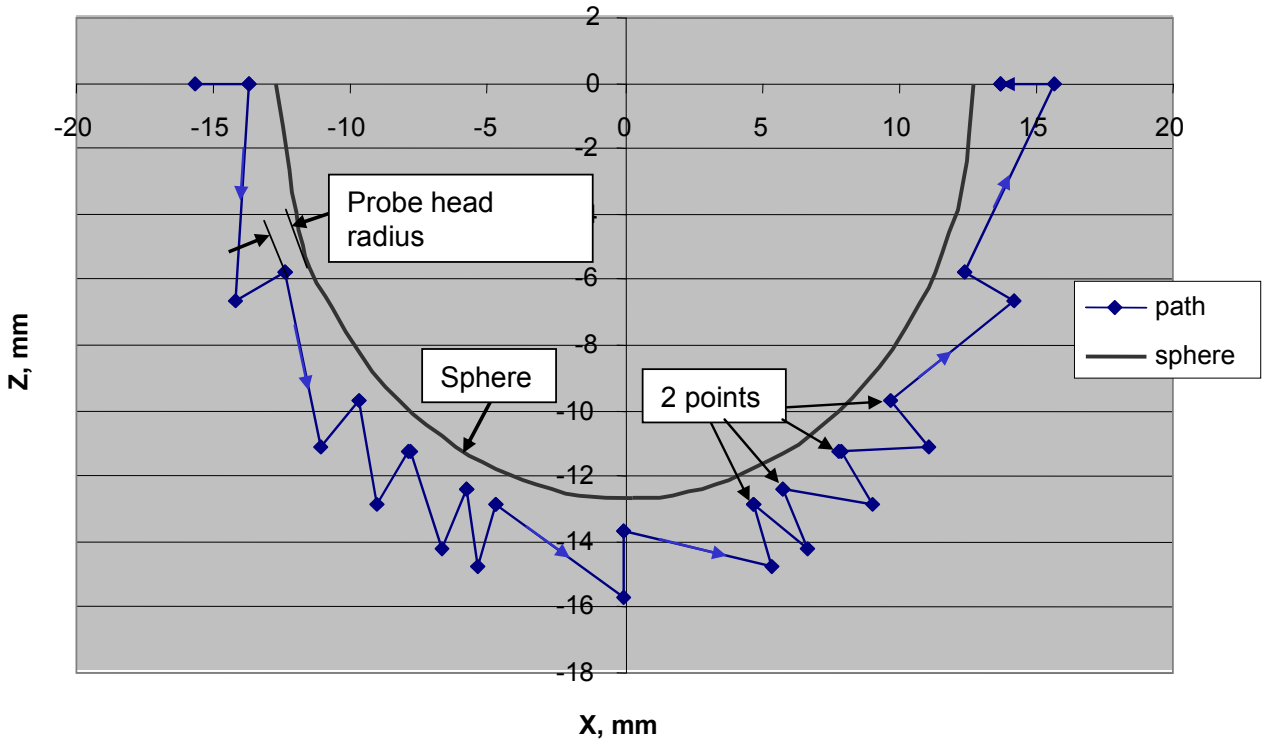

Figure 18: Calibration Sphere Touch Vectors

The measurements are repeated 10 times, and the standard deviation, σ, of the radius measured from each vector is calculated using Equation 3.

$$\sigma = \sqrt{\frac{\sum (r - \bar{r})^2}{n - 1}} \tag{3}$$

The probe is then rotated in Φ and the touches in Figure 18 are once again repeated 10 times. The results from three different Φ orientations are plotted in Figure 19 and Figure 20.

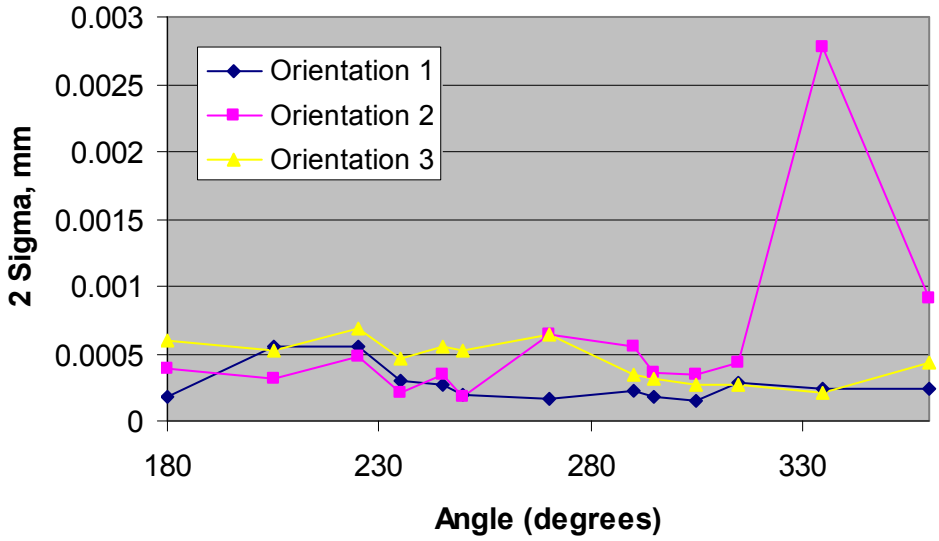

Figure 19: 2σ Trigger Repeatability from Calibration Sphere

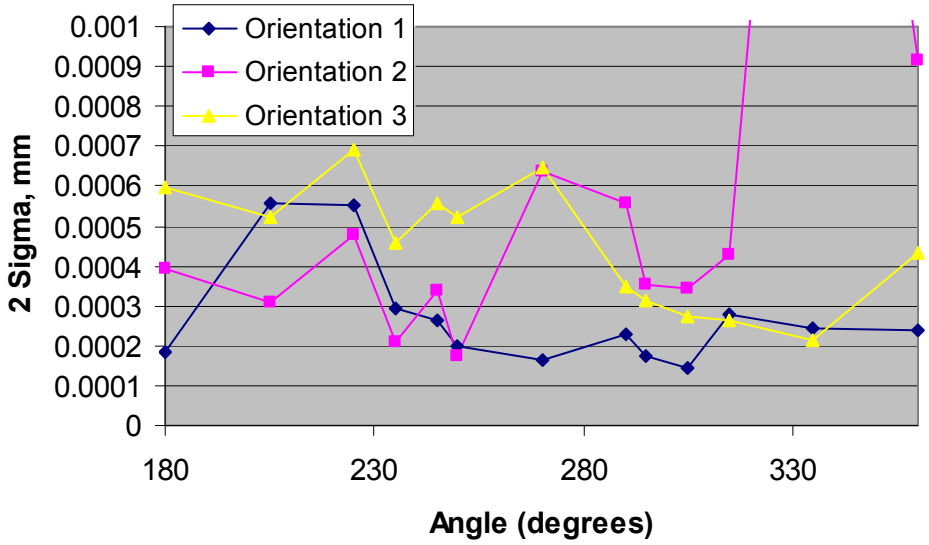

Figure 20: 2σ Trigger Repeatability from Calibration Sphere, Zoomed In

Figure 20 shows that the lowest 2σ of trigger repeatability occurred between 270 and 360 degrees in orientation 1. The spindle center line is not being crossed during measurement, and the part will only be touched on one side. Therefore, it is only necessary to use a 90 degree range of trigger vectors. Accordingly, we choose to use the portion of the probe that has the best repeatability. The maximum 2σ between 270 and 360 degrees in orientation 1 is 0.27 µm. For each touch of the probe, the error is a combination of this trigger repeatability and the calibration

sphere's maximum departure from perfect geometry, 63.5 nm. The two errors are combined as shown in Equation 4.

$$e = \sqrt{0.270^2 + .064^2} = 0.277\mu m \tag{4}$$

This radial error must accompany any measurement taken using the touch probe. Since it represents the 2σ trigger repeatability, 96% of all data points taken should fall within 0.277 μm of the value on the axis at the moment of trigger. Note that we are using an ASG 2500 diamond turning machine with laser interferometer feedback on the axis position. The axis position resolution is 2.5 nm, a negligible source of error.

Once the chucks are aligned and the probes placed in their final orientation, all that is needed to calibrate pre-travel errors is a touch on each point on the calibration sphere that correlates to the points to be touched on the hemishell. With the chucks aligned, the touches in Figure 21 are all that is required to locate the z origin, find the x coordinate of the apex (of both the calibration sphere and the part), and calibrate the significant pre-travel errors at the design touch points.

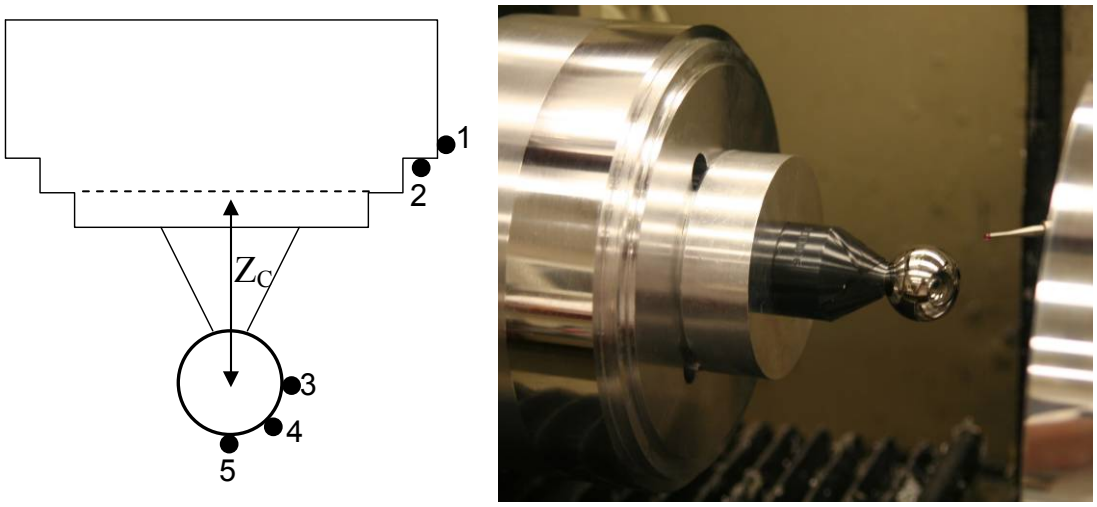

Figure 21: Final Touch Probe Calibration Points

To be able to calibrate the pre-travel effects, the radius of the calibration sphere needs to be known precisely, as does the separation between the center of the calibration sphere and the center of the part, labeled Z_C in Figure 21. The radius of the ball is 12.69937 mm with an uncertainty of 63.5 nm, and Z_C is 51.4497 mm with a 2σ standard deviation of 300 nm.

The correlating touch points on the hemishell part are labeled 3, 4, and 5 in Figure 22, below. Henceforth, the coordinates of 3, 4, and 5 on the calibration sphere in Figure 21 will be labeled

with the subscripts cal_3, cal_4, and cal_5, while the points 3, 4, and 5 on the part in Figure 22 will be labeled with subscripts part_3, part_4, and part_5.

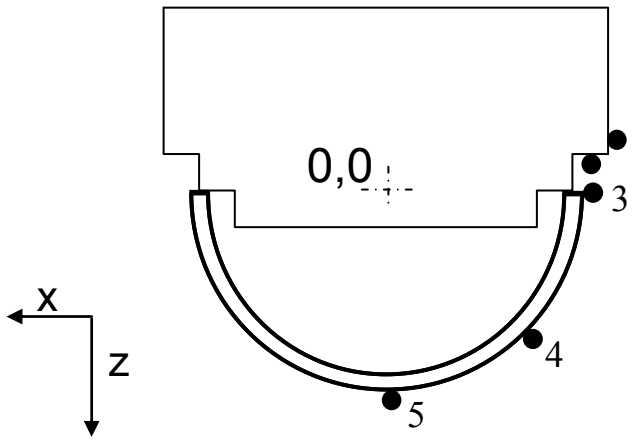

Figure 22: Hemishell Measurement Touch Points

The actual, calibrated coordinates on the part then become the left side of Equation 5.

$$\begin{aligned} x_3 &= x_{part\_3} - x_{cal\_3} - 12.69937 \\ z_3 &= z_{part\_3} \\ x_4 &= x_{part\_4} - x_{cal\_4} - 12.69937 \sin 45 \\ z_4 &= z_{part\_4} - \left(z_{cal\_4} - z_c\right) + 12.69937 \cos 45 \\ x_5 &= x_{part\_5} \\ z_5 &= z_{part\_5} - \left(z_{cal\_5} - z_c\right) + 12.69937 \end{aligned} \tag{5}$$

7.4 HEMISHELL MEASUREMENT

Once the touch probe is calibrated the part machined on the OD Chuck needs to be measured prior to transfer. This measurement will answer three questions:

1. Was the part machined correctly?
2. Will the part fit in the ID (pot) Chuck?
3. How far does the part need to move before the vacuums can be switched and the transfer can be made?

7.4.1 THREE POINT METHOD

The three point method allows us to determine the radius and center point of a circle that includes any three non-collinear points. The equation of this circle can be written in the form of Equation 6 [7].

$$\begin{vmatrix} X^2+Y^2 & X & Y & 1 \\ x_1^2+y_1^2 & x_1 & y_1 & 1 \\ x_2^2+y_2^2 & x_2 & y_2 & 1 \\ x_3^2+y_3^2 & x_3 & y_3 & 1 \end{vmatrix} = 0 \tag{6}$$

Solving the determinant in Equation 6 produces Equation 7.

$$X^2+Y^2+2dX+2eY+f=0 \tag{7}$$

From Equation 7, the $\text{center} = (-d,-e)$ and the $\text{radius} = \sqrt{d^2+e^2-f}$, where d, e, and f are defined in Equations 8, 9, and 10.

$$\begin{aligned} d := \Big(\frac{1}{2}\big(&y_3^2\,y_2 - y_3^2\,y_1 + x_3^2\,y_2 - x_3^2 y_1 - y_2^2\,y_3 + y_2^2\,y_1 - \\ &x_2^2\,y_3 + x_2^2\,y_1 + y_1^2\,y_3 - y_1^2\,y_2 + x_1^2\,y_3 - x_1^2\,y_2\big)\Big) \Big/ \big(-x_3 y_2 \\ &+ x_3 y_1 - x_2 y_1 + x_2 y_3 - x_1 y_3 + x_1 y_2\big) \end{aligned} \tag{8}$$

$$\begin{aligned} e := \frac{1}{2}\big(&-y_1^2 x_3 - x_1^2 x_3 + x_1^2 x_2 - x_2^2 x_1 + x_2^2 x_3 + y_1^2 x_2 + x_3^2 x_1 - \\ &x_3^2 x_2 + y_3^2 x_1 - y_3^2 x_2 - y_2^2 x_1 + y_2^2 x_3\big) \Big/ \big(-x_3 y_2 + x_3 y_1 - x_2 y_1 \\ &+ x_2 y_3 - x_1 y_3 + x_1 y_2\big) \end{aligned} \tag{9}$$

$$\begin{aligned} f := \big(&y_3^2 x_2 y_1 - y_3^2 x_1 y_2 + x_3^2 x_2 y_1 - x_3^2 x_1 y_2 - y_2^2 x_3 y_1 + y_2^2 x_1 y_3 \\ &- x_2^2 x_3 y_1 + x_2^2 x_1 y_3 + y_1^2 x_3 y_2 - y_1^2 x_2 y_3 + x_1^2 x_3 y_2 - \\ &x_1^2 x_2 y_3\big) \Big/ \big(-x_3 y_2 + x_3 y_1 - x_2 y_1 + x_2 y_3 - x_1 y_3 + x_1 y_2\big) \end{aligned} \tag{10}$$

The three circle method allows us to determine whether the sphere will fit in the pot chuck and whether there have been any gross errors in the machining of the OD. However, it will not allow an operator to discern tool centering errors, because tool centering errors cause the final part to be something other than a sphere, such as an ogive. This method assumes that the part is a

sphere to begin with. If the part is not a sphere, the center point calculation will be askew, and the radius measured will not actually tell us how big the part is. Fortunately, the location of points 3 and 5 in Figure 21 will tell the operator all he needs to know about the size of the part, which is symmetric about the spindle centerline.

Errors in the Three Point Method

If the tool is known to be centered, then the three circle method can be used to determine radius. It can also tell the operator whether the sphere machined is short or long of a hemishell. That is, the three circle method will tell us whether the shell face touching the chuck face located at z = 0 is indeed the equator of the shell, or whether that plane has some latitude. Regardless when the three circle method is used to measure a part, the errors from the trigger repeatability associated with each point are magnified.

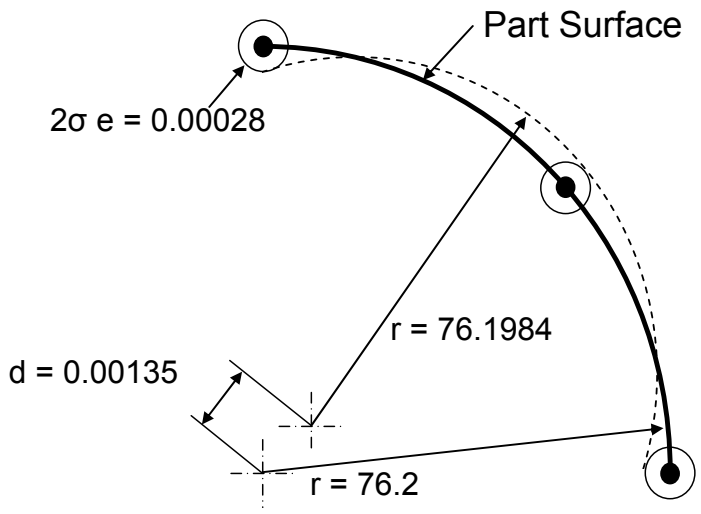

Figure 23: Three Circle Method Errors

Figure 23, above, shows how an uncertainty of 0.28 μm at each of the three points on a perfect sphere could indicate that the part has a radius that is smaller than the actual radius by 1.6 μm, represented by the dotted line. The same measurement could indicate a radius 1.6 μm larger than the actual radius. Also, the 0.28 μm error at each touch point could skew the location of the center point by up to 1.4 μm. As long as the tool is well centered and these errors are still acceptable, the three circle method can be used to measure a part inline, without adding any additional steps to the transfer procedure.

7.5 TOTAL TRANSFER ERROR

All of the error sources discussed thus far have created uncertainty in the value of individual measurements. However, the uncertainties of individual measurements need to be considered in the context of a transfer move. This serves to combine the errors from the initial alignment and the measurements into errors in the x, y, and z location for transfer. The setup and coordinate system are shown in Figure 24, below.

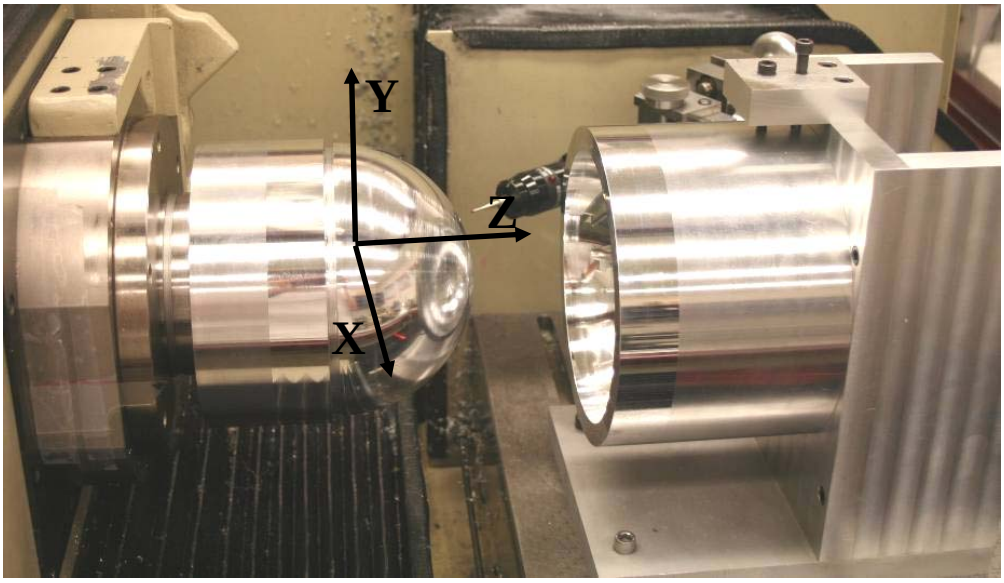

Figure 24: Transfer Setup and Coordinate System

7.5.1 X ERROR

The x transfer coordinate was set at x = 0 when the spindle and the ID Chuck were aligned in the first step of the transfer procedure. The location of the origin has not changed through the measurements, and the position of the DTM axis is repeatable to a negligibly small 10 nm. Therefore, the only error that needs to be considered for the x transfer coordinate is the initial alignment error. When the spindle and the ID Chuck were aligned by fixing a federal gage to the spindle and then rotating the spindle, a radial run-out of ±1.5 μm was achieved. This value of 1.5 μm is the x error of the transfer coordinate position. Take note that the pot chuck radius was cut 50 μm larger than the hemishell. When this procedure is implemented at BWXT-Y12, the initial alignment does not need to be accurate to ±1.5 μm, as long as the tool used for cutting the inner diameter is re-centered based on the second spindle center line.

7.5.2 Y ERROR

After the initial alignment, the y positions of the OD Chuck, ID Chuck, and part remain constant. Therefore, the only y error in the transfer coordinates is the initial alignment error, which is equal to the 1.5 μm x error. The spindles were aligned in both x and y simultaneously by rotating the federal gage about the spindle center line, so their errors were indistinguishable, and thus taken to be the maximum run-out of 1.5 μm.

The touch probe is centered with the spindle center line in y by using calipers to measure the height of the probe head off the stage. The relatively poor resolution of the calipers produces an error in touch probe centering of perhaps 50 μm. While this dimension itself is meaningless for the determination of y transfer coordinates, it does translate into small errors in the crucial x and z measurements. Figure 25 shows how a y-misalignment of d leads to an error of e in all of the x measurements made on the sphere.

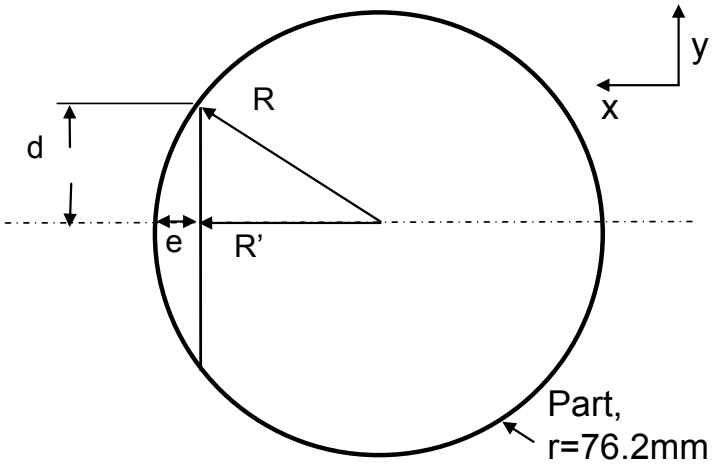

Figure 25: Effects of Probe Head y Misalignment

The calculations in Equation 11 show that the error passed on to all x (and z) measurements on the surface of a 76.2 mm sphere due to a 50 μm y misalignment is only 17 nm.

$$\begin{aligned} e &= R - R' \\ R' &= \sqrt{R^2 - d^2} = \sqrt{76200^2 - 50^2} = 76199.983\ \mu\text{m} \\ e &= 76200 - 76199.983 = 17\text{nm} \end{aligned} \tag{11}$$

7.5.3 Z ERROR

The uncertainty of the z transfer coordinate must include the errors from all of the terms of Equation 1, as well as the initial alignment errors. The initial alignment resulted in a pot chuck face alignment error that was identical to the radial run-out error of 1.5 μm. The pot chuck radius and shortness uncertainties of 1.9 μm and 2.1 μm must also be considered, along with the error from touch probe trigger repeatability of 0.28 μm from the touch at the shell apex labeled 5 in Figure 7. The total error is taken by the square root of the sum of the squares of the individual errors, calculated to be 3.2 μm in Equation 12.

$$Z_{error} = \sqrt{1.5^2 + 1.9^2 + 2.1^2 + 0.28^2} = 3.2\ \mu\text{m} \tag{12}$$

7.6 SUMMARY

A procedure for automating the measurement of a hemishell along with its transfer from its OD Chuck to ID Chuck will greatly reduce the human effort required in hemishell production. The system described includes both setup steps, which must be executed one time on each machine, along with measurement and transfer steps that must be repeated for each part made. The setup, measurement, and transfer steps are enumerated below.

Setup Steps

1. Measure dimensions of OD and ID Chucks on CMM.
2. Align OD and ID Chucks (ie. Align the opposing spindle centerline on a dual machine) by rotating a federal gage on the spindle.
3. Mount touch probe and roughly align (50 μm) with the spindle center line in y.
4. Use air-bearing LVDT to crown the touch probe head in x and y and find the high spot, then determine the touch probe's offset from the ID Chuck face in z.
5. Touch the OD Chuck radius and fiducial face with the touch probe to find probe's position with respect to the spindle centerline in x and the hemishell equator in z.
6. Center a calibration sphere on the spindle and touch it at the design points.

Measurement and Transfer Steps

1. Assume a part has just been machined, and is centered on the OD Chuck.
2. Touch the part at its equator, at 45 degrees latitude, and at its apex.
3. Check the size of the part to ensure it will fit in the pot chuck.
4. Calculate the coordinates for transfer based on the position of the probe and hemishell apex point, along with the ID Chuck geometry.
5. Move to the transfer coordinates and switch vacuums to complete the transfer.

These steps were repeated on the PEC's ASG 2500 Diamond Turning Machine. The DTM's axis ranges of 15 cm in z and 25 cm in x and axis repeatability of 2.5 nm provided a sufficient range and resolution for collecting the design data points. The fiducial surfaces on both chucks were machined on the DTM, as was the hemishell used in the procedure demonstration. The ID Chuck's pot radius was cut to be 50 µm larger than the hemishell OD.

Once the parts were finished, the Setup and Transfer steps above were executed, and the transfer coordinates were calculated. The vacuum was switched and the transfer completed as planned. The transfer was then repeated with an intentionally added z separation of 125 µm, which represents the necessary margin of error for the BWXT-Y12 requirements. This transfer was also successful. The position of shell with respect to the pot chuck at the transfer coordinates was determined through the initial alignments and the measurements. The possible error of the shell's actual position at transfer is tabulated in Figure 26 below.

	X	**Y**	**Z**
Error (µm)	1.5 µm	1.5 µm	3.2 µm

Figure 26: Error of Transfer Coordinates

7.7 FUTURE WORK

It has been observed that during a part transfer, the part itself finds a way to slide off of the center axis of the chuck and spindle. Since the pot chuck was machined with a radius 50 µm larger than the hemishell's, there is plenty of room for the part to slide around after vacuum has been released. The project required that the chuck be machined with some error, because in the BWXT-Y12 machining setup, chucks will be machined rapidly, with lower tolerances.

The next phase of the project is to extend the process and automatically measure the post-transfer run-out, and then re-center the part on the chuck. Run-out is possible transferring in both directions—OD Chuck to ID Chuck and ID Chuck to OD Chuck. The exaggerated result of run-out for both cases is shown in Figure 27. It is assumed that enough extra material has been left at the equator to flatten the equator face after a small rotational run-out. Therefore, only the ID to OD Chuck transfer case, shown again in Figure 28, need be considered.

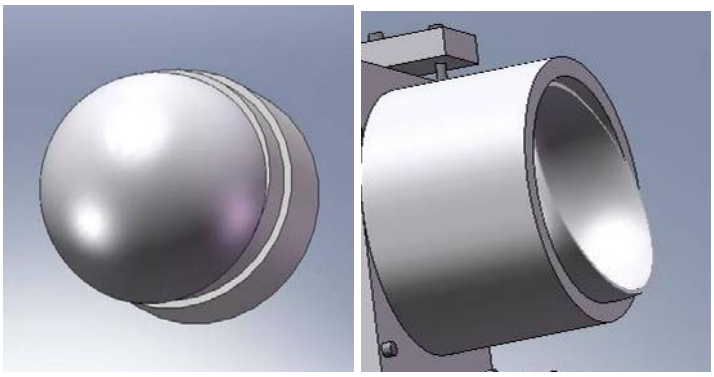

Figure 27: Hemishell Run-out Possibilities

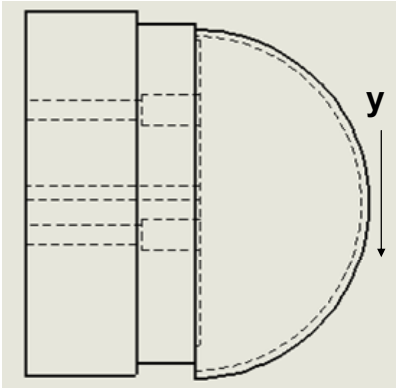

Figure 28: Run-out from ID to OD Chuck Transfer

When all phases of this project are complete, it will be possible to simply place a roughly machined hemishell on one of the chucks. Then the run-out system will automatically align the part and machine the first diameter. Then the part will be measured, transferred to the opposing chuck, and aligned on the opposing chuck automatically. The whole process will streamline the tedious part transfer and realignment process, which currently requires substantial human effort.

REFERENCES

1. Dobosz, M. and Wozniak, A., "CMM Touch Trigger Probes Using a Reference Axis", Precision Engineering, Vol 29, pg 281-289, 2005.
2. Estler, T., et.al., "Error Compensation for CMM Touch Trigger Probes", Precision Engineering, Vol 19, pg 85-89, 1996.
3. Estler, T., et.al., "Practical Aspects of Touch-Trigger Probe Error Compensation", Precision Engineering, Vol 21, pg 1-17, 1997.

4. American National Standard for Calibration. (1997). *U.S. Guide to the Expression of Uncertainty in Measurement* (ANSI/NCSL Z540-2-1997). Boulder, CO.
5. McMurtry, D. R. , "Probe for use in measuring machines", February 12, 1979, US Patent 4,138,823.
6. Renishaw. MI 8 Interface Unit, Installation and User's Guide. United Kingdom, 1995.
7. Dow, T., K. Garrard and A. Sohn. Automatic Handling Technology for Hemispherical Shells, Interim Report – Task I, Sensor Selection. Precision Engineering Center, North Carolina State University (2007).

FACULTY

THOMAS A. DOW

Director, Precision Engineering Center
Dean F. Duncan Distinguished University Professor in Mechanical Engineering
Professor, Department of Mechanical and Aerospace Engineering

BS, Mechanical Engineering, Virginia Polytechnical Institute, 1966
MS, Engineering Design, Case Institute of Technology, 1968
PhD, Mechanical Engineering, Northwestern University, 1972

After receiving his PhD degree from Northwestern University in 1972, Dr. Dow joined the Tribology Section of Battelle Columbus Laboratories and worked there for ten years. His research interests were in the areas of friction and wear and included studies on a wide variety of topics from lubrication of cold-rolling mills using oil-in-water emulsions to wet braking effectiveness of bicycle brakes to elastohydrodynamic lubricant film generation in ball and roller bearings. He developed experimental apparatuses, established analytical models, and corroborated those analyses with experimental measurements. Dr. Dow joined the faculty at North Carolina State University in 1982 and was instrumental in developing the academic and research program in precision engineering. His current research interests include the design of precision machining systems, real-time control, and metrology. He was one of the founders of the American Society for Precision Engineering and currently acts as the Executive Director.

JEFFREY W. EISCHEN

Associate Professor
Department of Mechanical and Aerospace Engineering

BS, Mechanical Engineering, UCLA, 1978
MS, Mechanical Engineering, Stanford University, 1981
PhD, Mechanical Engineering, Stanford University, 1986

Dr. Eischen has been with North Carolina State University since 1986 and his research areas of interest include: linear and nonlinear finite element analysis, multi-body kinematics/dynamics/control, fabric mechanics, and stress analysis in microelectronic devices. He teaches undergraduate courses in strength of mechanical components and mechanical design. His graduate courses include fracture mechanics and advanced machine design. He has collaborated with colleagues in the Precision Engineering Center for several years on computer simulation related projects dealing with precision shape control of disk drive read/write heads, stress and deformation analysis of high energy physics equipment, and contact lens mechanics.

RONALD O. SCATTERGOOD

Professor
Materials Science and Engineering Department

BS, Metallurgical Engineering, Lehigh University, 1961
MS, Metallurgy, Massachusetts Institute of Technology, 1963
PhD, Metallurgy, Massachusetts Institute of Technology, 1968

R.O. Scattergood is a Professor in the Department of Materials Science and Engineering. He received BS degrees in Mining Engineering and Metallurgical Engineering from Lehigh University. His MS and PhD degrees were obtained in Metallurgy from M.I.T. In 1968 he became a member of the basic research staff in the Materials Science Division at the Argonne National Laboratory. In 1981, he joined the faculty as a Professor of Materials Engineering at North Carolina State University.

Professor Scattergood's major research interests have been focused on the mechanical behavior of solids. He has worked in the areas of strengthening mechanisms in solids, mechanical testing, fracture, tribology, nanocrystaline materials and precision machining processes. He has expertise in He has published over 200 technical papers, books and reports.

STAFF

KENNETH P. GARRARD

Research Assistant
Precision Engineering Center

BS, Computer Science, North Carolina State University, 1979
MS, Computer Studies, North Carolina State University, 1983

As a full-time staff researcher at the Precision Engineering Center, Mr. Garrard's interests and duties have included the development of high performance control systems for ultra-precision machines and software development for custom, multiprocessor computer systems. He participated in the development of the original PEC fast tool servo as well as three other fast tool servo systems that have been delivered to commercial and government sponsors. One of these systems was built specifically for the on-axis turning of off-axis segments of conic surfaces of revolution and another is being used for the fabrication of inertial confinement fusion target mandrels. He has performed numerous prototype fabrication projects that required unique machine configurations and controller software. Mr. Garrard also has a long standing interest in the analysis of scientific data, programming language structures, sorting and searching algorithms, multiprocessor computer architecture and the design and implementation of hard real-time systems.

ALEXANDER SOHN

Research Assistant/Lecturer
Precision Engineering Center

B.S., Physics, University of Texas at Arlington, 1992
M.S., Physics, University of Texas at Arlington, 1994

Mr. Sohn joined the Precision Engineering Center in August, 1997 as a member of the technical staff. His current research interests range from machine design and metrology to the design and fabrication of nonimaging optics. Mr. Sohn's varied research activities began in microwave optics and atomic physics as a student at the University of Texas at Arlington and later progressed to precision machine design, design and fabrication of plastic optics as well as automation and machine vision at Fresnel Technologies, Inc. in Fort Worth, Texas.

PAULA J. KELLEY

Administrative Assistant
Precision Engineering Center

BA, Liberal Arts / Criminal Justice/ University of New Hampshire 1990

Ms. Kelley became a member of the PEC Staff in September 2007. Previously, Ms. Kelley has worked as the book-keeper for Lead Mine Elementary School in Raleigh; office manager for a private non-profit school in New Hampshire; supervisor for a school serving behaviorally challenged teens in Massachusetts and coordinator for a G.E.D. and job training program serving at risk teens. Ms. Kelley provides the overall administrative support for the Center.

CONSULTANTS

KARL FALTER

Consulting Engineer

BS, Mechanical Engineering, North Carolina State University, 1987
MS, Mechanical Engineering, North Carolina State University, 1989
PhD, Mechanical Engineering, North Carolina State University, 1992

Prior to working as an independent consultant, Dr. Falter was a senior development engineer with Eastman Kodak from 1997 to 2003. He designed and developed electrical and control systems for custom precision machine tools. Dr. Falter also worked for Rank Pneumo from 1994 to 1997.

DAVID YOUDEN

Senior Engineer, Olympic Precision, Inc.
Adjunct Lecturer, Department of Mechanical and Aerospace Engineering

ASME, Central New England College, Worcester, MA, 1965

Prior to joining Olympic Precision's Precision Valley Institute for Advanced Manufacturing in 2006, Mr. Youden was an Applied Research Engineer at Eastman Kodak Company's Manufacturing Systems Technology Division. Between 1984 and 1997 he was Research and Development Manager at Rank Pneumo, a division of Rank Taylor Hobson Inc. Before that, he was Director of Engineering at the Cone Blanchard Machine Company. He has also worked at Ocean Systems, Inc. of Reston, Virginia and the Heald Machine Company, a division of Cincinnati Milacron. During his professional career, Mr. Youden has been granted numerous patents in the field of machine tools, and he has published and presented technical papers on the design and testing of ultra-precision machine tools in the US, Japan, and Germany. In 2006, Mr. Youden received The American Society for Precision Engineering's Lifetime Achievement Award for his contributions to the field of precision engineering.

GRADUATE STUDENTS DURING 2007

DAVID BREHL's extensive industrial career includes a range of design, development, and project engineering roles with AERCO International, BOC Gases, and Babcock & Wilcox. A deepening interest in design of integrated electromechanical systems, along with a desire to focus his career on technology development, led him to pursue a PhD in Mechanical Engineering at NCSU; this follows a recent Master's in ME program at Stevens Institute of Technology (Hoboken, NJ). He joined the PEC in August 2004.

QUNYI CHEN first entered NCSU in 1997. obtaining a MSME in 1998 and a MSEE in 1999. After graduation, Qunyi worked at GE Healthcare to design and develop electro-mechanical subsystems for medical diagnostic X-ray equipment. His passion for technology development in precision electro-mechanical engineering led him to return to NCSU in 2005, where he was able to find an ideal match on the PEC's Fast Long Range Actuator project in June 2006. Qunyi was born and raised in Jiangsu, China. There, he received a BSME in 1993 and a MSME in 1996 before coming to the United States.

STEPHEN FURST is a native of Goshen, NY, came to NC State in 2003 to undertake a degree in Aerospace Engineering and run on the NCSU track and cross country teams. Stephen spent the summers after his junior and senior year at NASA studying Space Science and its applications. The PEC offered Stephen the opportunity to expand his skill set and gain valuable experience working on real-world engineering problems. After finishing a MSME, he hopes to continue to learn a systematic approach to technology development through PhD work.

TIM KENNEDY was born and raised in Chapel Hill, NC. Tim received his BS from NCSU in May 2004. Before working at the PEC, he worked at the Analytical Instrumentation Facility for two years as an undergraduate research assistant. He started working with the PEC August 2004.

LUCAS LAMONDS interned for RJ Reynolds, AMP and Getrag Gears. He began work at Getrag Gears in July 2002 and held the positions of Quality Engineer, Six Sigma Black Belt, and India-Joint Venture Project Engineer. Most recently, he managed the company's production yields, quality levels, and product launches for India. Lucas is scheduled to complete his master's degree in Spring 2007 and begin working for Micron Technology, Inc. in Boise, ID.

YANBO YIN received his BS and ME in Precision Instrument and Mechanology from Tsinghua University Beijing in 2000 and 2003, respectively. For his undergraduate thesis, he joined the micro-mechanical lab with experimental research on Micro-jet. For his master's degree, Yin developed a computer-aided system on wireless communication on-base station distribution. Currently, he is pursing his Ph.D. degree in Mechanical Engineering under the guidance of Dr. Ro. His research involves non-contact object transportation using ultrasonic.

GRADUATES OF THE PRECISION ENGINEERING CENTER

Student	Degree	Date	Company/Location
Jeffrey Abler	PhD	December 1994	ETEC Systems, Inc. Tucson, AZ
William Allen	PhD	December 1994	North Carolina State Univ. Raleigh, NC
Kelly Allred	MS	June 1988	
Christopher Arcona	PhD	May 1993	Norton Worcester, MA
Bradford Austin	MS	June 2000	IBM Corporation Fishkill, NY
Markus Bauer	PhD	December 2001	SCYNEXIS Chemistry & Automation, Inc. Research Triangle Park, NC
Tom Bifano	PhD	June 1988	Phillips Automation Pittsburgh, PA
Scott Blackley	MS	May 1990	Motorola Austin, TX
Peter Blake	PhD	December 1988	NASA Goddard Greenbelt, MD
Brett Brocato	MS	June 2005	Tessera North America Charlotte, NC
Nathan Buescher	MS	May 2005	Consolidated Diesel Rocky Mount, NC
Mark Cagle	MS	June 1986	NASA-Langley Norfolk, VA
John Carroll	PhD	January 1986	Cummins Engine Co. Columbus, IN

Matthew Cerniway	MS	October 2001	Naval Surface Warfare Ctr West Bethesda, MD
Damon Christenbury	MS	June 1985	Michelin Tire Co. Spartanburg, SC
Stuart Clayton	MS	May 2003	Naval Depot Cherry Point
James Cuttino	PhD	December 1994	UNC – Charlotte Charlotte, NC
Bob Day	PhD	July 1998	Los Alamos National Lab Los Alamos, NM
Joseph Drescher	PhD	May 1992	Pratt & Whitney East Hartford, CT
William Enloe	MS	December 1988	ITT Roanoke, VA
Karl Falter	MS	December 1989	Eastman Kodak Company Raleigh, NC
Peter Falter	PhD	May 1990	Lockheed-Martin Orlando, Florida
John Fasick	MS	May 1998	Kodak Rochester, NY
Steven Fawcett	PhD	June 1991	MicroE Natick, MA
Karalyn Folkert	MS	May 2005	Consolidated Diesel Rocky Mount, NC
Andre Fredette	PhD	May 1993	IBM Research Triangle Park, NC
Karl Freitag	MS	August 2004	Northrop Grumman Baltimore, MD
David Gill	PhD	August 2002	Sandia National Laboratories Albuquerque, NM

Jim Gleeson	MS	June 1986	Battelle Columbus Labs Columbus, OH
Mary Smith Golding	MS	May 1990	Harris Corporation Melbourne, FL
David Grigg	PhD	August 1992	Zygo Corporation Middlefield, CT
Hector Gutierrez	PhD	October 1997	Florida Inst. Of Tech. Melbourne, FL.
Christian Haeuber	MS	December 1996	Harris Corporation Melbourne, FL
Simon Halbur	MS	December 2004	
Matias Heinrich	MS	July 2001	Vistakon Jacksonville, FL
Gary Hiatt	PhD	May 1992	Caterpillar Zebulon, NC
David Hood	MS	May 2003	
Peter Hubbel	MS	December 1991	Delco Electronics Kokomo, IN
Konrad Jarausch	PhD	December 1999	Intel Corporation San Jose, CA
Bradley Jared	PhD	December 1999	Sandia National Laboratories Albuquerque, NM
David Kametz	MS	August 2002	Naval Air Warfare Center Aircraft Division Patuxent River, MD
Jerry Kannel	PhD	June 1986	Battelle Columbus Labs Columbus, OH
Byron Knight	MS	May 1990	US Air Force Washington, DC

Mark Landy	MS	June 1986	Battelle Columbus Labs Columbus, OH
Mike Loewenthal	MS	December 1988	SVG Norwalk, CT
Michael Long	PhD	June 2000	Eastman Kodak Rochester, NY
Bryan Love	MS	May 2001	Virginia Tech
Michael Hung-Tai Luh	MS	June 1989	Proctor and Gamble Cincinnati, OH
Dan Luttrell	MS	1987	Luttrell, Inc. New Boston, NH
Edward Marino	MS	September 1999	Pratt Whitney Hartford, CT
Edward Miller	MS	December 2000	General Electric Greenville, SC
Michele Miller	PhD	December 1994	Michigan Tech. University Houghton, MI
Paul Minor	MS	September 1998	Hartford, CT
Gary Mitchum	MS	June 1987	Harris Corporation Melbourne, FL
Charles Mooney	MS	December 1994	AIF – NC State University Raleigh, NC
Patrick Morrissey	MS	May 2003	
Larry Mosley	PhD	June 1987	Intel Corporation Chandler, AZ
Patrick Moyer	PhD	May 1993	UNC-Charlotte Charlotte, NC
Nobuhiko Negishi	MS	August 2003	
Ayodele Oyewole	MS	October 1997	Barnes Aircraft East Hartford, CT

Hakan Ozisik	PhD	December 1989	
Witoon Panusittikorn	PhD	December 2004	Fabrinet Kookot, Lumlookka Thailand
John Pellerin	MS	May 1990	Sematech Austin, TX
Travis Randall	MS	August 2004	MBA student NCSU
Ganesh Rao	MS	December 1994	Oak Ridge National Lab Oak Ridge, TN
John Richards	MS	September 1997	Intel Corporation San Jose, CA
Walter Rosenberger	MS	May 1993	The East Group Kinston, NC
Alex Ruxton	MS	December 1996	Pratt &Whitney Palm Beach, Florida
Anthony Santavy	MS	August 1996	Ford Dearborn, MI
Keith Sharp	PhD	May 1998	Morgan Crucible Dunn, NC
Gordon Shedd	PhD	March 1991	
Wonbo Shim	PhD	May 2000	Seagate Inc. Oklahoma City, OK
Robert Skolnick	MS	September 1997	San Diego, CA
Denise Skroch	MS	May 1989	IBM Corporation Raleigh, NC
Elizabeth Smith	MS	April 1989	
Stanley Smith	PhD	May 1993	

Ronald Sparks	PhD	May 1991	Alcoa Corporation Pittsburg, PA
Brent Stancil	MS	December 1996	Harris Corporation Melbourne, FL
Gene Storz	MS	May 1994	
Anand Tanikella	PhD	August 1996	Norton Industrial Ceramics Northboro, MA
Donna Thaus	MS	May 1996	Northern Telecom Research Triangle Park, NC
John Thornton	MS	December 1993	Digital Instruments Santa Barbara, CA
Michael Tidwell	MS	December 1991	
John Tyner	MS	June 1995	Naval Depot Cherry Point
Nadim Wanna	MS	December 2006	ExxonMobil Corporation Houston, TX
Robert Woodside	MS	December 2006	Harris Corporation Melbourne, FL
Tao Wu	PhD	December 2003	
Yanbo Yin	PhD	October 2007	

ACADEMIC PROGRAM

Problems and limitations associated with precision manufacturing can originate in the machine, the process, or the material. In fact, most problems will probably be caused by a combination of these factors. Therefore, improvement of current processes and development of new manufacturing methods will require knowledge of a multi-disciplinary array of subjects. The educational goal of the Precision Engineering Center is to develop an academic program which will educate scientists and engineers in metrology, control, materials, and the manufacturing methods of precision engineering.

The graduate students involved in the Precision Engineering Center have an annual stipend as research assistants. They can take up to 3 classes each semester while spending about 20 hours per week on their research projects. These students also work in the Center full-time during the summer months.

The Precision Engineering Center began in 1982 with an emphasis on the mechanical engineering problems associated with precision engineering. As a result, the original academic program proposed was biased toward courses related to mechanical design and analysis. However, as the research program has developed, the need for complementary research in sensors, materials, and computers has become obvious. A graduate student capable of making valuable contributions in the computer area, for example, will require a significantly different academic program than in mechanical engineering. For this reason, the Center faculty has set a core curriculum and each student in the program is required to take at least 3 of these core courses. The remainder of the courses for the MS or the PhD degree are determined by the university or department requirements and the faculty committee of the student.

The required courses are:

- MAE 545 Metrology in Precision Manufacturing
- PY 516 Physical Optics
- MAT 700 Modern Concepts in Materials Science
- CSC (ECE) 714 Real Time Computer Systems

PhD DEGREE PROGRAM

The PhD program in Precision Engineering has been set up as a multi-disciplinary program, drawing upon courses throughout the University to provide background and expertise for the students. It should contain required courses to insure solid grounding in the fundamentals plus electives to prepare the student in his area of specialization. Because Precision Engineering is concerned with an integrated manufacturing process, students interested in computer control, materials, machine structure, and measurement and actuation systems are involved in the program. Student research projects include the wide variety of topics addressed in this report. Each student's thesis should have an experimental component because Precision Engineering is basically a hands-on technology.

MS DEGREE PROGRAM

The Master of Science degree will have a higher percentage of application courses than the PhD degree. The emphasis will be to develop the foundation for involvement in precision engineering research and development. A total of 30 credits, including 6 credits for the MS thesis, are required. The thesis, while less comprehensive than the PhD dissertation, will be directed at important problems in Precision Engineering. Typically, the MS program will take four semesters plus one summer.

UNDERGRADUATE PROGRAM

The undergraduate degree broadly prepares an engineering student for industrial activities ranging from product design and engineering sales to production implementation. Because a large share of engineers only have the BS degree, these will be the people who must implement the new technology developed in research programs like the Precision Engineering Center. Therefore, a way must be found to acquaint engineers at the BS level with the techniques, problems, and potential of precision manufacturing.

In most undergraduate degree programs only limited time is available for technical electives. However, these electives offer the student the opportunity to expand his knowledge in many different directions. Beginning graduate courses (such as metrology) can be used as undergraduate electives.

Undergraduate projects and summer employment have also been utilized to include undergraduate students into the research program of the Center. During the 1998-1999 academic year, four undergraduate students in Mechanical Engineering were involved various projects at the PEC.

STUDY PLANS

Study plans for several example students are given below both for the MS and the PhD degree. Because of the breadth of the field and the wide range of thesis topics, few if any study plans will be exactly the same. The plan will depend upon the student's background, his interests, his thesis topic, the department, and the chairman and members of his committee.

PhD PROGRAM IN MECHANICAL ENGINEERING

Major Courses:

- MAE 740 Advanced Machine Design I
- MAE 741 Advanced Machine Design II
- MAE 706 Heat Transfer Theory & Applications
- MAE 713 Principles of Structural Vibration
- MAE 760 Computational Fluid Mechanics and Heat Transfer
- MAE 545 Metrology in Precision Manufacturing
- MAE 715 Nonlinear Vibrations
- MAE 716 Random Vibration
- MAE 714 Analytical Methods in Structural Vibration
- MAE 742 Mechanical Design for Automated Assembly
- MAE 895 Doctoral Dissertation Research

Minor Courses:

- MA 511 Advanced Calculus I
- MA 775 Mathematical Methods in the Physical Sciences I
- CSC 780 Numerical Analysis II
- PY 516 Physical Optics
- ECE 716 System Control Engineering
- MAT 700 Modern Concepts in Materials Science
- ECE 726 Advanced Feedback Control
- ECE 764 Digital Image Processing

PhD PROGRAM IN MATERIALS ENGINEERING

Major Courses:

- MAT 710 Elements of Crystallography and Diffraction
- MAT 700 Modern Concepts in Materials Science
- MAT 556 Composite Materials
- MAT 715 Transmission Electron Microscopy
- MAT 795 Defect Analysis/Advanced Materials Experiments
- MAT 753 Advanced Mechanical Properties of Materials
- MAT 712 Scanning Electron Microscopy
- MAT 895 Doctoral Dissertation Research

Minor Courses:

- PY 414 Electromagnetism I
- ST 502 Experimental Statistics for Engineers I
- MAE 740 Advanced Machine Design I
- MAE 741 Advanced Machine Design II
- MAE 545 Metrology in Precision Manufacturing
- PY 516 Physical Optics
- MA 401 Applied Differential Equations II

PhD PROGRAM IN ME (FOR STUDENT WITH MS DEGREE)

- ECE 716 System Control Engineering
- ECE 791 Gate Array Design
- MAT 700 Modern Concepts in Materials Science
- PY 516 Physical Optics
- MA 502 Advanced Mathematics for Engineers and Scientists II
- MA 775 Mathematical Methods in the Physical Sciences I
- MA 780 Numerical Analysis II
- MAE 732 Fundamentals of Metal Machining Theory
- MAE 740 Advanced Machine Design I
- MAE 741 Advanced Machine Design II

- MAE 545 Metrology in Precision Manufacturing
- MAE 716 Random Vibration

MS PROGRAM FOR ME STUDENT

- MAE 713 Principles of Structural Vibration
- MAE 740 Advanced Machine Design I
- MAE 545 Metrology in Precision Manufacturing
- MAT 700 Modern Concepts in Materials Science
- PY 516 Physical Optics
- MA 501 Advanced Math for Engineers and Scientists I
- MA 502 Advanced Math for Engineers and Scientists II
- MAE 695 Master's Thesis Research

MS PROGRAM FOR COMPUTER SCIENCE STUDENT

- CSC 501 Operating Systems Principles
- CSC 506 Architecture of Parallel Computers
- CSC 512 Compiler Construction
- ECE 521 Computer Design and Technology
- CSC 715 Concurrent Software Systems
- MAE 545 Metrology for Precision Manufacturing
- MAE 789 Digital Control Systems
- ECE 764 Digital Image Processing

MS PROGRAM FOR MATERIALS SCIENCE STUDENT

- MAT 700 Modern Concepts in Material Science
- MAT 710 Elements of Crystallography and Diffraction
- MAT 715 Transmission Electron Microscopy
- MAT 712 Scanning Electron Microscopy
- MAT 722 Advanced Scanning Electron Microscopy and Surface Analysis
- MAE 545 Metrology for Precision Manufacturing
- PY 516 Physical Optics
- ECE 738 IC Technology and Fabrication
- MAT 695 Master's Thesis Research

MS PROGRAM FOR PHYSICS STUDENT

- PY 516 Physical Optics
- PY 552 Introduction to Structure of Solids I
- PY 753 Introduction to Structure of Solids II
- PY 781 Quantum Mechanics I
- PY 782 Quantum Mechanics II
- PY 783 Advanced Classical Mechanics
- PY 785 Advanced Electricity and Magnetism I
- PY 786 Advanced Electricity and Magnetism II
- MAT 700 Modern Concepts in Material Science
- MAE 545 Metrology for Precision Manufacturing
- PY 695 Master's Thesis Research

SHORT COURSES AND TV COURSES

Six graduate level courses: Scanning Electron Microscopy (MAT 712), Advanced SEM Surface Analysis (MAT 722), Modern Concepts in Material Science (MAT 700), Mechanical Properties of Materials (MAT 705), and Metrology (MAE 545) have been offered as video courses nationwide via National Technological University. In a typical year, approximately 120 students from industry and national laboratories participate in these courses. Future plans call for a MS program in Precision Engineering to be offered via the television network.

TECHNICAL REPORTS

Volume 1 - 1983	December 1983	136 pages
Volume 2 - 1984	January 1985	168 pages
Volume 3 - 1985	January 1986	294 pages
Volume 4 - 1986	January 1987	255 pages
Volume 5 - 1987	December 1987	336 pages
Volume 6 - 1988	December 1988	362 pages
Volume 7 - 1989	March 1990	357 pages
Volume 8 - 1990	March 1991	385 pages
Volume 9 - 1991	March 1992	382 pages
Volume 10 - 1992	March 1993	289 pages
Volume 11 - 1993	March 1994	316 pages
Volume 12 - 1994	March 1995	268 pages
Volume 13 - 1995	January 1996	251 pages

Volume 14 - 1996	January 1997	232 pages
Volume 15 - 1997	January 1998	298 pages
Volume 16 – 1998	January 1999	258 pages
Volume 17 – 1999	January 2000	232 pages
Volume 18 – 2000	January 2001	274 pages
Volume 19 – 2001	January 2002	201 pages
Volume 20 – 2002	January 2003	328 pages
Volume 21 - 2003	January 2004	208 pages
Volume 22 – 2004	February 2005	207 pages
Volume 23 – 2005	February 2006	264 pages
Volume 24 – 2006	March 2007	274 pages

PUBLICATIONS

PAPERS PUBLISHED

1. Q. Chen, T. Dow and K. Garrard, A. Sohn *Fast Long Range Actuator (FLORA)*. Proceedings of the Twenty-Second Annual Meeting of the ASPE (2007).

2. D. Brehl and T. Dow, *Review of Vibration-Assisted Machining,* Precision Engineering, Vol.32 (2008)

3. D. Brehl, T. Dow, K. Garrard and A. Sohn, *Millimeter-Scale Reflecting Optics Fabricated Using Elliptical Vibration-Assisted Machining (EVAM),* Proceedings of the ASPE, vol. 42, pp.363-367 (2007)

4. D. Brehl and T. Dow, *3-D Microstructure Fabrication Using Elliptical Vibration-Assisted Machining,* Proceedings of the ASPE, vol. 40, pp. 21-25 (2007)

5. D. Brehl, MA. Cerniway, T. Dow and N. Negishi, *Machining Forces for Elliptical Vibration-Assisted Machining,* Proceedings of the ASPE, vol. 40, pp. 71-75 (2007)

6. CC Koch, RO Scattergood and KL Murty, *The Mechanical Behavior of Multiphase Nanocrystalline Materials, Jour. of Metals*, 2007 pp. 66.

7. KA Darling, CL Reynolds, DN Leonard, G. Duscher, RO Scattergood and CC Koch, *Self-Assembled Three-Dimensional Cu-Ge Nanoweb Composite*, Nanotechnology, in press (2008).

8. S Jang, Y Purohit, D Irving, C Padgett, D Benner and RO Scattergood, *Molecular Dynamics Simulations of Deformation in Nanocrystalline Al-Pb Alloys,* Acta Materialia, in review (2008).

9. K. A. Darling, RK Guduru, CL Reynolds, VK Bhosle, RO Scattergood, CC Koch, J Narayan and MO Aboelfotoh, *Themal Stability, Mechanical and Electrical Properties of Nanocrystalline Gu_3Ge*, Intermetallics, in press (2008).

10. KV Rajulapati, RO Scattergood, KL Murty, Z Horita, TG Langdon and CC Koch, *Mechanical Properties of Bulk Nanocrystalline Aluminum-Tungsten Alloys*, Met. Trans., in press (2008).

11. S Jang, Y Purohit, D Irving, C Padgett, D Brenner and RO Scattergood, *Mocelcular Dynamics Simulations of Deformation in Nanocrystalline Al-Pb Alloys* Mat. Sci. Engr. A, in press (2008).

12. RO Scattergood, CC Koch, KL Murty and D Brenner, *Strengthening Mechanisms in Naocrystalline Alloys*, Mat. Sci. Engr. A, in press (2008).

13. RK Guduru, AV Nagasekhar, RO Scattergood, CC Koch and KL Murty, *Thickness and Clearance Effects in Shear Punch Testing*, Adv. Engr. Materials, 9, no 3 (2007) pp 1.

REPORTS PUBLISHED

1. T. Dow, K. Garrard, A. Sohn, *Final Report to Lexmark, Phase I – Fresnel Scanning Lens Design*. Precision Engineering Center (2007).

2. K. Garrard, T. Dow and A. Sohn. *Final Report to Vistakon, Enhancement of Dynamic Error Compensation.* Precision Engineering Center (2007).